



Forschungszentrum Karlsruhe
in der Helmholtz-Gemeinschaft

Wissenschaftliche Berichte
FZKA 6876

**Proceedings of the
4th MEGAPIE Technical
Review Meeting**

Paris, France March 18 – 19, 2003

Editors

C. Fazio, J.U. Knebel

Programm Nukleare Sicherheitsforschung

F. Gröschel

Paul Scherrer Institut, Villigen, Switzerland

Dezember 2003

Forschungszentrum Karlsruhe

in der Helmholtz-Gemeinschaft

Wissenschaftliche Berichte

FZKA 6876

**Proceedings of the 4th
MEGAPIE Technical Review Meeting**

Paris, France

March 18 – 19, 2003

Editors

C. Fazio, F. Gröschel*, J.U. Knebel

Programm Nukleare Sicherheitsforschung

* Paul Scherrer Institut, Villigen, Switzerland

Forschungszentrum Karlsruhe GmbH, Karlsruhe

2003

Impressum der Print-Ausgabe:

**Als Manuskript gedruckt
Für diesen Bericht behalten wir uns alle Rechte vor**

**Forschungszentrum Karlsruhe GmbH
Postfach 3640, 76021 Karlsruhe**

**Mitglied der Hermann von Helmholtz-Gemeinschaft
Deutscher Forschungszentren (HGF)**

ISSN 0947-8620

Preface

The fourth technical review meeting of the **MEGA**watt **P**ilot **E**xperiment (MEGAPIE) took place on 18 - 19 March, 2003 in Paris, in coincidence with the finalisation of the detailed design and the launching of the manufacturing phase (phase 5) of the project. The present volume contains the proceedings of this technical review meeting. The 36 contributions presented at the meeting, coming from Europe, USA, Japan and Korea, pointed out once more the international frame of the initiative, which is supported by six European research institutions (PSI, CEA, FZK, CNRS, ENEA, SCK), by JAERI (Japan), DOE (USA) and KAERI (Korea).

A wide range of topics were covered during the meeting including a project overview, the target and the ancillary systems designs, safety and licensing aspects and relevant results from the working group of R&D design support obtained during year 2002.

The overview of the project did show significant progress. Indeed, it was shown that the target design is almost completed and the manufacturing phase has been launched. Further, in the case of the Electro Magnetic Pump, which was designed and developed at IPUL (Riga), performance tests were done showing adequate results. As another example, the design of the Target Heat Exchanger (THX), which consists of a single annulus of 12 cooling pins able to evacuate 650 kW from Pb-Bi, was finalised.

The design of the Ancillary systems (Heat Removal System (HRS), Cover Gas System (CGS), Liquid Metal Fill and Drain (F&D) System and Insulating Gas System (IGS)) is also progressing. In particular the reference solution for the CGS is to periodically drain the gas in a decay tank. As for the filling and draining procedure, a conceptual design for draining the irradiated Lead – Bismuth Eutectic (LBE) has been defined; nevertheless the non-active drain, i.e. the LBE freezing inside the target after the irradiation phase, is under technological evaluation.

Safety and licensing issues were also addressed. Examples are the focused beam transient and the thermal shock transient. For both cases CFD calculations and stress analysis were performed. Further, to directly monitor the intensity distribution of the incident proton beam and to switch off the beam quickly in case of anomalies, a Visual Monitor System (VIMOS) is under development and experimental validation was shown.

Throughout the design phase, the MEGAPIE project management as well as the designer have required significant development to the R&D working group. This group carries out theoretical and experimental activities in the frame of six research areas, i.e. thermal hydraulics, structural mechanics, neutronics and nuclear assessment, materials radiation damage, solid – liquid interface and liquid metal technology. The quantity and quality of the work performed in the frame of the MEGAPIE R&D group has been recognised. Some of the important activities and results obtained by the R&D group are summarised hereafter.

In the frame of the thermal hydraulic and structural mechanics task, a large amount of CFD calculations and stress analysis have been performed according to the needs expressed by the designers. At the meeting the following topics were presented: a) RELAP 5 Analysis of the MEGAPIE target thermal hydraulics in steady state and transient conditions; b) CFD simulation on the heat deposition distribution in the target; c) Stress analysis of the liquid metal container under normal operating conditions; d) the HYTAS water experiment, performed to investigate the cooling

characteristics of the MEGAPIE beam window and the 3D-CFD simulations associated to the experiment; e) the LBE KILOPIE and Heated Jet experiments, both under preparation;

The Neutronics and Nuclear Assessment task group has performed detailed benchmark exercises and a compilation was produced. During the meeting it was agreed to use MCNPX and FLUKA codes as reference tools for the project.

A presentation on microfission chambers to be inserted in the central rod of the target was given. It has been pointed out that issues still to be clarified are related to the performance of the chambers at high temperature and strong thermal transients. Moreover, during the discussion it was pointed out that a clear definition of the objectives of the experiment is still missing.

Materials radiation damage task group has produced data on the mechanical properties of T91 steel at high temperature. These data were used for the safety analysis. In addition, an attempt was made to estimate the window lifetime using DBTT as a criterion. Further, the risk of failure of the window was evaluated using linear elastic fracture mechanics. Finally, despite the fact that the synergetic liquid metal effect was not taken into account, studies indicated that an increase of the window temperature was favourable in order to enhance the window performance.

Compatibility tests on bare and welded T91 steel were performed in the frame of the solid - liquid interface task. Tests were performed at the laboratories of different associations, and a comprehensive compilation of the results seems to be mandatory. In addition, instantaneous liquid metal embrittlement, fatigue tests and tensile tests on T91 steel exposed to LBE were done. For the mechanical properties degradation a compilation of the experimental results is also expected. Further, the window material protection against liquid metal corrosion / embrittlement with artificial coatings is under evaluation.

Progress in the LISOR experiments was shown. In fact a successful assembling and disassembling of the LISOR test section has been shown. In addition, tensile test on T91 exposed for 24 h at 300 °C and irradiated for one hour did show ductile fracture mode. Further experiments in representative conditions (e.g. irradiation length) are expected.

Finally, in the frame of the Liquid Metal Technology task, different types of problems were successfully treated as, for instance, the LBE-coolant interactions, the evaluation of the use of oxygen control and monitoring method in the target, the Po issue and the LBE recrystallisation problem.

*CONCETTA FAZIO
FORSCHUNGSZENTRUM KARLSRUHE, GERMANY*

*FRIEDRICH GRÖSCHEL
PAUL SCHERRER INSTITUT, SWITZERLAND*

*JOACHIM KNEBEL
FORSCHUNGSZENTRUM KARLSRUHE, GERMANY*

Vorwort

Das vierte Technical Review Meeting der **MEGA**watt **P**ilot **E**xperiments (MEGAPIE) Initiative fand am 18./19. März 2003 in Paris statt. Die Initiative befindet sich augenblicklich in der detaillierten Design- und Herstellungsphase (Phase 5). Der vorliegende Band enthält die Proceedings dieses Technical Review Meetings. Die 36 Beiträge der Teilnehmer aus Europa, USA, Japan und Korea, verdeutlichten einmal mehr die internationale Einbindung der MEGAPIE Initiative, an der sechs Europäische Forschungseinrichtungen (PSI, CEA, FZK, CNRS, ENEA, SCK) sowie JAERI (Japan), DOE (USA) und KAERI (Korea) beteiligt sind.

Während des Meetings wurde ein breites Themenspektrum vorgestellt, das neben der Projekt-Übersicht das Design des Targets und der Hilfssysteme, die Sicherheits- und Genehmigungsaspekte und die Ergebnisse der F+E- Arbeitsgruppe umfasste.

Aus der Projekt-Übersicht wurde ersichtlich, dass beträchtliche Fortschritte erzielt wurden. Das Target-Design ist nahezu beendet und die Herstellungsphase ist angelaufen. Weiterhin wurde die elektromagnetische Pumpe, die bei IPUL (Riga) entworfen und entwickelt worden war, mit guten Ergebnissen getestet. Ein weiteres Beispiel für die erzielten Fortschritte ist die Tatsache, dass das Design des Target-Wärmetauschers (THX) abgeschlossen werden konnte. Er besteht aus einem einzelnen Ring mit 12 Kühlstäben und kann 650 kW aus dem Pb-Bi abführen.

Auch beim Design der Hilfssysteme (Wärmeabfuhrsystem (HRS), Schutzgassystem (CGS), System zum Einfüllen und Entleeren des Flüssigmetalls (F&D) und Isoliergassystem (IGS)) konnten gute Fortschritte erzielt werden. So sieht zum Beispiel die Referenzlösung für das CGS vor, das Gas regelmäßig in einen Abklingtank zu entleeren. Für das F&D wurde ein vorläufiges Design entwickelt, um das Target mit LBE zu füllen und am Ende des Experiments das bestrahlte Blei – Wismut Eutektikum (LBE) aus dem Target zu entleeren. Für dieses Hilfssystem wird eine zweite Möglichkeit evaluiert: Abkühlung des LBE nach der Bestrahlungsphase und Einfrieren im Targetcontainer selbst.

Auch Sicherheits- und Genehmigungsaspekte wurden behandelt, zum Beispiel der Einfluss eines fokussierten Protonenstrahls und eines Thermoschocks auf die Strahlfensterintegrität. Für beide Fälle wurden CFD-Rechnungen und Festigkeits-Analysen durchgeführt. Weiterhin wurde ein Visuelles Monitoring-System (VIMOS) entwickelt und experimentell validiert. Es dient dazu, die Intensitätsverteilung des Protonenstrahls direkt zu überwachen und bei Abweichungen den Strahl abschalten zu können.

Während der gesamten Design-Phase forderten sowohl das MEGAPIE-Projektmanagement als auch die Design-Gruppe umfangreiche Entwicklungsarbeiten von der F+E-Arbeitsgruppe. Diese Gruppe führt theoretische und experimentelle Aktivitäten auf sechs Teilgebieten durch: Thermohydraulik, Strukturmechanik, Neutronenphysik, Materialschädigung durch Bestrahlung, Wechselwirkung Flüssigmetall-Wand und Flüssigmetalltechnologie. Die Vielzahl und das Niveau der von der MEGAPIE F+E-Gruppe durchgeführten Arbeiten wurde während des Meetings bestätigt. Im Folgenden werden einige wichtige Arbeiten und Ergebnisse zusammengefasst.

Die Thermohydraulik und Strukturmechanik-Gruppe führte gemäß den Anforderungen der Design-Gruppe zahlreiche CFD-Rechnungen und Festigkeits-Analysen durch wie zum Beispiel: a) RELAP 5 Analyse zur MEGAPIE-Target-Thermohydraulik unter stationären- und transienten Bedingungen; b) CFD-Simulation der Wärmeverteilung im Target; c) Festigkeits-Analyse des

Flüssigmetallbehälters unter normalen Betriebsbedingungen; d) HYTAS Wasser-Experiment zur Untersuchung der Kühleigenschaften des MEGAPIE-Strahlfensters und die zu diesem Experiment gehörenden 3D-CFD Simulationen; e) die LBE Experimente KILOPIE und Heated Jet, die sich beide noch in der Vorbereitungsphase befinden.

Die Arbeitsgruppe Neutronenphysik hat detaillierte Benchmark-Rechnungen durchgeführt und analysiert. Es wurde beschlossen, dass die Codes MCNPX and FLUKA als Referenzwerkzeuge verwendet werden.

Es gab einen Beitrag zu den Miniaturspaltkammern, die im Zentralstab des Targets angebracht werden sollen. Es wurde betont, dass einige Punkte noch zu klären sind, wie etwa das Verhalten dieser Kammern bei hohen Temperaturen und bei starken Wärmetransienten. Bei der Diskussion wurde hervorgehoben, dass eine eindeutige Definition der Ziele dieses Experiments noch aussteht.

Die Arbeitsgruppe Materialschäden durch Bestrahlung hat Daten zu den mechanischen Eigenschaften des Stahls T91 bei hohen Temperaturen geliefert. Diese Daten wurden für Sicherheitsanalysen verwendet. Weiterhin wurde versucht, die Lebenszeit des Fensters abzuschätzen, wobei die Sprödbruchübergangstemperatur (DBTT) als Kriterium verwendet wurde. Auch das Risiko des Versagens des Fensters wurde mit Hilfe der elastischen Bruchmechanik bewertet. Es zeigte sich, dass sich eine höhere Fenstertemperatur günstig auf das Versprödungsverhalten auswirkt.

Verträglichkeitsuntersuchungen mit unbearbeitetem und geschweißtem T91 wurden im Rahmen der Arbeitsgruppe Wechselwirkung Flüssigmetall-Wand durchgeführt. Diese Untersuchungen wurden in den Laboratorien verschiedener Organisationen durchgeführt, so dass eine umfassende Zusammenstellung der Ergebnisse dringend erforderlich erscheint. Weiterhin wurden Untersuchungen zur Versprödung, zur Ermüdung und zur Zugfestigkeit von T91, das dem Flüssigmetall ausgesetzt war, durchgeführt. Auch über die Ergebnisse hinsichtlich der mechanischen Eigenschaften des Materials im Flüssigmetall wird eine Zusammenstellung erwartet. Weiter wird untersucht, inwieweit das Fenstermaterial mit Beschichtungen vor Flüssigmetallkorrosion und Versprödung geschützt werden kann.

Bei den ersten LISOR-Experimenten wurde ein Fortschritt erzielt. Die LISOR-Teststrecke konnte erfolgreich montiert und wieder zerlegt werden. Ein Zugversuch mit einer T91 Probe, die über 24 Stunden lang im Blei-Wismut bei einer Temperatur von 300°C ausgelagert und eine Stunde lang bestrahlt worden war führte zu einem Dehnungsbruch. Weitere Experimente unter repräsentativen Bedingungen (z.B. Bestrahlungsdauer) sollen durchgeführt werden.

Schließlich wurden im Rahmen der Arbeitsgruppe Flüssigmetalltechnologie verschiedene Fragestellungen behandelt, wie beispielsweise die Wechselwirkung zwischen LBE und Kühlmittel, die Bewertung der Sauerstoffkontrolle im Target, die Frage der Erzeugung von Polonium und die Ausdehnung des LBE im festen Zustand.

*CONCETTA FAZIO
FORSCHUNGSZENTRUM KARLSRUHE, GERMANY*

*FRIEDRICH GRÖSCHEL
PAUL SCHERRER INSTITUT, SWITZERLAND*

*JOACHIM KNEBEL
FORSCHUNGSZENTRUM KARLSRUHE, GERMANY*

INHALTSVERZEICHNIS

Session 0: Introduction – Chair: C. Fazio and M. Delpech

The MEGAPIE Project: Overview	1
<i>F. Groeschel</i>	
<i>Paul Scherrer Institut, 5332 - Villigen, CH</i>	

Session 1: Target and Ancillary – Chair: F. Gröschel and W. Wagner

MEGAPIE Target Design and Dimensioning	5
<i>T. Kirchner¹, A. Guertin¹, Y. Bortoli¹, A. Cadiou¹, Y. Foucher¹, J.S. Stutzmann¹, J.M. Gautier²</i>	
¹ <i>Subatech, Ecole des Mines de Nantes, 4 rue Alfred Kastler, BP 20722, F - 44307 Nantes cedex 3</i>	
² <i>LPC CAEN, ISMRA, 6 boulevard du Maréchal Juin, 14050 CAEN cedex, FRANCE</i>	
Prototype of the Electromagnetic Pump System for MEGAPIE Target: Design and Testing	23
<i>S.Dementjev¹, F.Groeschel¹, E.Platacis², S.Ivanov², A.Zik²</i>	
¹ <i>Paul Scherrer Institut, Villigen Switzerland CH-5332</i>	
² <i>Institute of Physics of Latvian University, Miera 32 Salaspils Latvia LV-2169</i>	
MEGAPIE Target Heat Exchanger Detailed Design	27
<i>L. Cachon, G. Laffont, J.M. Zuena, F. Dechellette</i>	
<i>CEA - France</i>	
Heat Removal System: Final Update of Concept and Detail Design, Dimensional and Functional Issues	34
<i>G. Corsini¹, M. Dubs², B. Sigg³, W. Wagner²</i>	
¹ <i>ANSALDO Nucleare, Genova, Italy</i>	
² <i>Paul Scherrer Institut, CH-5232 Villigen-PSI, Switzerland</i>	
³ <i>ETHZ-LKT, CH-5232 Villigen PSI, Switzerland</i>	
Cover Gas System: Updated Boundary Conditions and Current Concept	40
<i>W. Wagner¹, F. Gröschel¹, G. Corsini²</i>	
¹ <i>Paul Scherrer Institut, CH-5232 Villigen-PSI, Switzerland</i>	
² <i>ANSALDO Nucleare, Genova, Italy</i>	
Fill & Drain and Freezing: System Modifications for merely non-active draining	46
<i>W. Wagner¹, P. Turroni², P. Agostini², K. Thomsen¹, E. Wagner¹, J. Welte¹</i>	
¹ <i>Paul Scherrer Institut, CH-5232 Villigen-PSI, Switzerland</i>	
² <i>ENEA, Italy</i>	
Insulation gas system of MEGAPIE: A concept update	52
<i>W. Wagner¹, J. Welte¹, S. Joray¹, B. Sigg²</i>	
¹ <i>Paul Scherrer Institut, CH-5232 Villigen-PSI, Switzerland</i>	
² <i>LKT ETHZ, CH-5232 Villigen PSI, Switzerland</i>	
Target Handling: Concept for Transport and Dismantling	58
<i>A. Strinning, E. Wagner, A. Janett, F. Groeschel</i>	
<i>Paul Scherrer Institut, CH-5232 Villigen-PSI, Switzerland</i>	
On the preparation of the MEGAPIE Integral Test	64
<i>W.H. Leung¹, B. Sigg², J. Welte¹, S. Joray¹, F. Groeschel¹</i>	
¹ <i>Spallation Neutron Source (ASQ), Paul Scherrer Institut, Villigen, CH-5323</i>	
² <i>ETHZ-LKT, Villigen-PSI, CH 5323, Switzerland</i>	

Summary on Ancillary systems 77
Werner Wagner
Paul Scherrer Institut, CH-5232 Villigen, CH

Session 2: Safety and Licensing Issues – Chair: K. Woloshun and G. Laffont

CFD Simulation of Focused-Beam Transient 79
T. V. Dury
Thermal-Hydraulics Laboratory, Nuclear Energy and Safety Department, Paul Scherrer Institute, CH

Thermal Shock Transient: CFD Simulation of Water Jet Impaction on Target Window 83
B. L. Smith
Thermal-Hydraulics Laboratory, Nuclear Energy and Safety Department, Paul Scherrer Institute CH

Stress analysis of the LMC under accident conditions 87
A. Zucchini¹, B. L. Smith²
¹UTS Tecnologie Fische Avanzate, Sezione Metodologie e Diagnostiche, ENEA, Bologna, Italy
²Thermal-Hydraulics Laboratory, Nuclear Energy and Safety Department, Paul Scherrer Institute, CH

First Results with the Visual Monitor VIMOS 93
Knud Thomsen
Spallation Neutron Source Division (ASQ), PSI, CH-5232 Villigen PSI, Switzerland

Session 3: Thermal hydraulics & SM – Chair: B. Smith and B. Sigg

RELAP5 Analysis of the MEGAPIE Target 114
W.H. Leung¹, M. Petrazzini², A. Alembert²
¹Paul Scherrer Institute, Spallation Neutron Source, CH 5232, Villigen-PSI, Switzerland
²Ansaldo Nucleare, Divisione di ANSALDO ENERGIA S.p.A., Genova, Italy

CFD analysis of lower target: Latest steady-state simulations 124
T. V. Dury
Thermal-Hydraulics Laboratory, Nuclear Energy and Safety Department, Paul Scherrer Institute, CH

Stress Analysis of LMC under normal operating conditions 131
A. Zucchini¹, B. L. Smith²
¹UTS Tecnologie Fische Avanzate, Sezione Metodologie e Diagnostiche, ENEA, Bologna, Italy
²Thermal-Hydraulics Laboratory, Nuclear Energy and Safety Department, Paul Scherrer Institute, CH

Thermohydraulic investigations for MEGAPIE: The HYTAS- KILOPIE and Heated Jet Experiments 134
S. Gnieser¹, M. Daubner¹, C.-H. Lefhalm¹, F. Fellmoser¹, K.-J. Mack¹, H. Piecha¹ and R. Stieglitz¹
J. Patorski², I. Platnieks²
¹Institute For Nuclear And Energy Technologies (IKET), Forschungszentrum Karlsruhe, Post Box 3640, D-76021 Karlsruhe, Germany
²Paul Scherrer Institute, Ch-5202 Villigen, Switzerland

CFD analysis of the flow behaviour in a spallation target 144
A.Batta, N. I. Tak, G. Grötzbach, X. Cheng
Forschungszentrum Karlsruhe GmbH, Institut für Kern- und Energietechnik, Postfach 3640, 76021 Karlsruhe, Germany

Session 4: Nuclear Assessment + Materials & Radiation Damage – Chair: J. Henry

- Nuclear Assessment of the MEGAPIE Target 149
Y. Foucher
Spallation group, SUBATECH Laboratory, 4 rue Alfred Kastler, BP 20722, F-44307 Nantes Cedex 3
- Fission chambers for neutron flux measurements: Status report 162
A. Letourneau¹, M. Fadil¹, F. Marie¹, D. Ridikas¹, J.C. Toussaint¹, C. Veyssièrè¹,
Ch. Blandin²
¹CEA/DSM/DAPNIA, ²CEA/DEN/SPEX/LPE - France
- Triple ion beam tests for window materials of spallation targets 166
M.Futakawa¹, Y.Kurata¹, J. Henry², I. Ioka³, S. Saito¹, A. Naito³
¹Center for Proton Accelerator Facilities, JAERI
²CEA /Saclay
³Department of Nuclear Energy System, JAERI
- Discussion on the lifetime of the target based on preliminary STIP results 172
Yong Dai
Paul Scherrer Institut, 5232 Villigen PSI, Switzerland
- Risk of brittle failure of the Pb-Bi container window: A tentative Assessment 184
J. Henry
CEA /Saclay - France

Session 5: LM Technology + Solid-Liquid Interface Chair: J. Konys and P. Agostini

- Main results of static and dynamic corrosion tests in oxygen-saturated liquid PbBi 190
Y. Kurata, K. Kikuchi, S. Saito, M. Futakawa and T. Sasa
Center for Proton Accelerator Facilities, Japan Atomic Energy Research Institute
- Corrosion behavior of steels and refractory metals in flowing Pb-Bi 199
B.Long^{2**}, G.Scaddozzo³, C.Fazio^{1***}, M.Agostini¹, A.Aiello¹, G.Benamati¹
¹ENEA C.R. Brasimone, 40032 (BO), Italy
²China Institute of Atomic Energy, 102413 Beijing, China
³Politecnio di Torino, Corso Duca degli Abruzzi 24, I-10129 Torino, Italy
***Presently at Forschungszentrum Karlsruhe
- Influence of hydrodynamics on the corrosion of martensitic steel T91 in liquid Pb-Bi. Comparison between experiments and theoretical calculations 211
F. Balbaud-Célériér, C. Delisle, A. Terlain,
Service de la Corrosion et du Comportement des Matériaux dans leur Environnement CEA/Saclay – 91191 Gif sur Yvette Cedex - France
- Static PbBi corrosion tests of 316LN and ferritic-martensitic steels 219
T. Y. Song¹, J. E. Cha¹, C. H. Cho¹, G. Mueller², A. Heinzel², J. Konys³
¹Korea Atomic Energy Research Institute, P.O. Box 105 Yuseong, Daejeon, 305-600 Korea
²Forschungszentrum Karlsruhe GmbH, Institut fuer Hochleistungsimpuls- und Mikrowellentechnik, Postfach 3640, 76021, Karlsruhe, Germany
³Forschungszentrum Karlsruhe GmbH, Institut fuer Materialforschung III, Postfach 3640, 76021, Karlsruhe, Germany

Corrosion of welded T91 specimen in PbBi: results of a corrosion test in CYCLAD device	226
<i>A. Terlain, F. Balbaud-Célérier, C. Delisle</i>	
<i>Service de la Corrosion et du Comportement des Matériaux dans leur Environnement</i>	
<i>CEA/Saclay – 91191 Gif sur Yvette Cedex - France</i>	
Inspection of the first LISOR test section	231
<i>H. Glasbrenner, R. Brütsch, F. Gröschel</i>	
<i>Paul Scherrer Institut, 5232 Villigen PSI, CH</i>	
Summary on Solid Liquid Interface	237
<i>J. Konys</i>	
<i>Forschungszentrum Karlsruhe GmbH, IMF III, Postfach 3640, 76021, Karlsruhe, Germany</i>	
Experimental results from DTHT-LBE interaction experiments and DTHT irradiation tests	239
<i>Waihung Leung¹, Eyke Wagner¹, Keith Woloshun²</i>	
<i>¹Paul Scherrer Institute - CH</i>	
<i>²Los Alamos National Laboratory - USA</i>	
Pb-Bi eutectic recrystallization studies for MEGAPIE target	244
<i>Alberto Zucchini¹, Pietro Agostini², Elio Baicchi³</i>	
<i>¹ENEA FIS MET, ²ENEA FIS ING, ³ENEA FIS MET - Italy</i>	
<u>Annexes</u>	257
MEGAPIE design concerns (DOE)	
<i>K. O. Pasamehmetoglu, LANL, USA</i>	
Fatigue experiments on T91 steel in Pb-Bi	
<i>I. Serre</i>	
<i>CNRS - France</i>	
Importance of surface state of steel T91 regarding its mechanical properties In stagnant Lead or Lead-Bismuth Eutectic	
<i>T. Auger</i>	
<i>CNRS - France</i>	

SESSION 0: INTRODUCTION

THE MEGAPIE PROJECT: OVERVIEW

F. Groeschel
Paul Scherrer Institut, 5332-Villigen, CH

MEGAPIE an International Project

Based on an initiative of PSI, CEA and FZK, the MEGAPIE project was started officially in 2000 to design, build and operate a liquid metal spallation neutron target of 1 MW beam power as a key experiment on the road to an experimental Accelerator Driven System [1]. The project is well supported by an international group of research institutes (Fig.1) and also partially funded by the European Union within the 5th Framework Program. This part of the project is named MEGAPIE-Test and is integrated into the TESTRA cluster together with the SPIRE, TECLA and ASCHLIM projects within the EU P&T activities. A good information exchange on MEGAPIE relevant issues is thus assured. Further EU support for the project will be sought in the 6th FP.



Figure 1: Partners of MEGAPIE and MEGAPIE-Test

Projects on ADvanced Options for Partitioning and Transmutation (ADOPT)

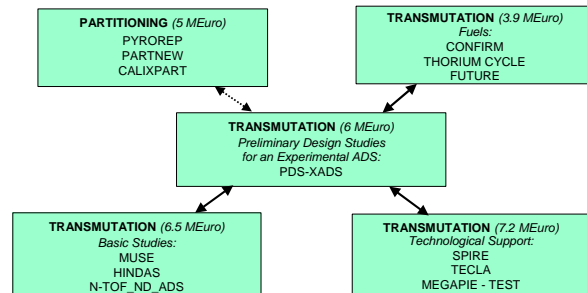


Figure 2: Integration of MEGAPIE-Test in the 5th FP

The MEGAPIE project is integrated in many national research programs on P&T and ADS developments, like the French GEDEON project and the US Advanced Fuel Cycle initiative (AFCI). Although we currently observe a focussing of priorities versus Partitioning and Fuels, the MEGAPIE project remains a key experiment within the Transmutation activities. It may thus even gain in importance by being only one the few large projects. The MEGAPIE partnership remained stable within the last year. Representing nearly all institutions with ADS related activities, the potential for additional partners is small. Negotiations are currently going on with the China Institute of Atomic Energy. The main interest of PSI lies in the potential use of a LM target as a SINQ standard target providing a higher neutron flux than the current solid targets.

We are aware of the fate of the target developed within the ISTC 959 project. Although rather different in design from the MEGAPIE target, an exchange of experience with the key persons of this project and their expertise on design and testing is considered beneficial for MEGAPIE and will be initiated.

The MEGAPIE Technical Status Meetings

The present Technical Status Meeting is the 4th Meeting. The former meetings were the

- Cadarache Meeting in June 2000, which was held at the end of the concept phase and lead to the conclusion that the target is considered feasible according to the concept proposed.
- Karlsruhe Meeting in February 2001, which was roughly in the middle of the design phase (according to the initial schedule) and was supposed to show the licensibility (completion of the PSAR), which was not achieved.
- Bologna Meeting in March 2002, which was at the end of the design phase (according to the old/new schedule) and provided a rather complete overview on the design of the target and the ancillary systems. The PSAR was also well advanced at that moment.

The Project Schedule and Budget

The current Status Meeting is again held at a critical point and milestone, which is the completion of the detailed design of the target and of some ancillary systems and the transition into the manufacturing phase as shown in Fig.3. The aim of the meeting is to stimulate the information exchange among the project members (in particular between the different support groups and the design team) and to discuss important technical issues. With the design completed, this may seem of no more importance. This is definitely a wrong perception, since important issues are still unresolved (as will be evident in this meeting), input is still required for qualification and proper operation of the target. In addition, improvements have to be weighted with respect to their impact on the technical merit, cost and schedule. The project schedule revised in December 2001 with an irradiation date in 2005 is still valid. The detailed design phase and the start of manufacturing, however, have slipped, which has been compensated up to now by a more flexible approach. By concentrating on critical components, advanced procurement and release of single lots, we were able to keep the schedule although at a higher risk of later changes. An update of the schedule is expected at the end of March 2003 as well as a new budget forecast.

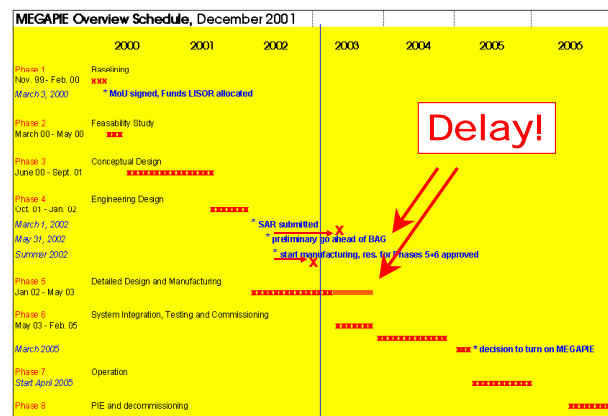


Figure 3: Project Schedule (simplified version)

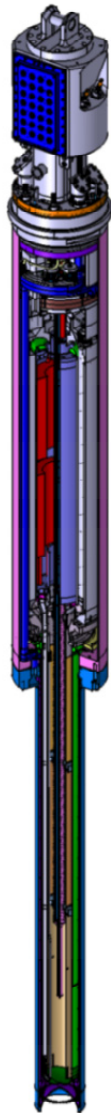
Progress and Open Issues

- Since the last meeting, progress has been made (and will be shown in this meeting) with
- The completion of the PSAR in June 2002 and its submission to the Swiss authorities (SFOPH). The licensing process is well underway, but will take some time. The KSA has been commissioned to establish an expertise on the licensibility, whose main objective is the protection of the public. A close collaboration has been established to achieve this goal.
- Completion of the target design (Fig. 4) and the establishment of drawings and specifications, which still need to be approved and complemented. Many important details, like sensors, connections, etc have been worked out. A concept change has been made by eliminating the absorbers. The

manufacturing process for the target has been initiated with ATEA, although the state of the THX development is still critical.

- Completion of the prototype test of the EMPS, the results of which will be reported in this meeting. The finding with respect to cavitation had a strong influence on the design of the gas handling system and the target operation.

Manufacturing of the EMPS is underway, whereas the pump housing still represents a problem area to be solved.



Dimensions

Length:	5.35.m	Weight:	1.5 t
LBE volume:	82 l	Gas Volume:	2 l
Design pressure:	16 bar	Operating pressure:	0-3.2 bar
Design Temperature:	400°C	Insulation Gas:	0.5 bar He

Materials

Lower Liquid Metal Container:	T91
Upper Container:	316L
Lower Target Enclosure:	AlMg3

Heat Removal and Beam Window Cooling

Deposited Heat:	650 kW
Forced convection assisted by buoyancy	
Main pump:	EM in-line pump (4l/sec)
Bypass pump:	EM in-line pump (0.35l/sec)

Figure 4: Cut-open model of the MEGAPIE target and main parameters

- Completion of the Intermediate Oil Loop Heat design of the Removal System (HRS) and start of the procurement phase and the design of the Intermediate Water
- Cooling Loop. The system has been well analysed (RELAP5) and shows the required performance. It also has to comply with the requirements of the integral test. A concept change was the elimination of the gas absorbers in the oil loop.
- Elaboration of new concepts to handle the spallation gases produced. Triggered by the relaxed cavitation requirements, some options have been investigated. The current situation will be presented in this meeting.
- Completion of the active Fill&Drain equipment. Active draining, however, was abandoned for cost and high-risk reasons. The possibility of freezing the target was elaborated supported by LBE experiments and structural mechanics calculations. The freezing option is still disputed among experts and partners and, with the situation presented at this meeting, a constructive discussion is expected to help to clear the situation.
- In order to assure the least amount of interruption, the components to adapt the beamline to the increased safety requirements will be installed during the 2004 shutdown. This allows gaining experience with these devices before putting the LM-target into operation. Some piping and cables will also be mounted. The design of these components is well advanced.
- Due to the size and the active inventory (-emitting Po), the decommissioning, conditioning and extraction of samples for PIE cannot be made in the standard

way for SINQ target. Evaluation of two options finally favoured the ZWILAG option, which will be presented in the meeting. Although still at high costs, this option requires the least modifications of the facilities.

- The target will be extensively tested off-beam in 2004. With the selection of the test site (Montagehalle) and the design and erection of the rig, good progress has been made.
- The design of the equipment and the execution of the experiment strongly depends on the support provided by the research groups investigating neutronic, thermo-hydraulic/-mechanic, materials (corrosion, LME and radiation damage) and safety and reliability issues. Valuable input has been made, although important issues still need to be elaborated (KILOPIE, materials suitability, Po properties, ..). Some of them are outlined and discussed in this meeting, others still will turn up later. Noticeable progress has been made by listing and actively tracking the activities.

Outlook on Commissioning and Operation

The goal is to operate the target for one operation cycle of SINQ (1 year, > 6000 mAh). The installation of a LM-target in SINQ has to be considered as an experiment, which may have a number of implications on the operation of SINQ during this period and implies some additional risks [2]. A major design feature is, that the MEGAPIE equipment is a stand-alone equipment and will

- Use either the existing installations without modification (D2O-loop of the safety hull)
- Bring in its own equipment without interfering with the existing installations.

This solution has the advantage that no modifications of the existing (contaminated) equipment is needed, that the MEGAPIE equipment can be easily removed at the end of the experiment and the next (solid) target can be installed without delay. The latter feature is extremely important for the case of an unscheduled termination of the experiment.

The actual start-up phase and the conditions of operation strongly depend on the progress achieved to qualify the experiment (confidence of PSI) and the limitations and procedures imposed by the authorities.

References

- [1] Bauer G.S., Salvatores M., Heusener G.: MEGAPIE, a 1 MW pilot experiment for a liquid metal spallation target; J. Nuclear Mat. 296 (2001) 17-35
- [2] Groeschel F., Thomsen K.: The MEGAPIE project – Status of the Project and implications on future SINQ operations; PSI Scientific Technical Report 2002, Volume III

SESSION 1: TARGET AND ANCILLARY

MEGAPIE TARGET DESIGN AND DIMENSIONING

T. Kirchner¹, A. Guertin¹, Y. Bortoli¹, A. Cadiou¹, Y. Foucher¹, J.S. Stutzmann¹, J.M. Gautier²

¹ Subatech, Ecole des Mines de Nantes, 4 rue Alfred Kastler, BP 20722, F - 44307 Nantes cedex 3

² LPC CAEN, ISMRA, 6 boulevard du Maréchal Juin, 14050 CAEN cedex, FRANCE

Abstract

In a collaborative effort, the MEGAwatt Pilot Experiment is an initiative to design, build, operate and decommission an exploratory liquid lead-bismuth spallation target for 1 MW of beam power, taking advantage of the existing spallation neutron facility and accelerator complex SINQ in PSI.

After a successful engineering design review in November 2001, the technical review meeting in March 2002 and the first detailed design review in April 2002, the target design is now almost completed, the manufacturing phase is launched and the construction will start in April 2003 after the second detail design review and the ready for manufacturing review in March. The present contribution is not a detailed description of the target design, but gives an overview on some selected issues of relevance before going into manufacturing.

This paper is based on the presentation held at the MEGAPIE Technical Review Meeting in Paris on March 18 – 19, 2003. The target heat exchanger and the electromagnetic pump system are presented in separate papers of the Meeting and will not be detailed in this paper.

Introduction

Figure 1 shows a schematic view of the different MEGAPIE target sub-systems and the list of ancillary systems.

The proton beam penetrates the target via two windows from below. The double-walled enclosure hull (lower target enclosure) is cooled by a forced convection heavy water flow. The inner beam window is cooled by the liquid lead-bismuth eutectic. The lower target enclosure and the beam window are separated by an insulating gap filled with Helium.

The lead bismuth flow is provided by two electromagnetic pumps: an axis-symmetric main flow down an annulus (between main flow guide tube and lower liquid metal container) and an additional flow via a by-pass tube. Due to the large height of the target the character of the flow is mixed convection. The combination of main flow and by-pass flow ensures the cooling of the beam window.

The spallation heat which is produced in the lower part of the main flow guide tube (in the region up to 30 cm above the beam window), is removed via double walled heat exchanger pins to an intermediate cooling loop and finally to an existing secondary cooling system. The fluid of the secondary system is high-pressure heavy water.

In the centre of the main flow guide tube an instrumentation pin (central rod) is inserted which holds instrumentation for the measurement of the neutron flux density and thermo-hydraulic data.

A shielding plug is provided in the top part of the MEGAPIE target, in order to avoid excessive radiation levels in the target head room from direct gamma radiation from the liquid metal.

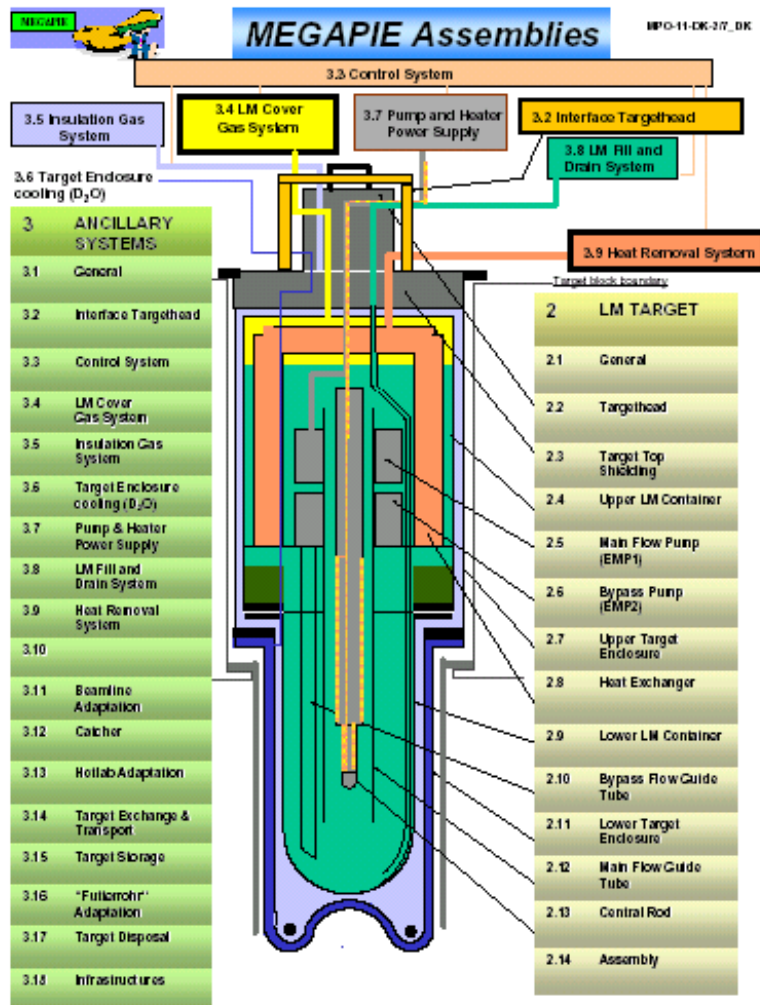


Figure 1: Schematic view of the MEGAPIE target with its target sub-systems and ancillary systems.

From the description above the main target sub-systems are:

- The target head (TH) assuring the interface of the target to the different ancillary systems;
- The target top shielding with the required shielding for in order to keep the radiation level above the target below the requested limits;
- The upper target enclosure (UTE) and the double walled lower target enclosure (LTE made of AlMg3 with a concave sphere shape), the upper liquid metal container (ULMC) and the lower liquid metal container (LLMC) that contain the liquid lead bismuth eutectic (LBE);
- The central rod equipped with heaters, instrumentation and neutron monitors;
- The 12 pin single walled target heat exchanger;
- The electromagnetic pump system, the main pump for the main flow and a second smaller pump for an LBE by-pass flow across the beam window;
- The main and by-pass flow guide tube for the separation of the down-coming cold LBE from the hot rising LBE in the centre and for improving the target window cooling.

The geometrical boundary conditions and the fact that the MEGAPIE target has to fit to the existing SINQ facility at PSI fixes the main dimensions of the target as shown

in figure 2. An outer view of the complete target is shown on the right side of the figure.

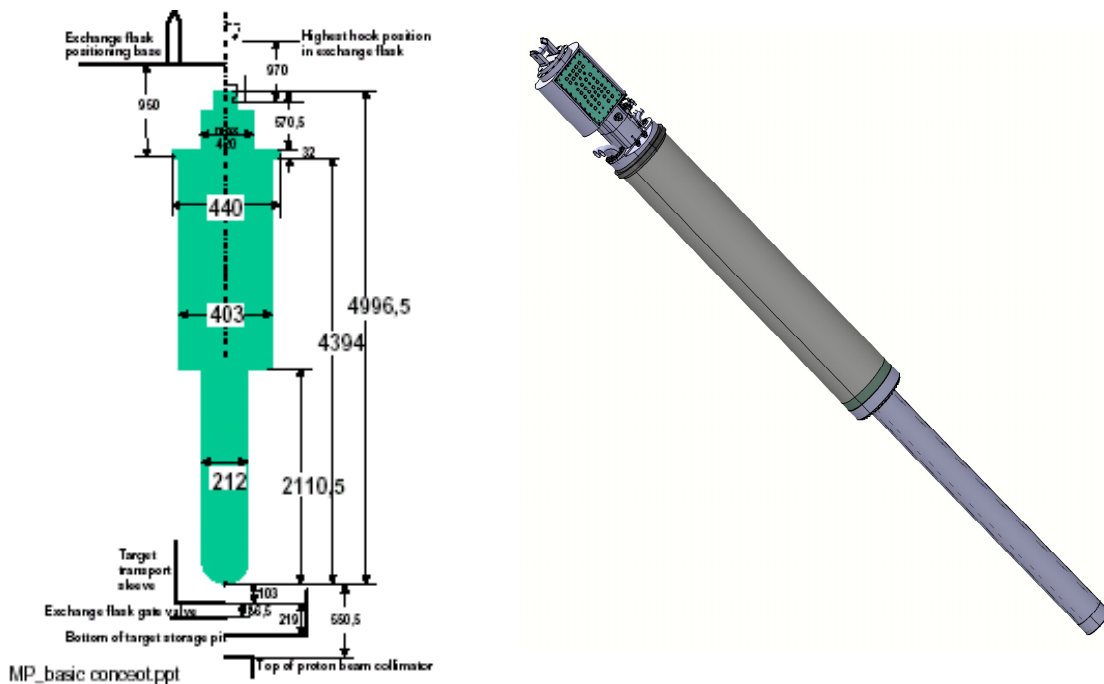


Figure 2: Main dimensions of the MEGAPIE target and a complete view of the target.

Target sub-systems

In this chapter some selected target sub-systems will be presented in an overview with some indications on temperature, stress and displacement levels. More details can be found in the corresponding design documents listed in chapter 2.6.

Target Head

The target head is the interface of the target to the different ancillary systems. All electrical signals and power supplies, pipes and tubes have to pass through the target head. The main access ports to the inside of the target are (see figure 3):

- The target hook system at the top of the target head to insert and extract the target into the SINQ. This hook will be manufactured out of a special steel (42CD4) with an optimum mechanical behaviour (at a load of 10 t that corresponds to the maximum weight of the crane in the SINQ hall the stress is about 143 MPa and the corresponding displacement 85 μ m).
- The Ar cover gas in and outlet with its second containment.
- The insulating gas inlet for He at 0.5 bar.
- Two connector plates for electrical cables at the front and back side of the target head.
- The oil and heavy water in and outlet pipes and the LBE fill and drain tubes.

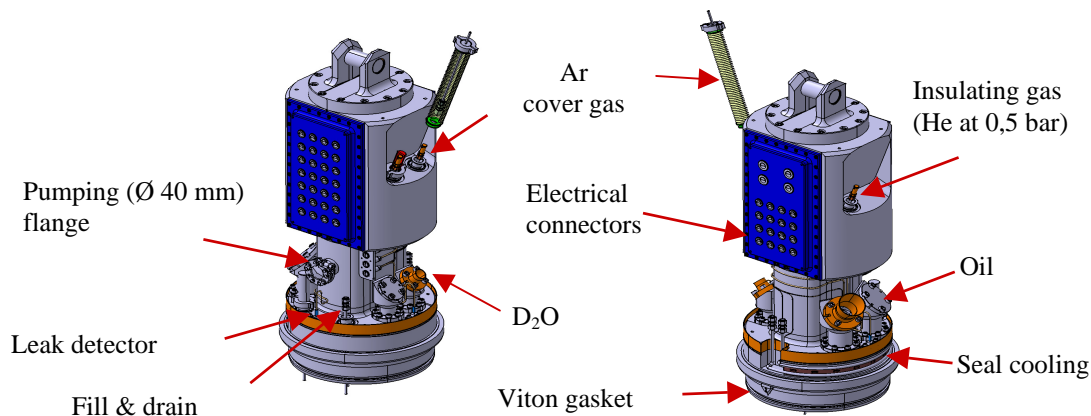


Figure 3: Drawing of the target head with the different interface connections.

The pumping flange (diameter 40 mm) serves to evacuate the target. At the outside of this pumping access a safety valve will be connected in order to release the overpressure from the insulating gap in case of an accidental LBE – water interaction inside the target.

Small contact leak detectors are mounted on the top flange in order to detect oil, water or an LBE leak coming from the connectors.

The tightness of the target with respect to SINQ target guide tube is achieved by a Viton seal at the lower part of the target head. Thermomechanical design calculations showed a strong temperature asymmetry due to the in and outlet temperature (60°C and 200°C respectively) of the heat exchanger oil. To avoid any problems with overheating of the viton seal a dedicated seal cooling is foreseen. This cooling system is not yet approved and might be replaced by a simple air cooling.

Target top shielding

The target top shielding covers the space between the target head and the top of the target heat exchanger (see figure 4). In this part are situated the water and oil boxes for the in and out-streaming fluids. Due to their particular shape, special attention had to be paid to the stress levels and requested the adaptation of the design. A linear static analysis with the 16 bars design pressure showed that stresses and displacements are within acceptable limits (oil boxes: 117 MPa and 0.18 mm, water boxes: 111MPa and 5.2mm).

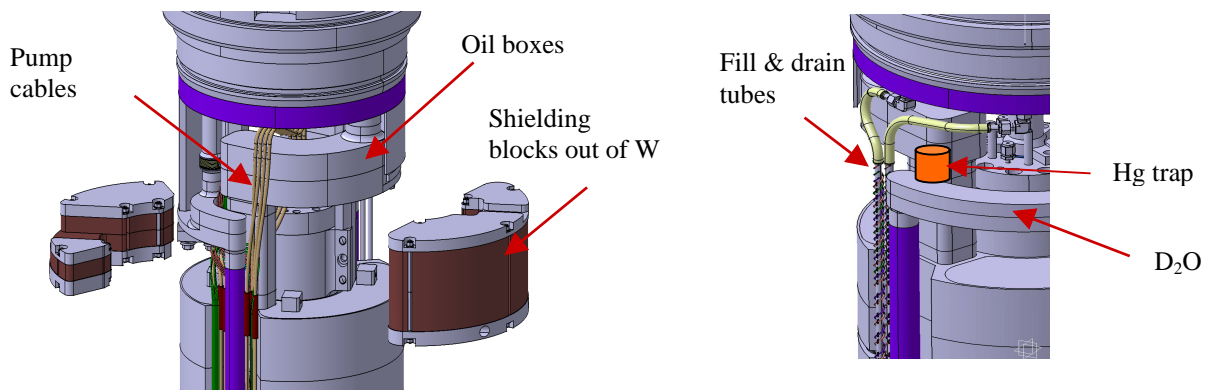


Figure 4: 3D view of the target top shielding sub-system.

The LBE fill and drain tubes pass at the outside target top shielding down to the lower part of the target. The outer tube diameter is \varnothing 8 mm (wall thickness 1 mm) and both pipes are heated with heaters performing 150 W/m in order to avoid freezing of LBE in the tubes. For monitoring of the temperature the tubes are equipped with two thermocouples.

Initially it was foreseen to implement in the target top shielding gas (H) and mercury absorbers. Based on a project decision these absorbers were skipped due to the absence of qualified systems and therefore also for safety and reliability reasons. Hydrogen will be managed together with the other gases produced in the target. For mercury it was decided to implement a cold trap in order to condense the mercury vapours. The trap (schematically indicated on figure 4) will be mounted on the water boxes in order to be kept at low temperature.

Main and by-pass flow guide tube

Figure 5 show on the left side the whole main and by-pass flow guide tube and on the right side a zoom on the lower part of the guide tubes. This system is connected to the electromagnetic pump system and is complete immersed in the LBE. The cold LBE from the target heat exchanger flows down at the outside of the tube. The hot LBE rises upwards at the inside of the main flow guide tube.

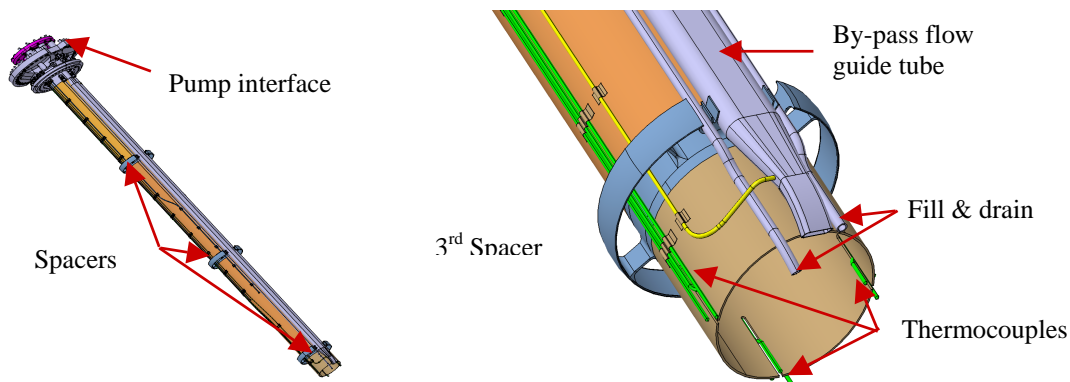


Figure 5: Main and by-pass flow guide tube with a zoom on the lower part on the right side.

Three spacers are foreseen in order to keep the main flow guide tube centred in the LBE.

The by-pass assures a directed flow of LBE parallel to the long axis of the proton beam along the inner target window surface. The reference cross section of the by-pass nozzle is 20 x 10 mm²

The main flow guide tube is slanted (not clearly seen in figure 5) with its short end at the side of the by-pass nozzle. The vertical distance at the nozzle side between the main flow guide tube and the target window shell is 25 mm (15 mm at the opposite side).

Lower liquid metal container

The lower liquid metal container is one of the critical structural parts of the MEGAPIE target. In particular the beam window is exposed to severe constraints: proton and neutron irradiation, thermal and mechanical load and the presence of flowing LBE. The structural material for the target container is foreseen to be martensitic (French designation T91 type) steel. For the upper liquid metal container (see above) the use of austenitic (316L type) steel is being considered, which is more readily available and easier to weld. This is contingent upon sufficiently high liquid metal corrosion resistance, because the highest temperature gradient in the system will occur along the heat exchanger. In order to facilitate the transition between two different materials the two parts will be joined by a flange system.

Figure 6 shows the lower liquid metal container (left side). For buckling reasons the thickness of the cylindrical part is 2 mm in the lower part and 4 mm in the upper part. The window thickness is 1.5 mm.

Stress calculations have been performed and under 16 bars design pressure the maximum displacement and stress values are 90 µm and 45 MPa respectively. As expected they are localised in the window region of the LLMC.

The results of a calculation performed for nominal operating conditions is given in table 1. For the calculations the following reference parameters have been used :

- LBE temperature: 300°C,
- T91 window temperature: 396°C (outside) and 362°C (inside),
- Heat exchange coefficient : 20000 W / (m².°C).

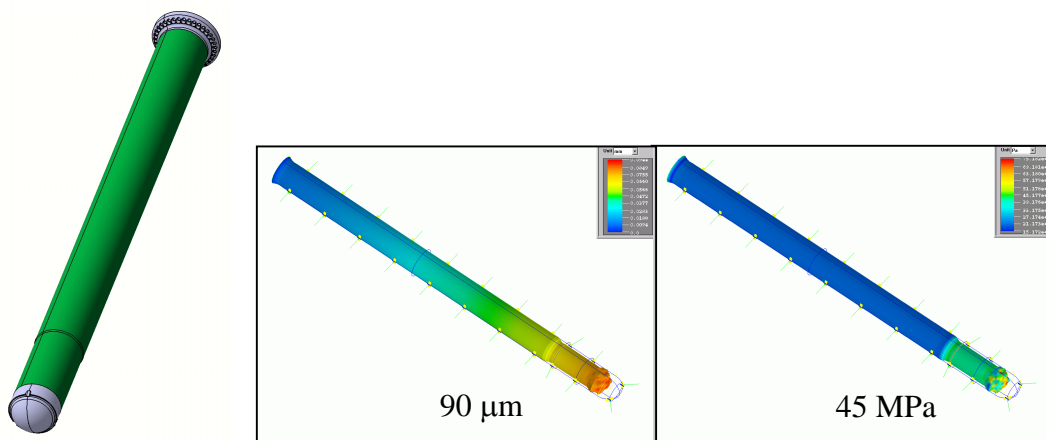


Figure 6: Lower liquid metal container with the maximum displacement and stress values for 16 bars mechanical stress calculations.

Nominal regime for target window (LBE at 300°C; const.)						
Container window		Convection	Max temp		Temp drop	Von Mises stress (MPa)
		$W / (m^2 \cdot ^\circ C)$ $T_{inf} = 300 \text{ } ^\circ C$	$^\circ C$		$^\circ C$	Pressure inside 6 bars Max stress located in beam region
	Steel T91 Thickness 1.5mm.	20000	Outside	Inside	95	
			395	362		

Table 1: Stress value in the lower liquid metal container under normal operating conditions.

Target instrumentation

The target is equipped with instrumentation for operation and monitoring purposes. The main instrumentation are level meters and thermocouples. In its actual design the different target sub-systems have the following instrumentation:

Target head:

- Two thermocouples (TC) on the heated upper part of the fill and drain tubes (one TC for each tube);
- Three TC are foreseen for the seal cooling of the target head;
- As mentioned in chapter 2.1 the target head is also equipped with two leak detectors. One for the oil and the second detector for leaks out of the water pipe connection. In both cases the principle of the detector is based on an “active level measurement”. The principle is illustrated in figure 7. In normal conditions the thermocouple indicates a temperature based on the heating power of the heater. In case of a leak (in this case an oil or water leak) the detector gets immersed in the liquid. The consequence is a change in the heat transfer characteristics between the heater and the thermocouple and a variation in the measured temperature.

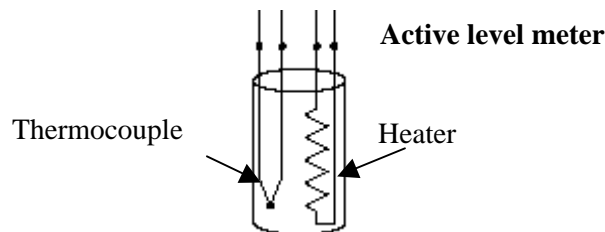


Figure 7: Principle scheme of the active level meter.

Target top shielding:

- Two redundant thermocouples in the cover gas;
- Two thermocouples for each fill and drain tube in the lower part of the heated section.

Electromagnetic pump system:

- The main flow and by-pass flow pump have their associated flow meter and one thermocouple for the LBE temperature;

- For the control of the pumps, both pumps are equipped with five thermocouples each in order to monitor the temperature in the pump during the different operating conditions;

Heat exchanger and upper liquid metal container:

- On the oil side of the heat exchanger each outlet of the cooling pin (12 pins) is equipped with one thermocouples for monitoring the oil outlet temperature.
- Four thermocouples are installed in the measure the LBE temperature in the LBE inlet manifold of the heat exchanger;
- The LBE temperature is monitored with 12 thermocouples at the LBE outlet of each cooling pin.

A problem in on one of the 12 heat exchanger pins could be detected by the temperature measurement of the oil and LBE outlet at the corresponding pin.

Lower liquid metal container:

- Below the target window a ring detector with 3 signal wires will be installed in order to detect an LBE leak out of the liquid metal container. It is a contact measurement between the electrically insulated detector and the lower target enclosure (see chapter 3.2).

The main flow guide tube:

- The bottom part of the main flow guide tube is equipped with 9 thermocouples (see figure 5). Three thermocouples are always grouped together: one TC measures the LBE temperature in the down-commer (outside of the main flow guide tube), the second TC measures the temperature in the lowest position, and the third TC the LBE temperature in the up-streaming LBE.
- Six additional TC in the upward flowing LBE to get the information on the temperature distribution;
- Two TC in the by-pass flow guide tube;

Central rod:

- The central rod has two heaters. Heat 1 is equipped with three TC and heater 2 with 4 TC;
- In the actual status of the project it is foreseen to install in the central rod 8 neutron detectors for the fluency measurement of thermal and epithermal neutrons produced in the target. Three TC are associated in order to monitor the operating temperature of the neutron detectors (see also the dedicated contribution to the Technical Meeting);
- The free LBE surface in the target is monitored by 4 active level meters (principle as shown in figure 7). Two additional identical level meters are added for redundancy.
- One TC is added on the top for measuring the temperature of the cover gas.

Upper oil leak detector:

The upper oil leak detector is mounted around the target heat exchanger and the upper liquid metal container. He is equipped with:

- Two active level detectors (as shown in figure 7);
- An additional contact leak detector made of a printed circuit on a ceramic support;

Design calculation

An overview of the performed design calculations is given in tables 2 and 3.

Topic		Ref. document
Thermal expansion of the Target		Q_MEG_2.01_M_DI_010_C
Hook flange behaviour in nominal conditions (10 t)	$\sigma = 143 \text{ MPa}$ disp. = 85 μm	Q_MEG_2.2_M_CA_107_B
Thermo-mechanical behaviour of TH in nominal conditions	T (oil side) T (water side) ~ 200°C ~ 60°C	Q_MEG_2.2_M_CA_110_B
Diphyl distribution boxes mech. behaviour (16 bars)	$\sigma = 117 \text{ MPa}$ disp. = 0,18 mm	Q_MEG_2.3_M_CA_050_B
Water distribution boxes mech. behaviour (16 bars)	$\sigma = 111 \text{ MPa}$ disp. = 5,2 mm	Q_MEG_2.3_M_CA_051_B
UTE behaviour in nominal conditions	$\sigma = 85 \text{ MPa}$ (16bar) disp. = 160 μm $\sigma = 5.3 \text{ MPa}$ (vac.) disp. = -10 μm	Q_MEG_2.7_M_CA_100_B
UTE temperature estimation	T = 198°C / 112°C / 87°C	Q_MEG_2.7_M_CA_102_B
LBE leak detector thermal behaviour	T = 473°C	Q_MEG_2.9_M_CA_132_A

Table 2: Overview of the performed design calculations (first part)

Topic		Ref. document
T91 behaviour in nominal conditions LBE inside, vac. outside Vac. inside 16 bar	$\sigma = 20 \text{ MPa}$ disp. = 0.05 mm $\sigma = 4 \text{ MPa}$ disp. = 0.008 mm $\sigma = 45 \text{ MPa}$ disp. = 0.089 mm	Q_MEG_2.9_M_CA_013_B
Lower LM container (pressure + T)	$\sigma = 41 \text{ MPa}$ $\sigma = 205 \text{ MPa}$ (norm. beam) (focussed. beam)	Q_MEG_2.11_M_CA_100_B
MFGT flange behaviour 5 bar internal pressure 16 bar external pressure	$\sigma = 10 \text{ MPa}$ disp. = 4 μm $\sigma = 26 \text{ MPa}$ disp. = 11 μm	Q_MEG_2.12_M_CA_105_A
MFGT spacer in nom. Conditions	$\sigma = 10 \text{ MPa}$	Q_MEG_2.12_M_CA_153_A
Heat transfer along MFGT	No insulation needed	Q_MEG_2.12_M_CA_200_A
Central rod 16 bar outside, vac. inside Vac. outside, 16 bar inside	$\sigma = 21 \text{ MPa}$ disp. = -0.12 mm $\sigma = 21 \text{ MPa}$ disp. = 0.1 mm	Q_MEG_2.13_M_CA_100_A
Screw calculations	Data for HELICOFLEX seals	Q_MEG_2.14_M_CA_010_A
Target gravity center		Q_MEG_2.14_M_CA_149_A
LBE free level height variation (filling at 200°C)	66 mm (LBE at 350°C) 31 mm (LBE at 250°C)	Q_MEG_2.14_M_CA_153_A

Table 3: Overview of the performed design calculations (first part)

The stress and displacement values correspond to the maximum of each that were obtained by the calculations. Most calculations were performed by taking the maximum pressure of 16 bars that has been fixed as design pressure. The operating conditions are in all cases less severe.

More details on the calculations can be found in the documents indicated by their reference number in the last column of table 2 and 3.

Safety issues

During the project the following four different type of accidents have been identified (design base accidents) to which the design has to be adapted in order to limit the consequences:

- The guillotine break of the liquid metal container and the impact of the falling LLMC on the lower target enclosure. For this case a catcher ring has been designed on the LLMC and the LTE (see also figure 9) in order to limit the impact of the LLMC. Finite element calculations have been performed in order to assess the behaviour of the LTE in case of an impact. Taking into account the material characteristics of the LTE (AlMg3) and an irradiation damage of 4 dpa the results of the calculations show that the integrity of the LTE could be assured.
- An LBE jet out of the LLMC on the LTE. To reduce the load due to an important LBE jet on the lower target enclosure the distance between the target window and the LTE has to be smaller than 10 cm.
- Filling of the insulating gap with LBE. If the lower liquid metal container fails the hot LBE will flow in the insulating gap and will come in contact with the lower target enclosure that is cooled down by heavy water. To avoid boiling of the heavy water a thermal shield has to be foreseen to fill up the insulating gap (in the cylindrical part only) to avoid the direct contact of LBE with the inner wall of the LTE.
- Water (oil ingress) into the insulating gap: Water leaking into the insulating gap would lead to a slow pressure increase up to 25 bars. The thermal shield mentioned above will reduce this pressure increase and the 40 mm flange at the target head will serve as pressure relief.

From the design three points have to be looked at carefully:

- The catcher on the lower liquid metal container and the lower target enclosure;
- The thermal shield in the insulating gap;
- The lower LBE leak detector in the gap between the target window and the lower target enclosure. This leak detector is most critical point. All the accidents mentioned above rely on this leak detector for shutting off the beam.

In the following section some more details are given with respect to these design base accidents.

Target elongation

To check and to make sure that the target dimensions respect the specifications some calculations have been performed to assess the target elongation in hot conditions. Figure 8 shows the schematic view of the relevant target dimensions and distances.

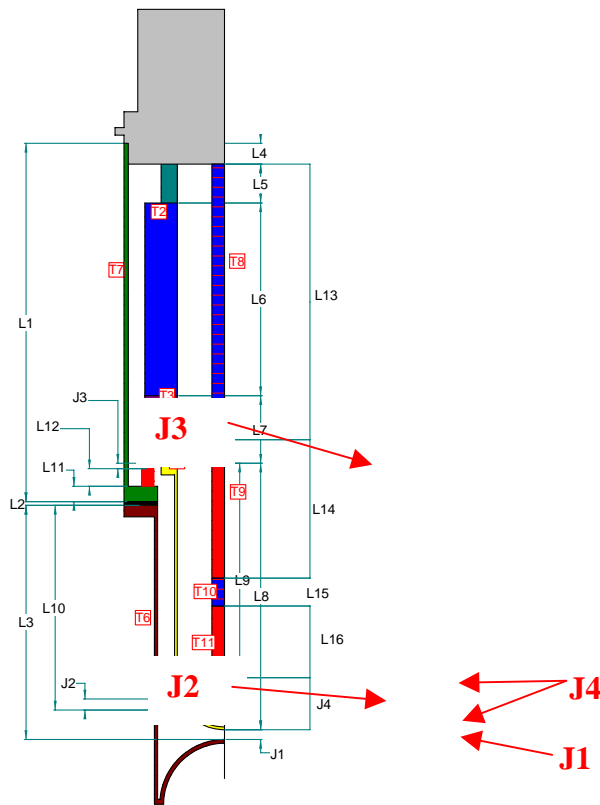


Figure 8: Scheme of the main target dimensions and the distances between different components. (J1: target window – LTE; J2: catcher LLMC and LTE; J3: flange of the upper liquid metal container – upper target enclosure; J4: central rod – target window).

The main values for J1, J2, J3 and J4 are given in the table 4.

	Cold	Hot
Target		
J1	17.6 mm	5.3 mm
J2	16.6 mm	4.5 mm
J3	10.5 mm	3.0 mm
Central Rod		
J4	311 mm	303 mm

Table 4: Variation of main distances in the target between cold and hot conditions.

The LBE leak detector

The LBE detector in the insulating gap is one of the critical safety relevant instrumentation in the target. Operation of the target relies on this detector for shutting of the beam as soon as there is a leak of LBE out of the liquid metal container.

LBE leak detector concept

For target assembling reasons the LBE leak detector will be mounted electrically insulated on the lower liquid metal container (see figure 9). The detector is a ring detector with ceramic spacers to be held in position on the spherical shape of the LTE. Three flat signal wires will be fixed along the T91 shell. In case of a leak the LBE will make contact between the ring detector and the LTE connected to the common ground of the target system.

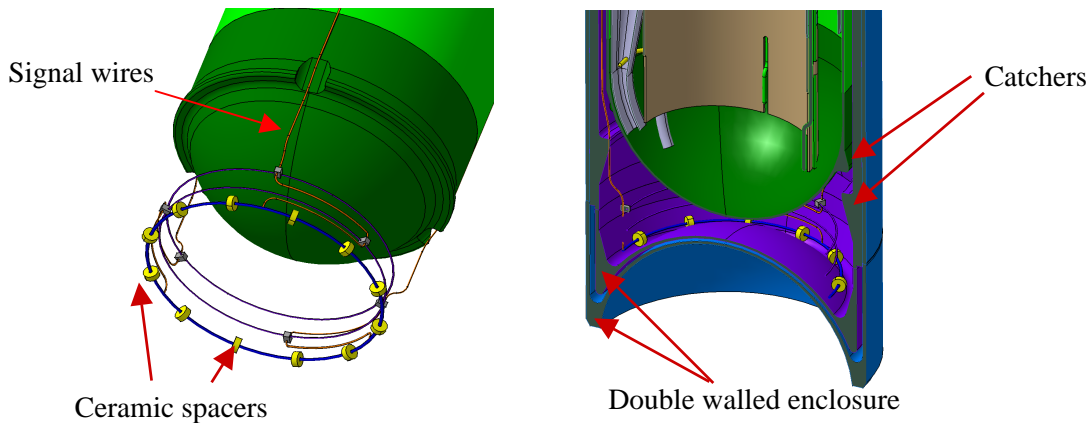


Figure 9: Design of the window region in the lower part of the target with a schematic view of the LBE leak detector.

Due to the importance of the LBE detector for a safe operation and a fast and reliable leak detection in case of an accident this type of detector has to be qualified before being installed on the target. For the detector qualification as well as for the assessment of the technical feasibility of the fixation and manufacturing of the detector tests have to be performed on a dummy of the lower target part.

Dummy of the lower target part

A 1:1 dummy of the lower target part (target window and inner shell of the LTE) has been realised by Subatech (see figure 10). The first step of the dummy test is to find out feasible solutions for :

- The positioning of the LBE leak detector on the LTE;
- The fixation of signal wires on the LLMC;
- The fixation of thermal and electrical insulation on LLMC (thermal shield in the insulating gap)
- The handling and workability of Zr – oxide which is foreseen as thermal shield.

In a second step the detector system has to be qualified. For this purpose a detailed qualification and test program has to be provided.



Figure 10: Photos of the dummy parts of the lower target part. (1) target window with the catcher and the schematically leak detector; (2) inner shell of the lower target enclosure; (3) assembling of (1) and (2); (4) zoom on the 4mm wide insulating gap between the T91 liquid metal container and the LTE (to be filled up with the thermal shield).

Target manufacturing

As already stated before the project has started the manufacturing phase of the target and machining will start in April, May 03. The target will be manufactured by the company ATEA (Group REEL) at Carquefou (FRANCE). For the manufacturing general specifications have been written that can be found in the corresponding reference document (L_MEG_2.1_G_DI_001_B). The aim of this document (to be approved by the project) is the assessment of the target manufacturing in order to define specifications for braising, welding, control process, leak tests, quality of welds and related equipment.

Highlights of some of the important items are listed below:

- Cleaning process : polixine 21-85 cleaning, rinsing and drying;
- Material certificate EN 10204-3.1; all tubes 100% radiography;
- Control :
 - Dimensional tolerances;
 - Welding: vacuum tightness and pressure test; He (min. leakage 2×10^{-8} mbar.l.s⁻¹); Pressure tests following AD2000; 100% radiography of all welds if possible; If penetration tests necessary they have to be performed after He tests; All control procedures have to be defined with the project;
- Welding and control specifications are worked out by ATEA and have to be approved by the project (example: electron beam welding of T91: no pre-heating; relaxation at 760°C after welding).

All relevant manufacturing documents will be released by PSI together with the manufacturing drawings prior to manufacturing during the Ready for Manufacturing Meetings with the company ATEA.

Pressure test requirement and notified body

One of the project requests was to follow the Pressure Equipment Directive (PED Directive 97/23/EC of the European Parliament and of the Council of 29 May 1997) for the design, manufacturing and conformity assessment of the MEGAPIE target. In order to find out what the application of the PED would have as consequence for the manufacturing process, PSI has summarised the main pressure volumes of the target as shown in table 5. Based on the parameters (pressure and volume) of the target sub-systems the last line in table 5 indicates the PED risk category. Risk category IV requests an EC unit verification for all target volumes.

EC unit verifications means :

- The manufacturer must apply to a notified body of his choice for unit verification;
- The notified body must examine the design and construction of each item of pressure equipment and during manufacture perform appropriate tests.
- In particular the notified body must :
 - examine the technical documentation with respect to the design and the manufacturing procedures;
 - assess the materials used and check the certificate issued by material manufacturer;
 - approve procedure for permanent joining of parts;
 - verify the qualification;
 - carry out final inspection

Such a unit verification might become very heavy to assure and could have an strong impact on the progress of the project. On the French side Subatech and ATEA will be looking for a notified body for discussing details on the understanding of the PED and the certification procedure trying to avoid strong impact on time and schedule and to check again whether the PED has really to be applied to the MEGAPIE target.

Pressurized volumes at Megapie Target

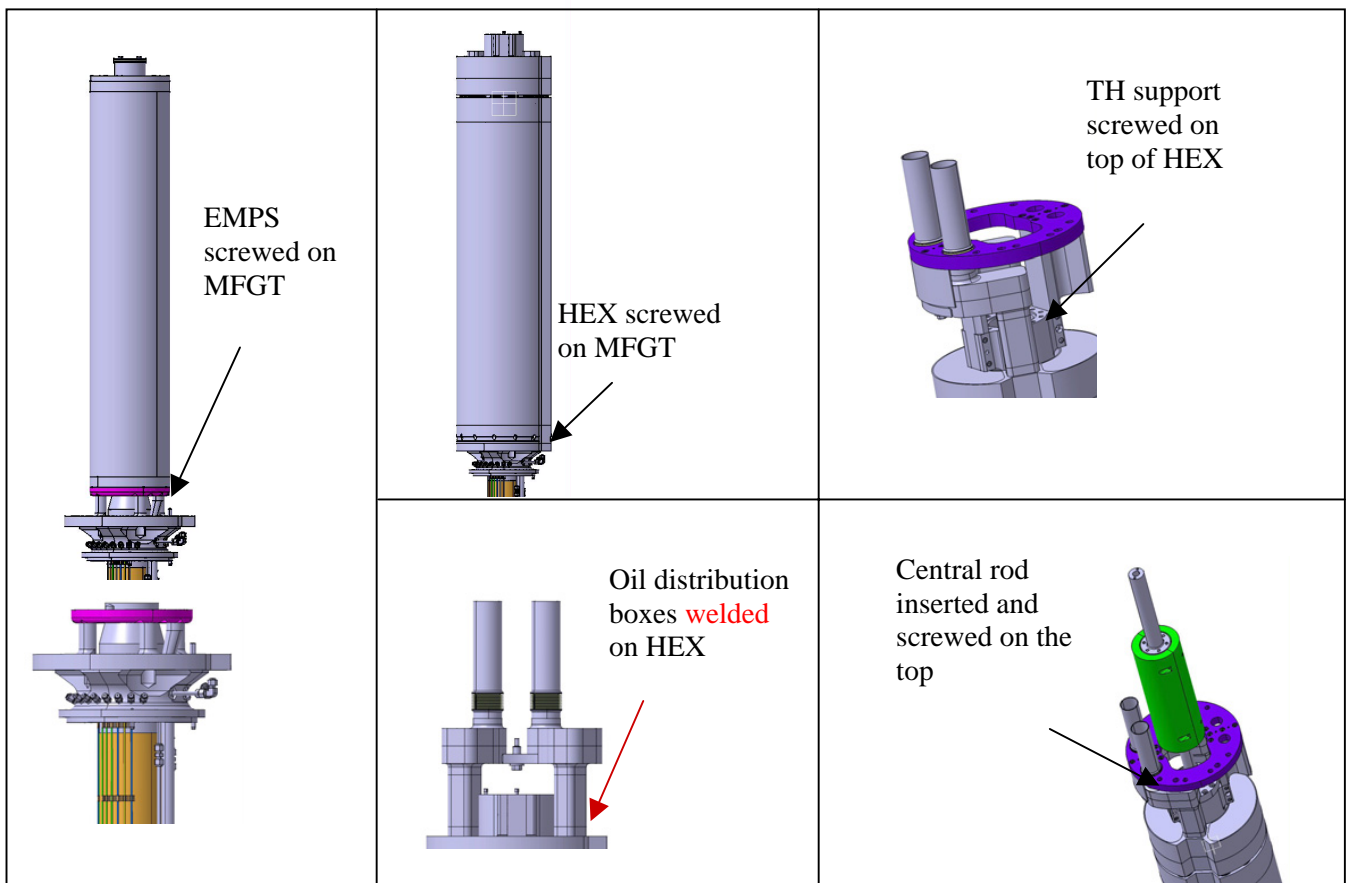
System	LMC	Insulat. Gas	Oil loop	D ₂ O loop
Fluid	PbBi, cover gas Ar	He	Diphyl THT	D ₂ O
Volume in target	80 l + 2 l CG	25 – 40 l	22 l	9 l
Norm. operat. pressure	0.2 – 2.2 bar(a) at bottom – 6.2 bar(a)	0.5 bar(a)	4 – 10 bar(a)	5 bar(a)
Accident press.	14 bar(a)	?	15 bar(a) (MIT)	?
Design pressure	16 bar (*) SAR	16 bar (*)	16 bar	16 bar (SAR)
Norm. operat. temp.	230 – 370°C	?	130 – 230°C	40 – 50°C
Design temperature	300°C, GT+THX 370°C	~ 200°C, THX 370°C	300°C	50°C
Test pressure at RT following PED	33 barg	33 barg	31 barg	23 barg
Pressure test fluid	Gas	Gas	Diphyl THT	Gas
Test pressure at RT proposed by PSI	13 barg (EMP) 33 barg for components	17.6 barg (with press. in LMC)	31 barg (Instrum. 24barg?)	17.6 barg
Involved devices	ULMC (THX), LLMC	ULMC, LLMC, UTE (TG-head, oil+D ₂ O pipes), LTE	THX, distr. box, manifold, pipes, HRS	LTE, manifold, pipes, D ₂ O cooling system
PED category	PS*V = 16*82 = 1312 => category IV => Module G (EC unit verification) -> for all target volumes			

(*) Design pressure for EMP only 10 bar (Extensive calculations will be needed to prove the tightness of EMP at 16 bar)

Table 5: Different pressurised volumes of the target with their operational parameters. The last line in this table gives the PED category.

Target Assembling

In this chapter will be presented the different steps for assembling the target. This is of course relevant for the final assembling before the target transport to PSI but it is also a valuable input for the group working on the post irradiation program and the dismantling of the target. To check what parts could be accessible (and how) for post mortem investigations after the operation phase it can be of interest to know where parts can be dismantled or where cuts have to be made. In figure 11 the sequence of assembling will be given with comments on where parts are welded ore screwed together.



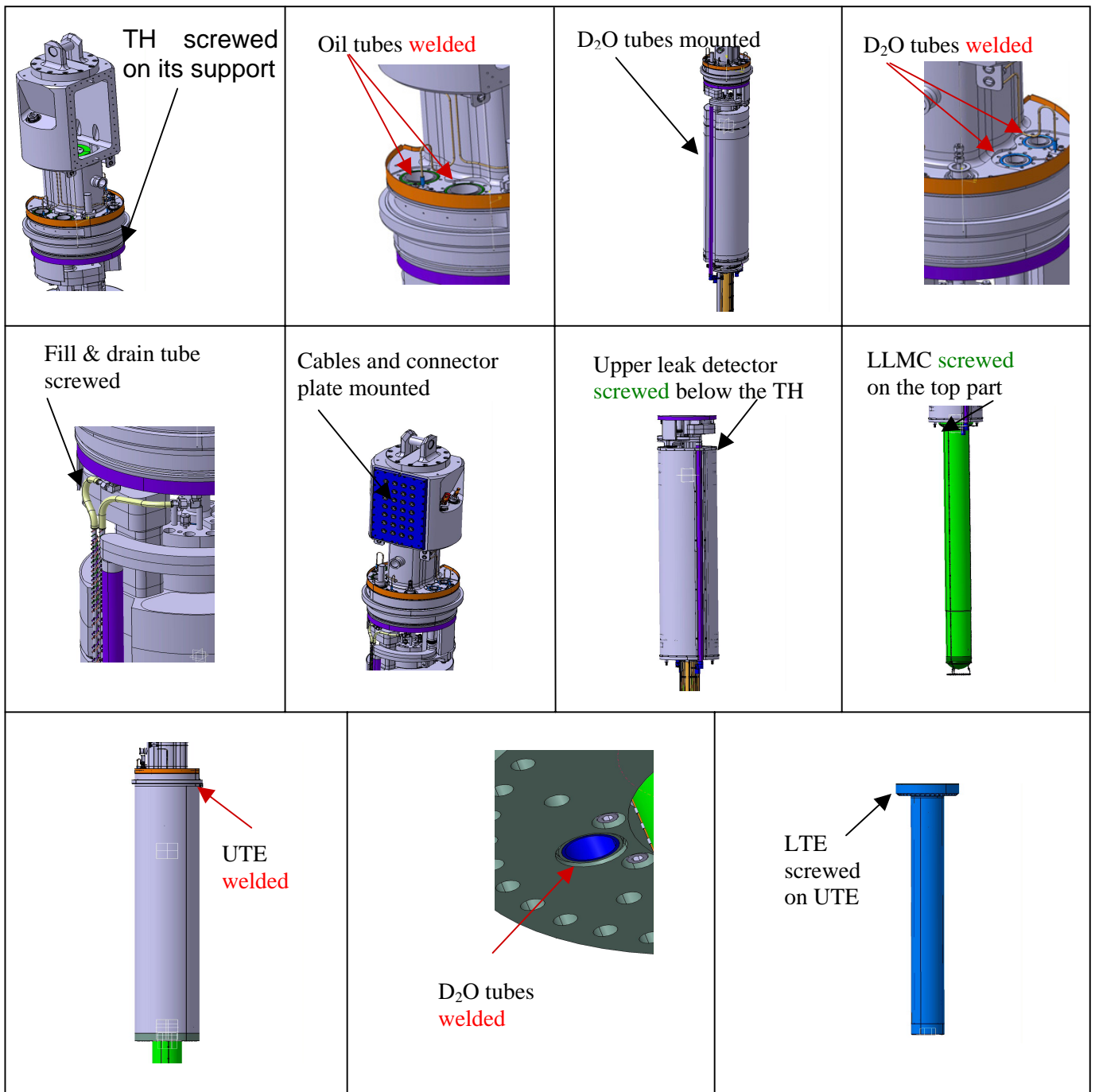


Figure 11: Sequence of the different assembling steps of the MEGAPIE target (in red: parts that are welded together)

Design status

The second detail design review of the target system was held at PSI the 25th and 26th of February 2003. The aim of this review was to check whether the target was well enough defined and detailed so that the manufacturer (ATEA) could finish the manufacturing planning and cost estimation.

A third detail design review was scheduled for the 25th and 26th of March 2003. During this meeting a special attention will be attached to the performed design calculations and the check of the design documents.

To launch manufacturing several Ready for Manufacturing Meetings will be held during the month of April and May 2003 in order to release the different target lots for manufacturing. PSI, ATEA and Subatech will participate in these meetings. During these meetings all documents and drawings will be released by PSI.

Machining of the target has to start in early April in order to meet the fixed deadline of the target delivery from ATEA to PSI by the end of the year 2003. A shift in the beginning of manufacturing might cause a shift of the delivery date at the beginning of 2004.

PROTOTYPE OF THE ELECTROMAGNETIC PUMP SYSTEM FOR MEGAPIE TARGET: DESIGN AND TESTING

S.Dementjev¹, F.Groeschel¹, E.Platacis², S.Ivanov², A.Zik²

¹ Paul Scherrer Institut, Villigen Switzerland CH-5332

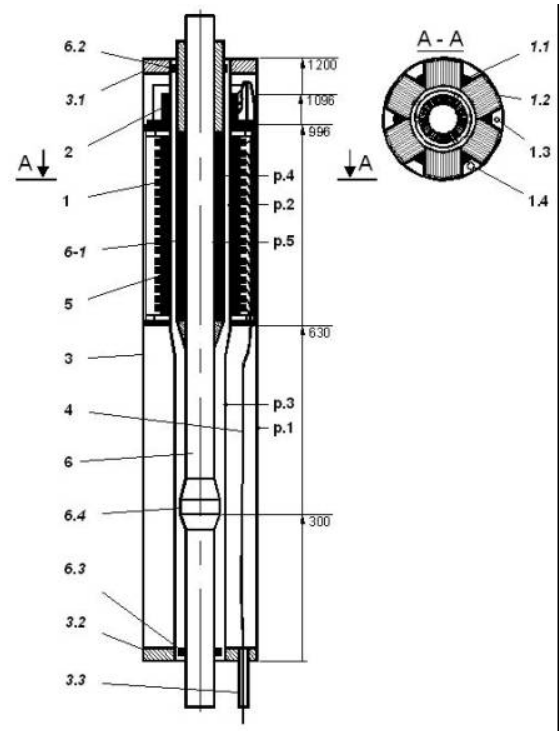
²Institute of Physics of Latvian University, Miera 32 Salaspils Latvia LV-2169

The electromagnetic pump system (EMPS) described in the article is designed for operation in MEGAPIE target [1]. It maintains a lead bismuth eutectic (LBE) flow between the beam entrance window (where an average of 600kW of heat power is released in spallation reaction) and the high performance heat exchanger. The first stage of the EMPS development was the engineering, manufacturing and test of the Prototype.

The Prototype of the EMPS, Fig.1, represents a block geometrically similar to the final EMPS [2] however consisting of only one pump (EMP, responsible for the main flow in the target) and associated electromagnetic frequency flowmeter (EMF). Process of the Prototype testing consists of following main stages: preliminary tests; technological tests; hydraulics test of the Prototype; reliability test; inspection of the Prototype after the hydraulics test.

Figure 1: Conceptual design of the EMPS Prototype:

1-inductor of EMP; 1.1-coil; 1.2-magnetic circuit; 2-EM flowmeter; 3-housing; 3.1 and 3.2-upper and lower flanges; 1.3, 1.4 and 3.3- channels for power and control cables; 4-cables; 5-LBE channel; 6-central pipe; 6.1-sliced silicon steel passive core; 6.2 and 6.3-spacers; 6.4-hydradynamics flowmeter; p.1 ... p.5 – pipes



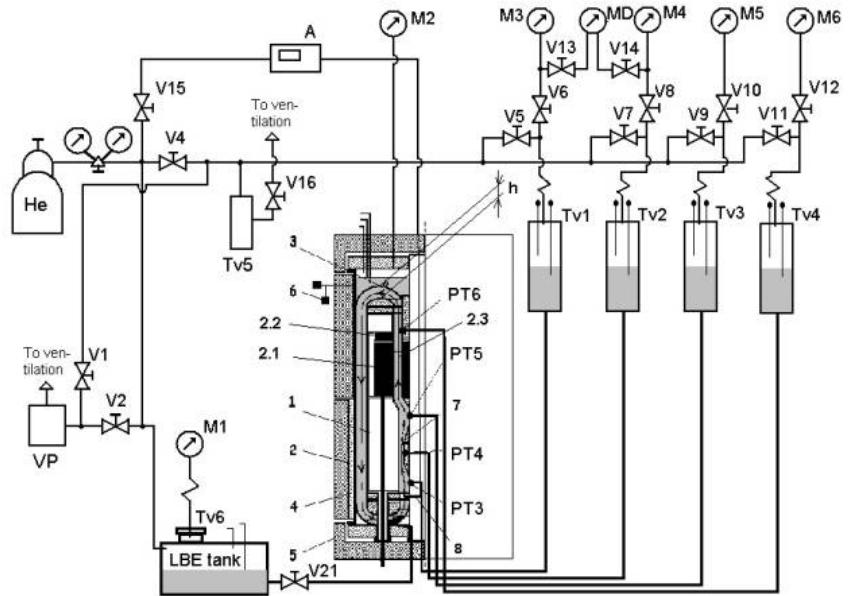
The aim of the preliminary tests was to provide the data needed for the EMPS's engineering: measurements of the by-pass nozzle hydraulics resistance [3]; LBE test of the electromagnetic frequency flowmeters mock-up [4]; irradiation test of the electrical insulation materials;

measurements of a silicone steel magnetic properties under temperature 500°C.

Technological tests were performed during and after finishing of the manufacturing process to verify quality and correspondence of the Prototype (or it's elements) to rated characteristics: detail withstand test of electrical insulation; measurements of the pump's and flowmeter's electrical parameters; preliminary mercury calibration of the electromagnetic flowmeter; measurements of integral electromagnetic force applied to solid body imitator installed in EM pump's LBE channel; dry (without LBE) temperature (up to 500°C) test of the ready to operation Prototype.

Figure 2: Stand for the Prototype's Hydraulics test:

1-Prototype; 1.1-EMP; 1.2 and 7- EM and reference flowmeters; 1.3 and 3- LBE channel and flow guide; 2-container; 4 and 5-el heater and insulation; 6-vibr probes; 8 and A- He injector and flow rate controller; V- valves; M and MD- manometers; Tv- LBE tanks; PT- pressure taps



The hydraulics test was combined with long run of the Prototype (see LBE test stand in Fig.2). The problems facing the test were: measurements of the electromagnetic pump performances (primarily, “Volt – Ampere” and “pressure – flowrate” characteristics); testing and calibration of the electromagnetic flowmeter; examination of LBE flow hydraulics regime (stability, influence of gas inclusions, cavitations on EMP inlet); reliability of the Prototype (long run, 1400 hours, for design and manufacturing quality verification).

During the long run the maximum temperature of LBE was 420°C, of the EMP's coils – 510°C. Velocity of LBE in the pump's channel varied in the range 2...9m/s, pressure of He on the LBE free surface - 0.15...1.6bar. Non-dimensional parameters: $Re=w \cdot l / \nu = 5 \times 10^5$; $Pr = \nu \cdot \rho \cdot c / \lambda = 0.02$; $Fr = w^2 / g \cdot l = 7$; $Gr = \beta \cdot \Delta t \cdot Re^2 / Fr = 2.5 \times 10^8$; $Gr \cdot Pr = 5 \times 10^6$, where w - velocity of LBE; Δt - temperature difference in radial direction; ν , ρ , c and λ - viscosity, density, heat capacity and heat conductivity of LBE.

Results of measurements of electrical and hydraulics characteristics testifies that performances of the EM pump meets the requirements of the technical specification, see Fig.3.

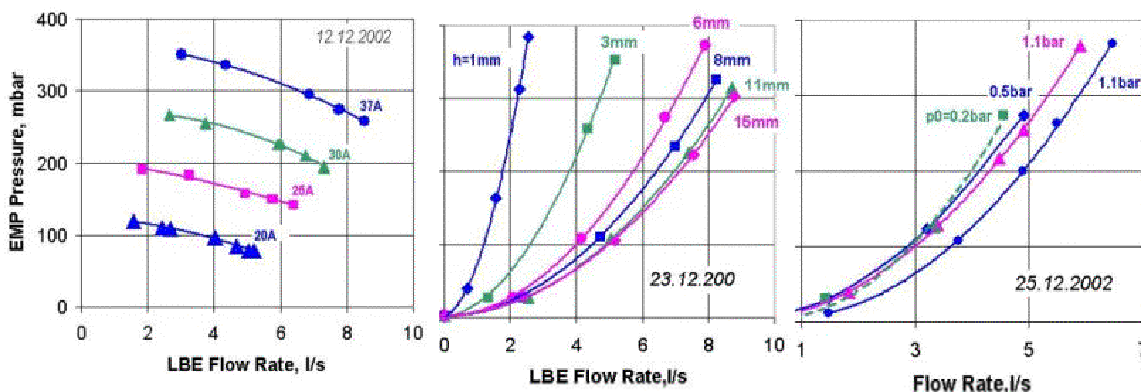


Figure 3: Measurements pressure – LBE flowrate characteristics of the EMP: left – current (I) in coils is constant, $h=1...11$ mm; middle – $h=const$, $l=20, 25, 30, 37$ A; right – helium pressure on LBE free surface 0.2...1.1bar.

The temperature of the pump's coils measured during the hydraulics test is little bit (5-6%) higher than predicted by A.Poznaks calculations. This can be explained by the absence of a heat exchanger on the test stand's periphery.

Test and calibration of the EM flowmeter was not performed during the hydraulics test in view of break in the sensor's electrical circuit.

The Prototype's housing was opened after the long run finishing and condition of the EM pump, flowmeter and LBE channel are carefully investigated. Photos of the pump, flowmeter and housing of the Prototype are reported in Fig.4. Basic directions of the Prototype inspection are following: Visual inspection of each element for the purpose of defects and deformations revealing. Max attention was put to the condition of electrical insulation coils; welding of silicone steel cores; results of overheating, corrosion, cavitations. SEM and EDX analysis of LBE channel's (samples) surface and cross section to clarify the reasons for the different wetting behaviour will be performed. Additionally the etched cross sections will be investigated by metallurgical examination to analyse the structure, the grain size and the thickness of the oxide layer. The measurements of EMP temperature, electrical characteristics and integral electrodynamics force applied to steel Imitator Installed in the LBE Channel were replicated.

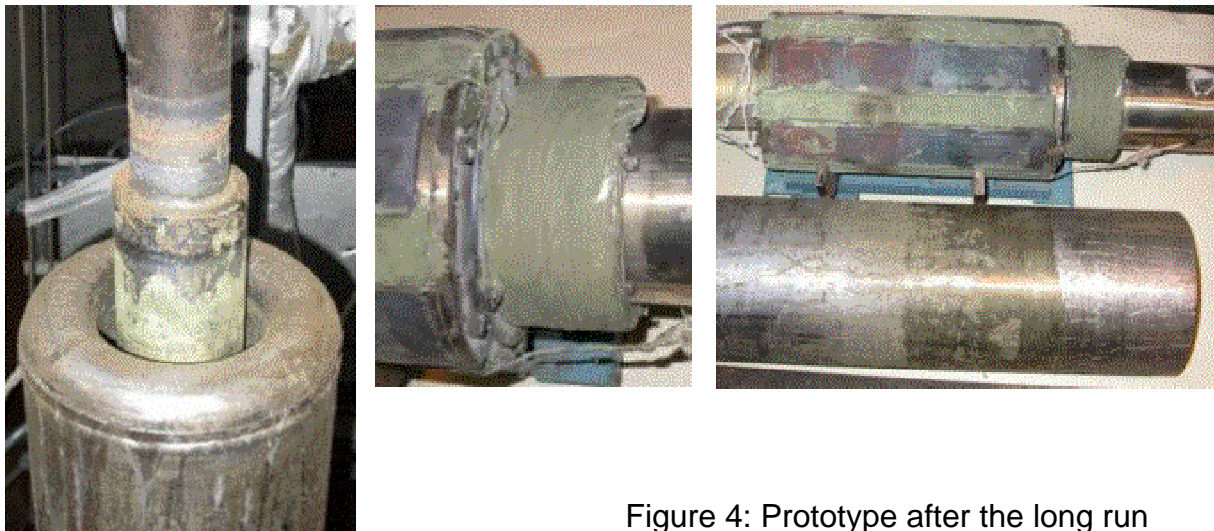


Figure 4: Prototype after the long run

The final inspection of the Prototype is not completed now, however it can be concluded that the design, performances and reliability of the electromagnetic pump corresponds to the technical specification. Electromagnetic flowmeters have not been calibrated and need further improvement and additional test, however it's workability is beyond questions now. Evidences of cavitations were not recognised even under cover gas pressure of 0.15 l/s. Injection of the He (approximately 1%) did not disturb the LBE flow behaviour.

References

- [1] G.S.Bauer, M.Salvatores, G.Heusener "MEGAPIE, a 1 MW pilot experiment for a liquid metal spallation target" Journal of Nuclear Materials 296 (2001) 17-33
- [2] J.E.Freibergs, E.Platacis "EMP-System for PbBi Melt at 280-450°C" Report. IPUL February 21, 2003, Salaspils (see on MEGAPIE server)
- [3] S.Dementjev, S.Ivanov "Measurements of MEGAPIE TARGET by-pass nozzle hydraulics resistance on mercury loop" PSI Technical Materials TM87-01-07, December 7, 2001
- [4] S.Dementjev, F.Barbogallo, F.Groeschel, I.Buceniaks, S.Krysko, A.Poznaks "Preliminary LBE test of Electromagnetic flow meter for MEGAPIE TARGET" MAGNETOHYDRODYNAMICS N4 2002

MEGAPIE TARGET HEAT EXCHANGER DETAILED DESIGN

L. Cachon, G. Laffont, J.M. Zuena, F. Dechelle
CEA - France

Abstract:

The Target Heat eXchanger (THX) is one of the 8 manufacturing packages of the target.

The THX consists of a single annulus of 12 cooling pins (2 sectors of 6 pins) inserted into separate channels in which the liquid PbBi flows. The space between the two sectors is reserved for the supply and return pipes of the D₂O safety-hull cooling. The heat removal is performed by an intermediate Diphyl® (Bayer) loop.

The THX is designed to evacuate 650 KW from Pb-Bi produced in the spallation zone at the bottom of the target, without risk of freezing in case of beam shutdown. The exchange surface and THX nominal regime was evaluated with engineering calculations and confirmed by E.F. calculations and by experimental tests.

The final version of the THX, based on thermo-mechanical calculations with E.F. code NASTRAN, minimized stresses due to mechanical loads and to thermal gradients in steady state and transient conditions.

The manufacturing file is now completed and the THX is ready to be manufactured.

Introduction

MEGAPIE (Megawatt Pilot Target Experiment) is an initiative launched by Commissariat à l'Energie Atomique, Cadarache (France) and Forschungszentrum Karlsruhe (Germany) in collaboration with Paul Scherrer Institute (Switzerland), to demonstrate, in an international collaboration, the feasibility of a liquid lead bismuth spallation target at a beam power level of 1 MW.

For the studies, design and manufacturing, the target has been sent in 8 packages. CEA is in charge of the Target Heat exchanger (THX) with the Upper LM Container.

Description of THX.

The THX consists of a single annulus of 12 cooling pins (2 sectors of 6 pins) inserted into separate channels in which the liquid PbBi flows. The space between the two sectors is reserved for the supply and return pipes of the D₂O safety-hull cooling. Heat removal is effected by an intermediate Diphyl® (Bayer) loop.

The THX is designed to evacuate 650 KW from Pb-Bi produced in the spallation zone at the bottom of the target, without risk of freezing in case of beam shutdown.



Figure 1 : View of THX made with CATIA V5.

Design methodology

In a first time engineering thermohydraulical calculations have been made to establish the exchange surface of the THX [1]. Geometry of each pins with channels diameter have been fixed.

In a second time, thermo mechanical finite element calculations have been performed to minimize stresses in structure due to pressure and thermal loads. Three kinds of calculation have been led :

- Accidental conditions, with a pressure load of 16 bar inside and outside the THX,
- Normal steady state thermal conditions,
- Normal thermal transient conditions, due to beam shutdown.

The final design integrates all the different evolutions needed to reach allowable stresses on THX. The main evolutions concern :

- Calculations made in accidental conditions, allow determining the thickness of the main critical component of THX, like UCF, ULMC and the Lower connecting Flange (LCF).
- Calculations made in steady state thermal conditions have shown that (figure 2) :
 - o Bellows are needed to accommodate thermal dilatation between Diphyll Distribution Boxes (DDB) and the Upper Connecting Flange (UCF).
 - o Thermal insulation between UCF and pins is needed to eliminate thermal stresses in UCF. Outlet tube of pin has been changed with a "Y" form.
 - o To protect "Y" outlet tube of thermal gradient, the Pin Thermal Insulation (PTI) has been added.

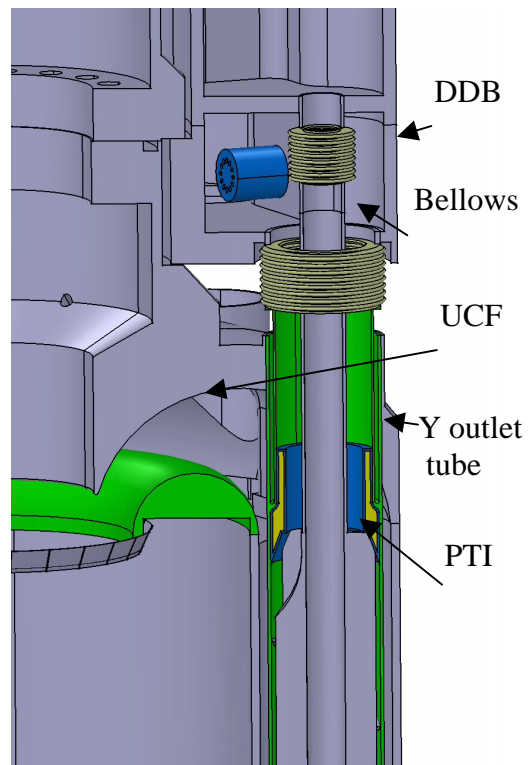


Figure 2: Design improvement due to steady state thermal calculation.

- Calculations made in thermal transient conditions, simulating beam shutdown, have shown that:
 - o The temperature field propagation through the thickness of UCF, which is a massive piece, leads to unacceptable stresses. A thrower has been inserted (figure 3). In this configuration the main part of the gradient temperature takes place in the quasi-static Pb-Bi gap contained between the UCF and the thrower.
 - o In the same time, grooves have been added to reduce massive area of ULMC. That way, the thickness of the ULMC remains as constant as possible to limit thermal stresses (figure 4).

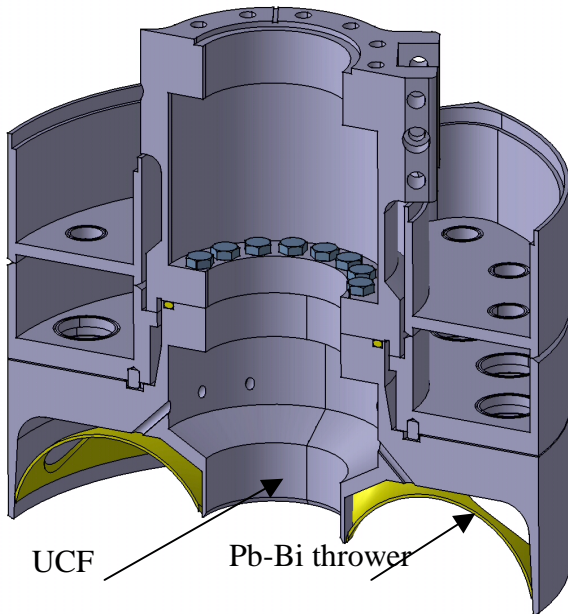


Figure 3: UCF with Pb-Bi Thrower

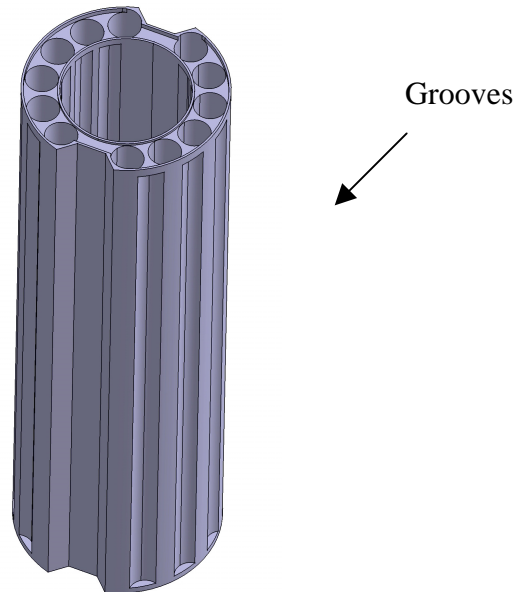


Figure 4: Upper LM Container

F.E. calculations

The THX has been design with the stainless steel 316 LN, which has 109 MPa as allowable stress at 350°C. The characteristics of the material are those given by [2].

Mechanical behaviour under accidental pressure load

An accidental leak of water in the target, could induce, depending on the location of the leak, two kinds of pressure loads on THX:

- Internal pressure of 16 bar,
- External pressure of 16 bar.

E.F. calculations were performed, simulating these two situations, with an additional force load presenting the weight of the lower part of the LM container with Pb-Bi. This weight was estimated at about 1000 daN.

Von Mises stresses results of these calculations (about 100 MPa Maximum), lower than allowable stress, confirm that the design is acceptable.

Normal steady state thermal conditions

The characteristics of the two fluids amount to the table 1.

	Temperature (°C)	Convection coefficient (W/m ² K)
Pb-Bi	333	9000
Diphyl	170	3600

Table 1: Exchange conditions of the two fluids.

This calculation shows the efficiency of the thermal insulation used between UCF and the pin (“Y” outlet tube, §3). In figure 5, you can see there is no thermal gradient in UCF, due to “Y” outlet pin tube: the temperature is homogeneous at 333°C. The stresses In UCF in steady state conditions are lower than 35 MPa (figure 6).

Due to the thermal gradient between Pb-Bi and Diphyl, the “Y” part of the outlet tube had to be protected by a thermal insulation made by a gap of stagnant Diphyl in a Stainless steel enclosure. Due to conductivity of stagnant oil (about 0,1 W/mK), this device reduce thermal gradient in the “Y” part of the outlet tube (figure 5) and in the same time the thermal stresses (lower than 90 MPa, figure 6).

Figure 5: Thermal field in steady state conditions.

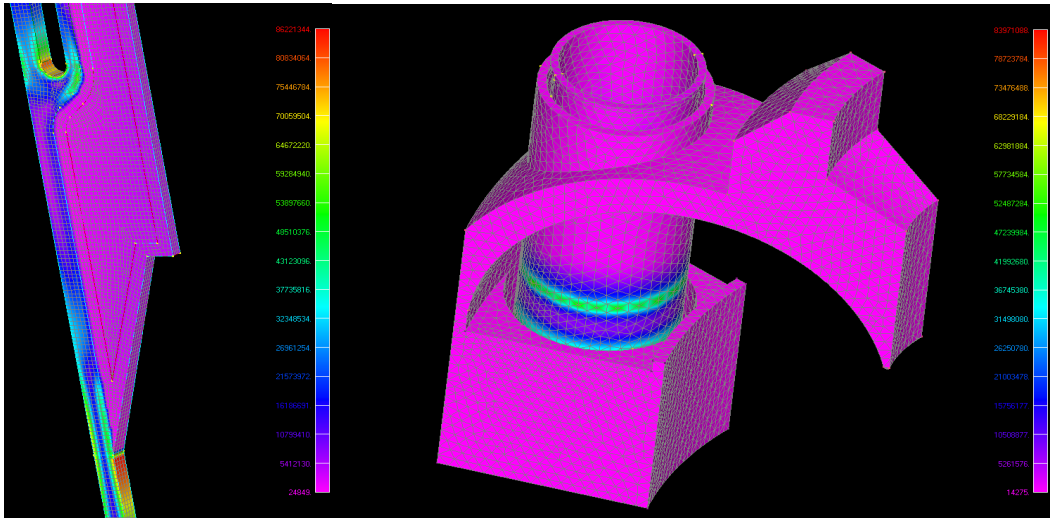
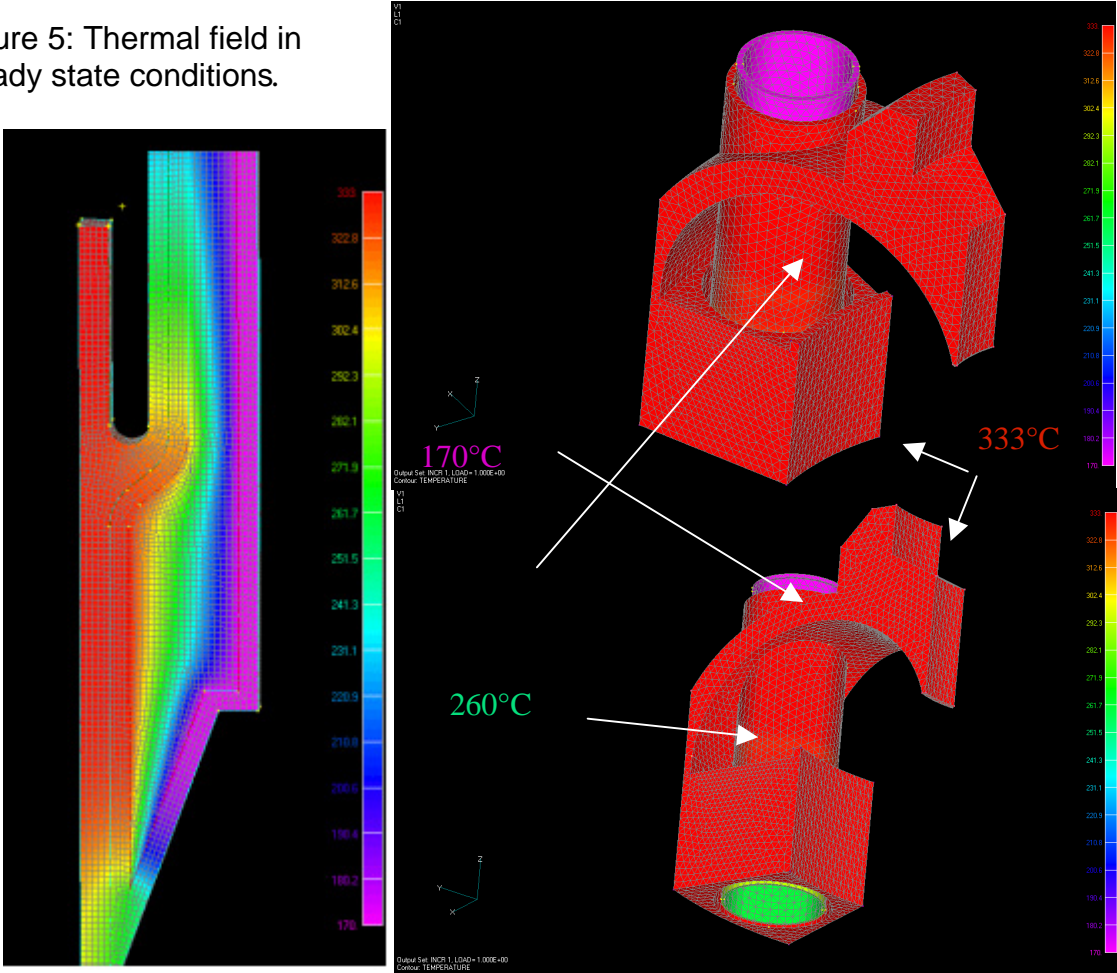


Figure 6 : VM Stresses field in thermal steady state conditions.

Normal thermal transient condition

The figure 7 shows the transient loads applied on the upper part of THX (RELAP5 calculations made by ANSALDO Energia).

The maximal thermal gradients are found in the time interval 10 – 16 s (figure 8). One can notice that the thermal gradient takes place in the liquid Pb-Bi, and the temperature in the UCF remains quasi homogeneous. The grooves made in the ULMC reduce thermal gradient. So, the VM stresses are lower than 70 MPa in the UCF and lower than 85 MPa in the most part of ULMC. Only one area has a level near 109 MPa, but it is not a critical area because its location is at the inside of ULMC, without influence of the ULMC resistance.

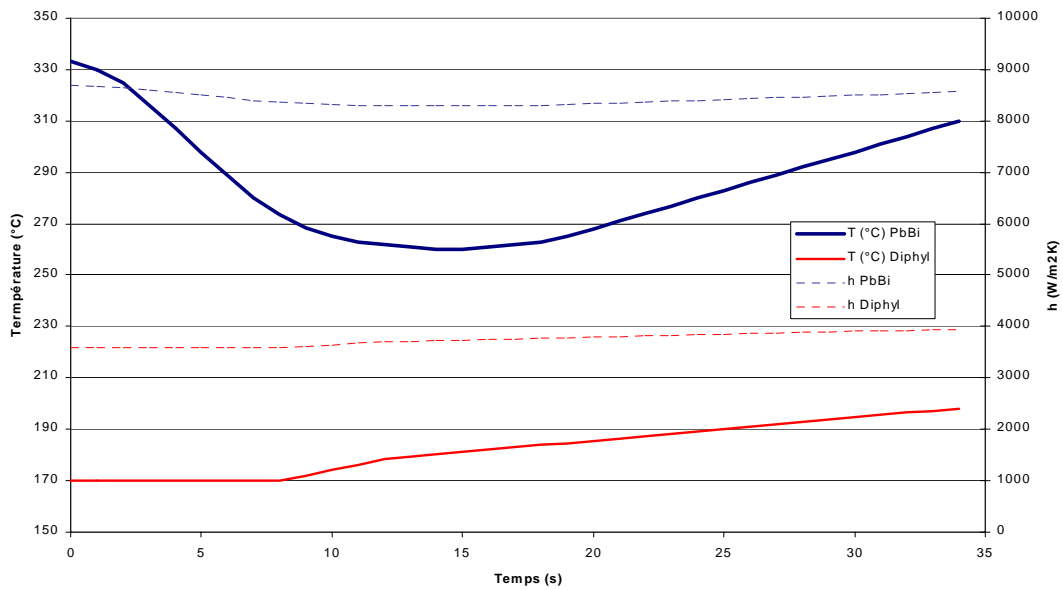
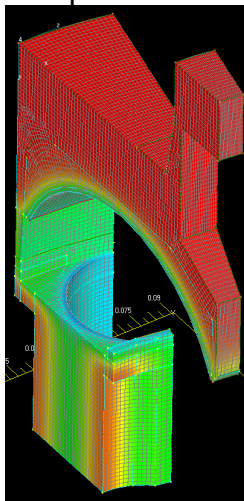
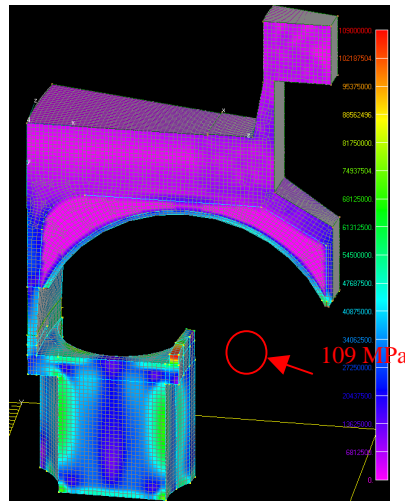


Figure 7: Transient loads of THX.

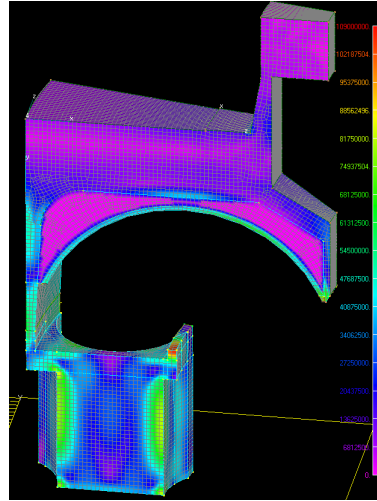
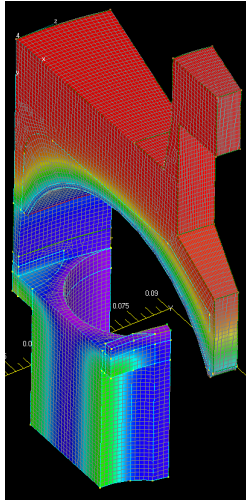
Temperature



VM Stresses



10 s



16 s

Figure 8: Results of transient calculations.

Fatigue calculations.

The design of the THX is made to have always stresses lower than allowable stress of 316 LN, which is 109 MPa at 350°C. The minimum elastic stress at 350°C is $Re_{0,2\%min}=121$ MPa.

Taking a stress concentration factor of $K_t=1,4$ [3],

$$\Delta\sigma_{totMaxi} = K_t \times 109 \text{ MPa} = 152 \text{ Mpa}$$

$$\Delta\varepsilon_1 = \frac{2}{3} \cdot (1+\nu) \cdot \left(\frac{\Delta\sigma_{tot}}{E} \right) = 0,08\%$$

With $K_\varepsilon = 1,035$ and $K_\nu = 1,03$.

$$\Delta\varepsilon_{tot} = (K_\varepsilon + K_\nu - 1) \cdot \varepsilon_1 = 0,086\%$$

The fatigue curve at 450°C of 316 LN [2], give a number of cycle higher than 108. It is very higher of the 10 000 cycles required.

Conclusions

Based on these results and on the CEA design code RCC-MX [2], the THX evolved to an optimised version made of 316 LN.

These results allow to conclude that:

- In accidental conditions, under the two pressure loads of 16 bar inside and outside, the stresses, resulting of E.F. calculation, are lower than the 316 LN allowable stress of 109 MPa.
- In normal steady state or transient conditions, E.F. calculations show that margin taken on the design are sufficient.

These E. F. calculations were only performed on parts or sectors representative of the global geometry (with symmetric conditions) or where maximum stresses levels were expected. The thermomechanical calculations for the global THX geometry were not performed because of the complexity of the THX and so, the too high number of meshes for computer capability.

In this work, the corrosion by Pb-Bi is not studied, but the choice of stainless steel 316 LN seems to be suitable in the work temperature range. For easier manufacturing, 316 L would be better: in this case allowable stress decreases from 109 MPa to 90 MPa. So the choice of 316 L has to be carefully evaluate part by part and can't be adopted for the whole THX. Some critical components such as the outer pin tube, or the ULMC, have to be made of 316LN.

References

- [1] L. Cachon, "Design of MEGAPIE Heat Exchanger", NT CEA/DEN/DER/STR/LCET 02/009.
- [2] RCC-MX, CEA, Edition avril 2002.
- [3] R.E. Peterson, « Stress concentrator Design Factor », J. Wiley and Sons ed., 1953.

HEAT REMOVAL SYSTEM: FINAL UPDATE OF CONCEPT AND DETAIL DESIGN, DIMENSIONAL AND FUNCTIONAL ISSUES

G. Corsini¹, M. Dubs², B. Sigg³, W. Wagner²

¹ANSALDO Nucleare, Genova, Italy

²Paul Scherrer Institut, CH-5232 Villigen-PSI, Switzerland

³ETHZ-LKT, CH-5232 Villigen PSI, Switzerland

Abstract

The Intermediate Cooling Loop (ICL) of the Heat Removal System (HRS) for the MEGAPIE target consists of the following main components: a plate-type Intermediate Heat Exchanger (IHX), a variable-speed motor pump, a three-way control valve and the Target Heat Exchanger (THX), which is integral part of the MEGAPIE target to transfer the heat from the primary liquid metal (LBE) to the secondary cooling loop. This ICL containing organic, diathermic cooling fluid, and its control system have been designed, by means of computer code simulations, to be able to properly control the LBE temperature at the target window inlet in case of proton beam interruption with subsequent power recovery or to lead the system to a stable hot stand-by condition. Initial provisions of chemical binding of gas generated by pyrolysis and radiolysis of the organic cooling fluid have been abandoned, because the existing cover gas plenum is able to temporarily store the gas between the scheduled monthly gas venting, without excessive pressure build-up in the system. Thermal insulation and heat tracing keep the ICL loop hot during extended shutdowns. A fluid thermal expansion compensator takes over the pressure-keeping function in case of isolation valve closure and protects the target window from overpressure in case of THX pin rupture. Attention has been given to the functional requirement of limited load from the ICL piping to the target head by providing a system of three hinged compensators to form a cardanic joint.

Introduction

The Heat Removal System (HRS) for the MEGAPIE target has the following functions:

- Removal of the heat introduced during beam operation by the nominal 1 Megawatt proton beam of SINQ.
- Control of the target temperature during beam trips and scheduled beam shutoffs to keep the target temperature at a level where the Lead Bismuth Eutectic (LBE) filling remains in the liquid state and to prevent excessive temperature excursions after beam interrupts.
- Preheating of the target and control of the target temperature before and during the filling and draining operation with liquid LBE.

The present paper summarizes the technical concept in the final status, gives information on the thermal cycle data, and describes the different operation conditions including transients after beam trips and interrupts. Further, radiolytic/pyrolytic gas production in oil, oil degassing and gas handling are addressed.

Reference Configuration

The main components of the Intermediate Cooling Loop (ICL) belonging to the Heat Removal System (HRS) of MEGAPIE are the plate-type IHX (Intermediate Heat Exchanger), that exchanges heat with water of the outer cooling system, the canned-motor pump installed upstream of the IHX, one three-way control valve, one

expansion tank coupled with a cover gas plenum tank, one thermal expansion compensator installed between the isolation valves. The Target Heat Exchanger (THX) is not included, because integral part of the MEGAPIE upper target section. The diathermic fluid, that fills the intermediate cooling loop, is a mixture of partially hydrogenated terphenyls (Diphyl THT, Bayer's trade name, referred to in this paper as the oil)).

The flow scheme of the Intermediate Cooling Loop is shown in the following Figure 1 [1].

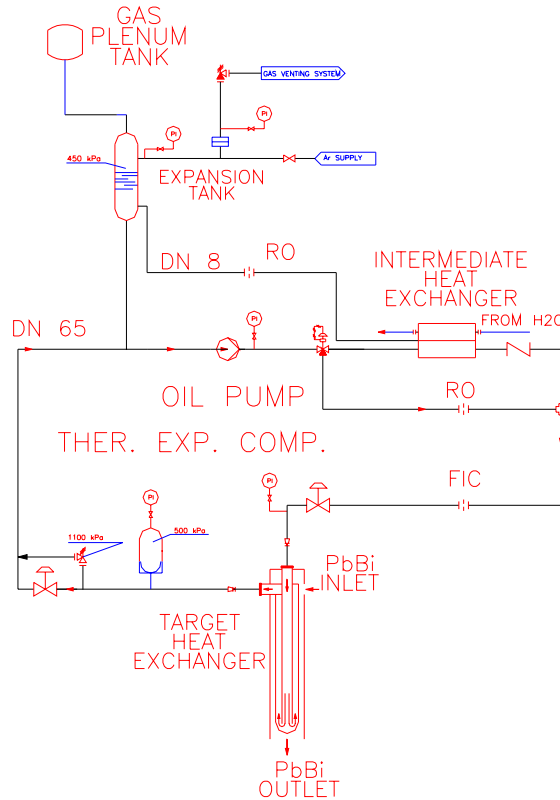


Figure 1: Flow scheme of the Intermediate Cooling Circuit of MEGAPIE HRS

Thermal Cycle Data

The following input data, relating to the Lead-Bismuth Eutectic (as the primary coolant) at nominal full-power, steady state condition, apply:

- THX outlet temperature (LBE): 230 °C
- THX inlet temperature (LBE): 333 °C
- W_{LBE} : 40.6 kg/s

Hence, the power removed by the THX is 620 kW. The corresponding thermal cycle data of the intermediate cooling circuit have been figured out as follows [2]:

- IHX inlet and IHX by-pass temperature: 166 °C
- IHX outlet temperature: 104 °C
- W_{oil} through the IHX: 5.22 kg/s
- (\cong 60% of the pump nom. flow rate, the remaining flow rate is bypassed)
- W_{oil} through the THX: 8.75 kg/s

Hence, the THX inlet temperature of the oil is 130 °C. A small oil stream (0.1 kg/s) is fed to the expansion vessel for radiolysis gas degassing purpose.

These thermal cycle data are actually the result of the RELAP5 computer run prediction of the performance of the HRS cooling circuit [3], which is consistent with slightly reduced proton beam power (620 kW instead of the previous 650 kW) and THX outlet temperature (230 °C instead of 240 °C). This and 15 kW additional power transferred from the canned-motor pump to the THT oil define the thermal duty of the IHX.

Steady-State Operation of HRS with Proton Beam

During beam operation, the Heat Removal System ensures:

- Cooling of LBE through the Target Heat Exchanger (THX),
- Control of the LBE temperature on the cold leg of the primary circuit (THX outlet).

During hot standby, the Heat Removal System contributes to ensure the control of the LBE temperature at the THX outlet.

At steady-state conditions, the system is operated in such a way that the LBE temperature on the THX outlet remains constant at 230°C over the beam power range¹ (¹ This means about 252°C at the entrance in the target zone, because of the heat exchange between downcomer and riser in the Target Unit [5]). The temperatures of the LBE and THT cooling circuits at zero beam power (see Fig. 2) are almost equal and slightly below this temperature, the latter because of the assumed heat losses, and this favours the control stability. It has to be noted that the equilibrium value of the LBE temperature at zero beam power depends, however, on the actual heat losses in the target unit and IHX and therefore the equilibrium value may turn out to be different.

The status of the HRS during beam operation is monitored as follows:

- the pressure in the system is monitored by pressure transmitters ensuring that the pressure remains within the upper and lower limits required by the system design; the pressure transmitters are on service to alert the operator in case of accidental overpressure or depressurisation of the HRS
- the temperature in the system is monitored by the temperature indicators located both on-line and on the expansion tank
- the level in the expansion tank is monitored through the level transmitter
- the flowrate through the THX is monitored by a flow transmitter

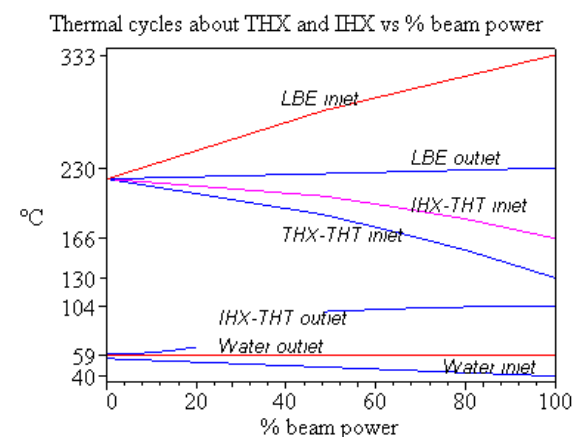


Figure 2: Steady-state thermal cycles over the 0 to 100% beam power range

At reduced beam power, Fig.2, a corresponding increase of the diathermic fluid bypass flowrate provides for reduced heat removal by the IHX. The heat removing capability can also be remotely adjusted down to about 60% by reduction of speed of the variable-speed pump motor.

HRS Transients

Besides the normal beam start-up and shutdown transients, the HRS must cope with beam trips and interrupts caused by frequent instabilities in the accelerator system. Power transients caused by beam interrupts lasting longer than about half a ms lead, at present, to a 10-s beam shutdown followed by a 20-s linear ramp power recovery (normal transient). The HRS does not require intervention by the operator to manage the transient, according to the results of the dynamical RELAP computer code simulation, because the automatic PID control of the LBE cold leg temperature, as it has been assumed in the simulation, is capable of bringing the HRS back to normal steady state, with associated relatively mild transients [3].

It should be noted that in case of significant deviation of the real control mode from the theoretical one, the system response as illustrated in this paragraph might need to be revised.

Two cases must be distinguished depending on whether the beam power can be recovered after 10 s or not:

Normal beam-interruption transients

This case is part of the normal operating mode of the HRS. The LBE THX outlet temperature is modulated by the automatic control system, which acts upon the 3-way bypass valve of the HRS oil circuit. In about 100 s from the beam trip, the normal, stable steady-state LBE cold leg temperature is recovered, see Fig. 3

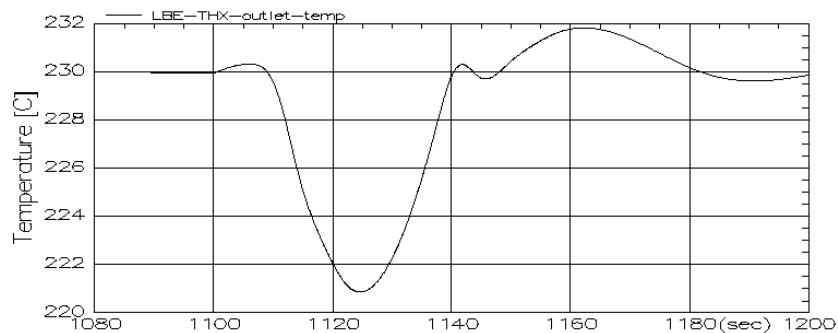


Figure 3: LBE temperature excursion at the LBE-THX outlet after a normal (10 s) beam interruption (result of RELAP calculation)

Transient to the hot stand-by condition

Unlike the case of normal beam interruption transient, action by the normal automatic control system is indispensable after the beam trip if the beam power cannot be recovered after 10 s. In this case the heaters in the central rods shall be switched on two seconds later or 2 s after any intentional beam shutdown, whichever case occurs [3]. The electric power of the heaters will be controlled in order to maintain the LBE THX outlet temperature at the value of the hot stand-by (about 220°C for the case of the simulation, see also Figure 2). Should the 3-way control valve fully by-pass the IHX, any reverse flow through the IHX towards the Expansion Vessel with the

associated overcooling of the oil, would be prevented by the tight-shutoff check valve installed downstream the IHX.

Oil Degassing

The advantages of selecting an organic synthetic fluid for the intermediate cooling loop of MEGAPIE are relevant for safety issues, particularly the low vapor pressure, the high boiling point with respect to the operating temperatures, the low toxicity to humans, the low induced radioactivity and the ensurance of no fast chemical reactions with the hot LBE or water, in case of accidental leakage of the heat exchangers.

Uncertainty about the amount of gas production by radiolysis under γ -rays from the activated LBE, the irradiation source prevailing at the level of the THX, had led to a concept of chemical binding *in-situ* of the radiolysis gas, mostly hydrogen, by means of mixed Cu and Ca oxides. A recent analysis (Doc nr AN-34-02-04 MEGAPIE, Radiation Dose Received by Diphyl in the MEGAPIE primary heat exchanger, by E. Pitcher, PSI issued 29/11/02,) however, carried out using MEGAPIE-specific neutron flux and spectrum, predicts a substantially lower deposited energy in the oil than previous estimates (The use of an organic fluid as diathermic coolant for the intermediate cooling circuit of MEGAPIE, paper presented at the previous MEGAPIE TRM, March 5/6, Bologna). The associated lower amount of radiolysis gas expands in the cover gas plenum provided formerly for the mixed oxides, without substantial pressure increase of the cover gas, and can be vented during the periodically scheduled shutdowns of the MEGAPIE facility. Degassing of the oil takes place in the expansion tank and is enhanced by a small bypass degassing line from the top of the IHX, thereby ensuring that no gas bubbles affect the heat exchange.

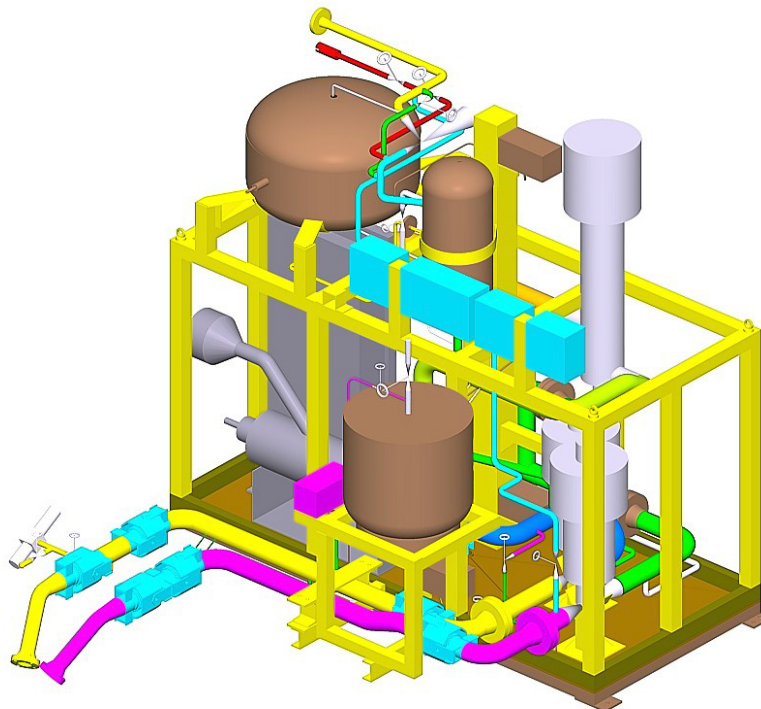


Figure 4: Isometrical view of the skid-mounted Intermediate Cooling System of MEGAPIE HRS

MEGAPIE Target Head Connections

The requirement of limited forces acting upon the target head from the two connection pipes has been met by a system of three hinged compensators provided

with tie-rods, i.e. one hinged compensator plus a combination of two compensators to form a cardanic joint, Fig. 4 [4, 5]. This arrangement has also the advantage of a built-in capability of adjusting small pipe-to-target head nozzles misalignments, which may occur after transfer of the HRS from the Integral Test Stand to the TKE.

MEGAPIE THX Isolation

In case of closure of both isolation valves on either side of the THX (isolation case), the trapped oil would heat up from 148°C mean temperature to about 270°C (Fig. 5). In order to accommodate the extra oil volume resulting from the thermal expansion of the trapped oil and the additional oil expansion brought about by the radiolysis/pyrolysis gas generated over one week of isolation, a thermal expansion compensator is foreseen (the vessel left from the target head in Fig. 1 and in the center of Fig. 4). During isolation, this compensator takes over the pressure-keeping function of the expansion tank and protects the target window from overpressure in case of THX pin rupture, i.e. 10 bar (g) max.

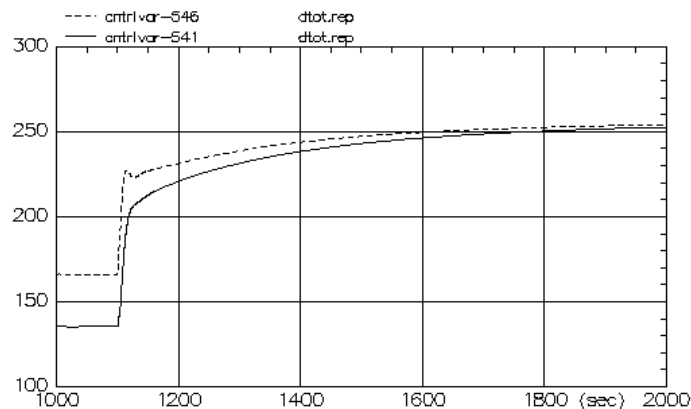


Fig. 5, Temperature (°C) transient of the oil trapped inside the THX (hot and cold leg) in the isolation case.

Status of HRS in March 2003

At present the ICL of the HRS is in the status of purchasing the individual components. Delivery of these components is expected in the period May to July 2003, and assembling can start in June. After the factory tests the delivery to PSI is expected for Dec. 2003.

References

- [1] MPIE 1 DMJX 008 – P&ID, Heat Removal System, Rev.3.
- [2] MPIE 1 SIFX 006 – System Specification, Heat Removal System, Rev.2
- [3] MPIE 1 TRIX 201- Thermal Hydraulic Analysis Report, Rev. 0.
- [4] MPIE 1 DCBX 010- Heat Removal System Composite Drawing, Rev. 4.
- [5] MPIE 1 TMLX 015- Heat Removal System Stress Analysis, Rev. 3.

COVER GAS SYSTEM: UPDATED BOUNDARY CONDITIONS AND CURRENT CONCEPT

W. Wagner¹, F. Gröschel¹, G. Corsini²

¹Paul Scherrer Institut, CH-5232 Villigen-PSI, Switzerland

² ANSALDO Nucleare, Genova, Italy

Abstract

The gas production during the target operation period of 6000 mAh has been reevaluated, resulting in a more precise value for the He production of 1.1 liter NTP, a value meanwhile confirmed by an experiment at CERN/ISOLDE irradiating a lead target with a proton beam. For the current concept decision was taken to omit the gas absorbers in the target (except of a condensation trap for volatile Hg), collect all gases in the plenum and vent the plenum in defined periods into a decay tank. Regular venting (every 4 to 8 weeks) is anyway required by reasons of radioactive inventory limitation. Pressure built-up considerations find that the maximum operation pressure in the cover gas plenum can then be limited to 2.2 bar absolute.

Cover Gas DESIGN CRITERIA

During normal operation of the MEGAPIE target, the spallation reactions in PbBi produce gases and vapors that accumulate in the gas plenum of the Target Expansion Tank. Consequently, a Target Cover Gas System (CGS) is required to perform the following functions [1,2]:

- Deflate the cover gas plenum of the Target Expansion Tank into a Decay Tank, down to the initial plenum pressure.
- Sampling the gas of the Target Expansion Tank before or during deflation.
- Sampling the gas of the Decay Tank before venting.
- Between the venting cycles the CGS pipes shall be evacuated and then filled with Ar gas.
- Deflate the Decay Tank to the controlled Exhaust System.
- After the end of the MEGAPIE experiment empty the target cover gas into the Decay Tank; successively disconnect the pipes at the outlet of the Target Expansion Tank.
- The whole Target Cover Gas System shall be removable by a hoisting device.
- From the CGS the environmental radiation level in the TKE shall not significantly be increased (stay below 0,2 mSv/h). Therefore a dedicated shielding around the CGS has to be provided.
- The thickness of shielding will be determined by the requirement to provide personnel protection during handling and by the wish to install conventional instead of very high radiation-resistant instrumentation, by consideration of the constraints of reasonable weight and available space for the GCS in the TKE.
- The sample used to transfer the gas to the γ -spectroscopy laboratory including necessary shielding has to meet a maximum weight of 10 kg, shall not harm the personnel involved in the operations and the radioactivity shall not trespass the saturation level of the γ -spectrometer. Therefore the maximum source strength of radioactive gas for sampling operations is required not to exceed 10^6 gamma per second and the dose rate outside its shielding to remain below 0,2 mSv/h.
- Every operation within the lead shielding must be remotely handled.
- In order to detect and contain a radioactive gas leakage from the components, the whole CGS is installed inside a metallic leak-tight envelope, kept under moderate vacuum and connected to the Secondary Containment Loop.

- CGS components shall be qualified to operate at the radiation level existing where it is installed; at present the CGS is located near the north-east corner of the TKE, where it can be hoisted by the local crane.
- All the CGS components shall be qualified "explosion-proof" according to the transport of hydrogen in the target cover-gas.

Gas production and pressure conditions

The anticipated gas production by spallation reactions in the liquid LBE during the full period of operation of 6000 mAh is given in Table 1. The value for He-production, initially uncertain within the limits of 0.24 to 2.6 liter NTP, has been recalculated to 1.1 liter NTP by E. Pitcher, a value meanwhile confirmed by an irradiation experiment at CERN/ISOLDE using a lead target that yielded an amount between 1.0 and 1.6 liter NTP. The concept of implementing absorbers inside the target head to bind the produced H₂ has been abandoned meanwhile such that the CGS has to manage the entire gas inventory. Generic pressure built-up considerations come to the following results:

- Total gas production: 7.2 liter NTP
- Starting operation pressure: ca. 200 hPa
- Target head volume: 2.5 liter (2.0 liter warm)
 - o after 6000 mAh: pressure-rise from 200 to 7600 hPa (at 250°C)
 - o after 750 mAh: (4 weeks) 1100 hPa (at 250°C)
 - o after 1500 mAh: (8 weeks) 2000 hPa (at 250°C)

By reasons of radioactive inventory limitation (iodine, Xe¹²⁷ etc.) for severe accident management regular deflation after operation periods of 4 to 8 weeks is anyway mandatory. This leads to the conclusion that a maximum operation pressure of the CGS of 2200 hPa is a feasible design limit (the design pressure of the components is 12000 hPa)

Note: Volatiles (Hg, ...) have not been considered in the above given considerations and might increase the pressure by up to 0.7 bar for the entire irradiation period. The pressure levels and limits for the CGS operation are:

- Target Expansion Tank, max. allowable operation pressure (at 240°C): 2200 hPa (a)
- Target Expansion Tank, initial operation pressure (at 240°C): 200 hPa (a)
- Target Expansion Tank, max. pressure requiring deflation (at 240°C): 2000 hPa (a)
- Decay Tank, initial pressure (at 40°C), deflated: about 40 Pa (a)

Design description

The CGS concept is characterized by the following operating principles:

- Periodical deflation of the target cover-gas plenum into the Decay Tank.
- Emergency deflation of the target cover-gas plenum, even if the Decay Tank contains still radioactive gas of a previous normal deflation.
- Vacuum pump used to evacuate decayed gas and target cover gas plenum.
- Radioactive gas sampling by means of a line branched off the main line, upstream of the filters.

The P&ID scheme of the Cover Gas System, Ref. [3], is given in Figure 1, where the system is shown during normal beam operation.

The main components of the CGS are a relatively large-volume Decay Tank, a two-filter set (HEPA filter, upstream of a carbon filter), a vacuum pump with another carbon filter in line, and interconnecting pipes, with pneumatic-actuated valves.

Gas sampling takes place by isolation and removal of a portion of the sampling line, which can quickly be disconnected by means of gas leak-tight, face-to-face couplings.

The whole CGS (except the main line coming from the Target Expansion Tank) is installed on a skid, inside a Pb shielding box (except the vacuum pump) and can be hoisted away at the end of the Megapie campaign, disconnecting the lines that pass through the shielding.

The whole CGS (except dedicated piping) and the line coming from the Target Expansion Tank are installed inside a metallic leak-tight envelope, in order to contain possible radioactive gas leakage. This metallic envelope is connected to the Secondary Containment Loop that normally assures the radiation monitoring of the CGS components.

System Description

In detail, the Target Cover Gas System (CGS) consists of the following components:

Lines between Target Cold Trap and valves AA101/AA106

Piping BR11 connects the Target Expansion Tank to the pneumatic-actuated valves AA101 / AA106 installed in parallel. The operator shall open these valves one at a time, beginning the deflation of the Target Expansion Tank.

Upstream AA101 (and AA106), the pressure transmitter CP01 and the pressure switch CP07 are installed to monitor continuously the pressure of the Target Expansion Tank both during normal proton beam operations and during the deflation process.

In order to limit the argon flow-rate during deflation, the restriction orifice BP001 is installed upstream of the AA101 valve, while the restriction orifice BP002 is installed upstream of the AA106 valve. The orifices are provided of leak tight flanges, to enable a quick disconnection and replacement, when needed.

An isolation valve is installed between the Cold Trap and the pressure elements CP01/ CP07, as close as possible to these instruments. This manual-actuated valve (AA201), provided with a stem extended outside the leak-tight guard pipe, permits the maintenance of the pressure instruments, the orifices BP001/ BP002 and the valves AA101 / AA106, by isolating the CGS from the plenum of the Target Expansion Tank.

All the line BR11 (isolation valves included and pressure-elements not included) is provided with a radiation-shielded protection. In addition this line, also with the pressure elements, is confined inside a dedicated leak-tight guard pipe, connected with the skid envelope to allow flow-stream circulation throughout the Secondary Containment Loop.

Lines between isolation valves AA101/AA106 and skid quick-connection

The line BR01 connects the valves AA101 and AA106 to the skid quick-connection. The line BR10, connected to the BR01 downstream of the valves AA101 and AA106, allows the fresh argon feeding through the pneumatic-actuated valve AA105 and the check valve AA301.

The lines BR01 and BR10, including also the valve AA105, are confined inside the dedicated leak-tight guard pipe. The guard-pipes of the lines BR01 and BR10, as for

BR11, are all connected with the skid envelope to allow flow-stream circulation throughout the Secondary Containment Loop.

Lines between skid quick-connection and Sampling Equipment

The line BR03 connects the skid quick-connection to the Sampling Equipment. The line BR06 connects the Sampling Equipment to the Decay Tank via the pneumatic-actuated valve AA104.

The Sampling Equipment, possibly provided with its own Pb-shielding (which still has to be defined), is installed outside both the skid shielding and the skid leak-tight envelope.

The Sampling Equipment, after isolation provided by the remotely actuated valves AA202 and AA203, can be quickly disconnected from the CGS skid by means of gas leak-tight, face-to-face couplings, in order to analyze its gas-content.

Lines between BR03 and filters AT001 and AT002

The line BR02 connects BR03 to the Decay Tank inlet; on the line BR02 the valve AA102, pneumatic-actuated, is installed upstream of two filters. These components, an absolute Aerosol Filter AT001 and an Active Carbon Filter AT002 are installed near the Decay Tank. Because they should accumulate radioactive matter (mainly aerosols and J, Hg) over their service life, the filters shall be installed inside the skid Pb-shielding.

Decay Tank BB001

The Decay Tank is a cylindrical vertical vessel; it is available for the radioactive gas, coming from the Target Expansion Tank during normal and emergency deflations. It is the main component installed inside the skid Pb-shielding.

Line between Decay Tank BB001 and Exhaust System

To empty the decayed gas towards the Exhaust System by means of the High Vacuum Pump AP001, a line (BR07) with the pneumatic-actuated valves AA107 and AA109 is provided. On this line the vacuum transmitter CP03 assures the monitoring of the Decay Tank pressure.

The pump AP001 is installed outside the skid shielding, but inside the skid envelope belonging to the Secondary Containment Loop; its local vacuum-meter CP05 is installed outside the skid envelope.

A carbon filter AT003 is installed inside the skid shielding, upstream the AP001 pump. This filter ensures trapping of any aerosol and traces which eventually escaped from the Decay Tank.

A quick leak-tight coupling connects the CGS with the Exhaust System.

Loop between vacuum pump AP001 and Decay Tank BB001

In order to allow the evacuation of the Target Expansion Tank to its minimum operation pressure (about 200 hPa), and, at the end of the MEGAPIE irradiation campaign, to high vacuum, it is possible to connect the Target Expansion Tank to the pump suction via the by-pass line BR08. The gas is so pumped into the Decay Tank by opening the manual valve AA110, installed on the line BR09.

Radiological Protection

During beam operation, in the north-east corner of the TKE, the gamma dose rate is 7,20 Gy/h and the neutron dose rate is 0,25 Gy/h.

Three hours after shutdown, as the gamma dose rate is approximately 0,8 mSv/h, the additional contribution from CGS components shall not exceed 0,2 mSv/h, in order to have a maximum of 1 mSv/h in the room TKE.

This criterion is fulfilled by means of a removable lead wall (made e.g. of lead bricks piled *in-situ*) that encloses the skid that houses the Decay Tank, filters and tubing.

For the skid radiation shielding (especially for Decay Tank BB001), the following are foreseen:

- lead-shielding skid: top and lateral walls 120 mm
- lead-shielding skid: bottom and rear wall 50 mm

For the instrumentation positioned outside of the CGS skid, in the north-east corner of the TKE, the required qualification of radiation resistant instrumentation may be alleviated.

Sampling Equipment

The cover gas dilution procedure allows a sampling line portion of about 100 mm length. This line portion is shielded by a lead layer, thickness about 50 mm, and, according to calculations, irradiates at a dose rate (measured at the outer surface of the shielding) that is largely below the limits for personnel protection.

References

- [1] MPIE 1 SIFX 005, 'System Specification – Target Cover Gas System', ANSALDO (2002)
- [2] [MPIE 1 SIPX 003, Technical Report: 'Target Cover Gas System – Design Criteria and Description' ANSALDO (2002)
- [3] MPIE 1 DMJX 009 'Target Cover Gas system P&ID', ANSALDO (2002)

H ₂	6.0
He	1.1
Ar	0.0026
Kr	0.06
Xe	0.024
Total	7.2

Table 1: Gas production (liter NTP) in the LBE target during 6000 mAh of beam operation (Source: Enderle: Neutronic Benchmark)

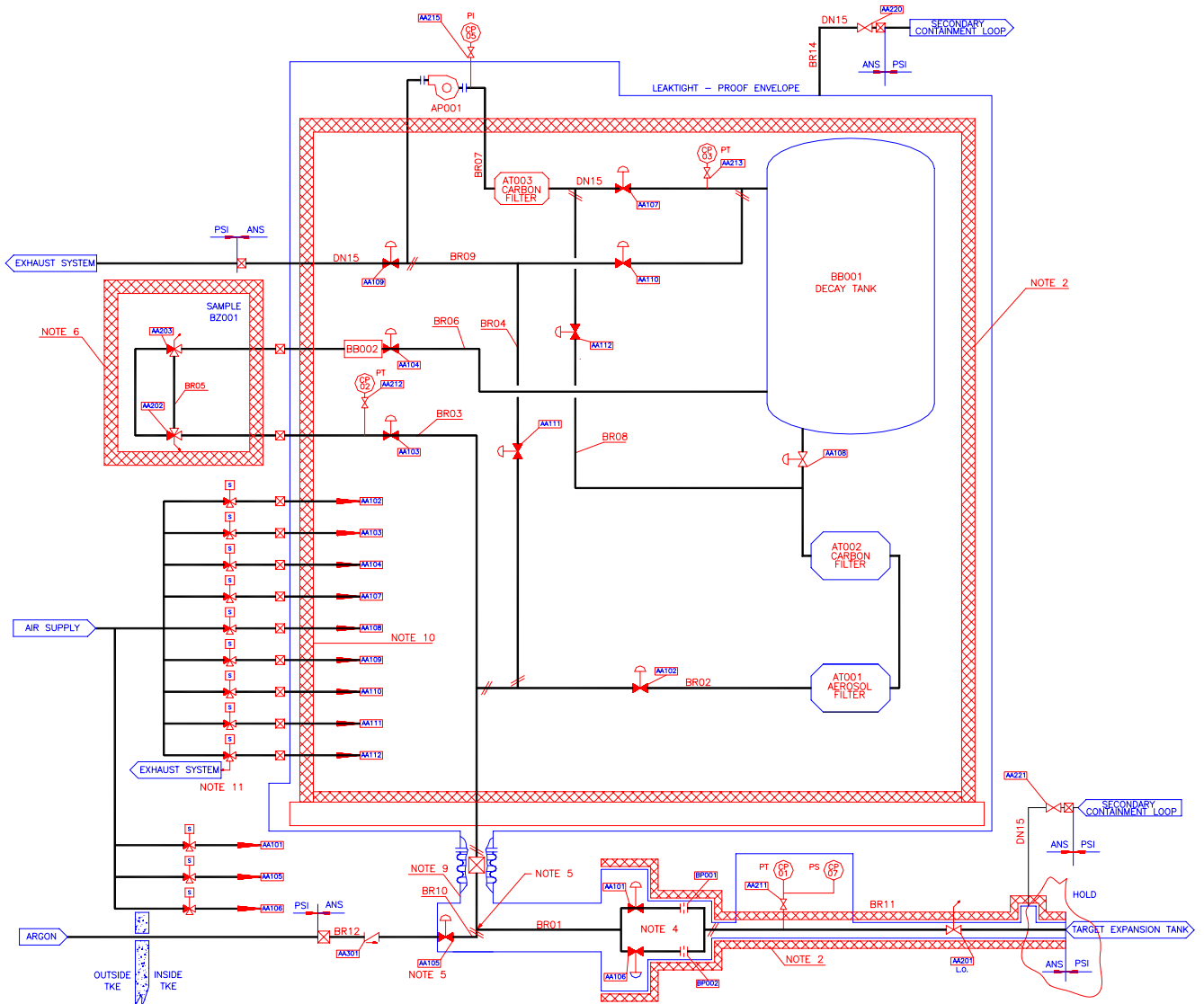


Figure 1: P&ID scheme of the cover gas system

FILL&DRAIN AND FREEZING: SYSTEM MODIFICATIONS FOR MERELY NON-ACTIVE DRAINING

W. Wagner¹, P. Turrioni², P. Agostini², K. Thomsen¹, E. Wagner¹, J. Welte¹

¹Paul Scherrer Institut, CH-5232 Villigen-PSI, Switzerland

²ENEA, Brasimone, Italy

Abstract

The consideration of merely non-active draining of the MEGAPIE target would allow the Fill&Drain System to be considerably simplified without changing the principle operational concept. The main measures of simplification comprise the possibility of manual operation, no need for radiation resistant equipment and no need for a second containment. A new concept was elaborated of covering plugs for the filling tubes, which assures that gas pressurization of the filling tubes after plugging is always possible and that no liquid LBE can raise up to the target head area.

Introduction

For filling and draining the MEGAPIE target with liquid Lead Bismuth Eutectic (LBE) a concept had been elaborated by ENEA, which allowed, besides filling and draining in an inactivated state, also the draining of the LBE after the target had been in service [1]. This concept meanwhile has been questioned, by reasons of system simplification, cost saving and, last not least, risks minimization. The latter was strongly emphasised by the licensing authorities. The present paper presents the system modifications for merely inactive draining.

Simplifications for the new inactive Fill&Drain System

The simplification of the Fill& Drain system functions by eliminating the draining of the LBE out of an irradiated target reduces very significantly the complexity, leading to a new inactive Fill&Drain system. It also renders unnecessary the tough tasks to be assigned to a protected hand operator in the proximity of the head of an irradiated target inside the TKE.

A first relevant relief on the hardware complexity comes by eliminating the necessity of the double containment all along the lines connecting to the target head including the draining vessel. That avoids the constraint that the process pipes and valves must be placed inside a compact gas tight structural box, which had imposed a high reliability for the instrumentation and for a remote operation of the valves.

Shielding and cooling as a consequence of the radioactivity is not any more required when draining merely inactive LBE. This allows to dismiss the heavy lead blanket around the draining vessel, and the cooling water circulation inside to control the inner temperature. Further, there is no need any more for radiation resistant equipment like valves and instrumentation. All operations can be made hands-on.

Main features of the inactive Fill&Drain System

The main functions of the inactive Fill&Drain System are the following:

- providing clean liquefied LBE out of solid ingot material
- filling the target with liquid LBE
- draining LBE out of the target when required before any significant irradiation exposure
- preserving the drained LBE for a subsequent target back-filling.

The filling and draining must be possible repeatedly with the target being placed either at the test stand or in the TKE.

Figure 1 shows the P&ID scheme of the inactive Fill&Drain System. It contains the following main components:

Two main vessels:

- The melting vessel S01 provided with a removable closing lid where ingots of the base material are loaded from the top.
- The vessel S02 where the LBE after liquefaction is poured into, flowing through a filter to separate the scum and slag.

The vessels are equipped with electrical heaters and thermal insulating blankets. Both have an upper gas plenum with non-oxidizing or oxide protecting gas mixtures.

LBE pipes connect the two vessels and the target head:

- The line T01 provided with a filter for transfer the LBE from vessel S01 to S02;
- The lines T02 for filling the target out of S02 and T03 for draining it. The separate inlet pipes into the target for filling and draining are maintained as for the previous system design [1].

Further, a set of gas and vacuum pipes is provide for:

- Inert oxygen protection gas (Ar) feeding (T12 and T13);
- Exhaust gas discharge (T11 and T14), and T11 with a bypass through a vacuum pump (P01);
- De-oxidation gas mixture flowing into the LBE tank S02 (T15).

A variety of instrumentation is provided for the system control (i.e. thermocouples for the heating sections of the LBE pipes and vessels) and for the process control (i.e. thermocouples for LBE plenum temperature and balance cells for LBE weighting). The full list of the valves and instruments is given in Tables 1 and 2.








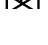



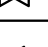

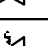
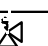


The system can be separated into sub sets for specific operation. After the first melting completion and LBE transfer, the vessel S01 can be disconnected from the vessel S02. The latter, due to the less demanding requirement for handling inactive LBE, can now be oversized with respect to the requested LBE capacity to allow easily for LBE expansion during recrystallization after solidification for long term holding and transportation. The vessel S02 together with the LBE filling and draining pipes and service gas pipes can be temporary placed in a position near the target head inside the TKE, just for the time required to fill and/or drain, and will be removed before the irradiation period. In case of an incident at the very beginning of the irradiation it can be brought back in again.

A new concept has been elaborated for plugging the fill and drain pipes at the target head after the final filling before irradiation. The scheme is illustrated in Figure 2, together with the different steps of filling the target and mounting the plugs. The plug fulfils several purposes: besides simply plugging the pipes with a Swagelok valve they prevent the LBE to raise to the top of the pipes in the target head. This is achieved by long cylindrical rods, flexibly connected, that intrude deeply into the pipes. Any liquid metal raising into this region would readily solidify in the remaining narrow gap. The plugs further allow to introduce pressurized gas into the fill and drain pipes (step 3 in Fig.2) and thus to blow out the liquid LBE down to the bottom. This operation can be important when the pipes are used as crushing zone to allow the solidified LBE to expand during recrystallization. After final plugging, the Swagelok valves will be covered by a gastight cup (step 4), which serves as a second barrier during operation.

References

Fill and Drain System Specification, P. Turrone, Oct.5, 2001 (draft)

Table 1: List of valves

Valves ("hand actuated" if not otherwise mentioned)				
Bellows sealed LBE valves			Notes	Data Sheet #
V01		LBE transfert from S01 to S02	/	
V02		LBE Filling	Electrically actuated	
V03		LBE Draining	/	
V04		Sampling at LBE filling	/	
V05		Sampling at LBE draining	/	
V06		Alternate LBE draining	/	
V07		LBE line separation of S01 from S02	/	
V08		Line deviation inteception from T02 to T03	/	
V09		LBE sampling filter by-pass out of S02 with enhanced oxyde reduction	/	
Gas tight vaives			Notes	
V11		Gas at discharge interception out of S01	/	
V12		No returne at gas discharge out of S01	/	
V13		Vacuum by-pass at gas discharge out of S01	/	
V14		Gas feeding interception into S01	/	
V15		Vacuum by-pass at gas discharge out of S02	/	
V16		Gas at discharge interception out of S02	/	
V17		No returne at gas discharge out of S02	/	
V18		Gas feeding interception into S02	/	
V19		Safety with overpressure release setting on S02	Set value at 300 hPa	
V20		Safety with overpressure release setting on S01	Set value at 150 HPa	
V21		Ar/H mix feeding interception into S01		

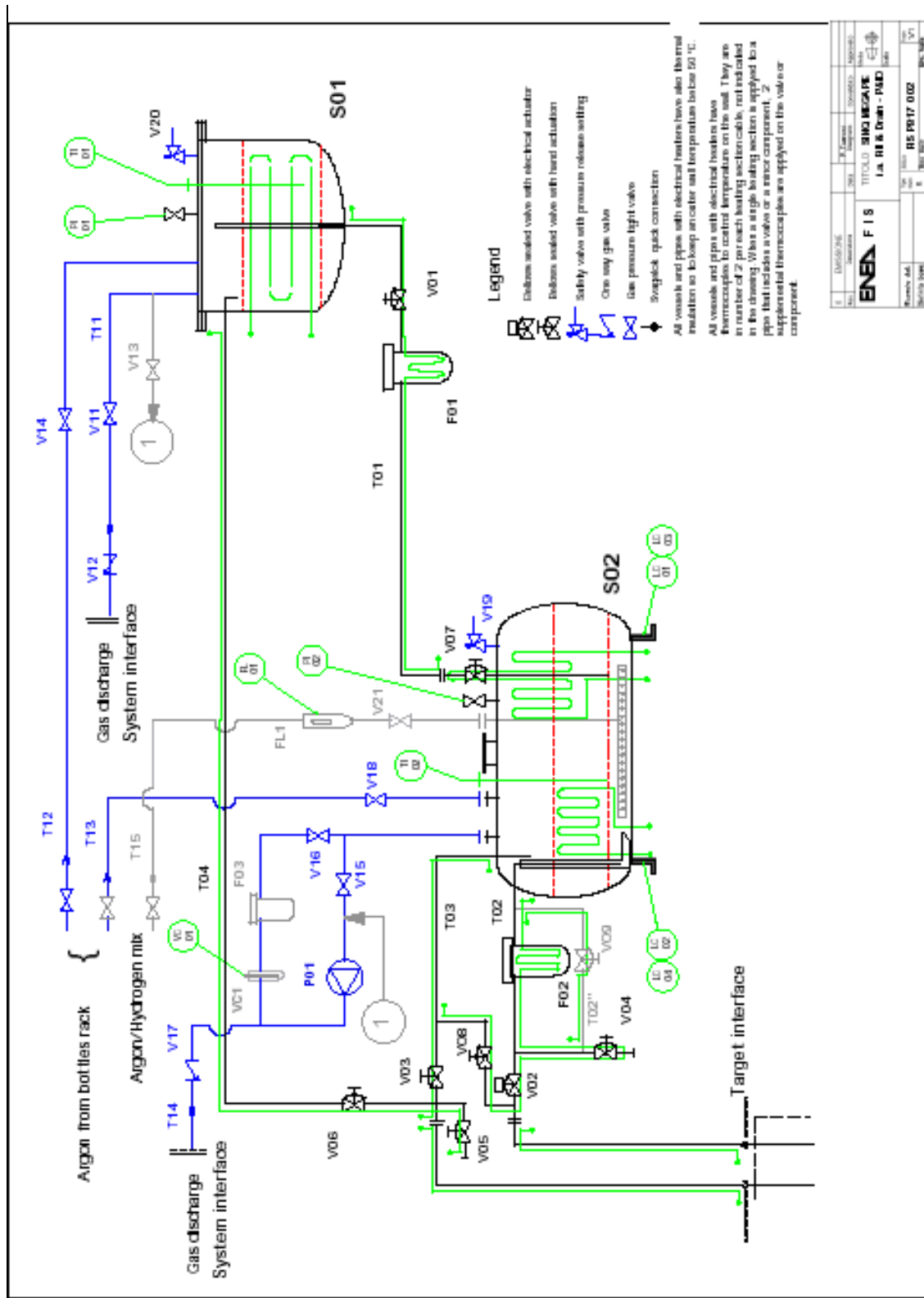


Safety valve with pressure release setting

One way gas valve

Table 2: List of the instruments

Instruments		
TL01	Thermocouple for temperaure LBE control in S01	
TL02	Thermocouple for temperaure LBE control in S02	
P01	Gas pressure measurement inside S01	
P02	Gas pressure measurement inside S02	
LC01	Loading cell (1/4) for weight measurement on S01 support	
LC02	Loading cell (2/4) for weight measurement on S02 support	
LC03	Loading cell (3/4) for weight measurement on S02 support	
LC04	Loading cell (4/4) for weight measurement on S02 support	
FL01	Gas flow mesurement for ingress of Ar/H mix	
VC01	Vapor content mesurement on the Ar/H mix at the discharge	



REV	DESCRIPTION	DATE	BY	APPROVED
1	ISSUE FOR CONSTRUCTION	01/11/2017	ENSA	ENSA

ENSA F I S		TITULO: SIMULACION	
1.A. REACTOR - P&ID		FECHA: 01/11/2017	
Numero de Proyecto:	RS P017_002	Version:	01
Fecha de Emision:	01/11/2017	Autores:	ENSA

Figure 1: P&ID scheme of the inactive Fill&Drain System

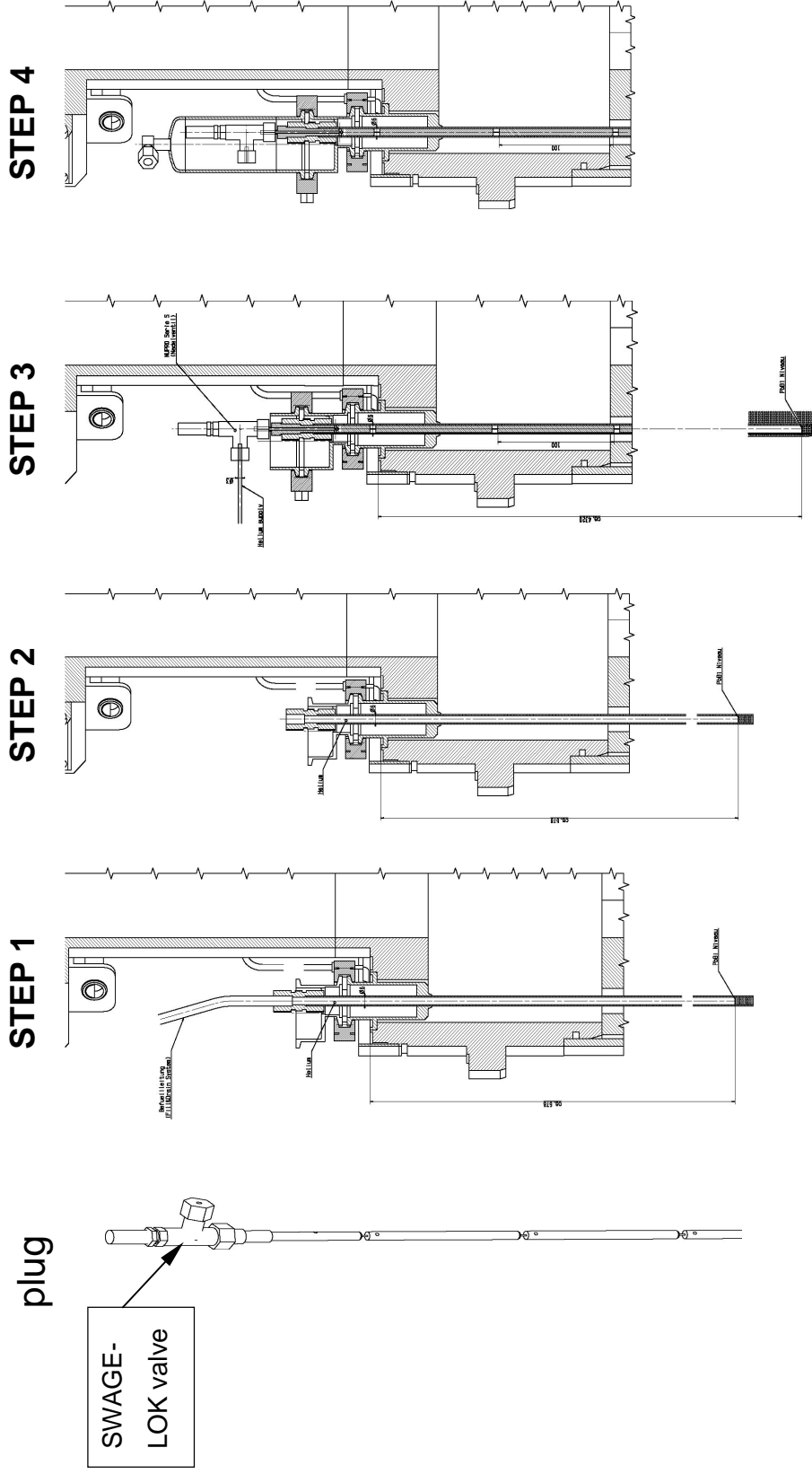


Figure 2: Concept for plugging the fill and drain pipes: the plug has a Swagelok valve at the top and long cylindrical rods underneath which are flexibly connected and intrude deep into the pipes. The different steps of filling the target and mounting the plugs are also shown. Filling with liquid LBE (step 1), removing the filling pipe connection (step2), after introducing the plug pressurizing the pipes (step 3) to blow out the liquid LBE down to the bottom, and finally covering the Swagelok valves by a gastight cup (step 4) which serves as a second barrier during operation.

INSULATION GAS SYSTEM OF MEGAPIE: A CONCEPT UPDATE

W. Wagner¹, J. Welte¹, S. Joray¹, B. Sigg²

¹Paul Scherrer Institut, CH-5232 Villigen-PSI, Switzerland

²LKT ETHZ, CH-5232 Villigen PSI, Switzerland

Abstract

The concept of merely inactive draining of the MEGAPIE target allows simplifications of the insulation gas system such that manual operation for draining (pressurization) is then possible and that there is no further need for a second containment, except for the direct connections to the target. Decision was taken to fill the insulation gas volume with He gas (at 0.5 bar) during target operation, instead of Ar. One of the consequences of this decision is an increased conductive/convective heat loss, which is calculated to be about 20 kW (compared to 3-4 kW for an Ar filling). Therefore, during the preheating phase without PbBi, when the target must be filled with pressurized He, the insulation gap between target containment and enclosure must contain Ar instead of He in order to balance the losses by the target heating. During hot standby, the available heating power in the target is high enough for covering the heat losses through the helium-filled insulation gap.

Introduction

Between the inner, hot part of the MEGAPIE target and the outer cold lower target enclosure (LTE, the so-called safety hull) and upper target shell there is an annular gap foreseen which suits the following purposes:

- Thermal insulation of the inner hot part against the outside to minimize heat losses.
- Double barrier between the water-carrying outer shell and the liquid Lead Bismuth Eutectic (LBE) container.
- Intermediate chamber for the detection of a possible leak in the LBE container.

Since a vacuum high enough to serve as efficient thermal insulation can hardly be achieved due to the narrow gaps and unfavourable pumping conditions, decision was taken to fill this insulation volume with a noble gas. In the most recent concept update He at a pressure of 0.5 bar (abs.) is foreseen. Before that an Ar filling was considered, which was abandoned by reasons of activation and radioactive inventory minimization. The consequences of this concept change on the heat losses from the inner hot part are presented and discussed further below.

Concept Update For Merely Inactive Draining

The concept of merely inactive draining allows significant simplifications for the insulation gas system. The main subjects of simplification are that manual operation for draining (pressurization) is then possible and that there is no need for a second containment, except for the direct connections to the target head.

Figure 1 shows a simplified P&ID scheme of the MEGAPIE ancillary systems which have direct connections to the target head, in a version appropriate for merely inactive draining. The main systems or components shown are the vapor condensation vessel (left), the Cover Gas System, the Target itself, the Fill&Drain System and the Heat Removal System.

The insulation gas system is the volume between the hot inner target structure and the water-cooled outer hull. One possible accident scenario is the ingress of water from the outer target enclosure into the insulation gap, thus getting in contact with the hot inner part that leads to rapid evaporation and pressure built-up. In order to

prevent the target structure from fatal damage in this case, the insulation volume has an outlet on top with 40 mm opening diameter, connecting to a water containing vessel where the outpouring vapour will condensate. Simulations confirmed that the envisaged outlet is sufficiently large to manage this incident safely. A rupture disk at the entrance to the condensation vessel ensures a tight separation from the insulation gas volume during normal operation.

A second accident scenario is the ingress of liquid LBE into the insulation volume through a possible leak in the inner target structure, in particular the lower LM container. In order to detect this incident a leak detector based on electric resistance measurements (short circuit detection) is foreseen to be placed inside the insulation volume, at the lowest point in the annulus of the lower LM enclosure. This leak detector is part of the target design.

Target Heat Losses for Hot-Standby and Preheating Conditions.

The choice of the insulation gas has a strong influence on conductive/convective heat transfer from the target containment to the heavy-water-cooled safety enclosure. Only two different operational conditions are considered in the following, for which different insulation gases must be used.

In the hot-standby case, where the target is filled with Lead Bismuth Eutectic (LBE) and the insulation gap contains helium, the heat losses from the target, which are essentially compensated by target heater and Electromagnetic Pumps (EMPs), depend somewhat on the operational status of the Intermediate Cooling Loop (ICL), i.e. the Diphyl THT oil loop of the Heat Removal System (HRS). With the loop in operation at 220 to 240°C, the heat transferred to the target head is delivered by the oil, whereas in the case with Target Heat Exchanger (THX) isolation, it has to be balanced by the target heating. For estimating the heat losses of the isolation case the following assumptions have been made:

- Temperature of target containment 240°C
- Temperature of Lower Target Enclosure (LTE) 40°C
- Temperature of shroud outside Upper Target Enclosure (UTE) 50°C
- Evacuated gap between UTE and shroud contains air with normal conductivity
- Emissivities of all surfaces $\varepsilon = 0.5$
- Neglect of thermal resistance of metal walls and of effect of protective insulation layer on Lower Target Containment (LTC)
- Axial heat transfer through the target head situated above the Upper Target Containment (UTC) simulated by conduction through 316L steel block with 400 mm thickness

For calculating heat transfer through the insulation gap, convective transport can be neglected because of the low Rayleigh numbers and the high aspect ratios of the gaps.

Table 1: Geometry data and heat losses for each section and losses for whole target at hot standby with THX isolation:

Section I	Diameter D_i [m]	Height [m]	Surface F_{i_i} [m ²]	Gap D_i [mm]	Conductive Heat Loss $Q_{i_{cond}}$ [kW]	Radiative Heat Loss $Q_{i_{rad}}$ [kW]
LTC in Spallation Zone	0.180	0.5	0.283	6.0	1.82	0.32
Rest of LTC	0.184	1.8	1.041	4.0	10.04	1.18
UTC	0.380	1.8	2.149	5.5/2.5	3.41	1.19
Target Head	0.380	0.4	0.113		0.99	
Total					16.26	2.69

The results show that the heat losses of lower and upper target can be separately compensated by the target heater (22kW) and the EMPs (20kW), respectively. During Target Preheating, thermal power produced in the heater rod and the EMPs can only be transferred by radiation and convectively by the target gas. Since natural-convection cooling of the heater rod by a gas is much less effective than by LBE, the insulation gap must be filled with argon, which has a ten times smaller heat conductivity than helium, and the target gas itself is helium, that optionally can be pressurised. The objective of the calculations is to show that all components of the target in contact with LBE can be sufficiently preheated before filling in the liquid metal

The following assumptions were made for the calculations:

- No natural circulation in target, based on the assumption that LBE remaining after the Integral Tests on the target window would close the gap between window and guide tube
- Neglect of thermal resistance of metal walls and of effect of protective insulation layer on LTC
- The short lower part of the heater rod is assumed to have the same diameter as the upper part and a reduced length of 0.15 m.
- The outer diameter of the lower part of the LTC is assumed to be equal to that of the upper part.
- The effective lengths of heater rod, guide tube and LTC are different, i.e. 1.75 m, 2.0 m and 2.3 m, respectively.
- The LTC is assumed to be cylindrical but includes the hemispherical window surface. (The geometry data are summarised in Table 2).
- The temperatures of heater rod and enclosure are $T_1 = 500^\circ\text{C}$ and $T_4 = 40^\circ\text{C}$, respectively, although the latter might be lower during preheating.

Table 2: Geometry data for each annular gap in lower target for preheating model:

Annular gap k:	Inner radius r_{ki} [mm]	Outer radius r_{ko} [mm]	Gap d_k [mm]	Height h_k [m]	Surface F_{ki} [m ²]
Riser k=1	28.5	61.0	32.5	1.75	0.3134
Downcomer k=2	62.5	88.0	25.5	2.0	0.7854
Insulation gap k=3	92.0	96.0	4.0	2.3	1.324

The data in Table 3) show the results for four different cases:

Table 3) Results for heat fluxes and temperatures in lower target for different gas pressures and surface emissivities:

Case	Heater power [W]	$T_2 = T_{\text{Guide tube}}$ [°C]	$T_3 = T_{\text{Containment}}$ [°C]
1) $p_{\text{He}} = 1 \text{ bar}$, $\varepsilon = 0.0$	876	274	163
2) $p_{\text{He}} = 1 \text{ bar}$, $\varepsilon = 0.5$	2281	330	206
3) $p_{\text{He}} = 6 \text{ bar}$, $\varepsilon = 0.0$	1086	297	193
4) $p_{\text{He}} = 6 \text{ bar}$, $\varepsilon = 0.5$	2487	334	217

The results show that:

- The melting temperature of LBE is exceeded in all cases
- Target pressurisation is relatively ineffective (The critical Rayleigh number for onset of convective heat transfer inside the target is only reached at a pressure of about 4 bar). The option of using pressurised gas during preheating must however be preserved.

The following comments have to be added, however:

- Radiative heat transfer can be influenced by surface treatment. Emissivities should be low on the outer surface of the LTC and the inner surface of the LTE, but high inside the target.
- The heat transfer to the target window region should be calculated by means of a more accurate method. Melting of LBE remnants on the window probably cannot be effected by heating with the central rod, and another heating method should be applied. Possibilities are the injection of hot helium through the fill pipe or through the heavy-water channel in the LTE.

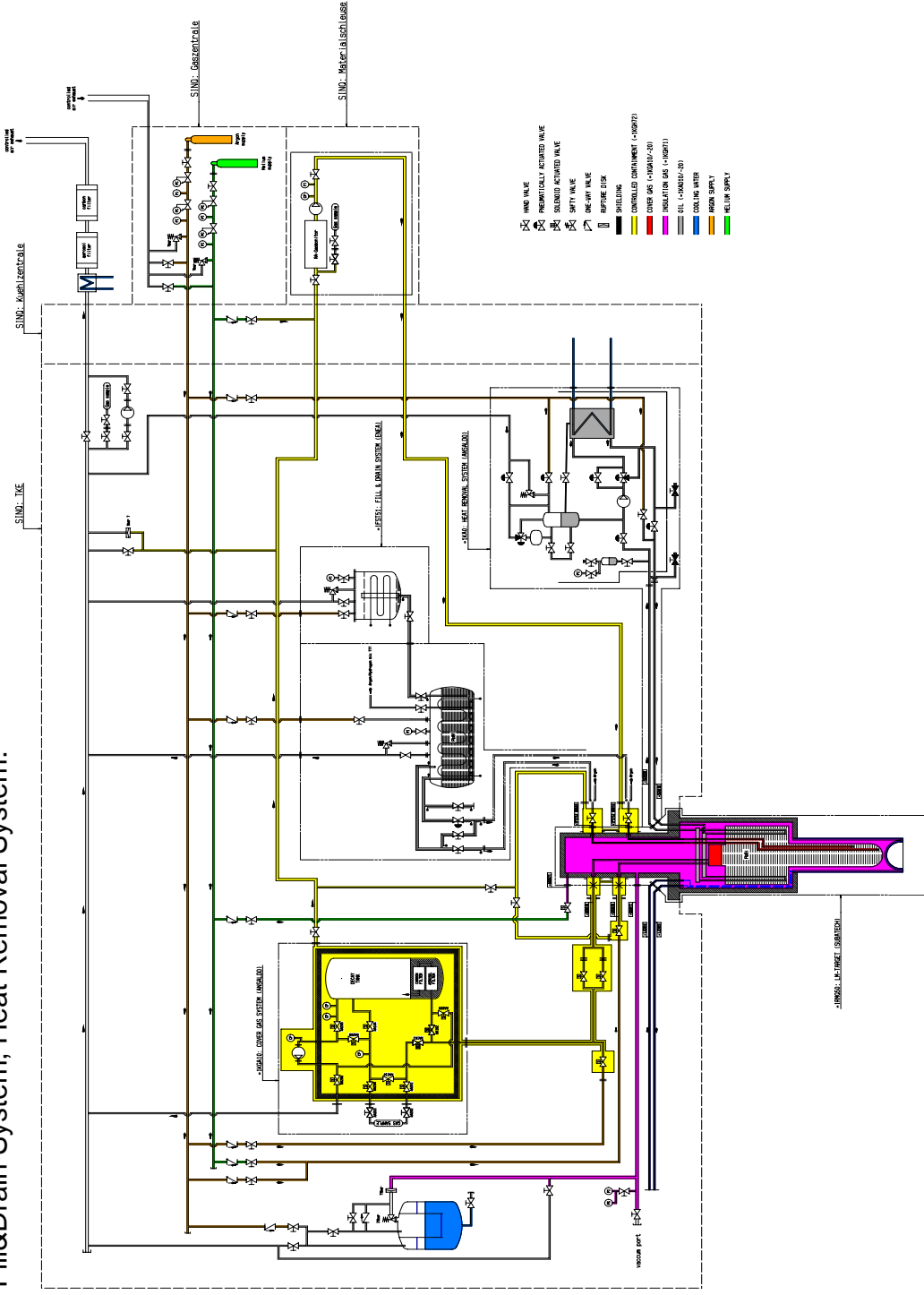
For the upper target the heat losses during preheating would be compensated by the hot oil in the THX pins and by the EMPs. The available power of about 7 kW is adequate since it could balance the losses of the UTC even with helium insulation gas (See Table 1).

References

The following literature was used for carrying out the calculations:

- [1] A. Banerjea et al: Thermodynamische Stoffwerte von He im Bereich von 20-1500°C und 1-100bar. Jül-1562 (1978)
- [2] VDI-Wärmeatlas, 3.Auflage, 1977.
- [3] M. Keyhani, F.A. Kulacki: Natural Convection in Enclosures Containing Tube Bundles, in: S. Kaçak, W. Aung, R. Viskanta: Natural Convection, Fundamentals and Applications. Hemisphere Publishing Corporation, 1985, pp. 330-380.

Figure 1: Simplified P&ID scheme of the MEGAPIE ancillary systems with direct connections to the target head, in a version appropriate for merely inactive draining. Main systems or components (from left to right): vapor condensation vessel, Cover Gas System, Target, Fill&Drain System, Heat Removal System.



TARGET HANDLING: CONCEPT FOR TRANSPORT AND DISMANTLING

A. Strinning, E. Wagner, A. Janett, F. Groeschel
Paul Scherrer Institut, CH-5232 Villigen-PSI, Switzerland

Abstract

The Megapie target will be mounted vertically for testing in the Montagehalle (WMHA) at PSI west. Transfer to the target storage area in the SINQ-hall will be made with the assembly horizontal. Transfer from the target storage to the operating position in the target block and back again after irradiation will be done with the transfer flask and tools used for the normal SINQ-Target.

Due to the character of the activity of the irradiated Megapie target the hot cell at PSI west cannot be used. All work on the activated target will be done in hot cells at PSI east and at ZWILAG (borders PSI east). For these transfers a new, shielded transport container has to be designed. The container and the transfer will require official licensing.

The present outline concept for extracting samples is to cut the target into pieces at ZWILAG, which can be handled in the PSI east hot cell (Hotlab).

Introduction

For transfer of operational SINQ-targets between the target storage and the target block the transport flask (figure 1) is vertical but to get a target into the hot cell at PSI-west (ATEC) the flask has to be tipped horizontally. Due to the character of the activity of the irradiated Megapie target, ATEC cannot be used. Our present concept is to do all work on the activated target in hot cells at PSI east (Hotlab) and at ZWILAG (Swiss interim storage for NPP, which is next door to PSI east). The plan is to cut the target into pieces at ZWILAG, to extract samples and make analysis at the Hotlab.

For transfer to PSI east and ZWILAG a new, shielded transport container has to be designed (the SINQ-transport flask can not be docked to the ZWILAG hot cell and will only be used for vertical transfers within the SINQ-hall).



Figure 1: SINQ-Transport flask

Transfer and Handling concept

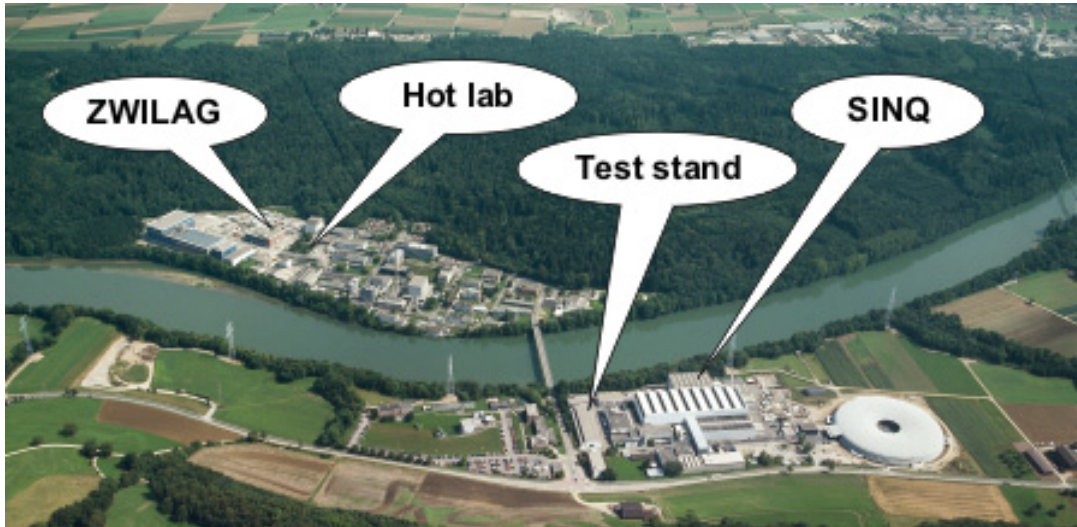


Figure 2: Overview of the PSI and the ZWILAG area and where the operations will take place.

- Transfer from test stand to SINQ-target storage with a special handling tool (Fig. 3)
- Transfer between target storage and the operating position (TKE) with the SINQ transport flask. (Fig. 4)
- Transfer from SINQ-hall to ZWILAG and from ZWILAG to Hotlab with a special transport container (Fig. 5).
- Target dismantling and disposal concept (Fig. 6 and 7)

Transfer from test stand to SINQ-target storage (inactive)

The final testing will be made at the test stand in the “Montagehalle” (figure 3). Because of the height of the “Montagehalle” crane the transport has to be done with the target horizontal. Therefore, after the final testing, the target must be turned horizontal for the transfer to the SINQ-target storage. This transfer has to be done without LBE in the target. A special tool will be designed and built to carry out these operations.

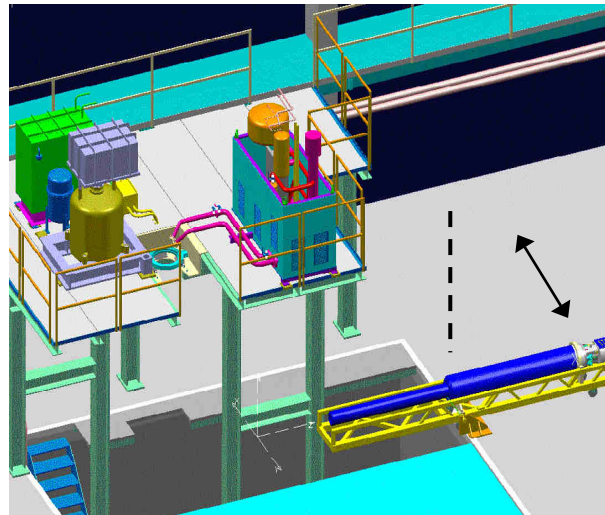


Figure 3: Test stand with Target and tool for transports and to turn the Target horizontal and vertical

Transfer between target storage and target block

The transfer between the target storage and the operating position in the target block will be made with the transport flask and tools used for the normal SINQ-Target. Figure 4 shows a schematic diagram of the flask in the TKE (target block) for a transfer of a target in and out of the operating position. The principal extra problems to be solved are the following:

- The MEGAPIE-Target is longer. The flask is long enough to accommodate the target, but a higher mounting support for the flask is needed because of the longer head section.
- Before the target can be moved, the LBE must be frozen and the oil and heavy water coolants removed. It must be guaranteed that the LBE will not re-melt due to the decay heat, during the transfers, in the target storage or in the hot cell.
- The dose rate outside the upper end of the flask will be much higher due to the distribution of the activity in the Megapie target. This can be solved by adding local shielding.
- After a worst case operating failure (leakage of LBE from the target), the collimator may become stuck (soldered) to the central column, by the solidified LBE. In this case, the collimator and the central column will need to be pulled out together into the flask and transferred to the hot cell at ZWILAG.

(Such an accident would cause a bad situation for PSI with operational failure for at least 1 to 2 years and high repair costs)

Transfer from SINQ-hall to ZWILAG and from ZWILAG to Hotlab (active)

For these transfers it will be necessary to build a new shielded and air tight container that can be docked to the bottom of the ZWILAG hot cell and which is small enough to fit into a hot cell at Hotlab. Figure 5 shows an outline design of the container. The concept can be summarized as follows:

- The container can be separated into two parts.
- The lower, and smaller, part is planned to be used for transfer of the cut target pieces from ZWILAG to the Hotlab
- To load the container with the target, it will be mounted vertically on a supporting structure and the SINQ-transport flask will be docked to its top.
- The transfer to ZWILAG will be made with the container horizontal and with an over-pack as contamination protection.

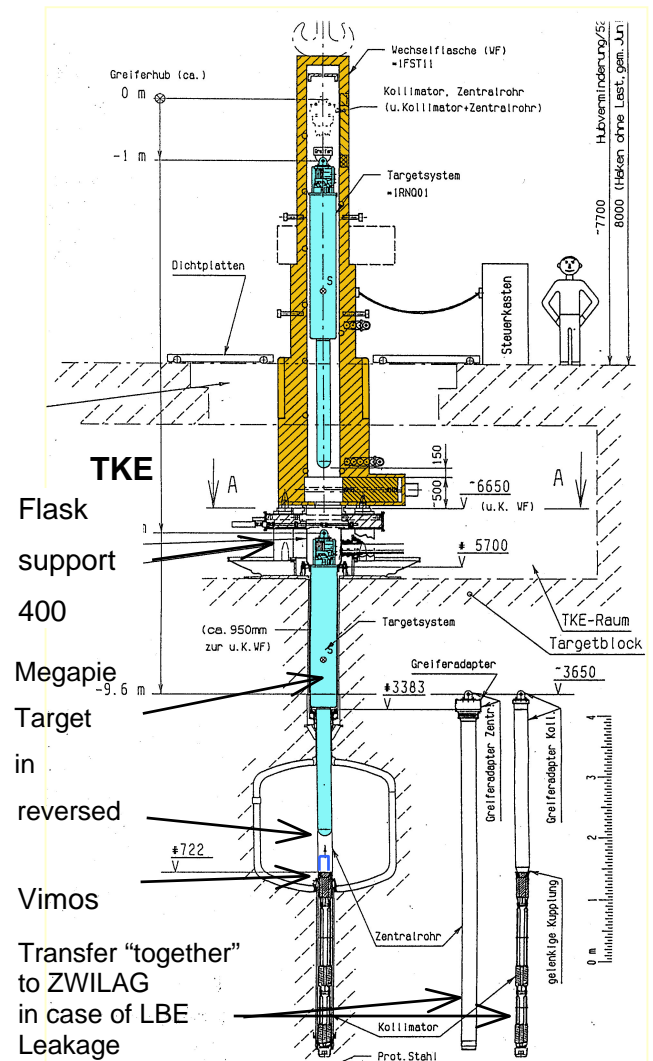


Figure 4: SINQ-Transport flask

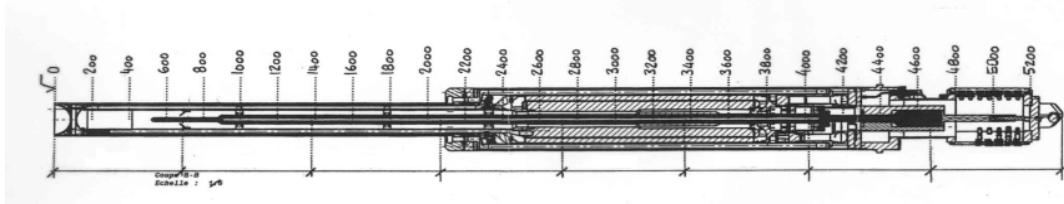


Figure 6

Dismantling and disposal outline concept

The following figure (7) shows the operations for the dismantling and the disposal of the Megapie target schematically:

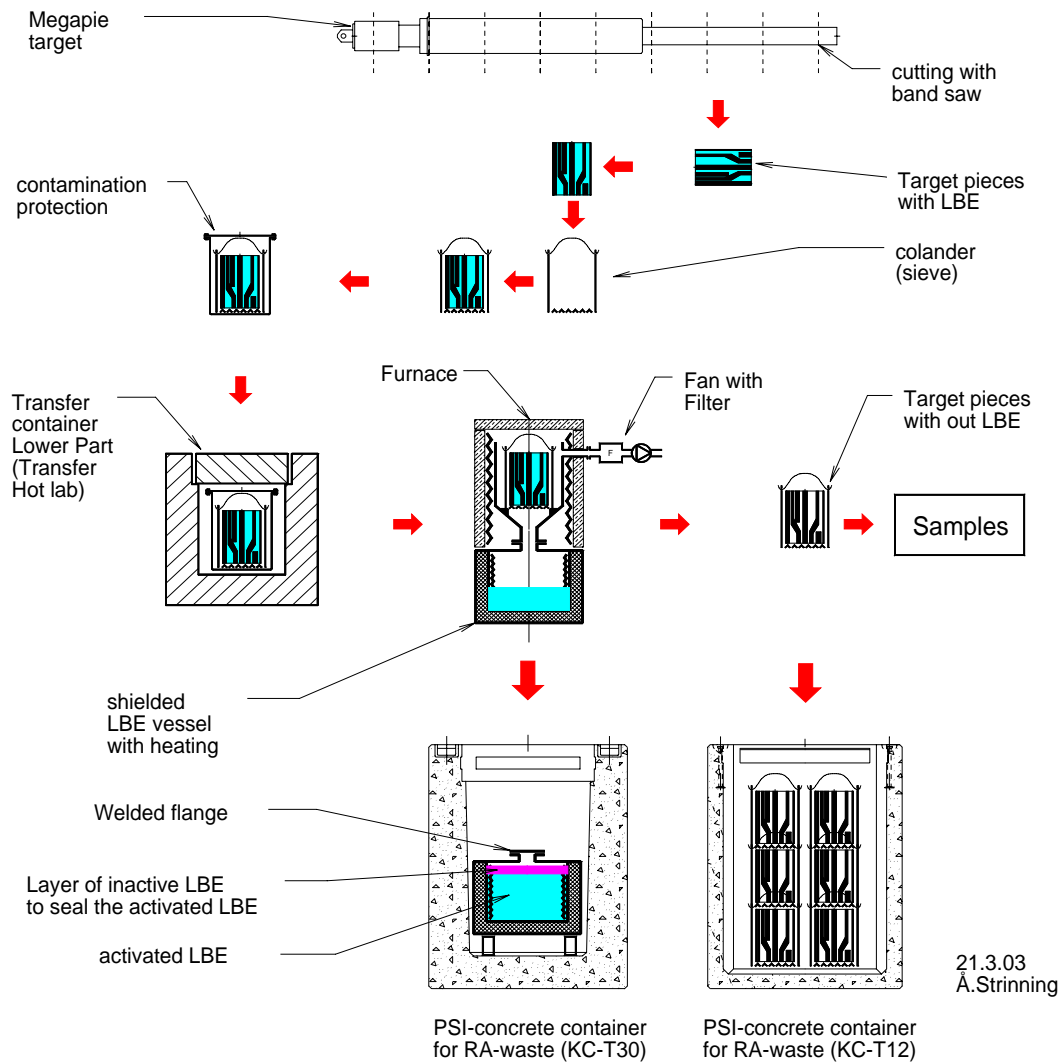


Figure 7

Dismantling:

- Saw the Target into “slices” at ZWILAG
- Put the pieces into colanders (sieve) to facilitate the handling of the pieces in the hot cell and keeping the parts together after removing the LBE.
- Put a colander (one of them) into a thin walled and air tight vessel (contamination protection) and transfer it with the lower part of the transport container to the Hotlab
- Get the colander out of the container in the Hotlab, heat it in a furnace so that the molten LBE flows out through the wholes into a shielded vessel placed underneath the furnace (It is not yet clear whether the LBE is going to be melt out at ZWILAG or the Hotlab).
- Extract samples from the target pieces

Disposal:

The conditioning of all parts of the target and the LBE for waste-repository disposal is planned to be done into PSI container in the hot cell in the following way:

- The shielded vessel with LBE will be sealed with inactive LBE and a welded flange.
It will then be conditioned into a standard PSI waste container of type KC-T30.
- The target structure (target pieces) and the colander will be conditioned into PSI waste containers of type KC-T12.
- The target structure can be treated as ordinary PSI west RA waste by supposing that all parts in the target have been coated with a layer of max. 0.1 mm of LBE.

ON THE PREPARATIONS OF THE MEGAPIE INTEGRAL TEST

W.H. Leung¹, B. Sigg², J. Welte¹, S. Joray¹, F. Groeschel¹

¹Spallation Neutron Source (ASQ), Paul Scherrer Institut
Villigen-PSI, CH 5323, Switzerland

²ETHZ-LKT, Villigen-PSI, CH 5323, Switzerland

Abstract

The two main tasks of preparing the Integral Test are i) to construct a large test facility to receive the target and all the ancillary systems ii) to sketch out test plans of the target system. Both tasks are progress in a good pace. As for the test facility, a large steel frame, the Test Stand, has been constructed. Electricity supply is pending for the design of the LMC (Lower liquid Metal Container) Heater and the main control cabinets. Cooling water will be installed at the time when the secondary water loop is installed on the Test Stand. Preparations of the other auxiliary systems of the Integral Test are progressing as planned.

The test program is divided into seven campaigns to mark the progress. At the beginning, most of the works are i) extended quality control, ii) system assembling, iv) system leak test, and iv) instrumentation checkups. As the test program progress, functional tests are going to be conducted on each ancillary system. A more elaborated thermal hydraulics will be commenced after all the ancillary systems are checked. The purpose of this part of the test is to verify the heat removal capacity and the transient controls of the target system. In the mid term, demonstration experiments are devoted to license application for irradiation test in SINQ. At the end of the Integral Test, the target will be reassembled to the original configurations, tested again, and dismantled from the Test stand. Then it will be made ready for transferring to the SINQ.

An electric heater is needed for testing the heat removal system in the Integral test. One reason of choosing a lower power heater is that the design brings minimum change on target geometry. Test conditions can be scaled by the heating power so that the more realistic case can be studied and the results can be scaled back to assess nominal conditions.

Introduction

The MEGAPIE liquid metal spallation neutron target is designed for 1MW proton beam power. A cluster ancillary systems are be installed to support the operation of this target, and they are the cover gas systems (CGS), fill and drain (F&D) system, insulation gas system (IGS), and heat removal system (HRS). These systems are designed in three different institutes in Europe, and constructed by different manufactures. Further, a control system is developed independently for operating this target system. Integral Test is the first and the only opportunity to test the system in the fully assembled state before installing in the Spallation Neutron Source (SINQ) for irradiation test in PSI. In other words, the Integral Test is an important milestone of system integration and design verification. The objectives of the test program are:

- To verify the designs
- To integrate the target and the ancillary systems,
- To license target for irradiation test,
- To gather technical and scientific data for model verification.

There is no existing facility in PSI that can house the target system, because it is simply too large (i.e. roughly 5 meter long) to fit in any experimental hall outside the SINQ hall. It is necessary to construct a new facility specially designed for the

Integral Test. Not only the supporting platform is needed but a whole array of infrastructures must be also installed to the support the test. Thus, the first part of this report is focus on the needs, the plan, and the progress of building such a test facility.

In the mean time, the test program must be mapped out so that the needs can be realized before they become too late. Furthermore, the test program is run on a very tight schedule. Clear goals must be set for each experiment and must be achieved in a given time. Hence, the second part of this report is focus on setting the milestones to demarcate each progress.

Heat removal is one of the most important functions of the target design, because the proton beam deposits roughly 620 kW to the LBE. The thermal power must be removed to avoid an instant heating up of the target. Thus, the thermal hydraulic characteristics of the HRS system must be studied thoroughly to give an accurate account of the system performance. Since the proton beam is not available to the Integral Test, an electric heater must be installed on the target to simulate the beam heating. In the last part of this report, a design of an electric heater is discussed in details (i.e. the size and type).

MEGAPIE Integral Test Stand (MITS)

The test facility is named MITS (**M**IGAPIE **I**ntegral **T**est **S**tand). The main part is a large steel frame structure, which is erected in Montagehalle/PSI. The design is presented in Fig. 1, and the 3-D frame structure is presented in Fig. 2. The target, the ancillary systems, power supplied and the instrument cabinets are all mounted onto this steel frame. The target is rested on a steel ring mount on the metal bracket, which is an exact copy of the TKE (target head enclosure). Layout of the ancillary systems is presented in Fig. 3, which is the same configuration as that in the SINQ (Spallation Neutron Source) irradiation test. A hole of 2×2.5 m and 1.5 m deep has been dug out in the basement to increase the total height of the region, because the final assembling the target need this extra height for changing the lower liquid metal container and slipping on the lower target enclosure in a vertical position.

Control system is not the responsibility of MITS, but it is needed for the operating the target system during the test. Besides system integration is only possible when the control can tie all the systems together. To construct the control system, it is first to

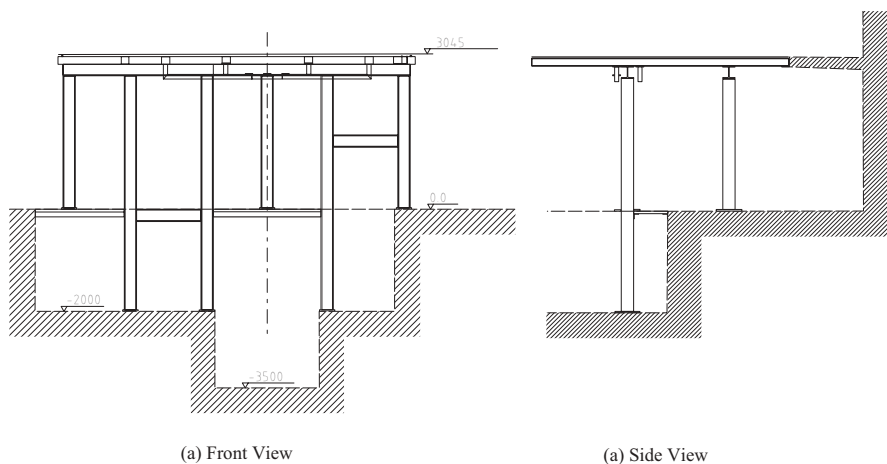


Figure 1: The steel frame structure of the MEGAPIE Integral Test Stand

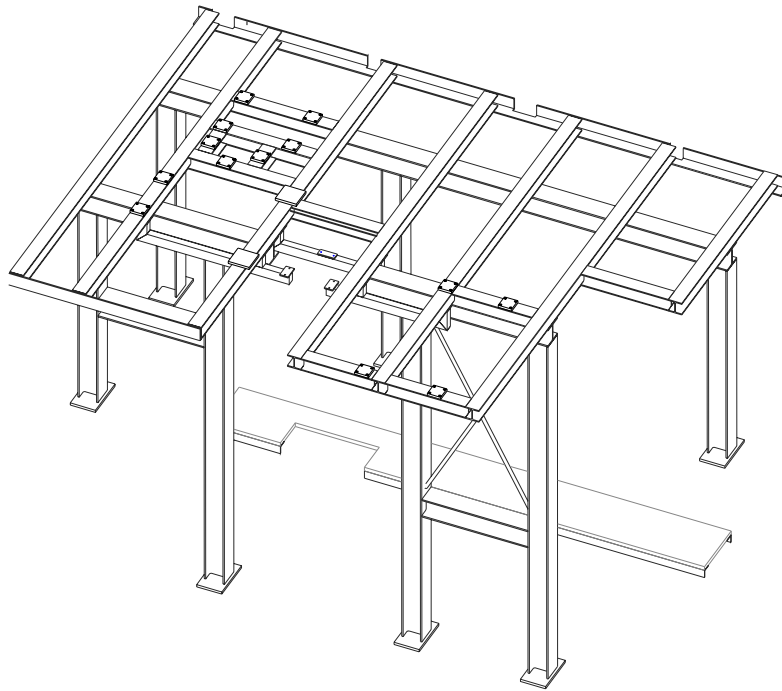


Figure 2: The steel frame structure of the MEGAPIE Integral Test Stand

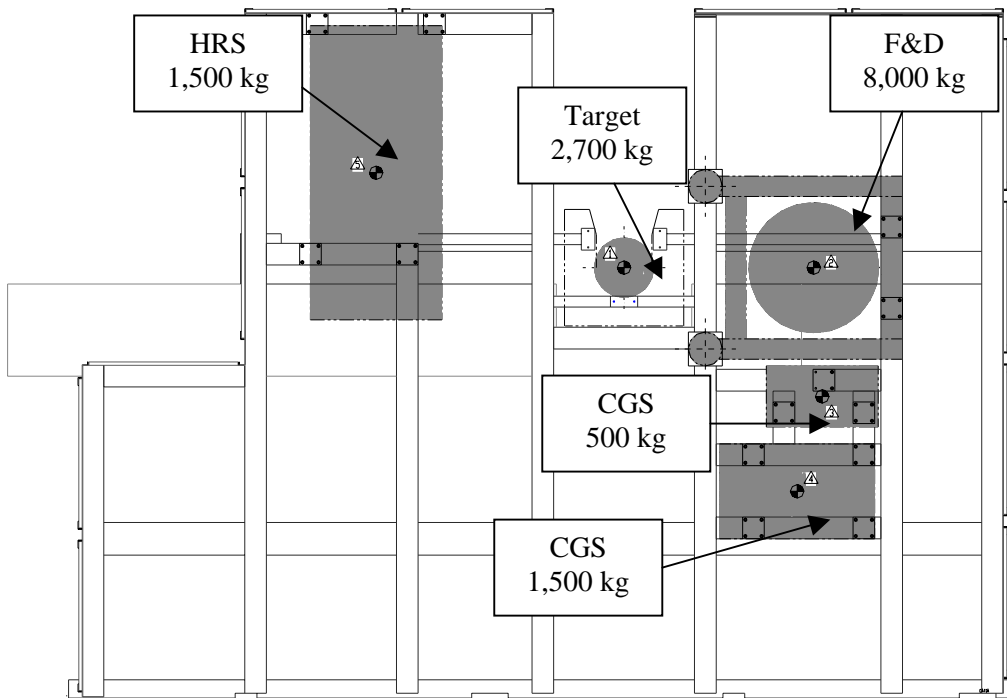


Figure 3: Layout of the target and ancillary systems on MITS, and their corresponding weights.

number the signal list according to the PKS (PKS: PSI - Kennzeichnungssysteme is a signal labelling system used for the SINQ control system) scheme. The signal type is embedded in the PKS number so that control function can be assigned accordingly. This hardware and software will be designed and constructed by an external company. The status is not clear at this moment because not a single document is released.

The control system has the sampling rate of 1 Hz, which is not fast enough for any transient study. A separated DAQ is needed for fast data sampling for the experiments. This task is assigned to the Electrical Engineering Department in PSI. The required hardware and software have been purchased, and the work should be started at the beginning of April 2003.

A whole array of supporting systems must be installed to MITS for testing the target. The descriptions and statuses of those installations are summarised in Table 1 below.

Table 1. Status of the infrastructure installations

Installation	Status
Electrical Power Supply: i. 250 kW for LMC heater, ii. 200 kW ancillary systems,	Ready to order
Montagehalle Cooling Capacity: 500 kW,	Acquired
Secondary Water Loop: Original loop but a smaller HEX i.e. 200 kW,	Engineering Design
Signal and Control Cabinets: About 4 cabinets are planned, where all PLC and SPS units will be installed. All the power will be in separate cabinet	Pending
Gas Pressurization System: Argon and helium bottles 200 bar, distributed through a piping network: i. Target fill and drain (Ar), ii. Leak test (He), iii. Target cover gas (Ar), iv. Oil loop cover gas (Ar), v. Insulation gas (He),	Conceptual Design
Vacuum System: i. Tightness test, ii. Target filling, iii. System purging,	Available
Power Supplies: i. Two EMPs, ii. Central heating rod, iii. LMC heater (MITS only), iv. All the trace heaters,	Item i is ready, all other unknown
MEGAPIE Test-Stand Safety i. Operation Safety, ii. Fire Protection, iii. Environnant Protection. iv. Personnel Protection	Revising

Test Program Of MEGAPIE Integral Test

The target and the ancillary systems are designed and manufactured separately. Integral Test is the first effort to examine how well the system can “fit” together. Upon the delivery of each ancillary system (i.e. CGS, IGC, F&D and HRS), the initial task is then to check whether the individual system is measured up to the specifications and past the tightness test. After each system past the checking, it will

then be installed on the Test Stand and connected to the target. After the target system is assembled together, it must go through another test of tightness as a complete system. Only all tests are past, the system will then be connected to the control and DAQ system for the final instrument checkups to ensure all the signals acquired or sent are correctly placed.

Functional Test of Ancillary Systems

The CGS, IGS and F&D required only testing operating procedures because they are operated independently from each other and while the target system is put on standby or complete shut down. The functions and tests of each system are summarised in Table 2.

Table 2: Functional tests of the Ancillary Systems

System/Functions	Tests
<p>Fill and Drain System (F&D):</p> <ul style="list-style-type: none"> • Fill the target with liquid LBE at the initial start-up at MITS and SINQ, • Drain the LBE from the target in MITS after the Integral Test 	<ul style="list-style-type: none"> • The procedures of actual filling and draining are tested on MITS and mostly likely with only manual control, • The target is preheated up to 140 °C before filling, the procedure must be invited and tested,
<p>Cover Gas System (CGS):</p> <ul style="list-style-type: none"> • Remove the gas and volatile spallation products accumulated on top of the liquid metal expansion tank (LET) inside the target, • Store up the radioactive gas extracted from the target in the decay tank so that the radioactivity can reduce to level that is acceptable to be discharged to the SINQ exhaust, 	<p>The process of evacuating the gas from the pressurized LET can be tested:</p> <ul style="list-style-type: none"> • Purge and fill the cover gas, Ar, to roughly 0.2 bar, • Pressurize the LET with He to roughly 3.0 bar, • Evacuate the decay tank, • Receive gas from LET and detect it by pressure measurement and leak detector,
<p>Insulation Gas System (IGS): Acts as insulation layer, which is filled with 0.5 bar of helium, between the hot part and the target enclosure,</p>	<p>Test for tightness is required,</p> <ul style="list-style-type: none"> • Evacuate and purge the IGS with He, • Fill the IGS to 0.5 bar, • Check the leak rate by the pressure measurement,

Thermal Hydraulic Test of the Target System

For the heat removal system (HRS), it is necessary to test functions of the pumps and valves, and more importantly to test the thermal hydraulic characteristics of the system with the target and a secondary water loop (SWL). As a matter of fact, removing 620 kW heat from the target material LBE is the primary function of the system during normal operation. The performance of the system can be assessed by conducting thermal hydraulic experiments in steady state and as well as in transient conditions. More detail will be discussed in the following section. The test can be divided into three main categories, i) Steady State Test, ii) Scaled Experiments, and iii) Thermal Hydraulic Transients.

Steady State Test

In steady state case, the system thermal hydraulics can be characterized by a few parameters. The overall frictional pressure loss must be determined so that flow rate of a give pumping head can be determined. However, the MEGAPIE target works in a mix convection mode, it is to say that the buoyancy has a significant contribution to the driving head, and must be subtracted from the friction pressure loss. The buoyancy head is due to temperature difference, which is created by the heat transfers to and from the coolant. On the other hand the, heat transfer is a strong function of the mass flow rate. Hence, it comes through a full circle that each parameter affects the other. The steady state test, we must determine accurately:

- Friction pressure loss, ΔP_{fri}
- Mass flow rate, \dot{m}
- Overall heat transfer coefficients, U
- Temperature profile, ΔT

Unfortunately, the target does not equip with any pressure transducer. The pressure head must be estimated from the flow rate and the pump curve. There is an electromagnetic flow meter, but, by far, there is no accurate calibration can be shown. The temperature profile, on the other hand, can be measured reasonably well, and there are plenty of thermal couples in many locations. Thus, the heat transfers can be determined in a higher accuracy then the mass flow.

In essence, the most important parameters derived from the steady state experiments are frictional pressure drop ΔP_{fri} and the overall heat transfer coefficients, U , of all the heat exchangers. With this information, the target thermal hydraulics can then be specified. Furthermore, those parameters will also be employed in the transient analysis too.

Scaled Experiments

The proton beam heating is simulated by an electric heater attach to the bottom of the LMC. This heater cannot reach the power density of the proton beam, unless lower target is expanding to a much larger tank. The question is whether the experiments at much lower heating power are relevant to nominal operation in the proton beam. The first idea is to scale the buoyancy with the inertial so that system behaviors can be preserved, and here is the argument:

- The buoyancy head, ΔP_{grv} , is proportion to the temperature difference ΔT (Boussinesq approximation),
- The temperature difference, ΔT , is directly proportion to the power input, Q , but inversely proportion to the mass flow rate, \dot{m}
- The flow resistant, ΔP_{fri} which counter acts the buoyancy, is proportion to the square of the mass flow rate, \dot{m}^2

Put them all together, one can get the relationships: $\dot{m} \sim Q^{1/3}$ and $\Delta T \sim Q^{2/3}$

At nominal condition the proton beam deposits 620 kW thermal power on the LBE, but the LMC heater power is most likely can product 200 kW. This gives the power ratio of roughly 0.32. Using the above relationships of flow rate and power, one can scale the nominal conditions down to 200kW operation and the results are summarized in Table 3. The problem is the operating temperature of the water loop becomes too high. To avoid boiling, the SWL must be pressurized over 10 bars.

Thermal Hydraulic Transients

The target does not operated in steady state all the time. In SINQ, there are hundreds of the beam interrupts in each week. Once the heat source is taken away,

it does not take long to cool the target down to freezing, which must be avoided by all means during the normal operation. The control system must switch off the cooling whenever the proton beam interrupt occurs. There also other transition must be considered, and the brief list is:

- Beam trip – The proton beam shut down over minutes and the target must be switched to hot standby,

Table 3: The operating conditions of nominal and scaled experiments

Target HEX	Nominal	Scaled
LBE side		
Flow rate, kg/s	40.6	27.8
Inlet Temp., T_{in} , C	333.0	278.9
Outlet Temp., T_{out} , C	230.0	230.0
$T_{in} - T_{out}$	103.0	
Diphyl-THT side		
Flow rate, kg/s	8.85	6.07
Inlet Temp., T_{in} , C	129.8	197.8
Outlet Temp., T_{out} , C	165.8	213.3
$T_{out} - T_{in}$	167.2	
Intermediate HEX		
Diphyl-THT side		
Flow rate, kg/s	8.85	6.07
Inlet Temp., T_{in} , C	166.4	213.8
Outlet Temp., T_{out} , C	103.55	172.4
$T_{in} - T_{out}$	62.9	
Water side		
Flow rate, kg/s	8.0	5.49
Inlet Temp., T_{in} , C	40.0	150.5
Outlet Temp., T_{out} , C	59.0	158.9
$T_{in} - T_{out}$	19.0	8.4

- Transition to hot standby – scheduled proton beam shut down for serving the facility,
- Target warming up – after LBE filling into the target at roughly 140 C at the beginning of the experiment, the system must be warmed up to the state of hot standby,
- Target Cooling down – at the terminal phase of experiment, the target must be cooled down to just above freezing at the end of the experiment,

These are the transients that will be examined in the Integral Test. The last transition condition is not very well defined, because it has not been considered in the earlier planning. The cooling down is not necessary related to the target freezing. Even for draining the target after the experiment, the LBE temperature must be reduced to roughly 140 C first. Thus, it is necessary to examine the process more carefully during the Integral Test.

Summary of the Integral Test Program

The list of tasks presented above shows the diversities of the tests in the Integral Test. It is necessary to group the tasks in a logic way and lay down the milestone to mark the progress in this long test program. Seven campaigns are defined to distribute tasks. A summary of all the campaigns and tasks is presented in Table 4. More regarding the licensing and final phase of the Integral Test are discussed in Table 4 but had not been mentioned in above discussions. Actually later stage of the test is more important because the real test of the target system is the irradiation test in SINQ. Integral Test is simply the precursor of achieving that goal.

Liquid Metal Container Heater

For the Integral Test, the proton beam heating is simulated by an electric heater inserted at the beam window region. In an ideal case, the electric heater should put out the same power as the proton beam and at the same time could fit in the main flow guide tube without any flow obstruction. In this way, all the thermal hydraulic characteristics of the target in proton beam operation can be studied without any distortion.

Table 4: Campaigns of the MEGAPIE Integral Test (MIT)

Campaign	Tests	Components
0. Acceptance Tests	<ul style="list-style-type: none"> I. Quality Assurance of Individual System, II. Instrumentations Tests, III. Control of Automatic Mechanism, IV. Loop Test if necessary, 	HRS, EMP, F&D, CGS, IGS, CHR, THX
1. System Checkups and Integration	<ul style="list-style-type: none"> I. Instrumentation Test as an Integral System, II. Control of Automatic Mechanism, III. Filling and Draining the Target, IV. Running the Target in Standby, V. Testing Cover Gas System. 	HRS, EMP, F&D, RLC, CHR, CGS, THX
2. Thermal Hydraulics Tests	<ul style="list-style-type: none"> I. Hydraulics Test with RLC, II. Start up and Shut down sequences with LCH, III. Steady State Tests (at different temperature, power, flow rate, and cooling rate), IV. Thermal hydraulics transient test for code verification. 	CHR, EMP, HRS, WCL, THX, RLC, and LCH
3. Thermal Hydraulics Transient	<ul style="list-style-type: none"> I. Simulating Beam Trip, II. Simulating Main EMP Trip/Failure, III. Simulating Bypass EMP Trip/Failure 	CHR, EMP, HRS, WCL, THX, RLC, and LCH
4. Licensing Process	<p>Demonstrating to the Swiss Authority:</p> <ul style="list-style-type: none"> I. The nominal operation conditions, II. The safety feature of the systems, III. *Will be more specific after obtaining information from the authority. 	CHR, EMP, F&D, HRS, WCL, THX, and LCH
5. System Responses and Safety	<ul style="list-style-type: none"> I. Protected and unprotected normal beam trip and conditions for automatic restart, II. Thermal hydraulics transient initiated by the components failures or by the leak detector, III. The responses of the control system, 	CHR, EMP, HRS, WCL, RLC, THX, and LCH
6. Complete Target System Test	<ul style="list-style-type: none"> I. Completely assembled (w/ original LMC and Upper and Lower Target Enclosures), II. Run the instrument check again III. The F&D Tests (Target heat up), IV. Target on hot standby to test the heat loss, V. The pump and demand curves of the system, VI. Control System Integration, 	CHR, EMP, F&D, IGS, HRS, THX, LMC, LTE, and UTE

It is, however, not quite possible in reality. The highest heat flux given by a commercial heater is roughly 40 W/cm². If higher number is called for, i.e. 80 W/cm², it is only possible with a customer made heater, but with a very high price tag. Then, the question is what would be the minimum power required for a meaningful heated test, but more importantly is what are the most important criteria of the heater design that could bring about the necessary data for verifying target design and the function of the HRS, and for determining the operating conditions of proton beam experiments.

Insertion of an electric heater is already brought the change of the target geometry. Consequently the dynamic behaviours of the target thermal hydraulics are modified. The arguments on the consequences suffered from a choice of the heater power are presented in Table 5.

Table 5: The options of LMC Heater

Heater Power (kW)	Configuration/ LBE Vol. Incr. (liter)	Percentage of Mass flow rate/ Heat transfer	Time distortion in transient events
> 500	External Container/ + 23.4 litre	93~100% / 94~100%	Due to increase LBE volume
250~500	External Container/ + 14.7 litre	73~93% / 78~94%	Increase due to LBE volume increase and velocity decrease
150 ~ 250	In Main Flow Guide / - 3.8 liter	62~73 % / 68~78%	Decrease due to decrease of LBE velocity

The volume change is calculated by assuming:

- The heater rod is 16 mm in diameter and 500 mm long with no non heating length,
- The surface heat flux is roughly from 40 to 50 W/cm²,
- The heater rods is arranged in hexagonal rings and the pitch is 24 mm and closest distance to wall is 12 mm,

It is clear that the mid range is some kind of worse choice, because the time scale distortion is compounded by both volume increase and velocity reduction. If full power cannot be realized, the second best is the 150~250 kW range. Note that heater power under 150 kW is not considered, because it is too low for any meaningful heated experiment. One of the ways to look at it is that the convection heat transfer is a strong function of the flow rate (i.e. $Nu \propto Re^{0.8}$). The heat transfer characteristics of the THX at the nominal condition can be determined only if measurements are conducted at the full flow condition (i.e. 4 l/s). In order to measure the heat transfer rate accurately, the sensible heat must be much higher than the measurement error of the thermal couple (i.e. roughly 10 °C). The temperature drop across the THX is roughly 15 °C if the LMC heater power is 150 kW. This level temperature drop provides sufficient accuracy to determine the capacity of the HRS, which is one of the important criteria to be verified in target design.

A design of 150~250 kW LMC heater is examined. The good reason for having a lower heating power is that the whole heater can be fitted into the main flow guide tube. This brings the least geometric modification of the lower head of the target, by which is a better way to preserve the thermal hydraulic characteristics. The other important criterion is that commercial heater is employed in the design. A conceptual design of the possible LMC heater is given in Fig. 4. In this drawing the 10 kW Watlow heater rods are depicted. The heating length of each rod is 490 mm, which may possibly collide with the inserted thermal couples projected the region. It is better to shorten length of the heater by increase the maximum surface heat flux. A few cartridge heaters are ordered and they will be tested in a liquid metal loop. A long-term heater test is also planned for reliability of the commercial heater in LBE operation.

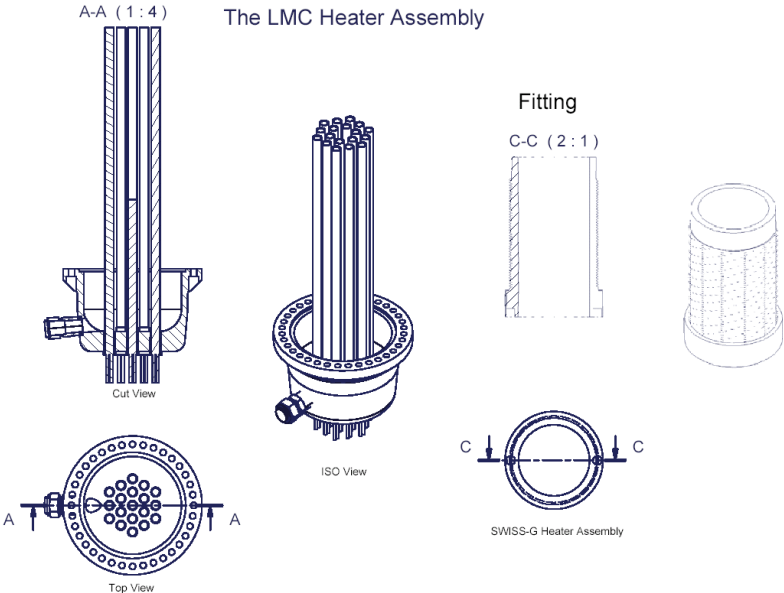


Figure 4: Conceptual design of the LMC heater.

The LMC Heater cannot be connected to the existing liquid metal container. A new lower liquid metal container (LMC) is needed. A conceptual design of a LMC replacement for Integral Test is presented in Fig. 5. It is a double flange design (DFC), on which the heater can be attached to the lower end of the container. Because to run the target must be run without the LMC Heater in some hydraulic tests, a small spherical cap is needed to close the end of the DFC. A design of such a spherical cap is presented in Fig. 6

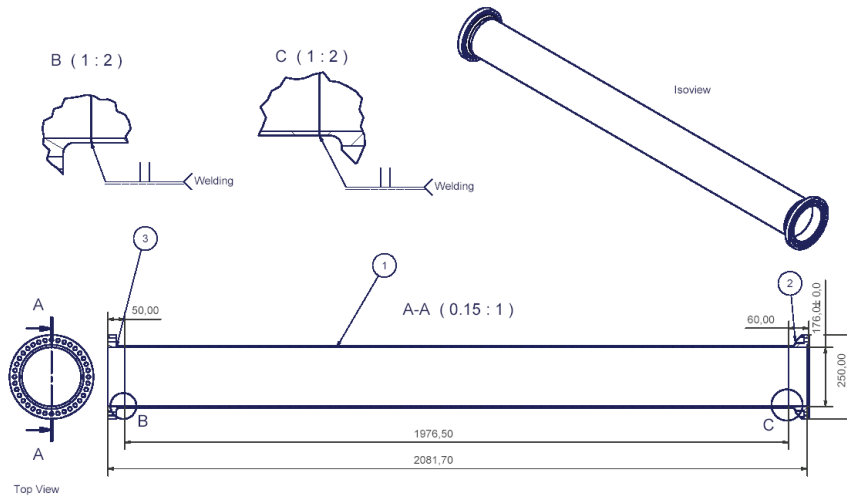


Figure 5: The double flanged liquid metal container for MITS

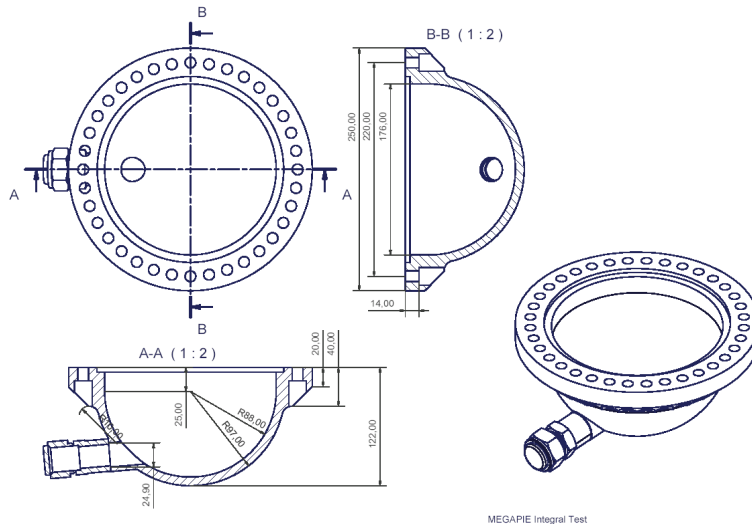


Figure 6: the lower spherical cap for closing the double flanged LMC,

Concluding Remarks

Integral Test is set for system integration and design verification. However, most of the tasks at this moment are focus on building up the supporting facilities for the test. Good progress has been made in building the steel frame Test Stand and building modification. The basic needs, such, as the electricity and cooling water supplies are pending, because the connecting interface to the Test Stand have not been defined. But the manpower and resources are allocated and can be activated in a short notice. There is some progress on the defining the interface of the cooling water. Engineering design of secondary water loop has just started.

For the Integral Test, the test program is divided into 7 campaigns with clearly defined goals. Campaign 0 serves as part of the quality assurance procedures. Each sub-system must be test against leakage and the primary functions. Campaign 1 is basically the instrument checkups to make sure the all the systems are operational and to test the functions of ancillary systems. Campaigns 2 and 3 are for testing the thermal hydraulics characteristics of the target HRS. All those efforts are leading to license the MEGAPIE target for irradiation test, which is defined in campaign 4. Campaign 5 is more or less for refining the control procedures during the normal and off normal transients. Campaign 6 is an important task to prepare the target in final assembled form for the SINQ test.

Thermal hydraulics test remains the most important part of the program. The LMC heater is needed to simulate the proton beam heating in the Integral Test. Arguments of the possible heater choices had been presented and it is concluded that the heater of 150~250 kW could provide the optimised experimental conditions for studying the target thermal hydraulics. Engineering design of the LMC Heater is pending on the long-term heater test, because information regarding the reliability of commercial heater is needed.

SUMMARY ON ANCILLARY SYSTEMS

Werner Wagner

Paul Scherrer Institut, CH-5232 Villigen, Switzerland

Six presentations were given in the session on Ancillary Systems, covering primarily the updates of boundary conditions and current concepts for the four systems directly connecting to the target head, which are needed most urgently for the integral test: Heat Removal System (HRS), Cover Gas System (CGS), Fill & Drain System (F&D) and Insulating Gas System (IGS). Further, the Target Handling Concept was presented and the status of preparation for the MEGAPIE Integral Test.

The Intermediate Cooling Loop (ICL) of the Heat Removal System was presented by G. Corsini of ANSALDO Nucleare, Genova (I). The loop contains organic, diathermic cooling fluid. Its control system is designed by means of computer code simulations to be able to properly control the LBE temperature in case of proton beam interruption with subsequent power recovery and to guarantee a stable hot stand-by condition. Some concept updates were reported: Initial provisions of chemical binding of gas generated by pyrolysis and radiolysis of the organic cooling fluid have been abandoned, because the existing cover gas plenum is able to temporarily store the gas between the scheduled monthly gas venting, without excessive pressure build-up in the system. Thermal insulation and heat tracing keep the ICL loop hot during extended shutdowns. A thermal expansion compensator takes over the pressure-keeping function in case of isolation valve closure and protects the target window from overpressure in case of THX pin rupture. Attention has been given to the functional requirement of limited load from the ICL piping to the target head by providing a system of three hinged compensators to form a cardanic joint.

The ICL system is now in the state of procurement. The oil pump was ordered, and the main components are released for purchasing. For manufacturing and assembling the company Criotec is identified as a competent tendering party. Although the schedule is tight, delivery to PSI is expected (and possible) at the end of 2003, after the factory acceptance tests in Italy.

For the Cover Gas System in principle three options exist for the gas handling: (a) complete enclosure in the target head expansion volume, (b) continuous pumping into a decay tank, or (c) periodic venting. The solution favored at present is periodic venting, in intervals of 4 to 8 weeks. This option guarantees that the radioactive inventory remains under the limits allowed for severe accident (heavy earthquake) management. A new boundary condition is given by the decision to omit the hydrogen absorbers in the target head, because of concerns regarding complexity and long term reliability of such an absorber system. Although this decision inhibits the option of complete and permanent gas enclosure, the expected accumulated gas inventory will not raise the cover gas plenum pressure during the venting periods (8 weeks maximum) to above 2 bar (abs), i.e. a maximum operation pressure of 2.2 bar (abs) in the gas plenum can be guaranteed. Although the current concept is that of periodic venting, the option of continuous pumping is a viable one, in particular if by that an expensive upgrade of the proton beam-line bunker can be avoided.

The design updates of F&D and IGS are governed by the new baseline concept of merely non-active draining. This allows considerable simplifications on both systems: The main measures of simplification comprise the possibility of manual operation, no need for radiation resistant equipment and no need for a second containment. A new concept was elaborated of covering plugs for the filling tubes, which assures that gas pressurization of the filling tubes after plugging is always possible and that no liquid LBE can raise up to the target head area.

For the IGS decision was taken to fill the insulation gas volume with He gas (at 0.5 bar) during target operation, instead of Ar. One of the consequences of this decision is an increased conductive/convective heat loss, which is calculated to be about 20 kW (compared to 3-4 kW for an Ar filling). Therefore, during the preheating phase without PbBi, when the target itself must be filled with pressurized He, the insulation gap between target containment and enclosure must contain Ar instead of He in order to balance the losses by the target heating. During hot standby, the available heating power in the target is high enough for covering the heat losses through the helium-filled insulation gap.

The current concept for target handling, transport and dismantling was presented by Ake Strinning. The ZWILAG option has been confirmed meanwhile, although the permit for the transport on the public road to ZWILAG is still pending. The concept for the transport is well elaborated, including a new transport flask. Sawing tests for a frozen target came out very promising and successful when using a band saw.

The preparation of the MEGAPIE Integral Test is making progress. The steel frame of the test stand meanwhile has been erected in the 'Montagehalle' at PSI. The necessary infrastructure (electric power, cooling etc.) is about to be installed. The secondary water loop design has started. Other than the secondary water loop in the SINQ hall later needed for the MEGAPIE operation, the loop of the test stand must allow water temperatures of up to 150°C and thus must withstand higher pressure. The remaining task is to design and construct the lower LMC heater for simulating the proton beam heating. The heater assembly will consist of 19 heater rods with a total power of nominal 190 kW. Individual heater rods will be tested in LBE for long term operation to ensure the integrity in the liquid metal environment.

Ancillary systems not addressed at the meeting were the safety devices for the beamline (funnels, catcher etc), and the control system. The latter is being developed in parallel to the main ancillary systems; call for tender for the hardware installations (racks, cables, processors) has begun. Preparation for the installations in the TKE and in the beamline bunker to be made in the shutdown Jan.-April 2004 are under way.

SESSION 2: Safety und Licensing Issues

CFD Simulation of Focused-Beam Transient

T. V. Dury

Thermal-Hydraulics Laboratory, Nuclear Energy and Safety Department, Paul Scherrer Institute, CH

Modelling assumptions

CFD transient simulations have been carried out for the situation when it is assumed that there is partial or total loss of the upstream de-focusing target, Target E, during operation. It has been assumed that the loss of Target E is instantaneous, and transients have been performed from a previous steady-state condition on this basis. The deposition profiles used for the calculations outlined here have radial exponential coefficients for the focused beam $\sigma_x = \sigma_y = 6.0\text{mm}$, and for the de-focused beam $\sigma_x = 21.0\text{mm}$ and $\sigma_y = 22.0\text{mm}$. The 1.0σ radial limits of both beams, and the 2.5σ limit of the de-focused beam, can be seen in Fig. 1. No radial cut-off of either the focused or de-focused beams was imposed, and the flow across the window from the bypass nozzle was aligned with the X-axis. Simulations were performed with a target design with bypass flow, a 20mm vertical gap between guide tube and window, and a flat end to the guide tube (Fig. 2). The current preferred target design is with a slanted end (15/25mm gap), but comparison between the behaviour of peak target window temperature for designs with either flat or slanted ends, with a 2.5mA focused beam and 100% loss of Target E, showed that there is no significant difference between the two designs, as far as these transients are concerned (Fig. 3).

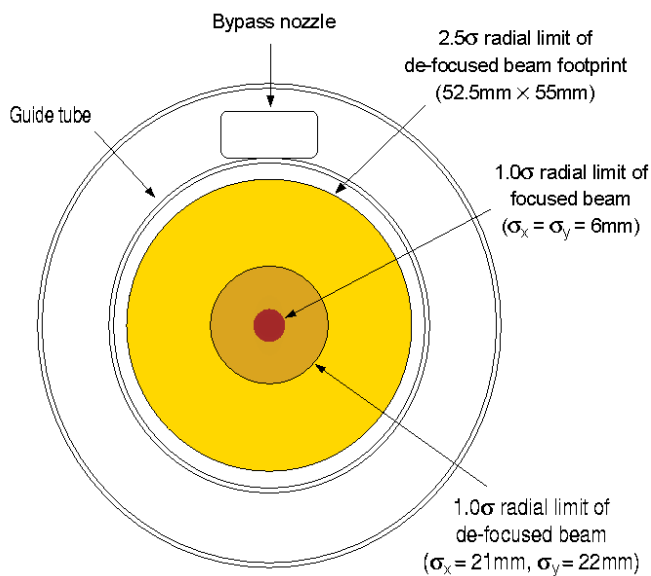


Figure 1: Radial focused and de-focused beam deposition profiles at the target window

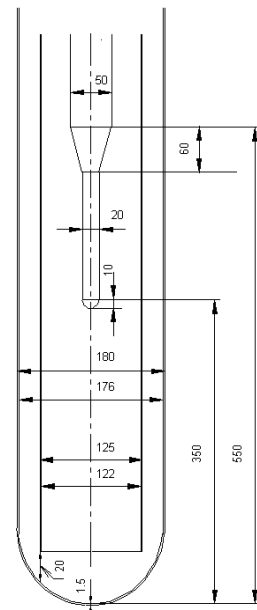


Figure 2: Lower Target Container with flat-ended guide tube

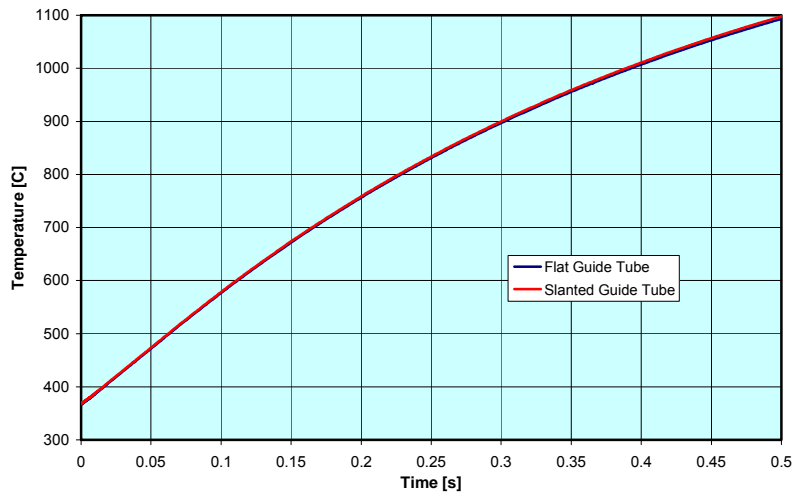


Figure 3: Peak window temperature: Transient with a 2.5mA focused beam
Flat and slanted ends of the guide tube

Results

Calculations were performed initially with 100% loss of Target E, i.e. the beam changed instantaneously from its de-focused deposition profile and beam current to its focused state. However, as it is conceivable, and also plausible, that damage to Target E could also occur with only partial loss of material, and hence only partial transmission of a component of focused beam to the target, calculations were also performed based on this scenario. In order to estimate the beam composition at the target window, an approximation was made in which percentages of focused and de-focused beam were summed at the window. For example, if 33% of Target E were lost, it was assumed that the effect at the window was averaged over the whole surface, and 33% of a full 2.5mA focused beam and 67% of a 1.74mA de-focused beam were deposited.

Calculations were also performed for a 2.0mA focused beam (which becomes a 1.4mA de-focused beam after passing through an intact Target E). The time for peak window temperature to reach 900°C is plotted for both beam powers as a function of the percentage of loss of Target E in Fig. 4.

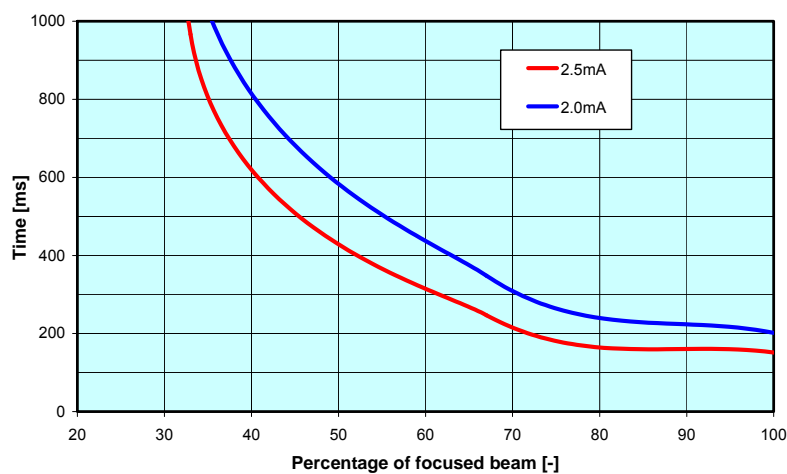


Figure 4: Time to reach peak window temperature of 900°C from steady-state with different percentages of focused ($\sigma_x=\sigma_y=6mm$) and de-focused ($\sigma_x=21mm, \sigma_y=22mm$) beams

It was found, however, that when the percentage of focused beam reaching the window dropped below about 35% for the 2.0mA beam, or 30% for the 2.5mA beam, the peak window temperature reached never reached 900°C, but achieved an equilibrium below this level, dependent upon percentage loss.

Concentrating on the case with 2.0mA focused beam, the development of peak window temperature as a function of percentage loss of Target E can be seen in Fig. 5.

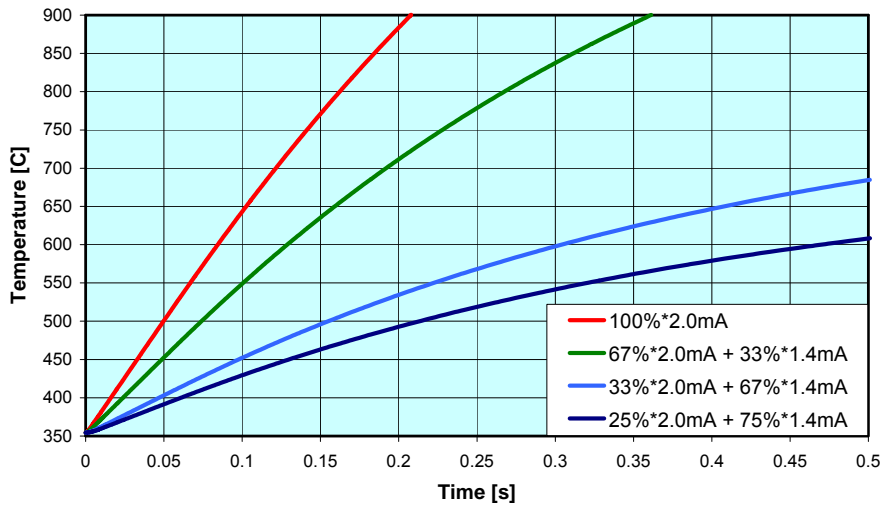


Figure 5: Development of peak window temperature as a function of percentage loss of Target E with 2.0mA focused beam

As an aid in assessing the response time required from a rapid detection system to control beam shutdown in the event of loss of Target E, results shown in Fig. 5 are also presented in Fig. 6 in the form of the peak window temperature reached after 150ms into the transient, as a function of loss of Target E. The rate of rise can be seen to be almost linear as a function of percentage of focused beam (i.e. percentage of loss of Target E).

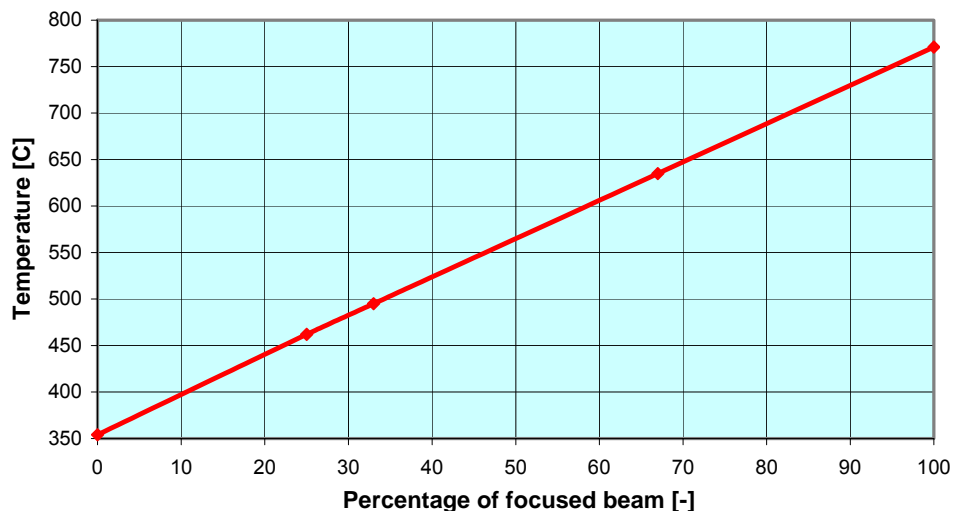


Figure 6: Peak window temperature at 150ms into transient as a function of percentage of focused 2.0mA beam reaching the window

Results are shown below in tabulated form, as a summary of Figs. 5 and 6.

Table 1:

Proportion of focused (F) and de-focused (DF) beams	Time [ms] to 900°C	Temperature rise after 150ms of transient [°C]
100% (F)	208	771
67% (F) + 33% (DF)	355	635
33% (F) + 67% (DF)	Peaks at 829°C	495
25% (F) + 75% (DF)	Peaks at 721°C	462

Conclusions

- CFD simulation of the lower section of the MEGAPIE target under steady-state normal operating conditions with a 1.4mA beam (radial deposition profile coefficients $\sigma_x = 21\text{mm}$ and $\sigma_y = 22\text{mm}$ at the window), has indicated that a peak temperature at the target window of 354°C or lower should be achievable at the current stage of design.
- Peak window temperature following the instantaneous, total loss of the upstream, de-focusing Meson Target (Target E) with a 2.0mA focused beam (with radial profile coefficients $\sigma_x = \sigma_y = 6\text{mm}$) reaches 771°C after 150ms and 900°C after 208ms.
- Partial loss of Target E reduces the rate of increase of peak window temperature, and the peak temperature achieved. Below an assumed evenly distributed loss of the effective de-focusing capability of Target E of about 35%, the peak temperature never reaches 900°C.

Thermal Shock Transient: CFD Simulation of Water Jet Impaction on Target Window

B. L. Smith

Thermal-Hydraulics Laboratory, Nuclear Energy and Safety Department, Paul Scherrer Institute, CH

Background

In the event of a rupture of the safety window, a jet of D₂O could impact the lower target enclosure. The rapid cooling effect could generate large thermal, and perhaps mechanical, stresses and threaten the structural integrity of the component, particularly the window, which is still being heated by the proton beam and could be cooled below the DBTT.

Consequently, there is a need to perform a detailed, local analysis of the heat transfer and mechanical loading process, and to estimate the resultant stresses in the structure. This requires the simultaneous application of an advanced Computational Fluid Dynamics (CFD) tool – the commercial code CFX-4 is used in the present analysis – and a structural analysis program – in this case ABAQUS – and a data interface between them. The paper describes the thermal hydraulics part of this combined analysis; the stress analysis part is reported by A. Zucchini, ENEA.

Accident Scenario

A schematic of the lower target is given in Fig. 1, which shows the target hull and the double-skinned, water-cooled safety hull. The accident is initiated by rupture of (at least) the inner wall of the safety window and a jet of D₂O being sprayed onto the hot external surface of the target hull.

Since the size and location of the break in the safety window is not known, a worst-case situation needs to be formulated. Given that the internal pressure of the D₂O is initially 7 bar, the impact velocity, except in the case of very thin cracks, will be about 35 m/s. As discharge proceeds, the pressure reduces but the water inventory of 7.5 litres would be enough to fill the gap between the safety window and the target hull.

At the start of the transient, the target is in normal operating mode, in which case the maximum (external) window temperature will be about 380°C [1,2].

The He in the gap between the safety and target hulls is 0.5 bar initially, and with such an ambient pressure the wall temperature represents over 300°C of superheat, which, according to Fig. 2^α, would imply film boiling, with associated low heat transfer. As the wall temperature reduces, boiling transition (to unstable film boiling) may be expected to occur, with a consequent increase in wall heat flux. The Critical Heat Flux (CHF) represents the maximum heat flux, which can occur except at extremely high wall superheats.

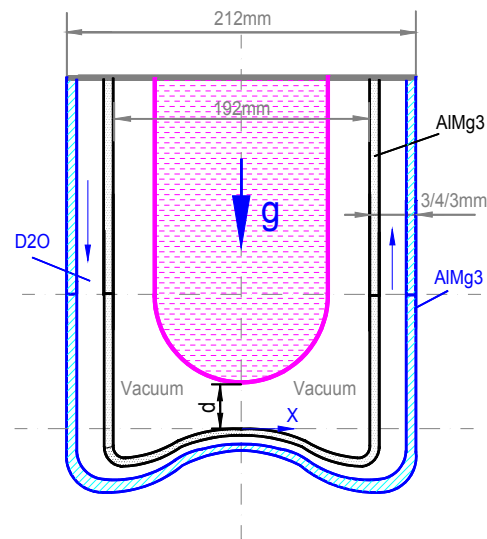


Figure 1: Schematic of the Target Lower Section

^αThe curve is taken from the literature [3] and applies to pool boiling, which is not strictly applicable in the present case. However, the fundamentals are similar to what is required here; see later.

A worst-case situation may therefore be defined in which:

- (1) the water jet impacts the centre of the target window, where the temperature is highest;
- (2) there is no window cooling during the stable or unstable film-boiling phases;
- (3) the heat flux is a maximum (CHF limit) until the wall temperature reduces sufficiently for a (conservative) heat transfer correlation to be applied (140°C);
- (4) the beam remains on during the accident.

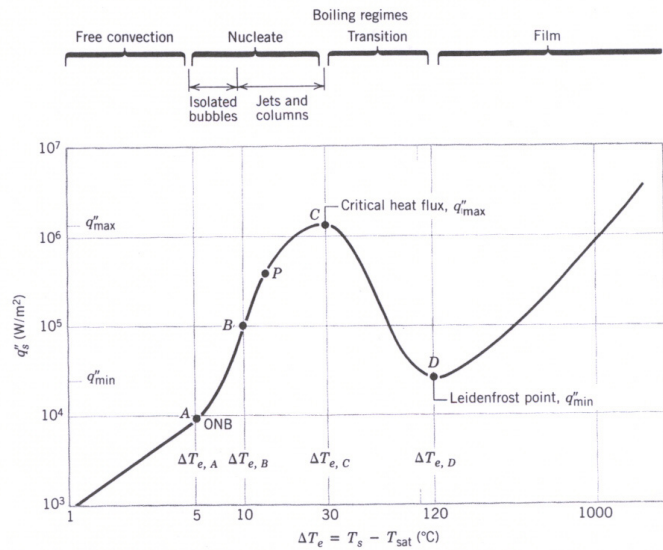


Figure 2: A Typical Boiling Curve for Water at 1 atm.

The classical Kutateladze/Zuber estimate of the CHF for water at 1 bar (with theoretical coefficient adjusted according to experimental data) gives [3]:

$$q'' = 1.25 \times 10^6 \text{ W/m}^2$$

but this estimate (which has been derived for pool boiling) needs to be considerably enhanced because of two effects. The first follows recent experiments reported by Ohtake *et al.* [4] on the enhancement of CHF due to jet impact on heated surfaces in which, for an impact velocity of 35 m/s (a slight extrapolation from the published data), the CHF was seen to be increased by about a factor 5 over the Kutateladze value. Also, away from the impact site, there would be tangential flow over the heated surface, so estimates of CHF should be obtained from flow boiling rather than pool boiling curves. Under the present, postulated flow conditions, the correlation of Lienhard and Eichhorn reported in [5] also indicates a CHF enhancement of about a factor 5.

Consequently, the following recipe is adopted for a worst-case heat transfer model. Initially, a heat flux of $q'' = 5 \times 10^6 \text{ W/m}^2$ is imposed over the entire target window. When the wall temperature drops to 140°C (i.e. 100°C above the D₂O temperature), a constant HTC of 50 000 W/m²/K is imposed. This value ensures continuity of heat flux from the CHF estimate, and its high value is consistent with the present conservative approach.

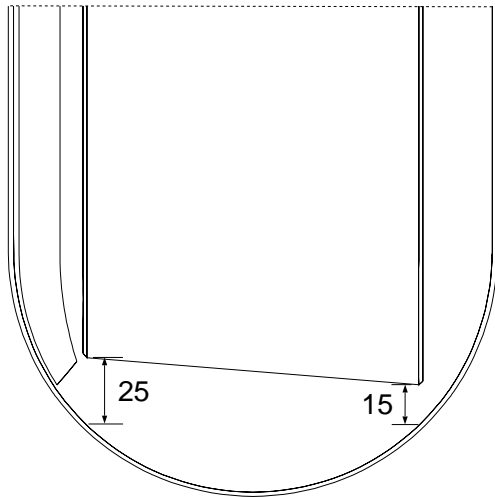
Computational Procedure

The CFX-4 thermal-hydraulics model used for the thermal shock analysis is that constructed by Dury [1] for steady-state target simulations, and reflects the latest design details. The model geometry is shown schematically in Fig.3, together with some details of the geometry and flow parameters.

A conjugate heat transfer problem is first set up, modelling both the fluid and structural components, and a transient calculation performed starting from a “normal operation mode” with the beam on. Appropriate coding has been added to the User Interface in the code to produce, at time intervals of 50 msec, 3 output files containing the following information:

1. Element/node topology for all structural (hexahedral) elements
2. Nodal x,y,z coordinates
3. Temperatures at nodes, and pressures on element faces adjacent to the LBE.

The files are written in a format consistent with the input specifications of the ABAQUS code. By this means, all the thermal and fluid-mechanical load data to the structures are computed using CFD, simplifying considerably the stress analysis procedures.



- 20±5mm gap at end of guide tube
- 20×10mm bypass nozzle dimensions
- 1.74 mA beam with major axis aligned with bypass jet
- Fluid temperature at HX outlet = 230°C
- 2.5 kg/s bypass flow of LBE
- 37.5 kg/s annulus flow of LBE

Model Geometry

Figure 3: Details of CFD Model used at the Start of the Transient

The temperature distributions on the inside and outside surfaces of the window at the start of the transient are shown in Fig. 4. The bypass flow is from right to left. The hottest region, which reflects the beam footprint, is displaced slightly from the central axis as a consequent of this cross-flow. For the conditions specified, the peak external temperature is about 380°C.

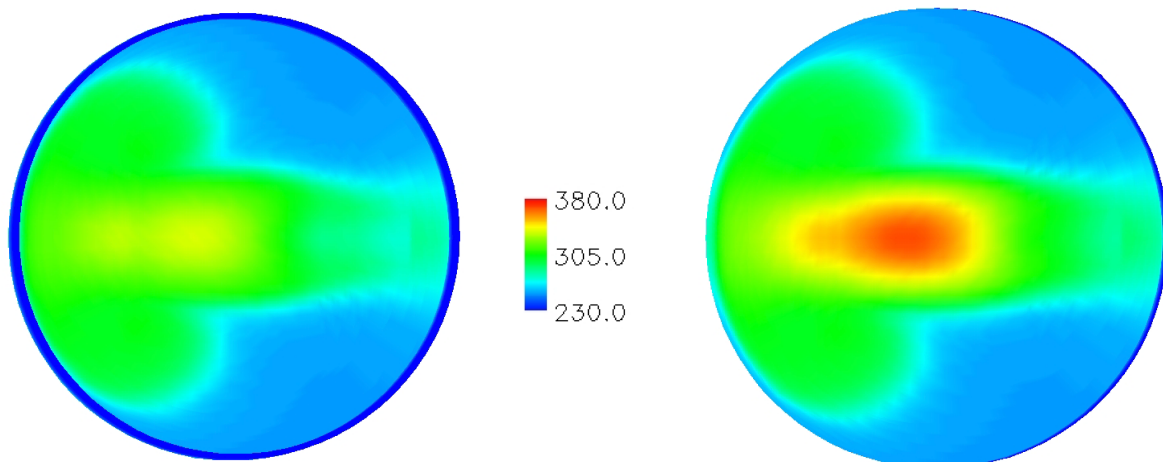


Figure 4: Contour Plots of Inside and Outside Window Temperatures at t = 150 msec

Figure 5 shows the window temperatures 150 msec into the transient; about the time at which the stresses in the window are at maximum [6]. The temperature scales are

different in the left and right plots. The inside surface is in contact with LBE at about 250°C, while the outside surface is being cooled by the water jet at 40°C. The strong temperature difference of about 130°C from the inside to outside is about four times larger than that which exists under steady-state conditions and is of the opposite sign. A significant increase in overall thermal stress levels may therefore be anticipated, with perhaps localised stress concentrations and the potential for buckling. The stress analysis part of this study addresses these issues.

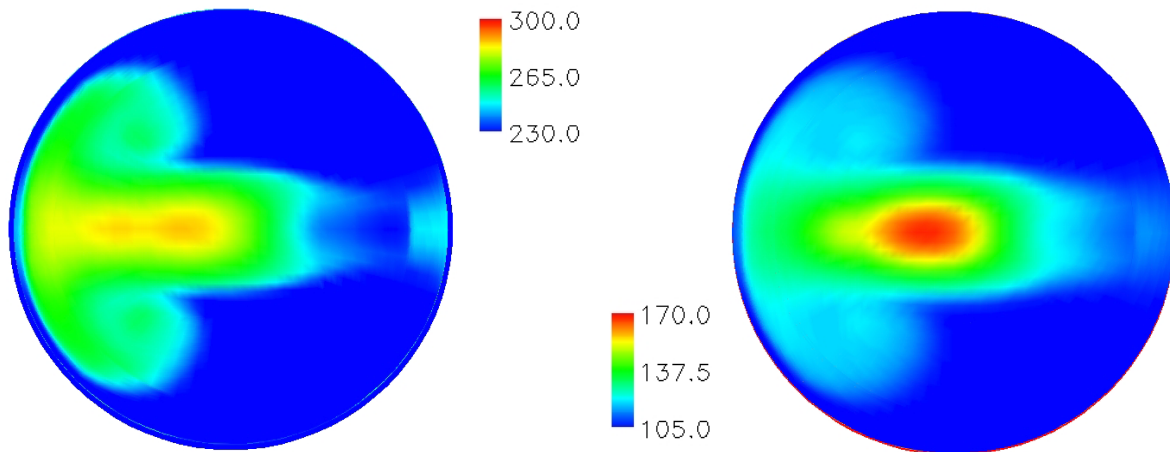


Figure 5: Contour Plots of Inside and Outside Window Temperatures at t = 150 msec

Final Remarks

Transient CFD calculations have been performed to simulate a jet of D2O impacting the hot surface of the target window. Initially, the heat transfer mechanism from wall to liquid is assumed to be the maximum under CHF conditions, and enhanced as a consequence of the impaction process and forced flow parallel to the heated surface. Later, as the window cools, an appropriate HTC is applied.

At time steps of 50 msec, data files are written which can be input into a structures program such as ABAQUS or ANSYS in order to perform the stress analysis. The results of this analysis are reported at this meeting [6].

References

- [1] T. V. Dury "CFD Analysis of Lower Target: Latest Steady-State Simulations", Megapie Technical Review Meeting, Paris, 18-19 March 2003
- [2] P. Roubin "Megapie Steady-State Simulation of the Lower Target Thermal Hydraulics", CEA Document, STH/LTA/2003-03, Jan. 2003
- [3] F. P. Incropera, D. P. DeWitt Introduction to Heat Transfer, 2nd Edition, John Wiley and Sons, New York, 1990, pp.546-564
- [4] H. Ohtake, K. Lui, Y. Koizumi "Study on Enhancement of Critical Heat Flux by Supplying Liquid Jets to Heating Surface (Mechanism on Enhancement of CHF and Measurement of Void Fraction near Heating Surface)", Paper IMECE2001/HTD-24171, Proc. 2001 ASME Int. Mech. Eng. Congress and Exposition, New York, NY, Nov. 11-16, 2001
- [5] Y. Katto, C. Kurata "Critical Heat Flux of Saturated Convective Boiling on Uniformly Heated Plates in a Parallel Flow", Int. J. Multiphase Flow, 6, 575-582 (1980)
- [6] A. Zucchini "Stress Analysis of the LMC Under Accident Conditions", Megapie Technical Review Meeting, Paris, 18-19 March 2003

Stress Analysis of the LMC Under Accident Conditions

A. Zucchini¹, B. L. Smith²

¹UTS Tecnologie Fische Avanzate, Sezione Metodologie e Diagnostiche, ENEA, Bologna, Italy

²Thermal-Hydraulics Laboratory, Nuclear Energy and Safety Department, Paul Scherrer Institute, Switzerland

1. Over-Focussed Beam

Structural analysis simulations have been carried out for an accident situation in which there is instantaneous, partial or total, loss of the upstream de-focusing target, Target E, during operation. The thermal field in the structures has been previously obtained from transient CFD analysis [1], and appropriate data files at specific time intervals prepared for the ABAQUS code.

All simulations refer to a target design with bypass flow, a 20mm vertical gap between guide tube and window, and a flat end to the guide tube (Fig. 1). This is not the current preferred target design with a slanted end (15/25mm gap), but is adequate for the present analysis of the window. The stress calculations have been performed for an assumed beam current of 2.0 mA.

Data were available for different proportions of focussing, and in each case the stresses were calculated at the point at which the maximum window temperature had stabilised, or reached 900°C, as appropriate.

All important are the assumed material properties for T91. Initially, yield-stress data were only available from Subatech up to temperatures of about 500°C, and have been used for preliminary studies [4]. Later, however, these were supplemented by results from some high temperature tests undertaken at PSI in the range 550°C to 900°C. The data are given in Fig. 2. As can be seen, in the normal operating range of the target – with maximum window temperatures below 400°C – the yield stress is well above the maximum stress in the window, which is around 60 MPa [2]. However, in the range 500°C to 700°C the material weakens considerably, and elasto-plastic response may be anticipated.

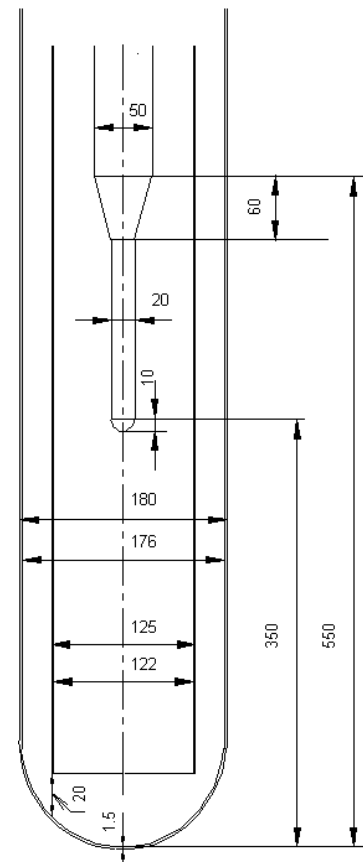


Fig. 1: Lower Target Container with flat-ended guide tube

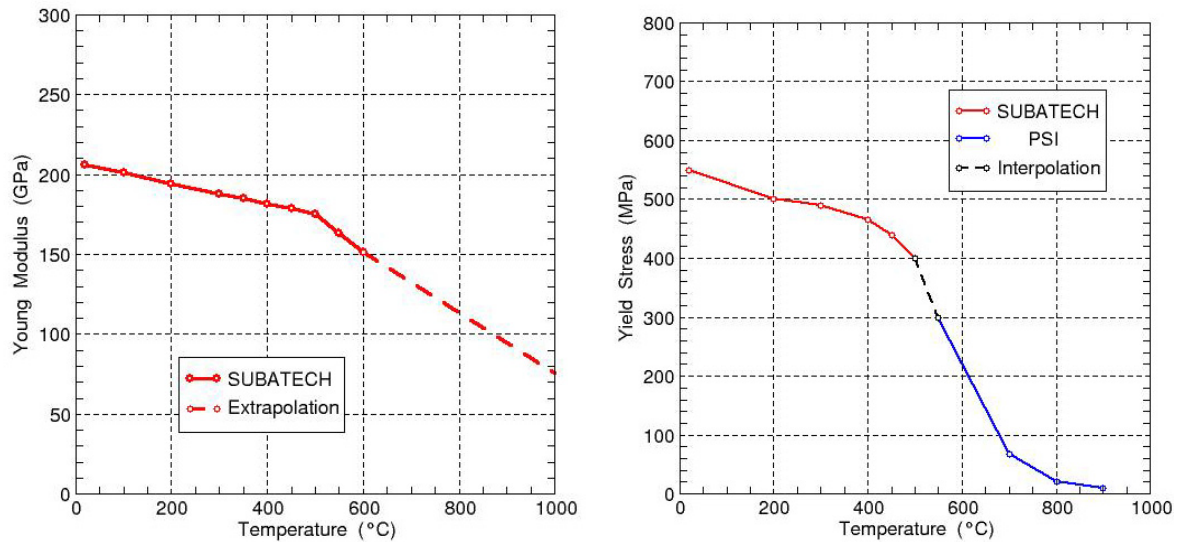


Fig. 2 Young's Modulus and Yield Strain for T91 as a Function of Temperature

Figure 3 shows the temperature and stress distributions on the external window surface for the case of 100% bypass of Target E. The beam focussing in the centre of the window is quickly apparent, and the temperature there has risen to 900°C after about 200 ms. The von Mises stress distribution at this time shows that the maximum stresses occur in a ring at the edge of the beam footprint, and that the center of the window over a diameter of about 1 cm is undergoing plastic deformation. Failure to trip the beam could result in burn-through of the window due to the very fast overheating.

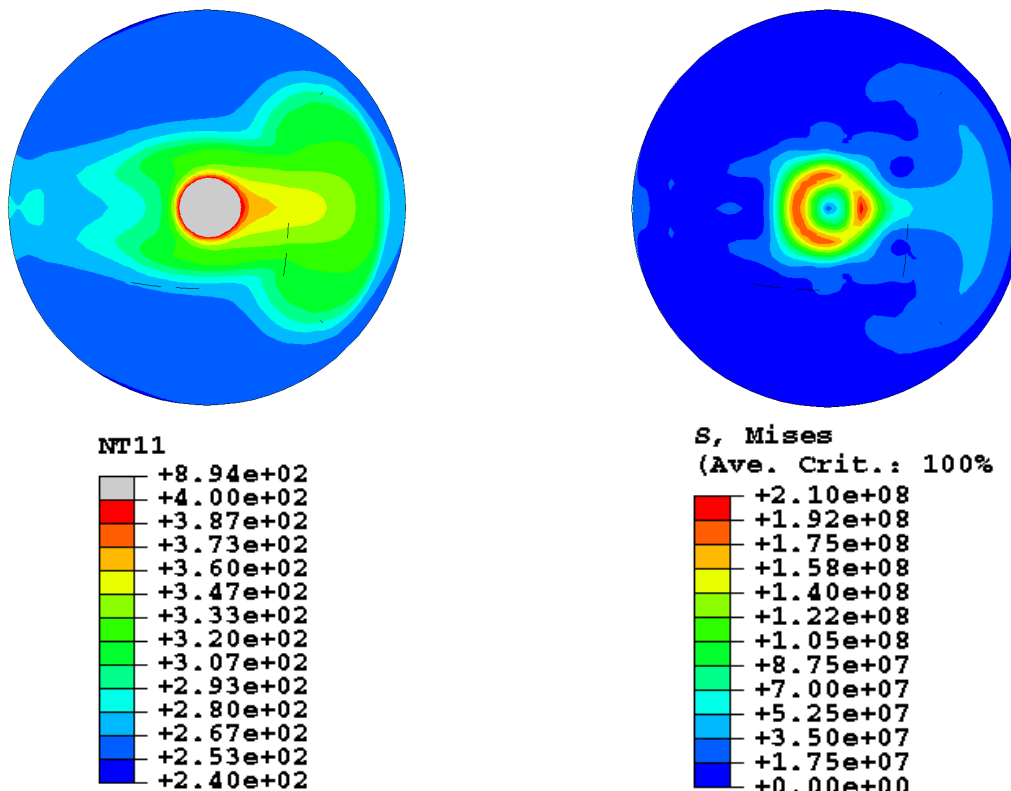


Fig. 3 Temperature and Stress Distributions at 202 ms for 100% Bypass of Target E

Cases in which there is partial focussing are summarised in Table 1. For lower values of the focussing parameter, the window temperature stabilises after a rapid initial increase, and no burn-through would then be expected. At higher degrees of bypassing, local cooling is inadequate, and the temperature at the window centre is predicted to exceed 900°C. The last column gives the plastic strain, and the second column the time required to reach 900°C.

Table 1. Maximum Temperatures, Stresses and Strains in the Window for Different Degrees of Focussing

Focus (%)	Time (ms)	T _{max} (°C)	σ _{max} (MPa)	ε _{p,max} (%)
0	Steady-state			0
25	Steady-state	712	158	0
33	Steady-state	819	184	0.29
67	348	900	194	0.58
100	202	900	202	0.61

2. Leak in Safety Hull

The background to this accident scenario has already been reported at this meeting [3], so only a brief outline will be given here. The case studied refers to an event involving rupture of the safety window in which a jet of D₂O impacts the target window. The rapid cooling effect generates large thermal gradients, and the associated stresses could threaten the structural integrity of the window, which is still being heated by the proton beam.

A schematic of the lower target is given in Fig. 4, which shows the target hull and the double-skinned, water-cooled safety hull. The accident is initiated by rupture of (at least) the inner wall of the safety window and a jet of D₂O being sprayed onto the hot external surface of the target hull.

Since the size and location of the break in the safety window is not known, a worst-case situation needs to be formulated; this point is discussed more fully in [3]. Briefly, an initial heat flux of $q'' = 5 \cdot 10^6 \text{ W/m}^2$ is imposed over the entire target window until the wall temperature drops to 140°C, then a constant HTC of 50 000 W/m²/K is imposed. This value ensures continuity of heat flux from the CHF estimate.

The CFX-4 thermal-hydraulics model used for the thermal shock analysis reflects the latest design details, and is based on a beam current of 1.74 mA at the target window. The model geometry at the lower end is shown schematically in Fig. 5, together with some details of the geometry and flow parameters [3].

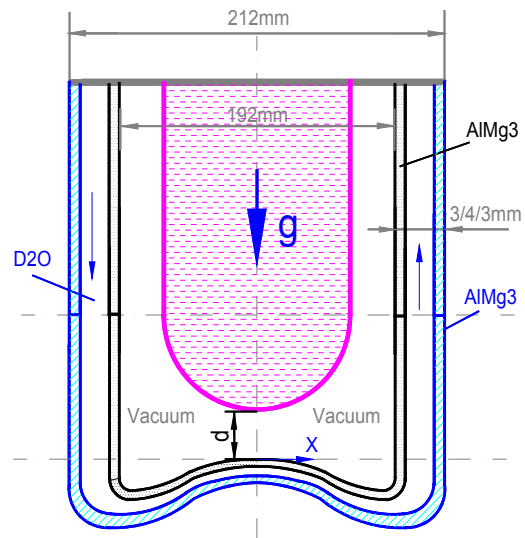
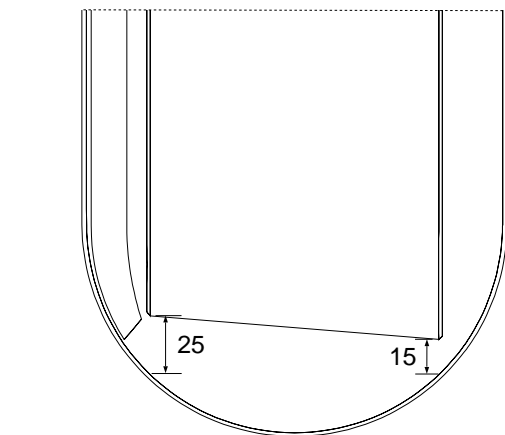


Fig. 4: Schematic of the Target Lower Section



Model Geometry

- 20±5mm gap at end of guide tube
- 20×10mm bypass nozzle dimensions
- 1.74 mA beam with major axis aligned with bypass jet
- Fluid temperature at HX outlet = 230°C
- 2.5 kg/s bypass flow of LBE
- 37.5 kg/s annulus flow of LBE

Fig. 5: Details of CFD Model used at the Start of the Transient

The temperature distributions on the outside surface of the window at the start of the transient and at 150 msec into the transient, about the time at which the stresses in the window are at maximum, are shown in Fig. 6. The bypass flow is from left to right. The hottest region, which reflects the beam footprint, is displaced slightly from the central axis as a consequent of this cross-flow.

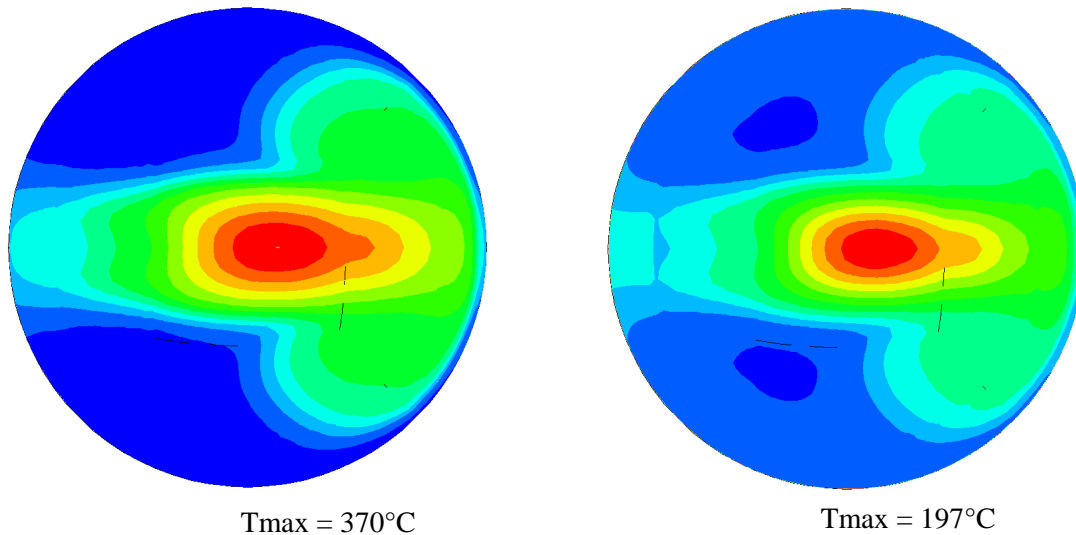


Fig. 6: Contour Plots Outside Window Temperatures at t = 0, 150 msec

Figure 7 shows the von Mises stress contours, on the outside window, at the same times. Initially, stresses are very low, with maximal occurring at the edge of the beam footprint in the central region of the window. After 150 msec, the window has cooled below the level of the incoming LBE stream from the annulus by the external heat flux into the D_2O . The maximum stress has increased to 210 MPa, and is located at the edge of the window, on the opposite side to the bypass flow. Note that at this time the window has not cooled sufficiently (below $140^\circ C$) for the HTC condition to be applied, so the maximum heat flux of $5 \cdot 10^6 W/m^2$ is still being imposed. This no doubt is conservative at the edge of the window where the maximum stress occurs.

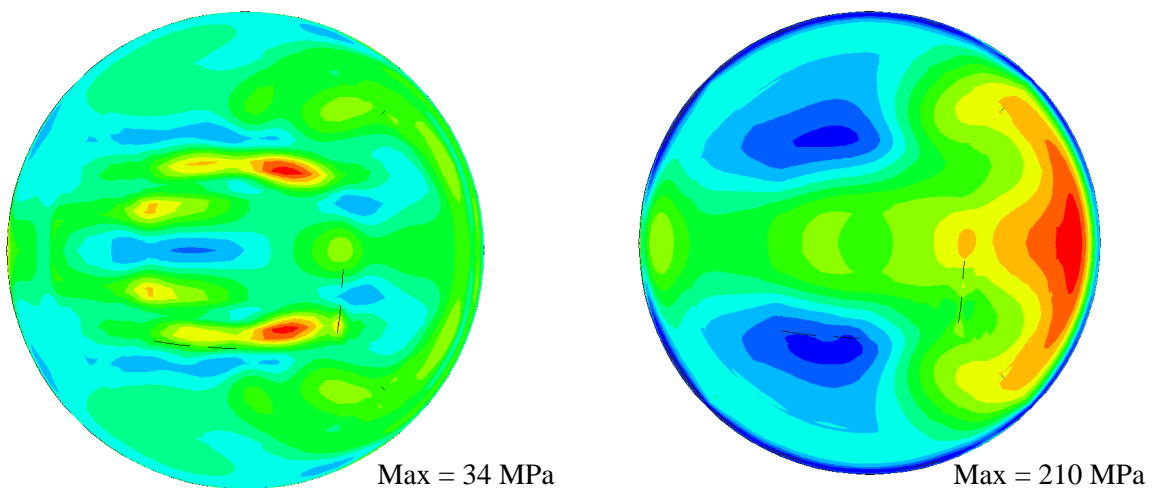


Fig. 7: Contour Plots of von Mises Stresses at t = 0, 150 msec

3. Final Remarks

Transient stress calculations have been performed using the ABAQUS finite element code to determine whether the structural integrity of the target window would be threatened by the impact of a jet of D_2O from the ruptured inner skin of the water-cooled safety window. Thermal data have been supplied from accompanying CFD simulations performed at PSI under suitable assumptions regarding the accident scenario. The computations reveal that window stresses peak at about 150msec into

the transient, but at levels well below the yield strength of the material (T91) at all irradiation levels.

4. References

- [1] T. V. Dury "Focussed Beam Transient", MEGAPIE Technical Review Meeting, Paris, 18-19 March 2003
- [2] A. Zucchini "Stress Analysis of the LMC Under Normal Operating Conditions", Megapie Technical Review Meeting, Paris, 18-19 March 2003
- [3] B. L. Smith "Thermal Shock Transient", MEGAPIE Technical Review Meeting, Paris, 18-19 March 2003
- [4] A. Zucchini "MEGAPIE: Stress Analysis of Lower Target Preliminary Design", RTI/FIS/MET/2002/1, ENEA, 2002

First Results with the Visual Monitor VIMOS

Knud Thomsen

Spallation Neutron Source Division (ASQ), PSI, CH-5232 Villigen PSI, Switzerland

Abstract

Safe MEGAPIE operation relies on the incident proton beam impinging on the target with a wide footprint due to scattering of the beam by the upstream Target E. In case there is a change in the flux distribution the target window might be locally overheated leading to a hole in the liquid metal container and possibly also in the lower target enclosure (safety hull). A new Visual Monitor System VIMOS is in preparation, which will allow to directly monitor the incident intensity distribution and to switch off the beam quickly in case of anomalies. Tests showing the principal feasibility of the system have been performed in a mock-up geometry.

Background

One of the most critical accidents that could happen to the MEGAPIE target would be that the incident proton beam misses Target E and arrives at MEGAPIE without being scattered (figures 1 and 2). At the center of the target window this would mean an increase in intensity by a factor of approximately 20 compared with normal operation ($\sigma_x = \sigma_y = 6\text{mm}$ instead of $\sigma_x = 21\text{ mm}$ and $\sigma_y = 38\text{ mm}$) [1], [2].

At an expected beam current of 2 mA delivered by the accelerator this would heat a spot of the window to about 700 °C within 120 ms, which would cause the window to break quickly [3]. The safety hull could maybe marginally withstand the direct incident non-scattered beam, but would most probably yield when a jet of overheated liquid metal out of the container impinges on the target enclosure at exactly the same center spot that is already seeing the highest beam intensity.

The most promising way to address this accident scenario appears to be to make sure that the beam is switched off before any damage can occur if the incident proton intensity increases.

The scattering of the protons by Target E might change in one dramatic step if Target E breaks and is completely lost, it might also change due to a misalignment of the beam path with only part of the beam bypassing Target E. The first case is deemed most unlikely in the light of the experience that has been accumulated with Target E in the course of decades. The second case, where some protons miss the target, cannot be totally excluded.

This would probably be detected by the current beam diagnostics, but as this is such a critical situation, two new and additional measures are being investigated to guarantee that any beam with improper intensity distribution is switched off as soon as possible, definitely within 120 ms.

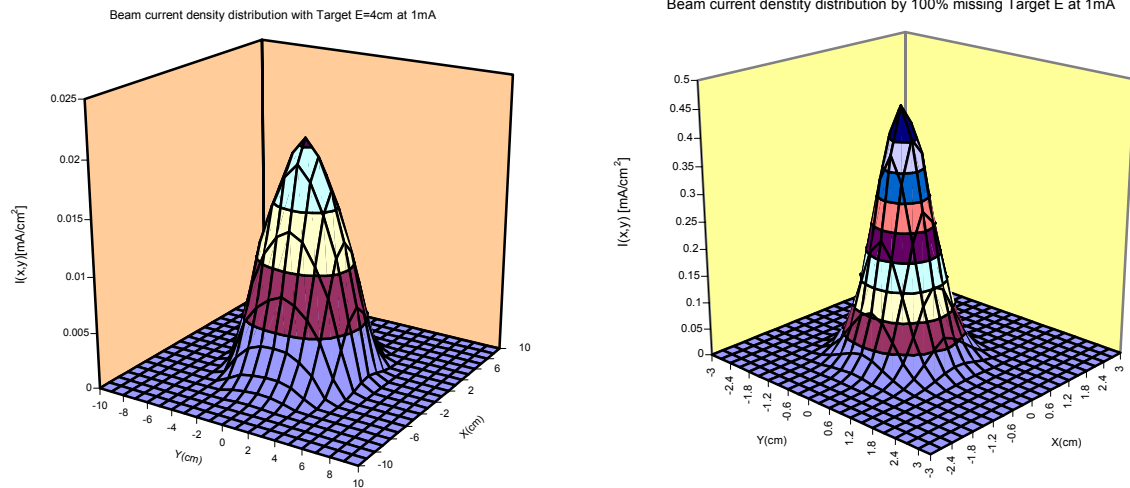


Figure 1: Proton intensity distribution on the Megapie target during normal operation for a 4 cm Target E @ 1 mA (*left*)
 Unscattered proton intensity distribution on the Megapie target when Target E is completely missed @ 1 mA; notice the much sharper peak and the reduced x/y-scale (*right*)

New monitoring systems

One proposed system consists basically of a passive beam blocker that takes advantage of the fact that scattered and unscattered protons take well-separated paths at a certain position between Target E and the Megapie target [4].

At the same time substantial effort is invested into an upgrade of the existing current monitoring system, which measures the beam intensity before and after Target E. It seems to be possible to detect a deviation in the attenuation corresponding to approximately ten percent of the beam bypassing Target E.

VIMOS

The device described here consists of some simple optics and a camera monitoring the optical flux from a thin foil representative of the actual intensity distribution in the incident beam very close to the liquid metal target [5]. The basic idea is that an unscattered proton beam, which can overheat the target window, would have the same effect on a foil, which is supported in front of the MEGAPIE target. A thin foil or mesh of any high temperature- and radiation-resistant material will react much faster than the target itself, i.e. it will show a much larger temperature excursion over any given time interval. This allows the anomaly to be detected very quickly and the beam to be switched off before the MEGAPIE target is damaged.

Requirements

In order to determine the requirements placed on such a monitoring device, calculations on target heating have been done for the expected 2 mA beam delivered by the accelerator (in 2005). The results show that the MEGAPIE target can withstand up to 20 % of the beam bypassing Target E permanently [3]. This means that, to be on the safe side, an unscattered beam fraction of the order of ten percent must be detectable. For a small part of the beam bypassing Target E the timing requirements are not so demanding, but a complete loss of Target E has to be detected within maximum 100 ms, as a quick shut-down of the beam takes a few ms, once the trigger signal has been generated.

Radiation Environment

A rough estimate of the expected dose at the position of the window in the catcher was 10^4 rad/h, corresponding to 6×10^5 Gy for a full period of 6000 hours [6]. This radiation level is mainly due to neutrons. A measurement extending over a period of 6 months yielded approximately 0.5 kGy (below the useful range of the dosimeter).

System components

The Visual Monitor VIMOS addresses the challenge with a very simple set-up. Its main components are:

- glowing foil (mesh)
- collecting mirror
- camera
- image acquisition electronics
- image processing software

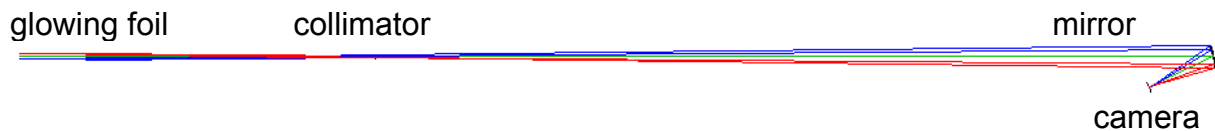


Figure 2: Optical path from the glowing foil through the collimator and via the collecting mirror to the detector, drawn to scale

Glowing foil

The “glowing foil” actually does not consist of a single piece of metal foil, but rather is a net structure. A mesh of mono-crystalline tungsten wires is supported by a light cylindrical structure, which sits on top of the last collimator, close to the Megapie target. A mesh has the advantage of highest possible resistance to going to pieces. An excessive number of temperature swings in the order of 10000 beam interrupts are expected during the irradiation period of Megapie probably leading to fatigue in a foil. If indeed a wire would break it is kept in place by the woven structure. Due to manufacturing constraints a non-symmetrical mesh has been chosen with wires of 100 μm in one direction and 300 μm in the other. The mesh will be made from three stripes with a width of 45 mm each thus providing enough structure for focusing. The thickness of the individual wires of 300 μm leads to a temperature of around 1000 $^{\circ}\text{C}$ (required by camera sensitivity) in the center of the mesh during normal operation (for 2 mA current from the accelerator, 1.4 mA after Target E). The temperature distribution is relatively flat in this case. Any local increase in intensity of the incident protons results in an immediate change of the temperature distribution over the foil. Non-scattered protons hit a spot close to the center and heat this

strongly, at the same time the intensity further out is reduced [1]. Thus the center glows more brightly while the outer region cools down.

By means of thermal simulations it has been shown that heat conduction in the foil is negligible. The energy deposited by the protons is dissipated via radiation, and the temperature at every point is a very direct measure of the local impinging power density.

Extensive calculations have been performed with the baseline of a silicon solid state MOS camera with a higher sensitivity in the IR than the current best choice camera (figure 7). These simulations assumed 100 μm thick W wires and 700 $^{\circ}\text{C}$ (1000 K) nominal glowing temperature [5,7].

The temperature of 700 $^{\circ}\text{C}$ in the center arising from a foil thickness of 100 μm corresponds to a very dim red glow. A completely unscattered beam heats the hot spot on the mesh to 1660 $^{\circ}\text{C}$ within 100 ms (see figure 9 and table1). The resulting enhanced glowing will be detected by the camera.

Collecting mirror

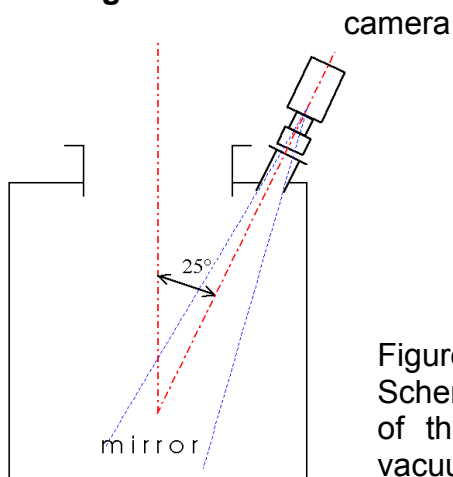


Figure 3:
Schematic location of the collecting mirror at the bottom of the catcher; the camera is positioned outside a vacuum window

Through the narrow diaphragms in the collimator there is only a rather limited field of view accessible from the bottom of the beam line where the catcher is located (figures 2, 3). With the use of a large-diameter (200 mm) collecting mirror it is still possible to collect light from the central area of the mesh over a region of about 100 x 110 mm (figures 11-14). This light is focused onto a video tube without additional optical elements. The imaged area is not circular, because of the non-circular open apertures in the collimator. The light from the glowing foil has to be deflected sideways out of the catcher to the camera. The offset of the focus location from the main optical axis (line of sight) through the vertical beam line is 240 mm, the exact deflection angle is 22.8 degrees.

The mirror of choice is an off-center section of a paraboloid with 620 mm focal length. It was possible to find one company, which was able to diamond cut the specified shape in aluminum with an overall form error of 2 μm . Thus the non-optimum optical boundary conditions posed by the narrow diaphragms of the collimator in the beam line are the dominant contributor to the distortions in the image of the mesh.

This has been shown by numerical simulations using OSLO and by actual measurements in a mock-up geometry (figures 4, 5, and 16).

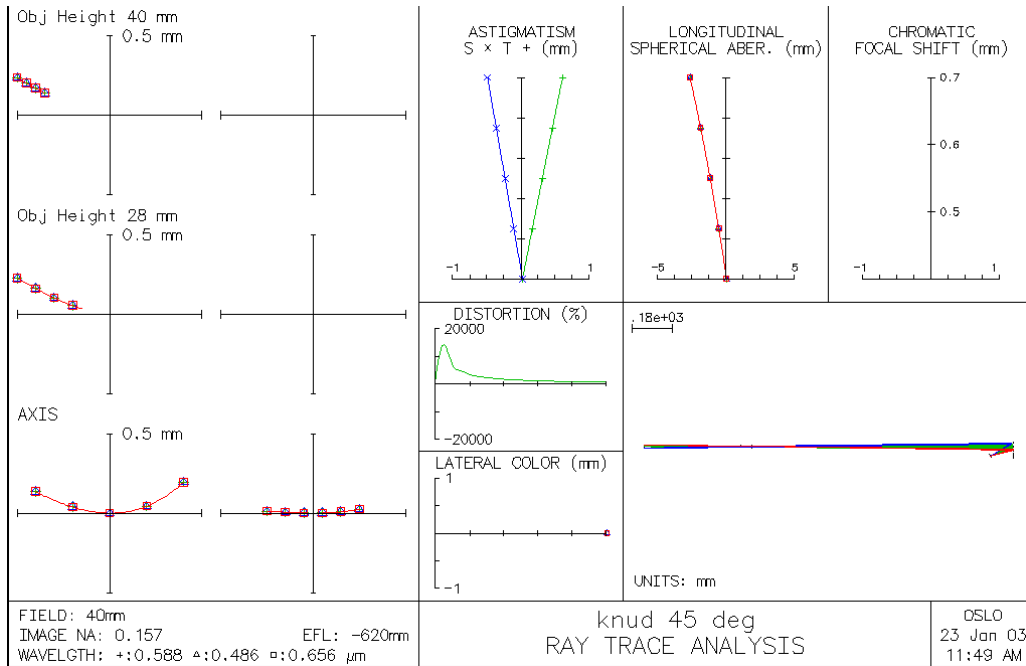


Figure 4: Calculated general image characteristics (with OSLO) for a perfect parabolic mirror in the Megapie geometry

A distance of 11 m between the foil and the mirror results in a focusing distance of 657 mm between the mirror and the detector. The scaling of the image is approximately 17 to 1; i.e. 110 mm on the foil correspond to 6.6 mm on the sensor of the camera (Chalnicon video tube). These numbers do not include optical imperfections. There are of course no chromatic aberrations as the collecting mirror is the only imaging component in the system.

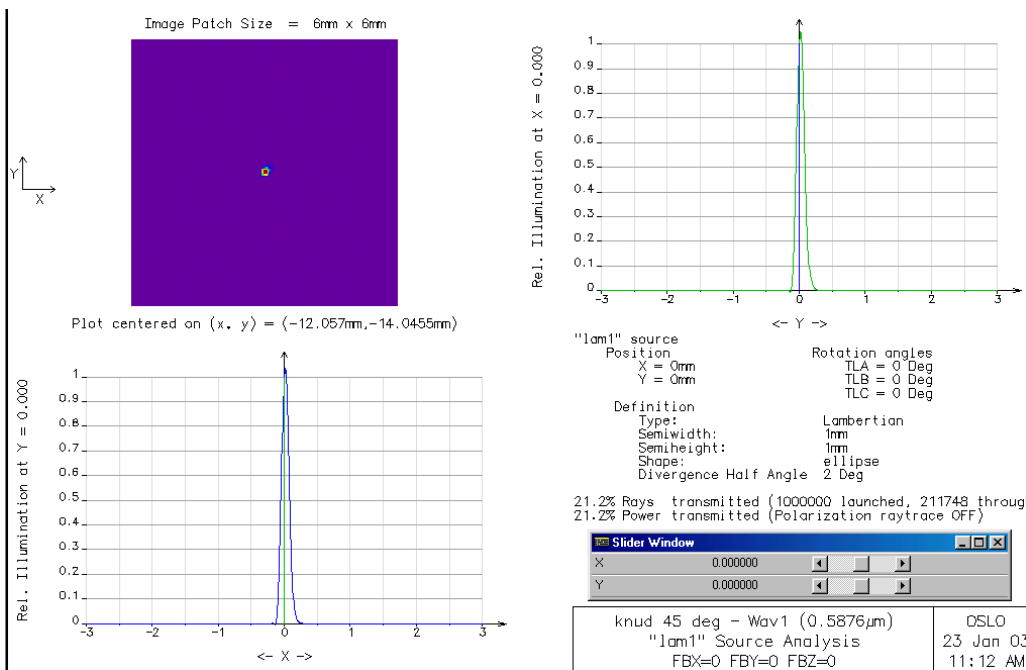


Figure 5: Ray trace for an extended source of 2 mm diameter in the center of the foil on a 6 x 6 mm sensor for the parabolic collecting mirror (compare with figures 11-16)

Optical image quality is not of high importance, because VIMOS does not really depend on it. The signal that primarily has to be detected is the changing temperature due to a local increase in proton intensity. With an increasing temperature, the emitted wavelengths are shifted to shorter values and to higher energies (figure 6). The dim-red glow seen during normal operation changes to a bright yellow. As the sensitivity of the video tube approximately matches the sensitivity of the human eye, the shift in wavelength is accompanied by a strong brightening of the hot spot. This is detectable, independent of the lateral resolution in the image.

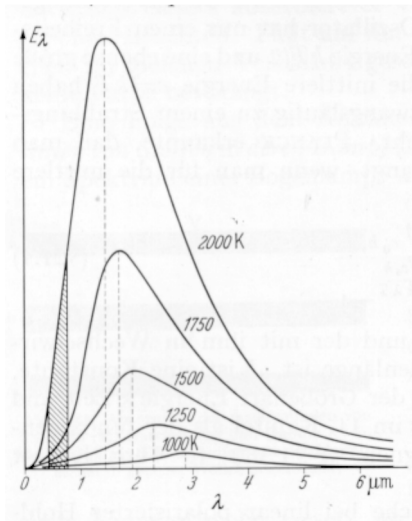


Figure 6:
Emission spectra and fraction of black-body radiation falling in the visible wavelength band (400 – 700 nm) for various temperatures

On the other hand, if a lateral resolution of the order of a few mm on the foil is possible, the displacement of the hottest spot can be detected directly and signal visibility is strongly improved. Non-scattered protons have an energy, which is slightly higher than that of those which are scattered. They hit the foil about 3 mm further away from the source than the “good” beam, i.e. they follow a larger radius of curvature as they are deflected upwards to the Megapie target [1,4].

Also with Target E firmly in place, it is still possible to tweak quadrupol magnets in such a way that the path and the distribution of the protons is altered. This would also give a different diameter and location of the hottest spot.

When an attempt was made to verify the possibility of finding beam parameters such that Target E is simply bypassed, the spot of maximum proton intensity moved sideways by 10 mm [4].

Camera

Only a few options exist for the choice of a suitable detector. The optimum solution would be to buy a ready-made radiation resistant video sensor, including full electronics and software. Several suitable commercial solutions are available on the market today.

Current baseline is a tube-based camera (Arcos 14c with a 2/3” Chalnicon video tube) which holds promise to survive the radiation environment for a sufficient time span. The sensitive electronics like frame grabber and control PC can sit nicely shielded behind a corner several meters away. The vacuum window on the catcher is made from special cerium-stabilized glass to tolerate high radiation doses.

With the sharp corner in its spectral response curve the camera tube acts like a spectrometer.

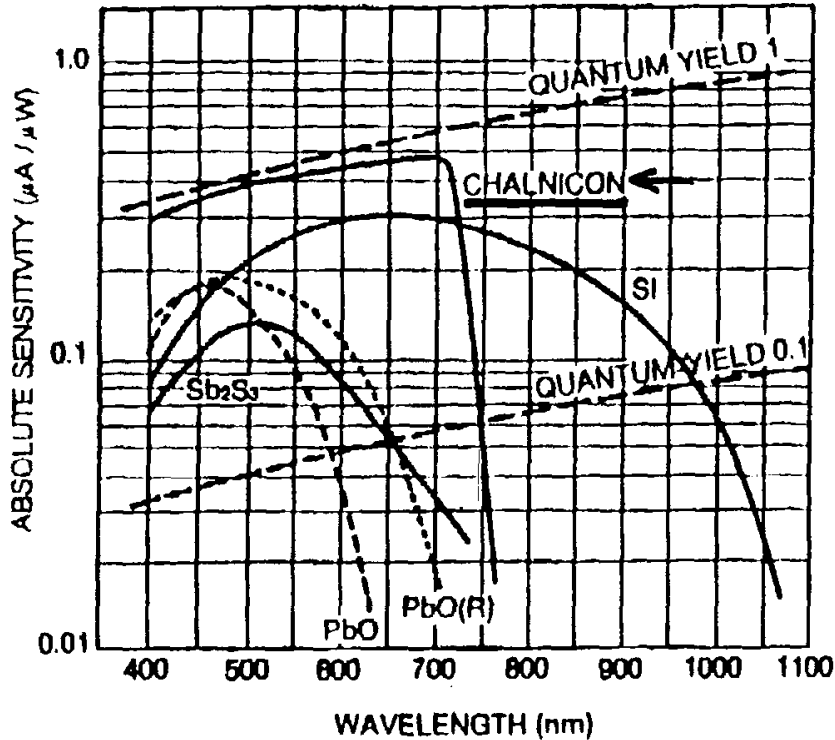


Figure 7: Spectral response curves for different camera tubes and silicon; it is planned to use a tube of the CHALNICON type in VIMOS

Control electronics and software

To generate the interlock signal fast and reliable enough it is not sufficient to work with the standard CCIR full frame rate of 25/s (50 half frames per second) as delivered by the camera. With a suitable frame grabber half frames will be sampled and processed for full images. Thus, the interlock signal can be generated based on a trend over several (up to 5) frames available in less than 100 ms. If the signal had to be generated based on only 2 or 3 images spaced 40 ms there would be a much higher danger for false alarms. Given the optical requirements and the achievable lateral resolution on the glowing mesh, the use of half frames does not limit the performance of the system.

For the image processing a well proven commercially available solution will be used running on a dedicated PC, which also houses the frame grabber [10,11].

Sensitivity

For a first rough estimate of the sensitivity of VIMOS, a simple axially symmetric numerical model was created. Equilibrium temperatures during normal operation have been calculated for eight concentric circular rings on a tungsten foil 100 μm thick (figure 8). For three cases, temperatures have been calculated for 100 ms after a change occurred: 10% and 30% bypassing Target E, and 100% of the beam unscattered (complete loss of Target E).

Table 1 shows temperatures after 100 ms in the center of the foil (radius 4mm) and in a ring between 13 and 18 mm radius (figure 8). For both areas the total thermally radiated power has been calculated as well as the spectral intensity that falls into the visible wavelength range (400-700 nm, square window).

As an example, for the signal of interest, the ratio has been calculated between the center and the ring, normalized to 1 for nominal operation conditions.

No detector noise or other imperfections in the signal processing have been incorporated. Given the present uncertainties, it is not possible yet to predict a reliable signal / noise estimate. There is considerable scattered light expected in the beam line, which will add as optical noise like stray light from mirror imperfections. Fortunately, this does not seem to pose a severe problem: already 10 % of unscattered proton beam leads to a rise in signal by a factor of almost two within 100ms, which should be rather easily detectable (figure 9, table 1).

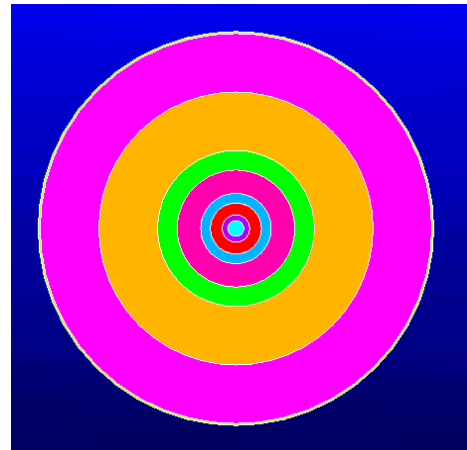


Figure 8: Simple radially symmetrical thermal model of the glowing foil, overall outer diameter 200 mm, "Signal" is derived from a comparison of the emitted visible power in the center with the power from the third ring (both light blue)

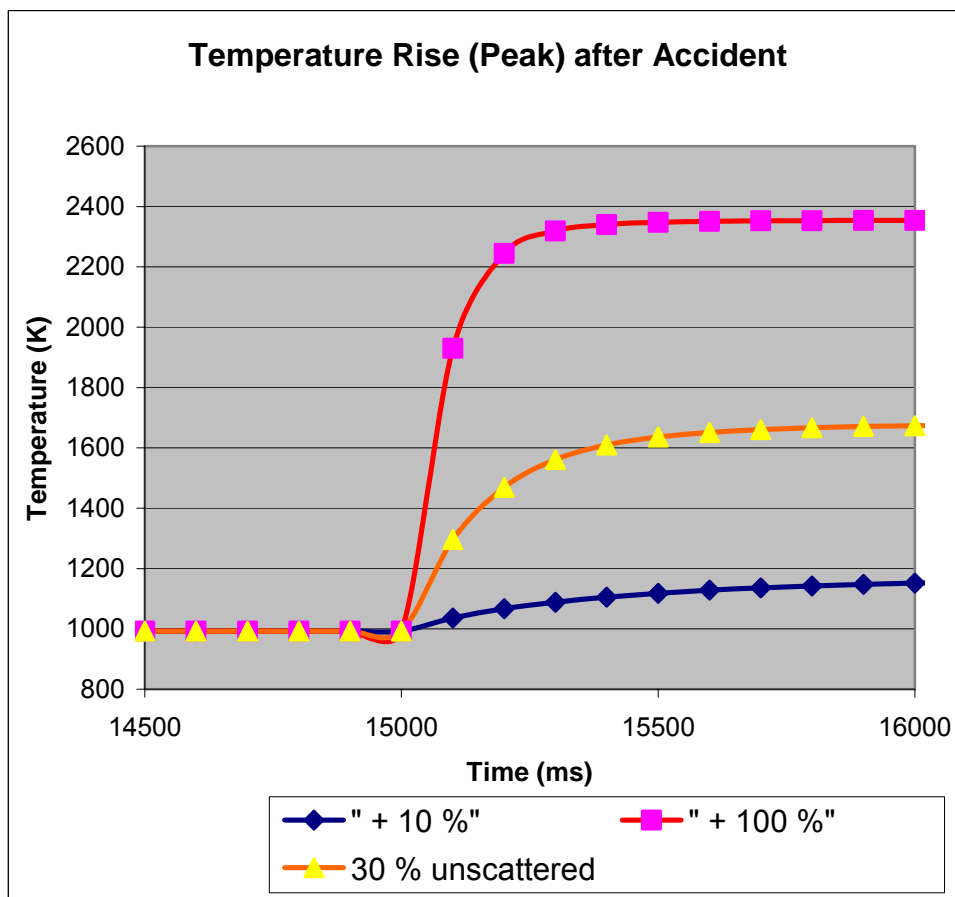


Figure 9: Rise of temperature in center of a 100 μm foil for different fractions of the beam bypassing Target E for a radially symmetrical model

Table 1: Temperatures and Signal after 100 ms starting from normal operation for a radially symmetrical model based on a 100 μm thick foil @ 400-700 nm sensor sensitivity; temperatures are given for the center ($r < 4 \text{ mm}$) and the rim ($13 \text{ mm} < r < 18 \text{ mm}$)

Case	$T_{c, \text{normal}} (^{\circ}\text{C})$	$T_{r, \text{normal}} (^{\circ}\text{C})$	$T_{c, 100\text{ms}} (^{\circ}\text{C})$	$T_{r, 100\text{ms}} (^{\circ}\text{C})$	Signal @ 100ms
normal	720	670	-	-	1
10%	-	-	765	685	1.9
30%	-	-	1020	680	70
100%	-	-	1660	700	24500

The values given in Table 1 are based on an emissivity of 0.8, which might be a little too high, but is not completely wrong given that the “foil” in fact consists of a mesh and is thus darker than a continuous sheet of metal. In fact, simulations show that the emissivity makes little difference in the glowing temperatures.

With the tube-based camera the operational set-point of the system will be moved to higher temperature values, i.e. 1000 $^{\circ}\text{C}$ instead of 700 $^{\circ}\text{C}$ (1000 K) under nominal conditions. This does not change the principle validity of the here presented modeling; with the tub-based camera the color discrimination approaches the sharp discrimination in the model (figure 7).

With a total visible area of 100 mm in diameter a “rim” much wider and much further out than the ring area between 13 and 18 mm radius taken for the first assessment can be used; this sharpens the transient in the case of “focusing”, offsetting the loss of sensitivity due to the higher baseline operation temperature of the mesh.

Taking advantage of the shift in the location of the hottest spot out of the center of the glowing foil to one or the other side, should allow to obtain a signal considerably higher than derived here with the radially symmetrical calculations. For this, the ratio has to be taken between well-specified locations where an increase and a decrease are expected in case of an anomaly, respectively. This means, that the signal has to be calculated taking into account the emitted intensity from an area including patches 3 to 10 mm off-center and from an outer area on the opposite side with respect to the center.

Reliability

VIMOS does not include any moving parts and should thus feature a very high intrinsic reliability. The most delicate and also stressed part in the radiation environment is the video camera with its attached front-end electronics. For the chosen type (Arcos 14c) there exists a good record of many units running for years without problems in nuclear installations. Test reports addressing the radiation resistance of the camera as well as concerning performance under heavy mechanical / vibrational loads are available [8, 9].

The proper functioning of the system can be verified in-situ and online during normal operation. The presence of the mesh can be verified from a steady glow during normal operation. Each beam trip offers the possibility to observe the increase in temperature as the beam returns. This also allows for repeated calibration, which is useful as the sensitivity as well as the signal / noise ratio in the detector might change with time due to radiation damage.

Expecting that also the electronic signal processing chain can be made very reliable by using well-proven commercial products, VIMOS should not cause false alarms, while reliably detecting true relevant changes in the incident beam profile.

Only a local proton intensity that is potentially harmful to the Megapie target can make the glowing foil light up sufficiently to generate an interlock signal. Improper beam paths with a reduced total current, e.g. during set up, can thus not trigger the system.

Experimental Results

During the summer and the autumn of 2002 a full-scale geometrical set-up has been installed at PSI where the achievable image quality could be measured and compared to ray-tracing simulations.

The following optical characteristics were determined for VIMOS:

1. observable area on the mesh 100 x 110 mm
2. resolution in the order of 1 mm
3. depth of field +/- 50 mm at the foil and +/- 1 mm at the camera

In a quiet corridor in a basement the beam line was simulated by means of sewage tubes with the collimator built from Styrofoam (figure 10). This installation is still available and will be used also in the future to further develop and test VIMOS components.

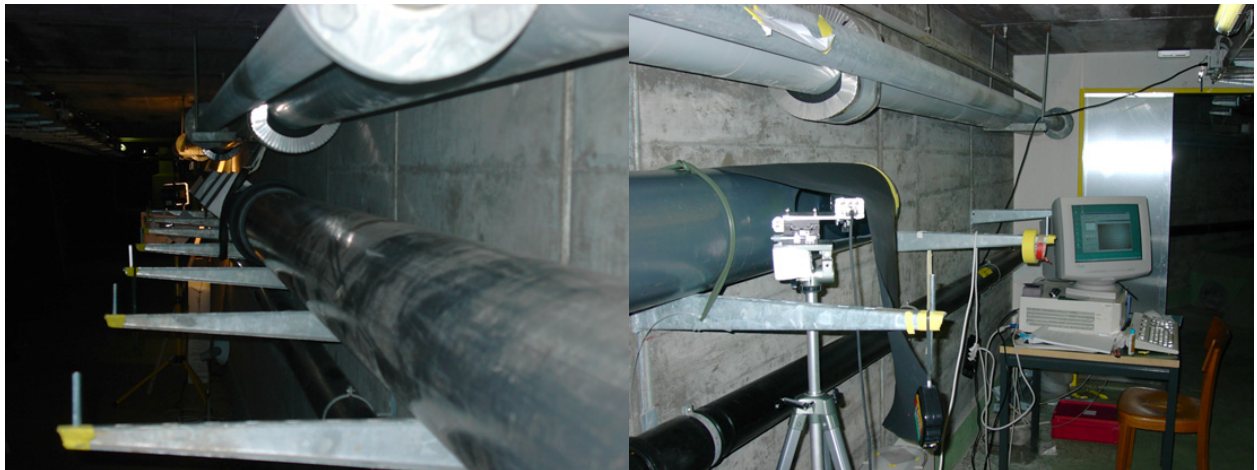


Figure 10: Full-scale mock-up of the vertical beam line beneath the Megapie target

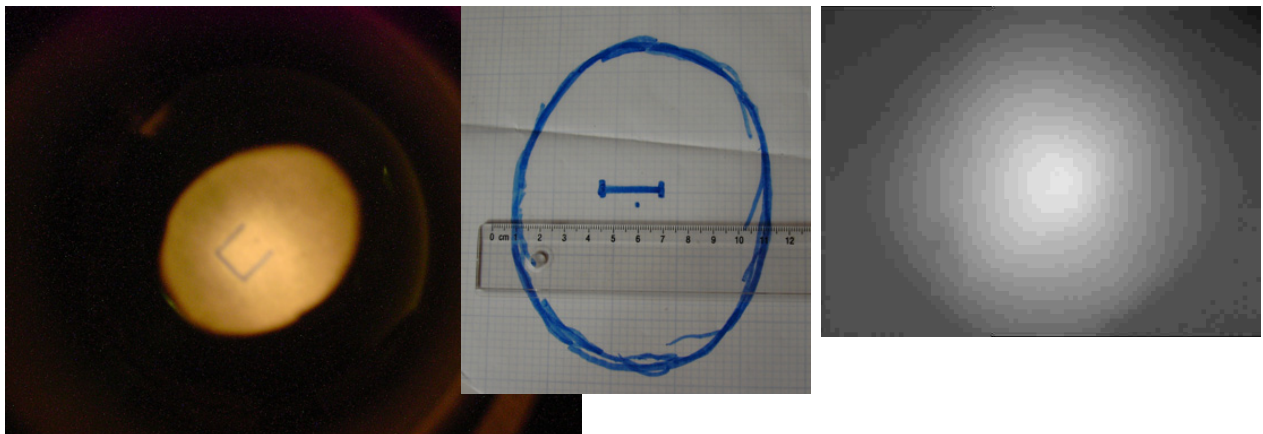


Figure 11: Foot print of the visible area on the glowing mesh (diffuse light source at camera focus), the side length of the open square is 1" (left) Sensitivity distribution over the mesh, coded in a gray scale (right)

The sensitivity is not uniform over the visible elliptical area on the glim foil of approximately 100 x 110 mm because of the peculiar optical conditions where only light from the very center of the foil is collected by a large central area of the mirror (figures 11, 12). Points further out are only seen with smaller collecting portions towards the rim of the mirror.

During a first series of experiments a silicon CCD camera was used. For a second campaign an old and heavily irradiated Arcos 14c camera could be obtained on loan from the manufacturer. The use of the right camera with a Chalnicon video tube was essential for the tests with a simulated glowing mesh.

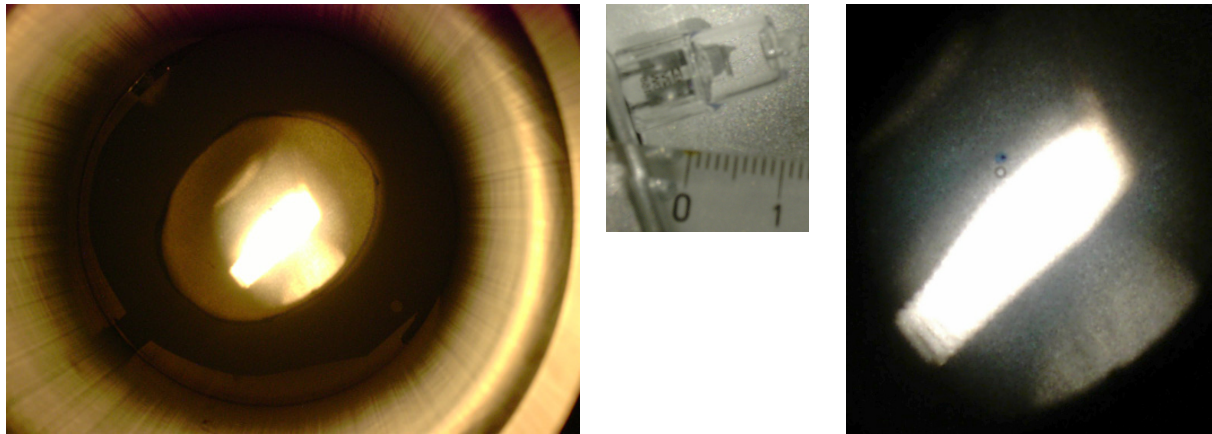


Figure 12: Reversed optical path, a small lamp at the position of the VIMOS camera is focused by the collecting mirror onto a screen in place of the glowing foil, single windings of the lamp's filament are discernable

In good (front illuminated) lighting conditions, which give high contrast, single threads in a mosquito netting with a mesh size of approximately 1 x 1.2 mm can be seen over almost the whole area with a CCD camera (figure 13).

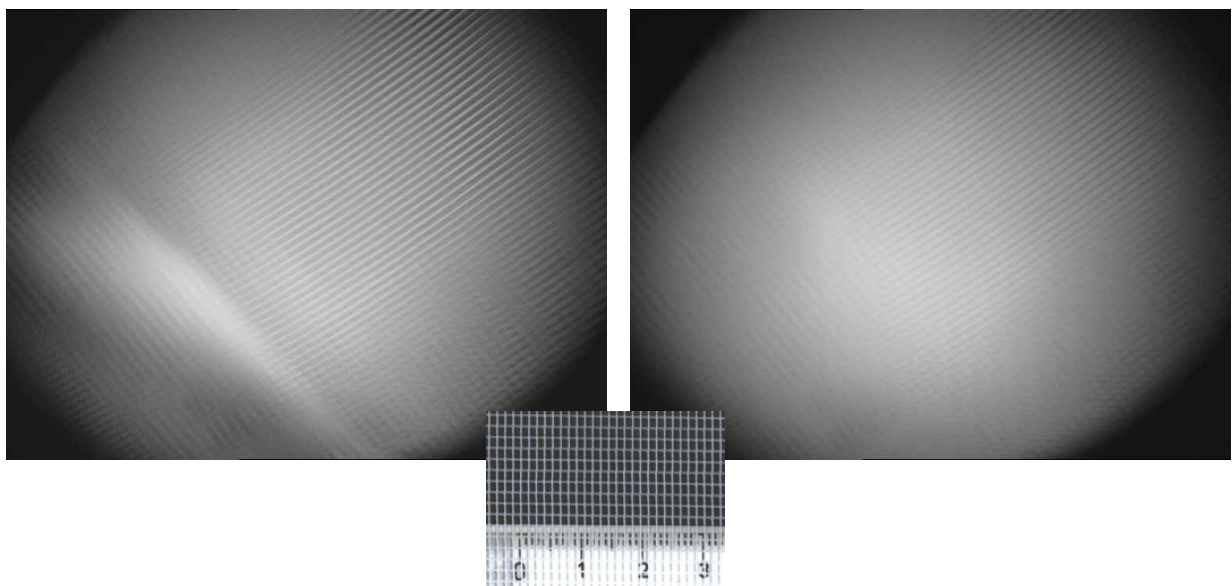


Figure 13: Mosquito netting in front illumination (*left*) and in backlit condition (*right*)

A comparison of the point spread calculated with OSLO with actual measurements show that in addition to the large scale image distortions deriving from the overall optical set-up there are some imperfections in the mirror causing blur. This is no problem, it deteriorates the obtainable image of the foil to an acceptable degree only (figures 14 - 16).

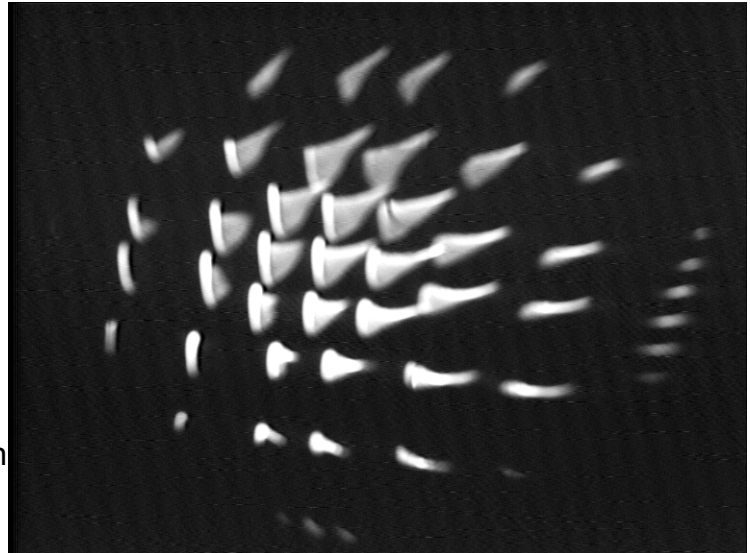


Figure 14: Backlit through-holes in

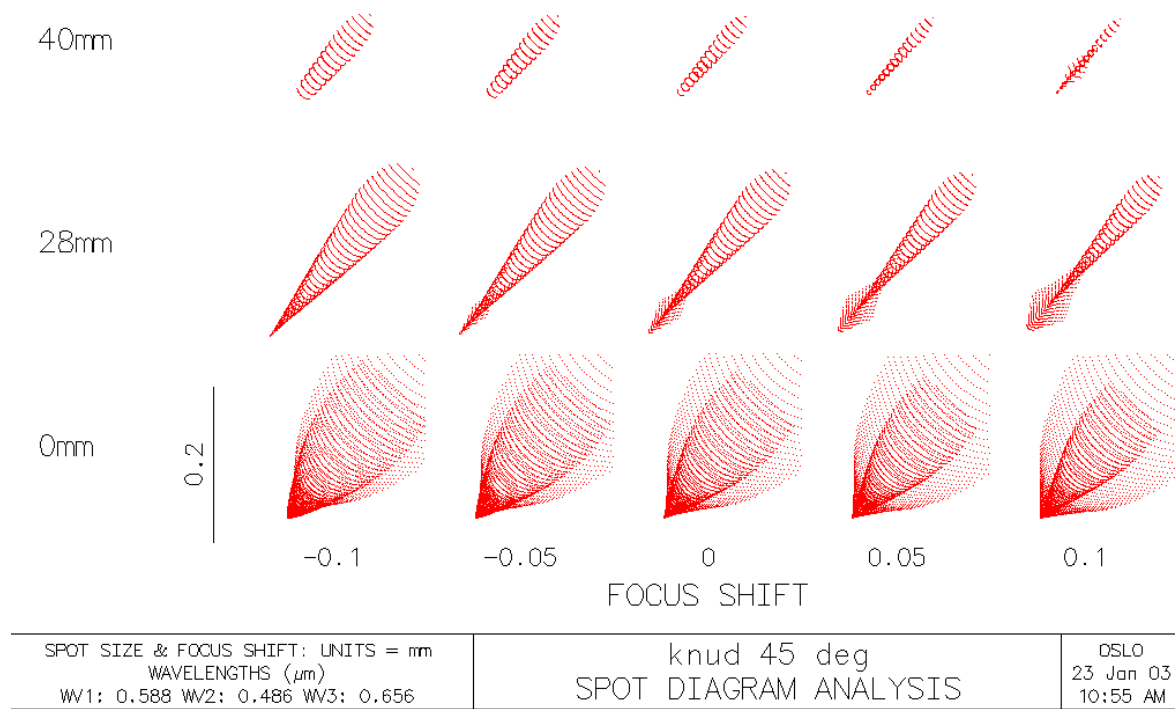


Figure 15: Calculated images (point spread with OSLO) of a point source for different distances from the foil center and for various focal offsets (from nominal position) for the parabolic reflector, the 45° tilt is caused by the orientation of the catcher with respect to the collimator

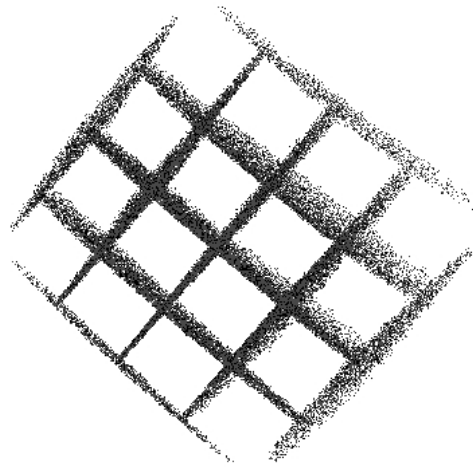
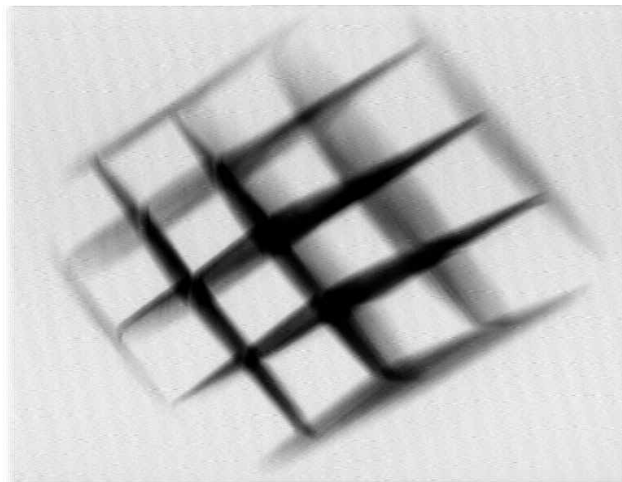


Figure 16: Satisfactory overall matching between a measured (with Arcos 14c) (*left*) and calculated (*right*) image of a grid 80 x 80 mm with 2 mm wide slats; cardboard target used in the above measurement with front illumination (*far right*)

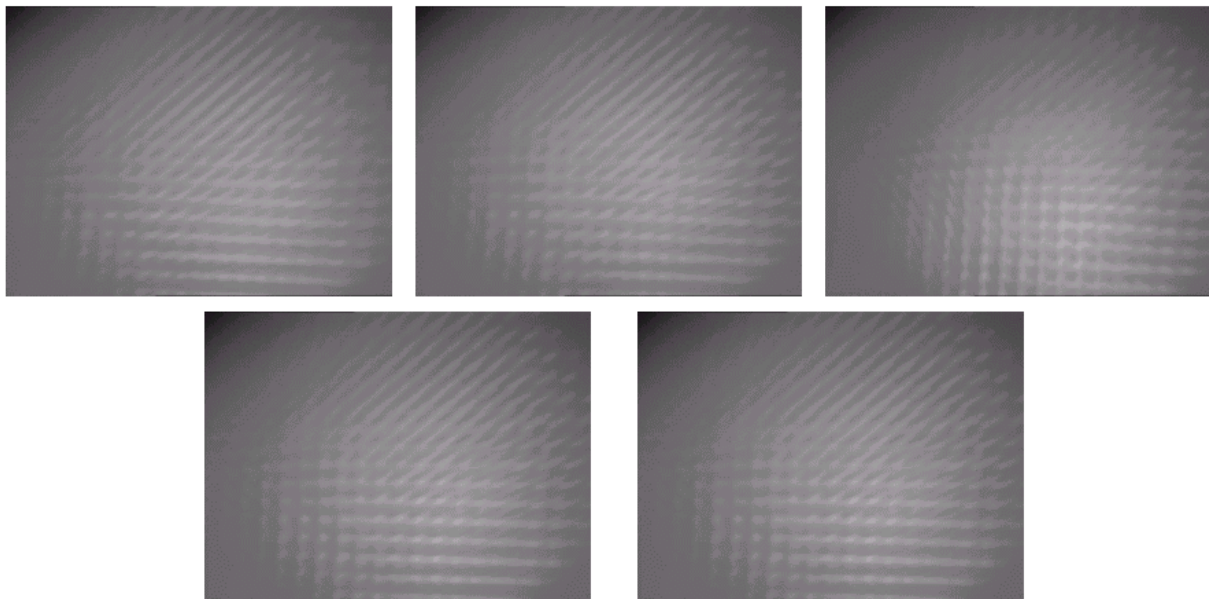
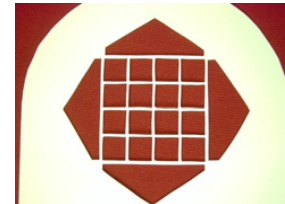


Figure 17: Depth of field, the image at the center in the top row was obtained in the focus position, the images left and right correspond to a shift in the position of the target (glowing foil simulated by a low-contrast pin hole array) by + / - 50 mm, the images in the bottom row were taken with a displacement of the camera by + / - 1mm; no dramatic differences are seen

During the second test campaign with a heavily used Arcos 14c it was verified that the sharp drop in spectral sensitivity of the Chalnicon camera tube makes it

necessary to adjust the thickness of the glowing mesh for a temperature of approximately 1000 °C during nominal irradiation conditions (figure 18).

Figure 18:
With an Arcos 14c camera the weakest detectable glowing of a small lamp was found to occur at 1000 +/- 20 °C

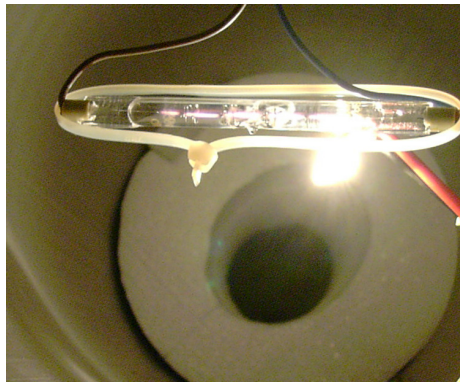
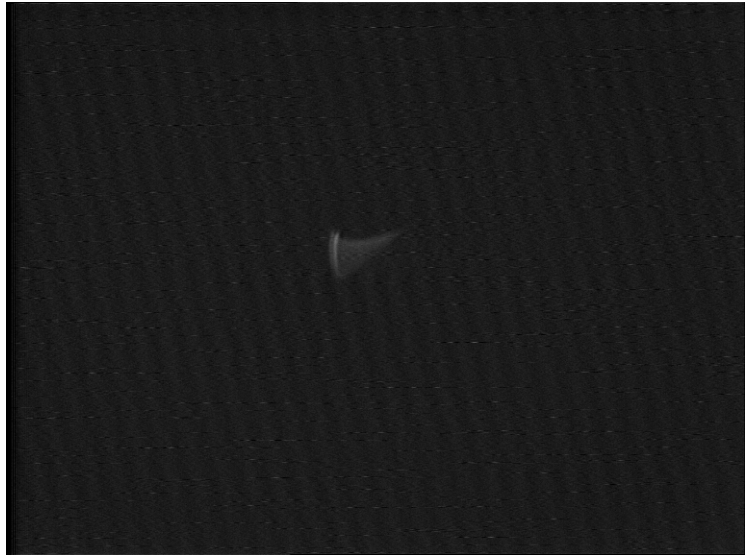


Figure 19: Set-up for simulation of hot spot with a long and a small lamp as seen from the position of the LM-target (*left*), processed image (two thresholds set) taken with the Arcos 14c (*right*)

Work on the selection of a suitable frame grabber and associated image analysis software is in progress. First discussions with potential suppliers show that there should be no problem to find the necessary components. Histogramming tools for example need only about 5 ms to process a full 768 x 576 pixel CCIR frame. A high-end frame grabber will be used to sample and process individual half frames, yielding effectively 50 frames / second. A decision can be based on the trend in the "signal" over several successive frames [10].

With the simple set-up consisting of two lamps many static snapshots have been taken, these are used now for testing the capabilities with divers software packages (figures 19 - 23).

Examples of readily available functions in standard image evaluation software packages include the setting of thresholds (figure 19), differences (figure 20) between or multiplications of frames, histogramming (figure 21) and many more.



Figure 20: “Subtraction with overflow” of image 1 (“Tv52”) @ 1200 °C / 1550 °C and image 2 (“Tv53”) @ 1250 °C / 2250 °C

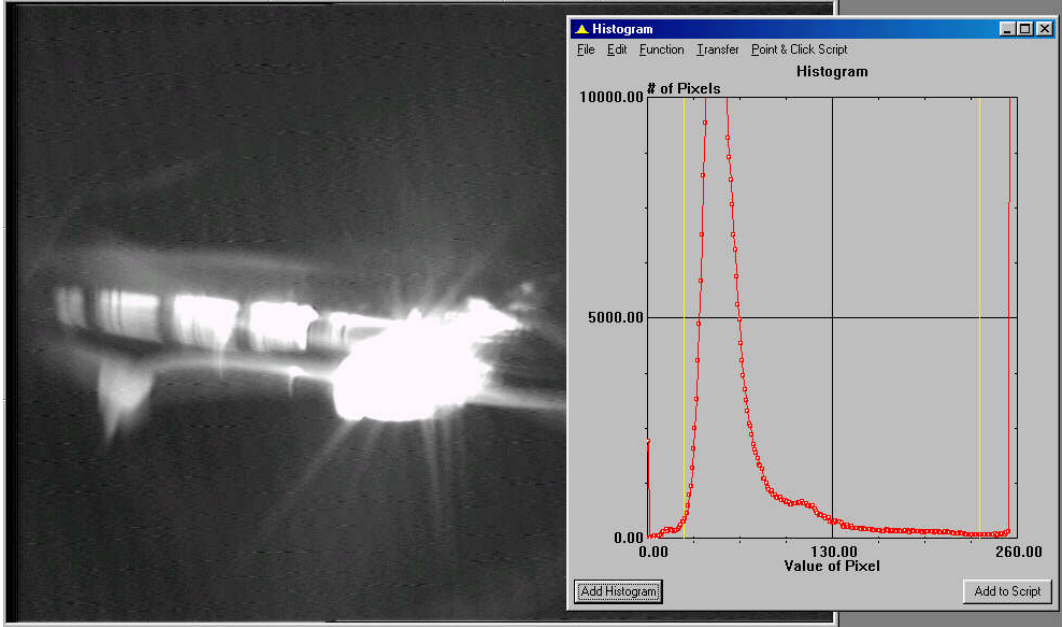
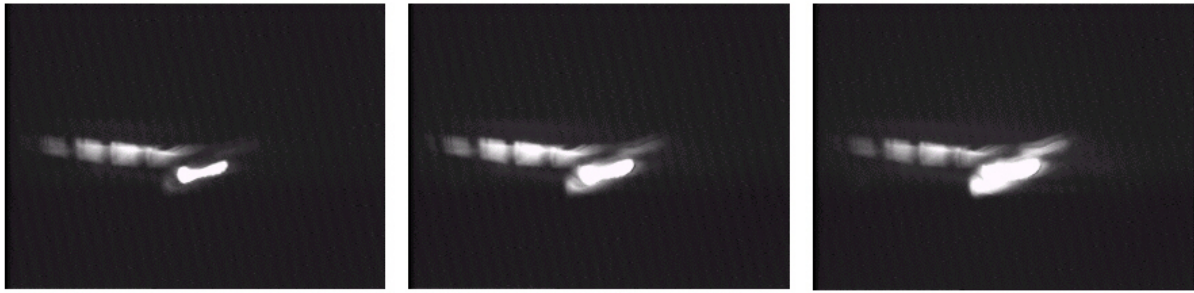
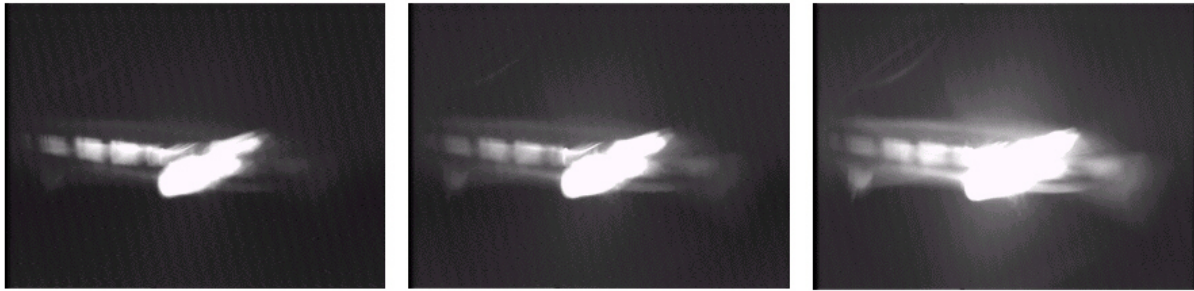


Figure 21: Histogram of image 2 above @ 1250 °C / 2250 °C



Tv34, $T_{\text{small}} = 1150 \text{ }^{\circ}\text{C}$ Tv35, $T_{\text{small}} = 1300 \text{ }^{\circ}\text{C}$ Tv36, $T_{\text{small}} = 1450 \text{ }^{\circ}\text{C}$



Tv37, $T_{\text{small}} = 1650 \text{ }^{\circ}\text{C}$ Tv38, $T_{\text{small}} = 1850 \text{ }^{\circ}\text{C}$ Tv39, $T_{\text{small}} = 2150 \text{ }^{\circ}\text{C}$

Temperature of large (long) lamp = 1100 °C

Figure 22: Series with different temperatures for small lamp and fixed temperature for large lamp; in this geometry with the small lamp in front of the large one (figure 21) light from the small lamp is reflected from the large lamp and its support deteriorating the contrast considerably (figure 28), this is taken as a worst case simulation of the real conditions

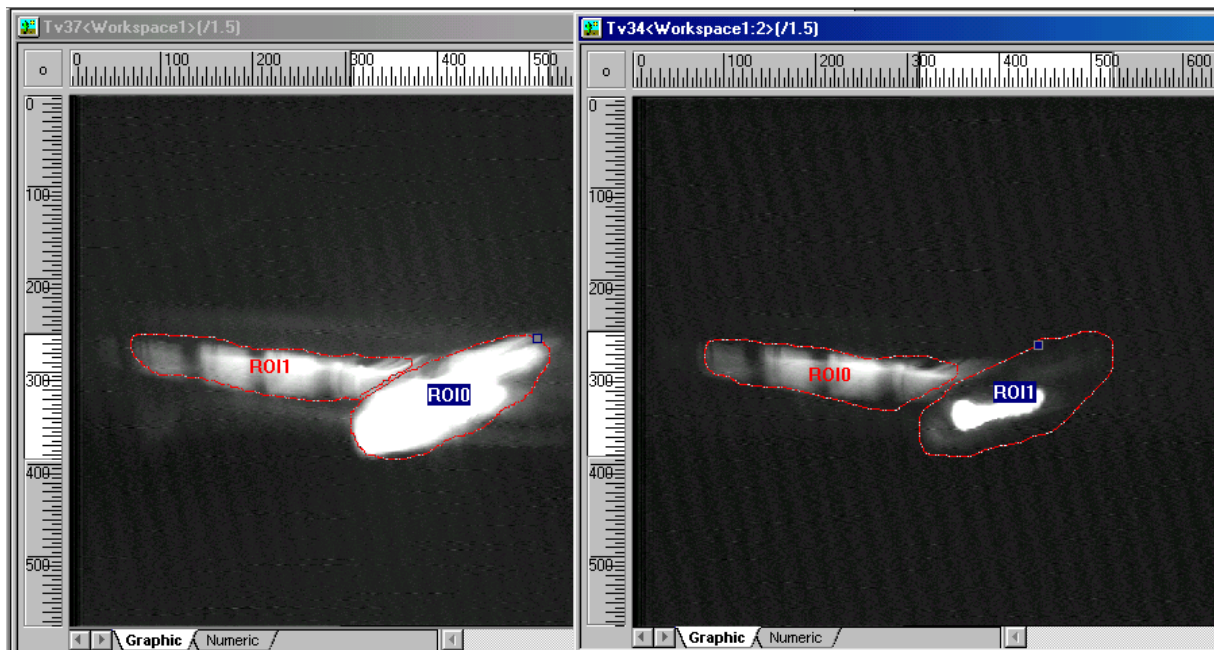


Figure 23: Regions of interest (ROI) can be defined in each software package

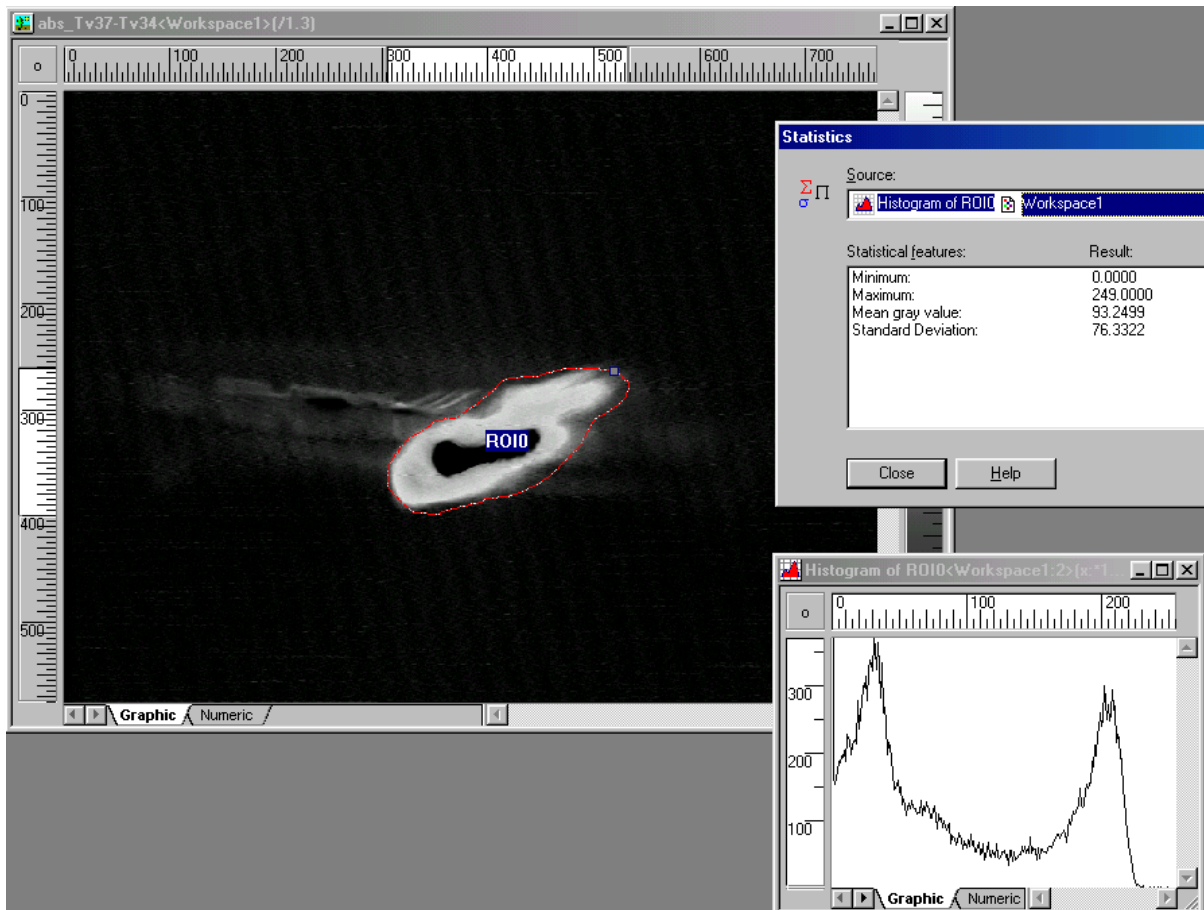
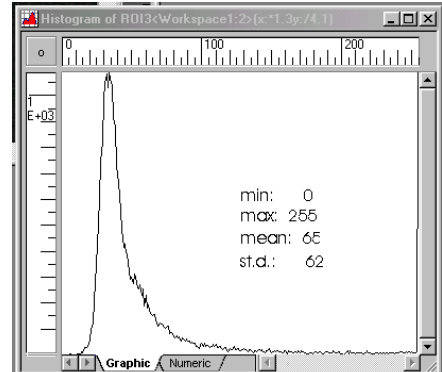


Figure 24: Region of interest (ROI) around the small lamp in a difference “abs(Tv37-Tv34)” (top); in this mode ImpactS- histograms are calculated for rectangular selections with pixels of the complement set to zero
Same ROI in reference Tv34 (right)



As of February 2003 ImactS, data analysis software by the German company Matrix Vision (Impuls-imaging) is the favorite choice. Evaluations are still ongoing [10,11]. A general problem with the camera on loan was related to the automatic gain control, which could not be switched off; this resulted in overflowing pixels and brightness changing uncontrollable between exposures. The camera to be used in VIMOS will have a (high) fixed gain; possibly saturating baseline signals will be attenuated optically by means of filters.

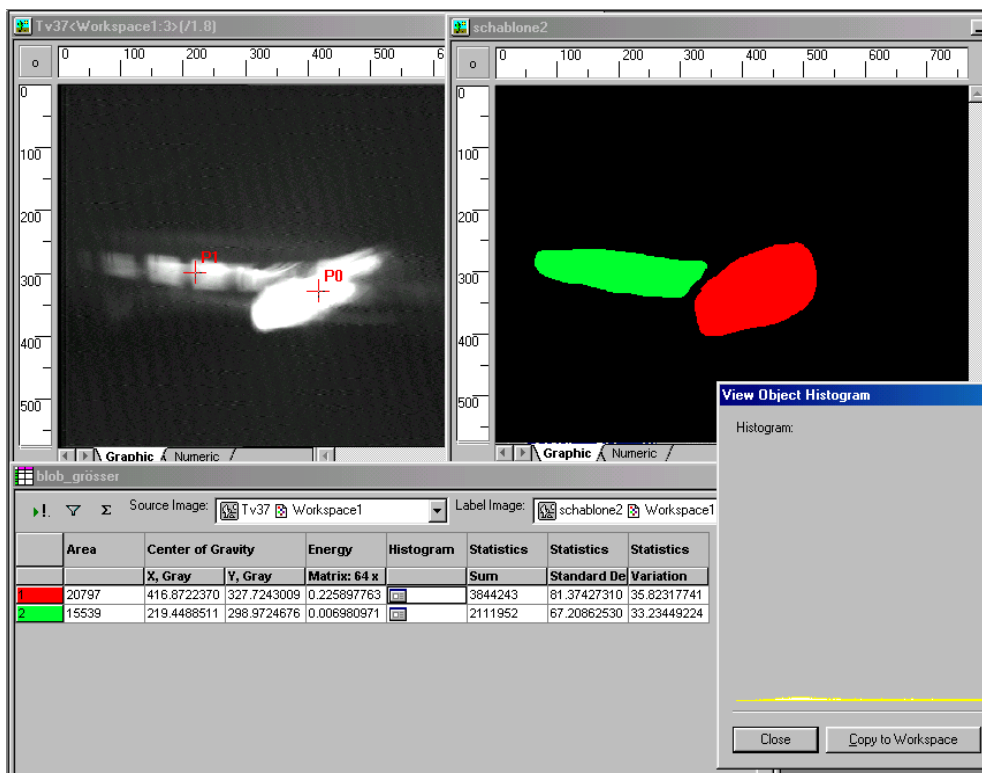
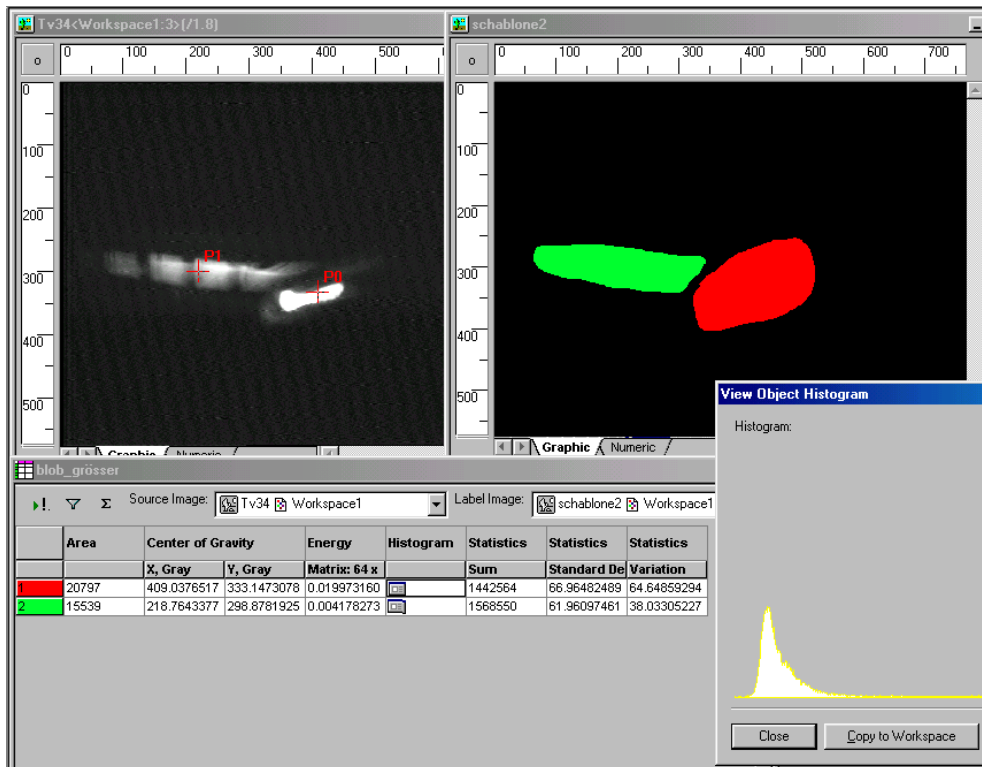


Figure 25: “blob-analysis” comparing Tv34 with Tv37, both processed with a mask with two blobs; the most significant differences are observed in the integrated intensities of blob1 (red) and the corresponding histograms

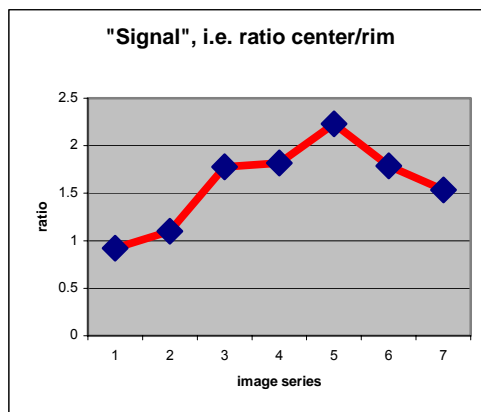
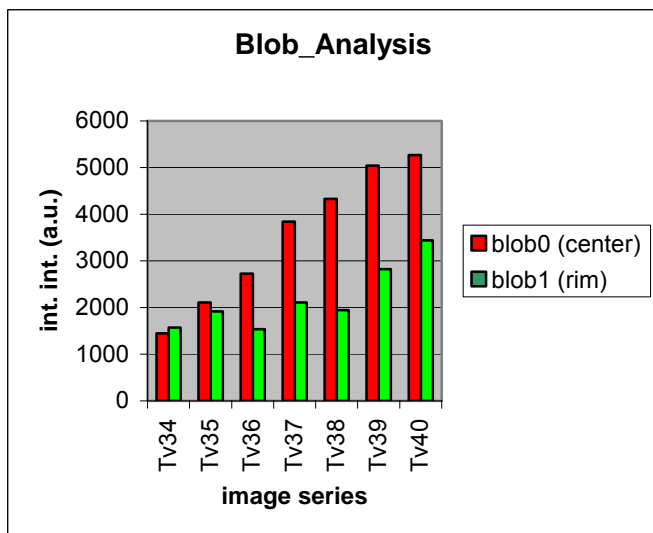


Figure 26: Blob analysis for image series Tv34 ... Tv40

The “signal” for a test series of images as plotted in figure 26 suffers clearly from a very reduced contrast between “center” and “rim”. This is attributed to light from the small lamp being backscattered via the large lamp and to early saturation of the camera for the center area. Any criterion like a given number of successive frames with a ratio center/rim > threshold would switch off the proton beam.

Installation

It is intended to install VIMOS as soon as possible, in any case well before the Megapie target is inserted into SINQ. VIMOS does not interfere with the target itself and can also be used with the existing solid target. Thus it should be possible to obtain some experience and verify the performance of the optical monitor before its application for Megapie is really needed. Only then the final data evaluation procedures will be developed and fine tuned.

Manufacturing and procurement of VIMOS hardware is planned for spring 2003. During the summer of 2003 a new extended and very realistic test shall be performed using as much as possible the real hard- and software in the mock-up facility in the basement.

Acknowledgements:

The following persons provided valuable contributions and support to the work on VIMOS sofar:

M. Djiango, M. Dubs, T. Dury, R. Dölling, Y. Foucher, G. Frei, R. Fütterer, G. Heidenreich, E. Lehmann, the late L. Ni, Ch. Perret, M. Reder, U. Rohrer, B. Smith, A. Strinning, E. Wagner, and H. Walther.

References

- [1] U. Rohrer, 3 papers autumn 2001:
- [2] "p-Strahlbreiten und Profil-Formen beim SINQ-Target mit und ohne Target E (4cm Graphit)", 31. Oktober 2001
- [3] "p-Strahlbreiten und Profil-Formen beim SINQ-Target mit und ohne Target E (6cm Graphit)", 13. November 2001
- [4] "Nachtrag zu p-Strahlbreiten und Profil-Formen beim SINQ-Target mit und ohne Target E (4cm oder 6cm Graphit)", 22. November 2001
- [5] T. Dury, "Best-estimate Fit for Megapie Heat Deposition Profiles", 6 September 2002
- [6] T. Dury, "CFD Calculations in Support of Safety Issues of the Megapie Lower Liquid-Metal Container", MEGAPIE Technical Review Meeting, Bologna, 5-6 March 2002
- [7] U. Rohrer, "A novel method to improve the safety of the planned MEGAPIE target at SINQ", PSI Scientific and Technical Report 2001, Volume VI, pages 34-35
- [8] K. Thomsen, "Visual Monitor VIMOS", MEGAPIE Technical Review Meeting, Bologna, 5-6 March 2002
- [9] E. Wagner, private communication February 2002, refined after long-term measurements in February 2003
- [10] T. Dury, "Heat Distribution in the VIMOS Foil", MEGAPIE Technical Review Meeting, Bologna, 5-6 March 2002
- [11] Prüfbericht zur Strahlungsprüfung, Arcos 14c, Strahlungszentrum der Universität Gießen, 13. 11. 1998
- [12] Prüfbericht MHM-EST-7.980186684, Schwing- und Schockprüfungen, Arcos 14c, TÜV Mannheim, 5. 11. 1998
- [13] <http://www.matrix-vision.de/>, frame grabber Mvtitan-G1, software ImpactS
- [14] <http://www.impuls-imaging.com/>, developer of ImpactS ("Vision")

Annex A, OSLO input listing:

// OSLO 6.1 21577	AIR	DRW ON
61482 57467	TH 650.0	CBK 1
LEN NEW "knud 45	APN 1	WV 0.58756 0.48613
deg" -620 9	AY1 A -18.0	0.65627
NAO 0.0098	AY2 A 18.0	WW 1.0 1.0 1.0
OBH 40.0	AX1 A -29.6	END 9
DES "OSLO"	AX2 A 29.6	DLID 400.0
UNI 1.0	ATP A 1	DLRS 3
// SRF 0	AAC A 4	DLNR 0 11
AIR	DRW ON	DLNR 1 11
TH 400.0	NXT // SRF 5	DLFP 1 -1.0
AP 40.0	AIR	DLMN 1 -1.0
DRW ON	TH 300.0	DLMX 1 1.0
NXT // SRF 1	APN 1	DLNR 2 11
AIR	AY1 A -27.2	DLAS On
TH 300.0	AY2 A 27.2	SDAD 97.1
APN 1	AX1 A -18.0	OPDF 1.0e-08
AY1 A -53.8	AX2 A 18.0	OPOC "opcb_abs"
AY2 A 53.8	ATP A 1	VAR NEW
AX1 A -44.0	AAC A 4	V 1 9 0 TH 0.0 0.0 1.0
AX2 A 44.0	DRW ON	0.0003920188252
ATP A 1	NXT // SRF 6	END
AAC A 4	AIR	OPE NEW
DRW ON	TH 7500.0	O 1 "OCM1" 1.0 "PY"
NXT // SRF 2	APN 1	O 2 "OCM2" 1.0 "PU"
AIR	AY1 A -35.0	O 3 "OCM3" 1.0 "PYC"
TH	AY2 A 35.0	O 4 "OCM4" 1.0 "PUC"
1125.5999999999999	AX1 A -18.0	O 5 "OCM5" 1.0 "PAC"
APN 1	AX2 A 18.0	O 6 "OCM6" 1.0 "PLC"
AY1 A -45.7	ATP A 1	O 7 "OCM7" 1.0 "SAC"
AY2 A 45.7	AAC A 4	O 8 "OCM8" 1.0 "SLC"
AX1 A -39.0	NXT // SRF 7	O 9 "OCM9" 1.0 "SA3"
AX2 A 39.0	AIR	O 10 "OCM10" 1.0 "CMA3"
ATP A 1	AST	O 11 "OCM11" 1.0 "AST3"
AAC A 4	NXT // SRF 8	O 12 "OCM12" 1.0 "PTZ3"
DRW ON	RFH	O 13 "OCM13" 1.0 "DIS3"
NXT // SRF 3	RD -1240.0	O 14 "OCM14" 1.0 "SA5"
AIR	TH	O 15 "OCM15" 1.0 "CMA5"
TH 300.0	658.6114347703805	O 16 "OCM16" 1.0 "AST5"
APN 1	CC -1.0	O 17 "OCM17" 1.0 "PTZ5"
AY1 A -25.0	DT 1	O 18 "OCM18" 1.0 "DIS5"
AY2 A 25.0	DCY -260.624	O 19 "OCM19" 1.0 "SA7"
AX1 A -35.0	TLC 45.0	O 20 "OCM20" 1.0
AX2 A 35.0	NXT // SRF 9	"TOTAL_SPH"
ATP A 1	AIR	O 21 "OCM21" 1.0 "EFL"
AAC A 4	TH -7.3644199466	END
DRW ON	AP 50.0	
NXT // SRF 4	DT 1	
	TLA 30.86	

SESSION 3: THERMAL HYDRAULICS & SM

RELAP5 ANALYSIS OF THE MEGAPIE TARGET

W.H. Leung¹, M. Petrazzinni², A. Alemberti²

¹Paul Scherrer Institute, Spallation Neutron Source, CH 5232, Villigen-PSI, Switzerland

²Ansaldo Nucleare, Divisione di ANSALDO ENERGIA S.p.A., Genova, Italy

ABSTRACT

The MEGAPIE liquid metal target is a multi-loop, multi-fluid system. A RELAP5 model been built for analyzing this thermal hydraulic system. The three main loops of the target system are i) primary LBE loop (target) ii) intermediate Diphyl-THT cooling loop and (ICL) iii) secondary water loop (SWL). Thermal physical properties of LBE and Diphyl-THT have been modeled and input to RELAP5 through external files. Computational experiments have been conducted for assessing the system behaviors both in steady state and transient conditions. In nominal operation, 620 kW thermal powers are deposited on the target by a proton beam and must be removed from the system. Lower power heating is used in the non-irradiation test, in which the proton beam is simulated by an electric heater. A simple scaling rationale by the buoyancy is examined in this study. For the steady state study, the focus is on the operation conditions at different levels of heating. The parameters such as the mass flow rates, inlet and outlet temperatures of the heat exchangers, and the buoyancy head in the target are calculated to examine whether the operating conditions are scaled appropriately. For transient study, proton beam trip¹ is studied, and the initial conditions are set for the nominal and 200kW. The essential thermal hydraulics and control characteristics are presented in this report.

INTRODUCTION

RELAP5 is a thermal hydraulic code developed for analyzing the lost of coolant accident (LOCA) in a large light water reactor (LWR) system [1]. The conservation equations are based on the two-fluid model. It is a general-purpose code for both single and two-phase flows, and the primary working fluids are water and steam. On the other hand, the MEGAPIE target is a 3-loop, 3-fluid system:

- Primary LBE loop, where the LBE serves as the target material and well as the coolant,
- Intermediate cooling loop (ICL) with Diphyl-THT coolant,
- Secondary water loop (SWL) with water as coolant,

The loops are thermally connected by Heat EXchangers (HEXs). The three main HEXs are the **T**arget **H**eat **e**Xchanger (THX) (or cooling pins) where heat is taken out from LBE, the **I**ntermediate **H**eat **e**Xhanger (IHX) where heat is taken out from the Diphyl coolant, and **S**econdary **H**eat **e**Xchanger (SHX) where the heat is taken out from the cooling water to the building cooling plant.

For modeling the MEGAPIE target by the RELAP5 code, it is necessary to supply the thermal physical properties of LBE and Diphyl-THT to the code through external files. The properties of LBE are modeled from the data given in the Lawrence Livermore Report [2]. Diphyl-THT properties can be obtained directly from the manufacture--Bayer. Those two property files for RELAP5 have been created by Ansaldo ([3] and [4]). The details can be found in those reports and not to repeat here.

¹ Beam trip is actually called "BEAM INTERRUPT" in the SINQ operation.

MODELLING THE TARGET SYSTEM

The target multi-loop system is modeled by the RELAP5 code. The model basically consists of hydraulic channels, which are linked by junctions. The sketches of the main LBE loop and the ICL are presented in Figs 1 and 2. The primary LBE loop actually consists of a main loop and a bypass branch. The bypass branch is not of much interest for the system analysis, but it is very important for the local cooling of the beam window. The water loop, SWL, is left out in this model, and is represented simply by the inlet and outlet of the secondary side of the IHX. The hydraulic channels of the loops are specified by the flow area (A), length (L), hydraulic diameter (D_H), type (i.e. pipe, annulus, etc.), and elevation difference between inlet and outlet. The definition of some target and ICL channels are presented in Tables 1 and 2, respectively. Note that specifications of all junctions, valves and the expansion tank of ICL are left out of the tables, but they are included in the model. The pipe walls and structure materials participate in a thermal transient and must be modeled. In Figs. 1 and 2, the darkened strips sit next to the hydraulic channels represent the thermal mass of the structures. Nearly all the channels are made of stainless steel. The electromagnetic pump is modeled as a composite of inductor wire, insulation, laminated magnetic steel jaws, and the steel housing. The other exception is the T-91 lower liquid metal-container, but it differs only a little from the normal steel. More details of the thermal structures can be found in the Ansaldo report [5].

RELAP5 code facilitates the pump model, which is defined by its characteristic pump curve, through the input deck. The mechanism of an electromagnetic pump (EMP) is quite different from a centrifugal pump, but it is simply modeled in a similar way. The pump curve of the main EMP is presented in Fig. 3 and similar ones for the bypass EMP and oil pump.

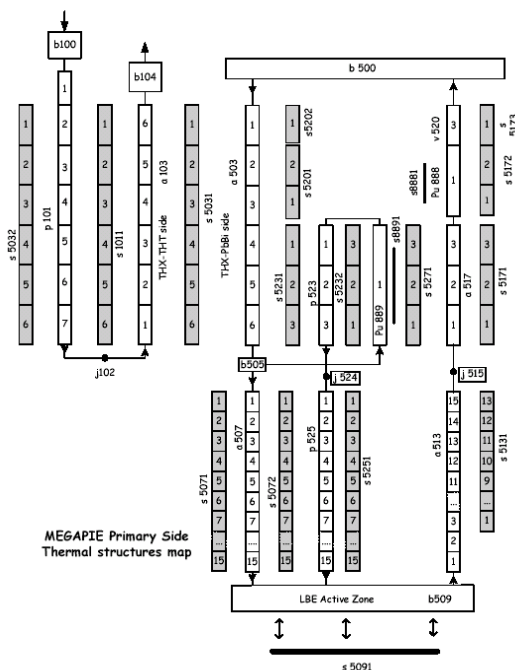


Figure 1: The main and by pass LBE loops of the MEGAPIE Target

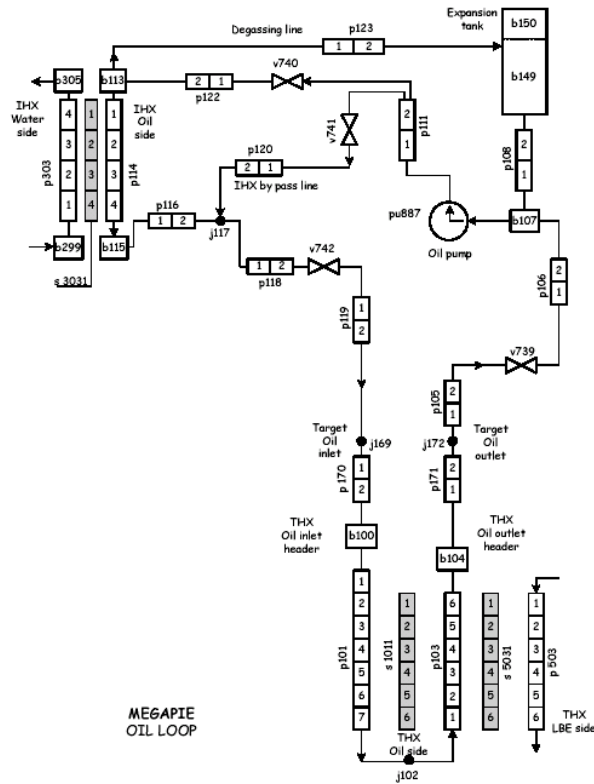


Figure 2.2-1

Figure 2: The Intermediate Cooling Loop (ICL) of the HRS

Table 1. Channels of the Target

Component	Number.	Channel	Flow (m ²)	Area	Length (m)
Expansion Tank	500		6.9e-2		0.1
Heat Exchanger	503	Annulus (×12)	8.74176e-03		1.212
Middle Flange	505	Convergent annulus	8.742e-03		0
Downcomer	507	Annulus	1.205e-2		2.295
Beam Window	509	Hemispherical	1.2050e-2		0
Riser	513	Round Tube Annulus Annulus	1.168e-2 1.119e-2 9.043e-3		0.244 0.388 0.960
Reser Junction	515	Convergent annulus			0
Main Pump Inlet	517	Annulus	5.1496e-3		.606
Main EMP	888	Annulus	5.0397e-3		.404
Main Pump Outlet	520	Annulus	5.039e-3		.202
Bypass Pump Inlet	527	Small tube	1.8369e-3 2.1980e-3		.202 .606
Bypass EMP	889	Annulus	2.1980e-3		.606
Bypass Outlet	523	Convergent	6.0e-4		.606
Bypass Junction	524	Junction	--		--
Bypass Guide	525	Tube	4.150e-4		2.295

Table 2 The Channels of the Intermediate Cooling Loop (ICL) with Diphyl THT

Components	Number	Channel	A, m ²	L, m	D _H , m
THX inner	101	Tube	0.254e-3	1.414	0.018
THX outer	103	Annulus	0.308e-3	1.252	0.004
Inlet pipe	105	Pipe	3.318e-3	4.682	0.065
Pump inlet	107	Pipe	3.318e-3	1.662	0.065
Pump	887	--	3.318e-3	1	0.065
Pump outlet	111	Pipe	3.421e-3	1.622	0.066
IHX inlet	122	Pipe	3.318e-3	0.796	0.065
IHX pipe*	114	Small tubes	9.375e-3	0.792	2.42e-3
IHX outlet	116	Pipe	3.318e-3	5.574	0.065
Bypass line	120	Pipe	3.318e-3	1.600	0.065
Outlet Pipe	118	Pipe	3.418e-3	2.27	0.065

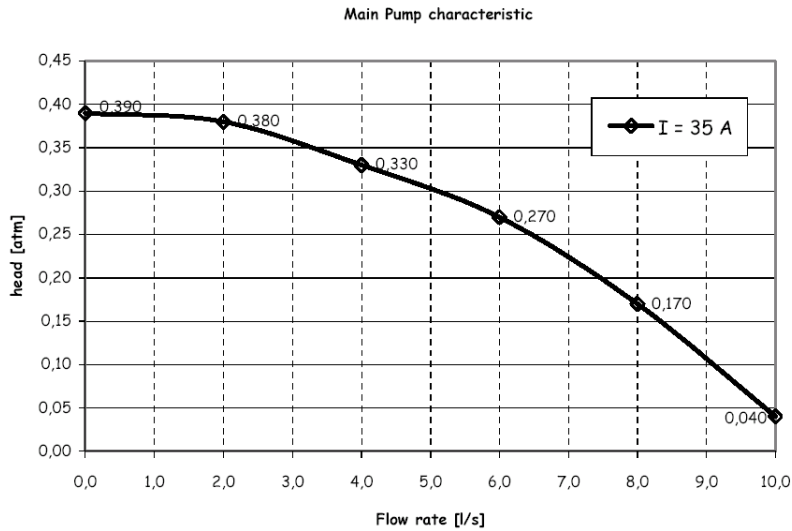


Figure 3: The Main Electromagnetic Pump-Curve

STEADY STATE ANALYSIS

Up till now, all the thermal hydraulics studies are conducted for nominal conditions of 620 kW heating (or roughly in that range, because the thermal power deposition is not in complete agreement in different reports). It is rightly so because those studies are part of design support. Before the target can be sent to the proton beam, it must go through very extensive thermal hydraulic tests at a much lower heating. In those tests, the proton beam is simulated by an electric heater inserted in the main flow guide tube through the beam window, which can only achieve the maximum power of 200 kW.

Table 3. Results of the RELAP5 calculation:

(a) *Flow rate, pump power and pressure head*

P-Beam Heating kW	Mass Flow Rate kg/s			Pump		Pressure Head, bar			
	LBE	THT	H ₂ O	Main LBE, A	Oil THT, rpm	LBE			THT
						ΔP_{pump}	ΔP_{grv}	$\Delta P_{\text{grv}}/\Delta P_{\text{fri}}$	ΔP_{pump}
700	42.28	9.22	8.33	23.32	299.29	.1158	.0419	.265	6.2
620	40.60	8.85	8.00	22.36	286.54	.1069	.0387	.266	5.74
400	35.08	7.65	6.91	19.32	251.28	.0804	.0290	.265	4.33
200	27.84	6.07	5.19	15.37	203.20	.0514	.0184	.264	2.80
150	25.30	5.51	4.98	13.99	185.57	.0428	.0152	.262	2.33

(b) *Temperatures of heat exchanges*

P-Beam Heating kW	Temp. °C Top of Active Zone	HEX Inlet Temperature, °C				HEX Outlet Temperature, °C			
		THX		IHX		THX		IHX	
		LBE	THT	THT	H ₂ O	LBE	THT	THT	H ₂ O
700	381.3	357.0	139.2	177.7	19.8	245.0	177.7	178.4	40.4
620	355.3	333.0	129.8	166.4	40.0	230.0	165.8	166.4	59.0
400	324.1	307.0	167.8	194.1	95.9	230.0	193.5	136.9	110.1
200	290.1	278.9	197.8	213.9	150.1	230.0	213.4	172.4	158.0
150	274.9	270.6	205.3	218.4	164.7	230.0	217.9	182.5	171.9

In light of that, it is necessary to derive a scaling method for lower power test. Since the target is operated in mix convection mode, it makes sense to scale with the buoyancy. By a simple argument that the natural circulation flow, \dot{m} , is proportion to square root of the temperature rise, ΔT , and the temperature rise, where the fluid passes a heat source, is inversely proportion to the velocity. Then, the flow rate and the temperature can be scaled by:

$$\frac{\dot{m}_s}{\dot{m}_n} = \left(\frac{Q_s}{Q_n} \right)^{1/3} \quad \text{and} \quad \frac{\Delta T_s}{\Delta T_n} = \left(\frac{Q_s}{Q_n} \right)^{2/3}, \quad \text{respectively,}$$

where Q is the thermal power delivered to the target, and the subscript s and n denote the variable of scaled and nominal conditions, respectively. In this computation study, the mass flow rate and inlet temperature are calculated according to relations given in above, and the RELAP5 is employed to compute the rest of the steady state conditions. Since the scaling gives only the temperature difference, it is necessary to set one referent temperature, which the exit LBE temperature of THX is chosen and set to be 230 °C. The nominal condition is given at 620 kW proton beam heating. The results of this study are summarized in Table 3.

The scaling does achieve the primary objective, the buoyancy contribution is kept at ~26.5% of the overall pressure head (see Table 3.a) in all the cases. The exact value

should not be taken literally, because they were computed from very coarse meshes. Apparently, all the operating conditions have been scaled properly in all cases, but there are some unwanted consequences. Here are two:

The Main EMP is operating at too low power for instability:

At nominal condition, the main EMP is operating at 22.36 Ampere. For the full power at 37 Ampere, the pump works nominally at 60 % of the full power. Further decrease in heating power, the pump must be forced to operate at below 60% range. In the Integral test, the flow rate is scaled to 67% of the nominal, but the pump is operated at roughly 42 % of the full power, where the EMP stability could be a problem. Unfortunately, the flow rate cannot be compromised if one wants to keep a scaled test operation.

- The SWL operating temperature is too high:

At 400 kW heating, the water temperature in the SWL is already exceeding boiling point at NPT. Although the loop is pressurized to 3 bar, water subcool becomes questionable at the IHX exit. Much higher temperature is called for at 200kW heating, which is heater power in the Integral Test. At the operating temperature roughly 160 °C, it is necessary to pressurize the SWL to above 10 bars just to be on the safe side. However, it may violate the safety restriction that ICL must be operated at higher pressure than SWL to avoid water ingress to ICL if a leak is developed. The nominal operating pressure of ICL is roughly 6 bars and should it be increased over that value, there is concerns of pressurization of the beam window in case of an accident,

It may be lesser a problem with ICL at low power heating operation. With the saturation

Table 4 The performance of the HEXs

<i>Target HEX (THX)</i>	Nominal	200 kW
Reynolds number, --	2.83×10^5	1.94×10^5
Velocity, ms^{-1}	0.452	0.307
HTC, W/m-K	1916	1741
Total Heat Transfer, kW	612.4	199.4
Temperature Difference, ΔT , K	93.0	48.9
<i>Main Flow Guide (MFG)</i>		
Reynolds number, --	5.06×10^5	3.27×10^5
Velocity, ms^{-1}	0.296	0.195
HTC, W/m-K	1316	1035
Total Heat Transfer, kW	124.3	45.7
Temperature Rise, ΔT , K	22.08	5.89

temperature over 300 °C in NTP, boiling is not an issue of Diphyl-THT. But the vapour pressure starts to appear at 160 °C and increases rapidly after 200 °C. Thus, operating the ICL at temperature higher than 160 °C may not be desirable, because the Diphyl vapor pressure must be reckoned with during the Integral Test.

The heat exchangers are the key components of defining the system thermal hydraulics. The performance of THX is of special interests, because it determines whether sufficient amount of heat can be removed to maintain steady state operation. As aforementioned the target is operated in mix-convection mode, the temperature distribution in the target is of great interests. There is substantial amount of heat is transferred through the main flow guide (MFG) (i.e. from the riser to the downcomer), by which it modifies the buoyancy effects. The performances of both units are summarized in Tables 4. Comparisons between the nominal conditions and the scaled experiment (i.e. 200kW heating) are made based on the Reynolds numbers and the overall heat transfer

coefficient (HTC). They are not the same for sure, but in the same order of magnitudes. That is important because it means same hydrodynamic regimes observed in nominal operation can be closely reproduced in the Integral Test. In nominal condition, there is roughly 124 kW from the riser to the downcomer, by which it incurs 22 °C rise.

TRANSIENT ANALYSIS

One of the important transients in MEGAPIE target operation is the proton beam trip, because the proton beam suffers hundreds of trips in a week operation. Due to the high capacity of HRS, it won't take long to chill the LBE down to solidification. More importantly, the target must be protected from thermal shock, especially for the beam window, to avoid excess thermal stress on the structure material. One of the options is to maintain a constant LBE temperature at the THX exit in any thermal transient. A control sequence is implemented by Ansaldo [5] in the RELAP5 model to test whether the LBE temperature can be controlled. The details have been discussed in the report [5] and would not be repeated over here. In essence, the inlet and outlet LBE temperatures of THX, and their derivatives are fed to an integral controller to actuate the 3-way valve in ICL to bypass the IHX in case of a beam trip. Since the LBE is protected from large temperature fluctuation, this thermal transient is called "protected beam trip". In this study, the other important aspect is to examine whether the control process would be modified in the scaled experiments.

The initial conditions and the input files are obtained from the steady-state calculations. In other words, the results presented in Table 3 are the initial conditions for these transient calculations. The rows of 620 kW and 200 kW are chosen, by which they represent the nominal and Integral Test conditions, respectively. A normal beam trip transient is sketched in Fig. 3a. Power instantly falls to zero at the beginning, follows by a 10 second delay, and then the proton beam is switching on in a 20 second ramp to full power. For the case of the Integral Test (i.e. 200kW), the 20 seconds ramp is replaced by steps increases: 10 steps of 20 kW increments (see Fig. 3b). It is because the LMC Heater is made of 19 individual heating elements, and each of them is controlled by an independent "ON/OFF" switch. The 20-step sequence is chosen just to make it easier to determine the intervals. One must also notice that the time of 10/20 sequences has not been scaled to 200 kW experiment.

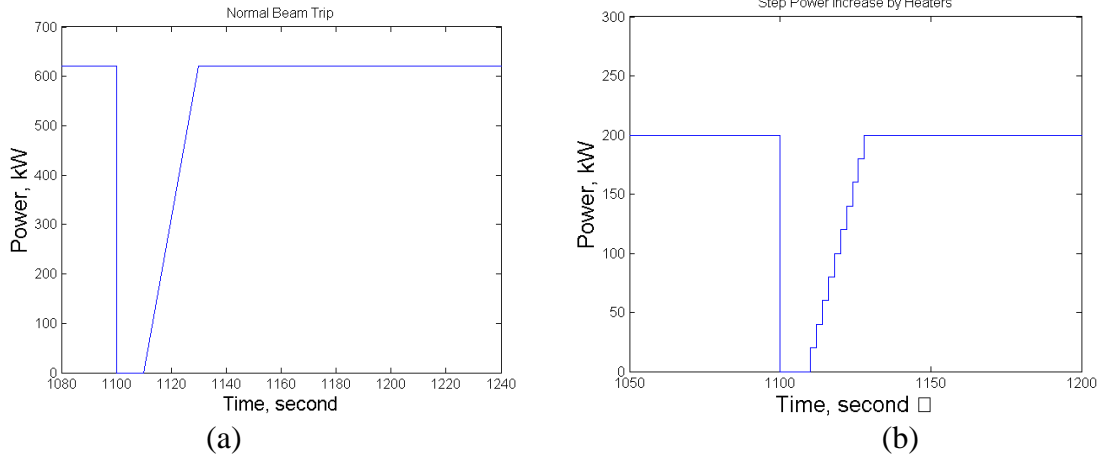
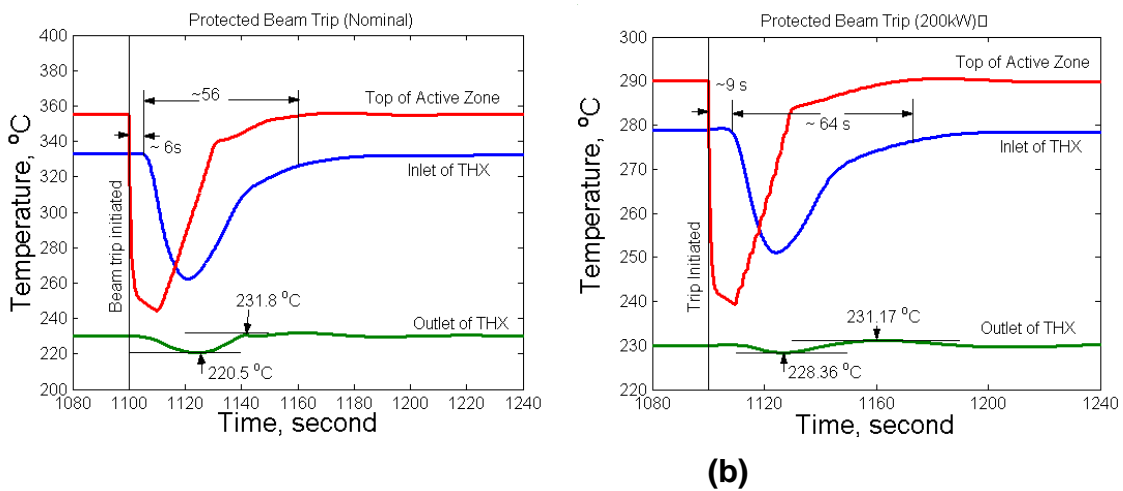


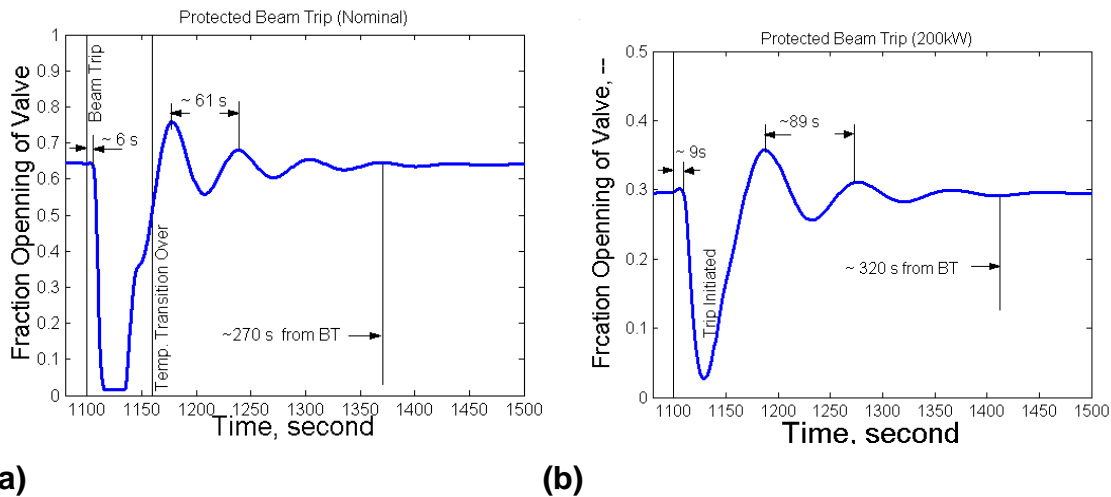
Figure 3: Simulation of the power interruption of (a) Proton Beam at nominal case, (b) Step change in the Integral Test.

The results of the RELAP5 calculations are presented in Figs 4 and 5. Since the control use the inlet and outlet temperatures of the THX, it makes sense to study those temperature transients more closely. The temperature of the active zone is also plotted in Fig 4(a) and (b). The observations are:

- The shape of all corresponding curves look very similar in nominal and 200kW cases,
- The temperature in the active zone change almost instantly at the beam trip,
- There is a time lag on the temperature responses at entrance of THX; ~6 s for nominal and ~9 s for 200kW. This is due to the fact that the unheated LBE cool slug takes time to traverse the distance from the beam window to the top of THX,
- The control did a very good job to limit the fluctuation of exit LBE temperature to within 10 °C for the nominal case and within 3 °C for 200kW case, and the swing is more on the negative side than the positive side, (see Fig. 4(a) and (b)),
- The stepwise power increments of the 200kW case created only small ripples on the temperature rise in the active zone. The ripples were completely smoothed out at the inlet of THX, and they have no effect on the overall transient



(a) (b) Figure 4: Temperature transients of the a protected beam trip (a) nominal (b) 200kW

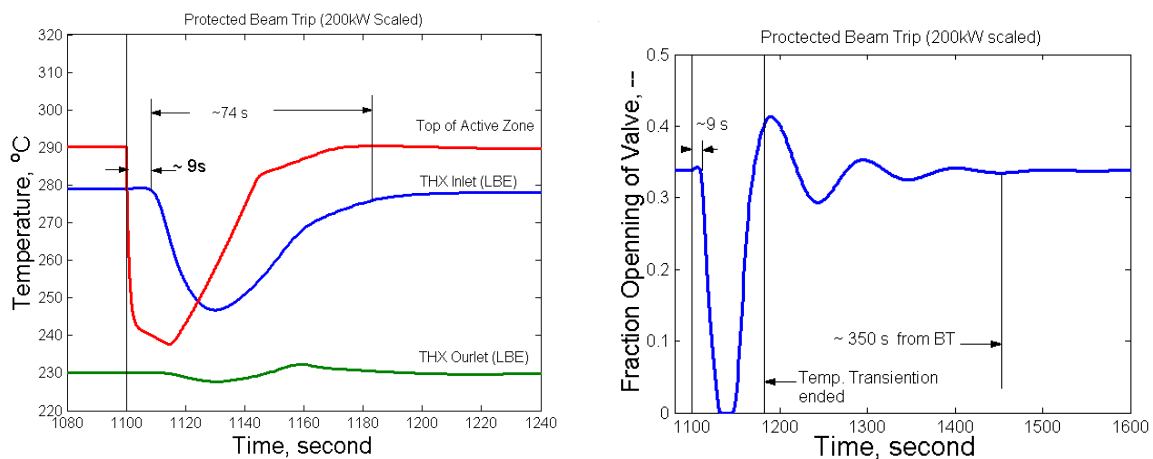


(a) (b)
 Figure 5: Fraction opening of the 3-way valve in a protected beam trip (a) nominal, and (b) 200kW

- For both cases, the LBE temperatures took much longer time to recover than the 30 seconds transient. The reason is probably combination of the thermal inertial of the materials and heat transferring through THX. For the nominal case, it took roughly about 56 seconds, while the 200kW case took more than 64 seconds. (Note that the recover is defined as the time duration between start of the transition to recover 90% of the temperature drop).

Although the temperature transients are quite similar between two cases, it does not guarantee that the control does behave the same. To examine the control sequence, it is better to check signal of the 3-way valve, which is the object of the control. The plot of the fraction opening of the 3-way valve against the time is presented in Fig. 5. The phase “fraction opening” simply means the fraction of the valve opening toward the intermediate heat exchanger (IHX) in ICL. Here are the observations:

- The actuation signal started at the same time when the cool slug of LBE hit the top of THX. In other words, the response of the 3-way valve is almost instantaneously. Whether this is physical can only be determined without testing the real system,
- The valve continued regulating long after the temperatures were full recovered. The regulation control was oscillatory and it took much longer time to settle: roughly 270 seconds for the nominal case and 320 seconds for 200 kW case,



(a) (b)
 Figure 6: The scaled protected beam trip (a) Temperature transient, and (b) Fraction opening of 3-way valve.

- The 3-way valve almost completely shut down the IHX for roughly 20 second for the nominal case, (see Fig. 5.a.), while the valve never went to nearly shut down the IHX for the 200kW case,

Apparently, the time distortion due to the reduced velocity stopped the control to go into full swing. The logical step is to scale the beam trip time by the flow rate itself. The mass flow rate of the 200kW experiment is given to be 27.84 kg/s, while the nominal flow rate is 40.6 kg/s. The time scale is inversely proportion to the velocity. Thus, the beam trip time must be multiplied by a factor of 1.46. The 10/20 beam trip times become 14.6/29.2. Take that scaled beam trip and redo the calculation, and the results are presented in Fig. 6. Both the temperatures and the control signal do show the same characteristics as the nominal case. It is clear that the all the phenomenon studied in the Integral Test must take into account of the time distortion due the scaled down flow rate.

CONCLUSIONS

Modeling the target system with the RELAP5 has completed. An extensive computation experiment has been conducted afterward. A simple scaling rationale scaling the flow rate by 1/3 power of heating (i.e. $\dot{m} \sim Q^{1/3}$) is proposed. In this way, the buoyancy effect in the mix convection target can be scaled appropriately. RELAP5 has been employed to calculate the scaled steady state conditions at different power levels. The results confirmed that scaling rationale did work well in a wide range of heating powers. With flow rate scaled by the over all power, the buoyancy contribution to the total pressure head is kept at 26.5% in all cases studied. Even though the nominal conditions can be scale down properly to 200kW, the system may not be able to operate that given conditions. It is to say that the EMP is operated at too low power for instability (42 % of the full power) and water loop ran at too high temperature (160 °C).

The capability of solving the transient problem is surely the big advantage of using a RELAP5 code. A protected single beam trip is studied for both the nominal and scaled down condition. The control sequences did a very good job to limit the LBE temperature fluctuation at the exit of THX within 10 °C in the nominal case. Whether this control can be recognized by the physical system is also questionable, because valve inertial and actuation time have not been taken into account in this model. The temperature transients took a little longer time to settle (roughly 56 s in nominal case) than the beam trip time (30 s). The control is somewhat oscillatory and takes roughly 300 s to restore equilibrium. It is shown that the scaled down case also distorted the control sequence. The beam trip time must be scaled accordingly to give enough time to complete the control events.

REFERENCES

- [1] V.H. Ramsom, The RELAP5 Two-Fluid Model and Associated Numerical Method, Purdue University, 1994,
- [2] D.A. Young, Soft Sphere Model for Liquid Metals, Lawrence Livermore Laboratory University of California UCLR-52352,
- [3] Ansaldo, Lead Bismuth Eutectic Physical Properties and Thermodynamic Tables, XADS 20 TRX 0003, Genova, Italy, Jan. 2002
- [4] Ansaldo, Mathematical Model and Thermophysical Properties Correlations for Organic Heat Transfer fluids, ADS 1 TRIX 0244 rev.1, Genova, Italy,
- [5] M. Petrazzini, A. Alemberti, Input and RELAP5 Model Description, Ansaldo Report MPIE 1 TRIX 200, Genova, Italy, Sept, 2002

**CFD analysis of lower target:
Latest steady-state simulations**

T. V. Dury

Thermal-Hydraulics Laboratory, Nuclear Energy and Safety Department, Paul Scherrer Institute, CH

HEAT DEPOSITION IN THE TARGET

As calculation of the heat deposition profile in the Megapie target had been continually refined over the period since CFD simulation began, parameter studies made to date have been calculated with slightly different profiles at different periods. After close interaction with the Megapie neutronics study group, a more detailed set of equations was finally defined in September 2002. This is summarised in the following equations, for a 1.74mA proton beam:

Window: In the T91 steel of the target window, i.e. the hull region between $0.0 < z \leq 0.088m$, the heat deposition profile is given by the equation:

$$Q = 1.428 * 10^9 * e^{-\frac{1}{2} \left[\left(\frac{x}{\sigma_x} \right)^2 \right]} * \left[-0.3846 + e^{-\frac{1}{2} \left[\left(\frac{y}{\sigma_y} \right)^2 \right]} \right] \quad W/m^3 \quad (1)$$

where x and y are the planar coordinates, in metres, centred on the target centre-line, and the radial beam profile parameters are: $\sigma_x = 0.021 m$ and

$$\sigma_y = 0.0378 m$$

Lead-Bismuth Eutectic (LBE): Heat is deposited within the LBE over the axial range $0.0 < z \leq 0.27m$. The equation defining the deposition rate is:

$$Q(z) = A * e^{-\frac{z}{z_a}} * \left[1.0 - e^{-\frac{(z+z_b)}{z_c}} \right] * \left[1.0 + 550.0 * (z_d - z) * e^{-\frac{|z_d - z|}{z_e}} \right] * e^{-\frac{1}{2} \left[\left(\frac{x}{\sigma_x(z)} \right)^2 + \left(\frac{y}{\sigma_y(z)} \right)^2 \right]} \quad W/m^3 \quad (2)$$

- where:
- $Q(z)$ = Local volumetric heat deposition rate ($W/m^3/mA$)
 - A = Constant = $1.48 * 10^9 (W / m^3)$
 - z = Local height, from the lowest point of the LBE (m)
 - z_a = 0.145 m z_b = 0.045 m
 - z_c = 0.045 m z_d = 0.267 m
 - z_e = 0.0045 m
 - $|\dots|$ = Absolute value of the expression (m)
 - x = Local x-coordinate (m)
 - y = Local y-coordinate (m)
 - $\sigma_x(z)$ = $0.0205 + 0.0155z + 0.121z^2$ m
 - $\sigma_y(z)$ = $0.0256 + 0.0256z + 0.0839z^2$ m

The last two expressions define the height-dependent radial profile parameters.

Hull above the domed window; Guide tube; Bypass, fill and drain pipes: Equation 2 is applicable, using the constant $A = 1.39 * 10^9 (W / m^3)$.

Heat generation comparison

Comparison can be made of the heat generated in the different components of the target calculated by the CFD code CFX-4.3 and from the FLUKA neutronics code from Table 1, and the agreement of the axial deposition profile on the target axis from Fig. 1:

Table 1: Heat deposition from FLUKA ($0.0 < z \leq 0.3125m$) and CFX-4.3 ($0.0 < z \leq 0.3125m$)

Material	FLUKA (kW)	CFX-4.3 (kW)
LBE	705.8	709.9
Window	5.56	5.28
Hull (above window)	2.68	1.21
Guide tube	5.55	6.03
Total	719.6	722.4

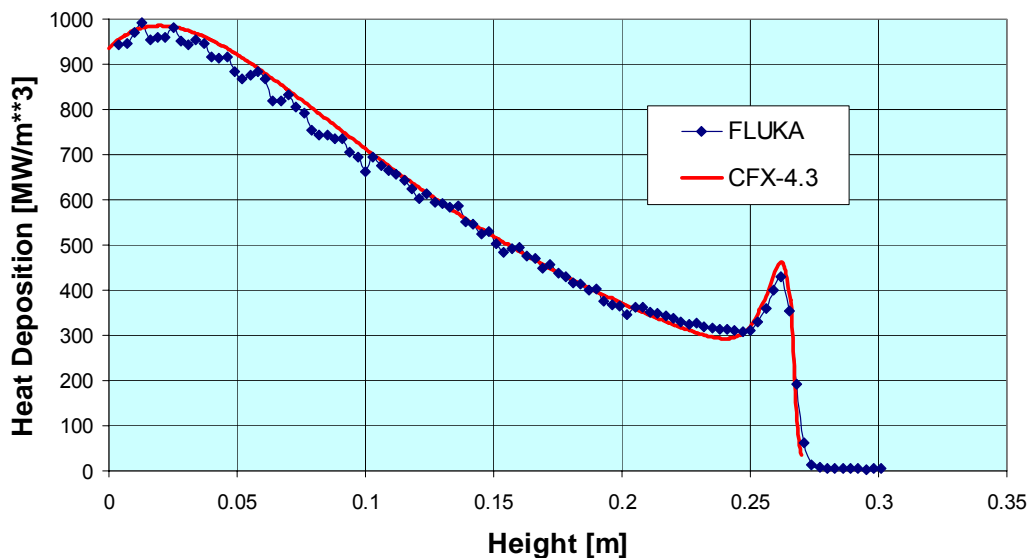


Figure 1: Comparison of radial deposition profiles, 1.74mA beam

STEADY-STATE CONDITIONS, WITH 1.74MA AND 1.4MA PROTON BEAMS

Most parameter studies made using CFX-4.3 for steady-state operation of the Megapie target have been performed with a 1.74mA proton beam at the window (2.5mA focused beam upstream of Target E). However, calculations with a beam of 1.4mA at the window have also been performed recently with a target design which appears to show good performance at present. Characteristics of the design are listed and illustrated below:

- 20±5mm gap at end of guide tube
- 20×10mm bypass nozzle
- Beam major axis aligned with bypass jet
- Fluid temperature at HX outlet = 230°C
- 2.5kg/s bypass flow of LBE
- 37.5kg/s annulus flow of LBE
- Instrumentation rod 340mm from bottom of target

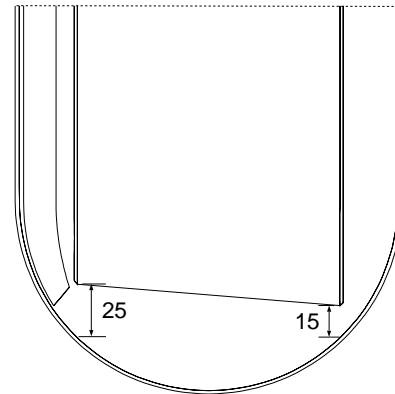


Figure 2: 15/25mm slanted guide tube with 20×10mm bypass nozzle

Peak temperatures occurring within the target for both proton beam currents are listed below in Table 2. The total heat generated within the target is given in Table 3, together with the heat transported by the fluid in the annulus to the riser, either deposited there by the beam (about 44kW according to FLUKA calculations) or transferred into the annulus by thermal conduction through the guide tube and by convection, from the hot riser fluid:

Table 2: Peak steady-state temperatures: Basic case

Conditions		T_{peak} (°C)			
		LBE	Guide tube	Inst. rod	Window
1.74mA	Major beam axis aligned with bypass flow	422.7	368.2	386.8	370.2
	Minor beam axis aligned with bypass flow	424.1	363.1	389.5	360.3
1.4mA	Major beam axis aligned with bypass flow	384.4	339.4	355.7	342.5

Table 3: Heat deposited in target and deposited/transported by annulus fluid (CFX-4.3)

Beam current (mA)	Total heat deposited in target (kW)	Heat deposited/transferred into annulus (kW)
1.74	722	238
1.4	581	189

Temperatures on the outer window surface, viewed from below, are shown in Figs. 3 and 4. The distributions are qualitatively similar, with the prime difference being the temperature level.

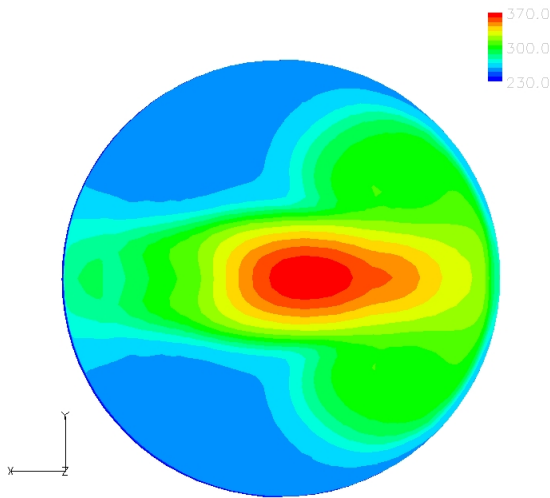


Figure 3: External window temperatures (C), 1.74mA beam, major axis aligned with jet

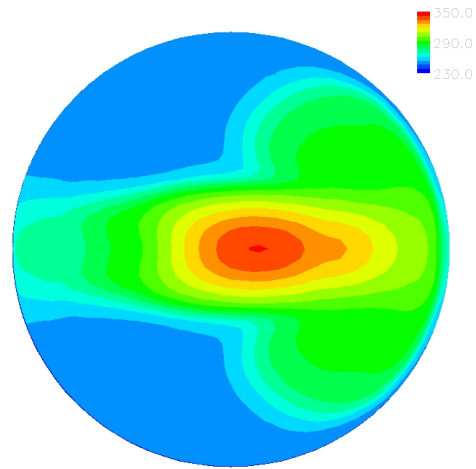


Figure 4: External window temperatures (C), 1.4mA beam, major axis aligned with jet

AZIMUTHAL OFFSET OF BYPASS NOZZLE

One of the critical issues concerning the performance of the heat exchanger units in the upper target is the temperature distribution at their inlets. Consequently, two steady-state calculations were performed, with the azimuthal position of the bypass nozzle (and bypass supply duct) varied by 15° and 30°, to examine what effect nozzle position has on fluid motion within the riser, and the temperature distribution at the upper regions of the riser (NB. The riser outlet in this model is at the vertical level of the heat exchanger outlet plane). For these calculations, the heat deposition profile of March 2001 (total heat deposited in the target = 682 kW) was used, with the beam footprint major axis aligned with the slant of the end of the guide tube.

Peak temperatures in the target, and the maximum temperature difference over the riser outlet plane, for these two conditions are listed in Table 4, where they can be compared with the values for the aligned case:

Table 4: Peak target temperatures and temperature difference over the riser outlet for different azimuthal positions of bypass nozzle

Azimuthal nozzle offset	T _{peak} (°C)				ΔT _{max} over the riser outlet (°C)
	LBE	Guide tube	Inst. rod	Window	
0°	413.4	365.5	380.8	368.7	57
15°	414.5	361.4	376.9	370.2	55
30°	415.5	354.8	376.9	370.4	50

The influence of the change in the distribution of external window temperature, compared with the no-offset case (Fig. 3), can be seen in Figs. 5 and 6 (viewed from below), for the 15° and 30°-offset cases, respectively. The surface shaded contours of temperature in these Figures have been made semi-transparent, to enable the position of the bypass duct to be seen behind the window. The combination of annulus flow and bypass flow from an offset nozzle and supply duct have created a distorted temperature

distribution over the window, which is steady in these CFD simulations, but which will certainly have some variation with time in the real target. The stress distributions within either the window or the target as a whole, with nozzle offset, have not yet been obtained.

Temperature distribution across the riser outlet plane are plotted in Figs. 7 to 9, for the cases of 0°, 15° and 30° offset, respectively.

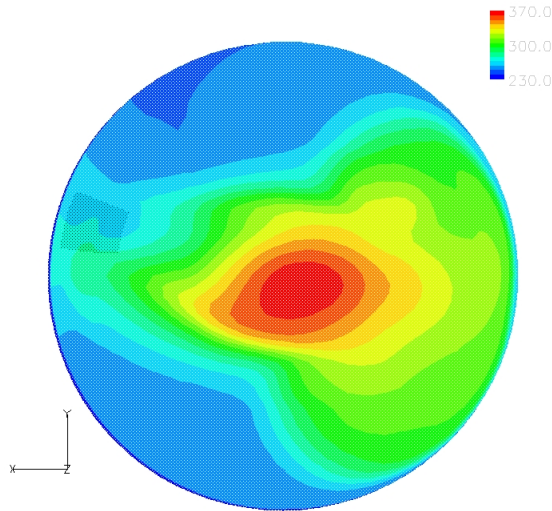


Figure 5: External window temperatures (C), major beam axis aligned with slant, nozzle offset 15°

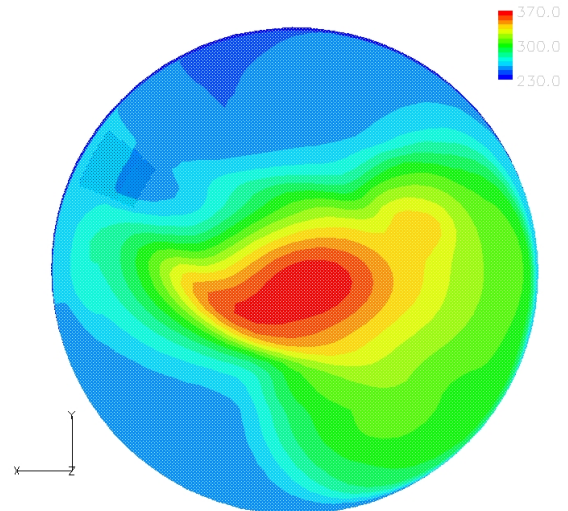


Figure 6: External window temperatures (C), major beam axis aligned with slant, nozzle offset 30°

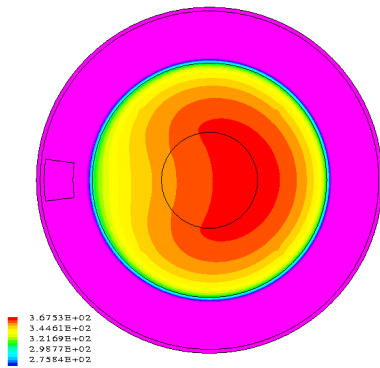


Figure 7: Outlet plane temperatures (°C), no offset

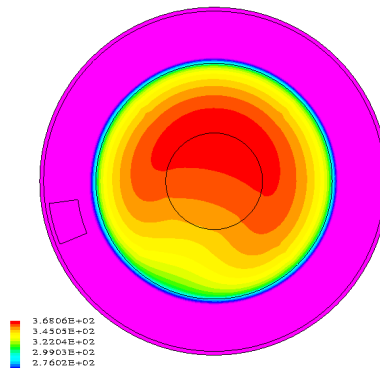


Figure 8: Outlet plane temperatures (°C), 15° offset

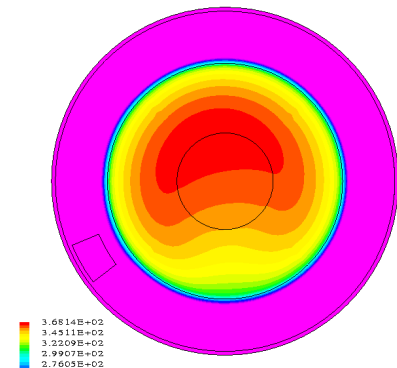


Figure 9: Outlet plane temperatures (°C), 30° offset

It can be seen that offsetting the bypass nozzle does generate some mixing of the rising LBE, hence the 14% reduction in temperature difference over the outlet plane in this model. However, the shape of the temperature profile shows that the degree of mixing is low, and some other mechanism would be required to generate a flatter temperature distribution over the riser. Nevertheless, the consequences on the stresses in the target may be worth investigating, when CFD simulations are done on the final target design (including fill and drain pipes, and with the necessary geometrical shape of bypass duct).

TARGET TEMPERATURES WITH SLOTS IN THE GUIDE TUBE WALL

To examine how the recirculating vortex behind the guide tube wall in the riser (at the side next to the bypass duct and nozzle) could be damped or eliminated, a short

exploratory study was made on the basic target design by adding bleed slots for LBE to the guide tube wall. These slots were inserted by simply removing horizontal bands of metal from the guide tube wall. Slots were at a variety of heights and of different vertical widths, incorporated empirically on the basis of observation of the recirculation vortex and the influence of steadily increasing numbers and dimensions of slots.

The influence of three different sets of slots on peak target temperatures can be seen in Table 5, in comparison with the values without slots. As expected, the greatest improvement does occur within the guide tube wall (reduction in peak temperature of about 12°C). This reduction would reduce the bending imposed on the guide tube by the differential temperature across it. Window temperature decreases by up to 3°C as the efficiency of the bypass flow improves as annulus flow into the window region decreases slightly.

Table 5: Peak target temperatures with and without slots in the guide tube wall

Number of slots in wall	Total area of slots (cm ²)	T _{peak} (°C)			
		LBE	Guide tube	Inst. rod	Window
0	0	413.4	365.5	380.8	368.8
3	17.3	411.0	356.9	376.9	366.4
5	52.8	409.1	353.6	373.6	365.8
6	44.8	410.8	353.9	374.1	365.7

Velocity vector distributions and temperature contours on vertical sections through the target can be compared for the case with no slots and the case above with 3 slots in Figs. 10 to 13. The reduction in recirculation behind the guide tube is clearly visible, as is the thermal effect and the reduced penetration of the bypass jet along the window.

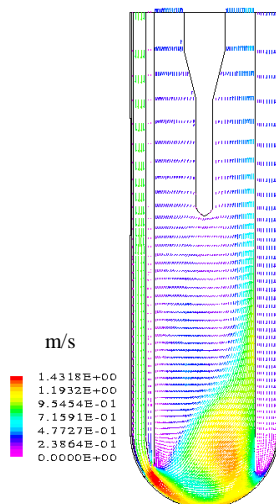


Figure 10: Velocity vectors, no slots

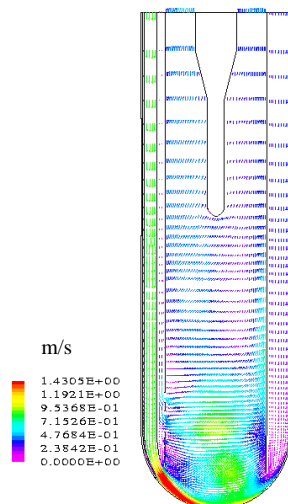


Figure 11: Velocity vectors, three slots

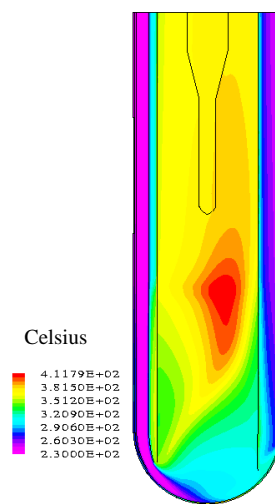


Figure 12: Temperature contours, no slots

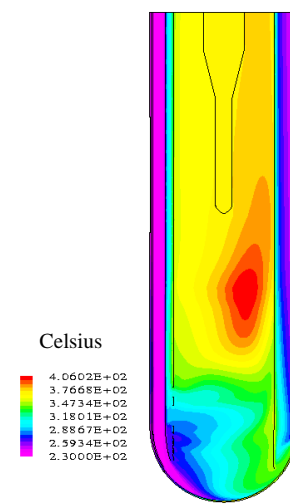


Figure 13: Temperature contours, three slots

CONCLUSIONS

- Heat deposition in the target has now been defined in detail after extended consultation with the neutronics group, and satisfactory agreement obtained between FLUKA and CFX-4.3 deposition rates
- Total heat deposition with CFX-4.3 with a 1.74mA proton beam at the target is 722kW, and with a 1.4mA beam is 578kW
- CFD parameter studies of a target with bypass flow of LBE of 2.5kg/s, annulus flow of 37.5kg/s, 20×10mm bypass nozzle, and 15/25mm vertical gap between guide tube and window have shown that:
 - Azimuthal offset of the bypass nozzle of 30° reduces the temperature difference in the LBE across the riser at the height of 2.15m by about 14%
 - Slots introduced into the guide tube wall to bleed LBE into the recirculation region in the riser can reduce peak guide tube temperatures by at least 12°C, while also decreasing peak window temperature by 3°C

Table 1: Peak steady-state temperatures

Conditions		T_{peak} (°C)			
		LBE	Guide tube	Inst. rod	Window
1.74mA	Major beam axis aligned with bypass flow	422.7	368.2	386.8	370.2
	Minor beam axis aligned with bypass flow	424.1	363.1	389.5	360.3
Heat Deposition (kW)		710.0	6.0	0.0	5.3

STRUCTURAL MODEL

The geometry and mesh discretisation are adopted directly from the CFD model. Consequently, we use 8-nodal hexahedral elements to represent the structures. Though most components consist of thin shells, there are 5 elements across the thickness to ensure adequate representation of the bending stresses. Details of the material properties are given in Table 2.

Table 2: Material Properties

Component	Material	Young's Modulus	Poisson Ratio	Expn. Coefficient
Target Hull	T91	2.0×10^{11} Pa	0.3	11.5×10^{-6} K ⁻¹
Guide Tube	AISI 316	2.0×10^{11} Pa	0.3	16.0×10^{-6} K ⁻¹

For convenience in defining the boundary conditions, each structure is suspended from its top axial section, by imposing zero axial displacements to all nodes on these section, and 3 anchor points on the top rim are constrained to move in the radial direction only. This prevents the rigid body movements of the structures and simulates well the flange attachment in the actual target. Local stress concentrations around the anchor points are ignored. From earlier studies it was found necessary to have spacers between the guide tube and the LMC to limit lateral displacement of the guide tube resulting from differential heating. The spacers are simulated in the model by constraining 3 pairs of nodes around the bottom edge of the guide tube and the LMC to have the same radial displacement.

RESULTS

Calculations have been performed for both flat and slanted guide tubes, for different beam currents (1.74 mA or 1.4 mA at the target window), for different beam orientations (0° or 90° to the bypass flow), and for different estimates of the heat deposition profile. Only results pertaining to the latest estimate of the beam heating are included here, and these are summarised in Table 3.

Comparing rows 1 and 4 of the Table, we see that a 20% reduction in beam power leads to a 20% reduction in temperature excess (over the 230°C inlet temperature) and about 20% reduction in maximum stress. The main effect of beam orientation is a reduction (by 27%) of the maximum stress in the guide tube, with little effect on the window stresses. The main benefit of slanting the guide tube is a reduction in maximum window temperature of 9%, with a corresponding decrease in stress levels. Overall, the stresses are acceptable.

Table 3: Summary of Results

Guide Tube	Beam		Max. Temperature (°C)		Max. von Mises Stress (MPa)	
	Power (mA)	Orientation	Guide Tube	Window	Guide Tube	Window
Slanted	1.74	0°	367	370	63	55
Slanted	1.74	90°	362	359	46	58
Flat	1.4	0°	337	353	49	51
Slanted	1.4	0°	338	342	49	46

FINAL REMARKS

The mechanical behaviour of the lower target under normal operating conditions has been analysed for two different guide tube geometries, two beam currents, and two beam orientation options. General conclusions are:

- The calculated maximum von Mises stresses in the target window are always less than 60 MPa, and almost insensitive to the parameter variations considered.
- In contrast, the maximum stress in the guide tube is dependent on the design, and is least if the beam is orientated at 90° to the bypass flow.
- The latest estimate of the heat deposition profile leads to much lower predictions of the stresses in the guide tube than those previously calculated[2].

REFERENCES

- [1] T. V. Dury “CFD Analysis of Lower Target: Latest Steady-State Simulations”, Megapie Technical Review Meeting, Paris, 18-19 March 2003
- [2] A. Zucchini “MEGAPIE: Stress Analysis of Lower Target Preliminary Design”, RTI/FIS/MET/2002/1, ENEA, 2002

THERMOHYDRAULIC INVESTIGATIONS FOR MEGAPIE- THE HYTAS- KILOPIE AND HEATED JET EXPERIMENTS

S. Gnieser, M. Daubner, C.-H. Lefhalm, F. Fellmoser, K.-J. Mack, H. Piecha and R. Stieglitz
J. Patorski*, I. Platnieks *

Institute for Nuclear and Energy Technologies (IKET), Forschungszentrum Karlsruhe, Post Box 3640, D-76021 Karlsruhe, Germany

*Paul Scherrer Institute, CH-5202 Villigen, Switzerland

The Lead Bismuth operated MEGAPIE window is a representative example of a highly heat loaded surface. Within this configuration the proton beam is facing a convexly shaped hemisphere. In order to cool this geometry adequately the liquid metal is flowing in an annular gap downwards towards the hemisphere and is then U-turned into a riser tube. Since in this cylinder symmetrical arrangement a stagnation point velocity profile will establish at the lower part of the hemisphere, which will lead to inacceptably high material temperature. Thus a cross flow realized by a jet is introduced to cool this region. In a series of experiments, being accompanied by supportive CFD calculations, the coolability of this window is investigated.

The strategy to demonstrate this critical feature is first to study the kinetic energy exchange within a water experiment, where flow visualization techniques by means of laser light sheets (LLS) or shadow graphs can be used. Isothermal water experiments in HYTAS at the same hydraulic Reynolds number are performed in various geometries in order to study the kinetic energy transfer within the window part of the target. The obtained results serve as a data basis for the numerical models currently being developed. In all studied configurations owing a bypass jet to avoid stagnation point velocity profiles a satisfactory cooling of the beam window was found for the flow configuration considered in MEGAPIE. An even improved coolability was found for the configuration with a slanted riser tube. There, a significant swirl flow was found accounting to about 40% of the main flow, which leads to a perfect mixing of the flow.

In second step two lead bismuth experiments are in preparation for the MEGAPIE geometry and will start in March 2003. Within the Heated Jet experiment a hot bypass jet is injected in the MEGAPIE flow configuration. By using heating powers up to 72kW MEGAPIE relevant Peclet numbers can be achieved. Since the internal heating as in MEGAPIE can not be simulated experimentally, the temperature is acting as a passive scalar. Using this fact the monitoring of the temperatures at the liquid-solid interface of the hemisphere allows to deduce Nusselt number correlations. Additionally, in the Heated Jet experiment the temperature mixing behavior in the riser tube (mean and fluctuating components) can be monitored as a function of the flow rate in the main flow and the bypass in order to determine time constants. The series of LBE experiments is closed by the KILOPIE experiment, in which a heat emitting temperature sensing surface (HETSS) is used both as a heat flux simulator applying considerably high surface heat flux to the hemispherical window part and acting simultaneously as a sensing element determining the local heat transfer coefficient. In contrast to the Heated Jet, different heat flux conditions for the window can be simulated by means of different HETSS sensors. Using the HETSS technology allows an online monitoring of the heat transfer at the liquid solid interface by means of infra-red thermography (IRT).

INTRODUCTION

Only the knowledge of the convective-diffusive heat transport phenomena in laminar and turbulent liquid metal flows enables an adequate design of heat transfer units near highly heat loaded surfaces. A prominent representative of such a highly heat loaded surface is the beam window of the MEGAPIE spallation target. Due to the low Prandtl number of liquid metals being usually of the order $O(10^{-1}-10^{-2})$ a decoupling of kinematic and thermal transfer processes appears, which is often not treated in commercial CFD codes. Thus, numerically calculated temperature distributions may lead to design misconceptions. This problem is enforced in most technical applications where the flows are thermally developing so that the heat exchange through the boundary layer plays a significant role.

A major step to overcome these problems for a specific problem like the cooling of the MEGAPIE beam window is a combined experimental-numerical effort by treating the "real" geometry.

Therefore, a plexiglass module (HYTAS) operating with water and representing nearly at 1:1 scale the MEGAPIE geometry has been built up and set into operating. Here, numerous design options can be investigated in an isothermal flow using LDA, Laser light sheet and UVP techniques in order to achieve an optimal design.

In parallel to the HYTAS module two lead bismuth experiments (LBE) called Heated JET and KILOPIE with the same geometry are in preparation in the Thermohydraulic Loop THEADES of the Karlsruhe Lead Laboratory KALLA at Forschungszentrum Karlsruhe. Here, a prototypical Nusselt numbers or heat exchange rates can be simulated using either a preheated jet to study turbulent mixing in the fluid flow and Heat Emitting Temperature Sensing Surfaces (HETSS) to determine locally the heat transfer at the solid fluid interface. The measurement instrumentation consisting of thermocouples, pressure and velocity sensors as well as the time schedule will be presented.

EXPERIMENTAL SETUP OF HYTAS

The MEGAPIE HYTAS test module is manufactured completely of plexiglass and all its geometrical dimensions are displayed in figure 1. The flow is extremely sensitive to smallest deviations from concentricity of the annular gap and to inhomogeneities arising from the inlet flow. Therefore, at the top of the module a flow straightener is installed in order to produce a homogeneous grid turbulence at the inlet flow of the annular gap. In case of the absence of a flow straightener a swirl motion was found persisting throughout the whole module. The same effect have smallest deviations of non-concentricity in the gap (of less than 1mm).

Within the HYTAS program Laser Light Sheet (LLS), Laser Doppler Anometer (LDA) and Ultra-Sound Doppler measurements are performed. The Reynolds numbers range Re which is investigated in seven planes is:

$$Re=10^4, 2 \cdot 10^4, 4 \cdot 10^4, 6 \cdot 10^4,$$

where the Re is built with the hydraulic diameter of the annular gap. Measured within the LDA program are the mean axial velocity u_z , the mean circumferential velocity u_ϕ as well as their fluctuations u_z' and u_ϕ' and the RMS-values. In the so called base case no bypass is installed, whereas in two other cases curved rectangular bypass orifices of 20x10mm and 100x2mm are studied.

Additionally, two different cases of the distance d between riser tube and window are studied. Also setups, in which the riser tube are slanted by 15mm and 25mm with respect to the radial coordinate r are planned. This design is aimed to prevent a stagnation point in the bottom center of the window. Reynolds number are performed

in various geometries in order to study the kinetic energy transfer within the window part of the target. Moreover, the obtained results serve as a data basis for the numerical models currently being developed. Additionally, two different cases of the distance d between riser tube and window are studied. Also setups, in which the riser tube are slanted by 15mm and 25mm with respect to the radial coordinate are performed. This design is aimed to prevent a stagnation point in the bottom center of the window by introducing an additional swirl flow. For the bypass cases the flow rate ratio variations of main to bypass flow are performed is from $10 \leq Q_{main}/Q_{bypass} \leq 20$.

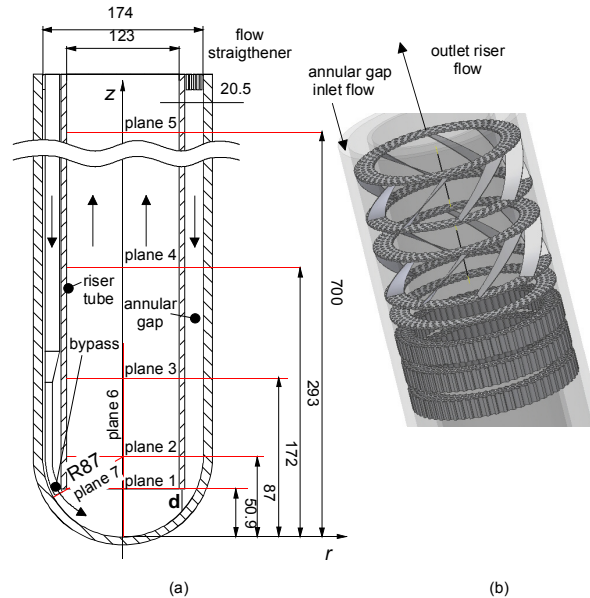


Figure 1: (a) Geometric dimensions of HYTAS and coordinate system used. (b) Flow straightener in HYTAS.

MEGAPIE HYTAS BASE CASE

In figure 2a laser light sheet (LLS) of the lower window part is shown at a Reynolds number of $Re=5.4 \cdot 10^4$ and for an illumination time of 196ms in case of the base case. At the expansion from guide tube to riser large recirculation areas appear which leads to an intense kinetic energy exchange. Vortices detaching from this pressure discontinuity persist far upstream in the riser. After about 6 characteristic length these alternately appearing vortices are destroyed by viscous dissipation. The experiments show that above Reynolds numbers of $Re=4 \cdot 10^4$ the stagnation point is not steadily positioned in the center/lowest point of the beam window; it is rather oscillating thereby.

In figure 3 the normalized axial velocity u_z in the annular gap is shown as a function of the radial coordinate r/R for different z/R at a Reynolds number of $Re=6 \cdot 10^4$. Furtheron, all geometric scales will be normalized by the inner radius R of the window and the velocities are scaled by the mean velocity u_z . The inflow in the annular gap ($0.76 \leq r/R \leq 1$) is rather homogeneous for all Reynolds numbers characterized by a flat velocity profile close to unity; then the profile tends to decrease towards the outer wall at $r/R=1$, indicating that the experimental set-up is not providing completely hydraulic symmetric conditions. As the flow approaches the geometrical jump at the riser tube it is accelerated forming a jet in the gap center. The velocity fluctuations in the gap expressed in terms of the RMS value are about 4% directly after the flow straightener corresponding almost to homogeneous grid turbulence and are continuously increasing downstream to values of about 0.4 at $z/R=1.1$. The

circumferential velocities are insignificant in the range of $u_\phi/u_z \approx 0.05$, indicating that the current set-up is symmetric.

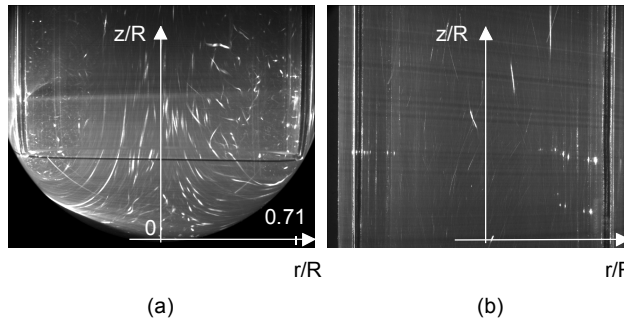


Figure 2: (a) LLS-Photographs at the lower part of the beam window at $Re=5.4 \cdot 10^4$. (b) LLS at $6.5 \leq z/R \leq 8$. In both graphs the illumination time is 196ms.

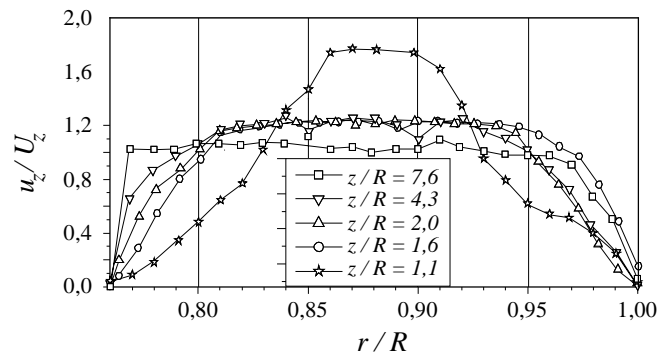


Figure 3: Normalized axial velocity u_z in the annular gap as a function of r/R at different measurement planes z/R for $Re=6 \cdot 10^4$.

Directly after the U-turn of the flow a flow pattern evolves, which is characterized by a jet in the center and alternating vortices close to the riser tube, as suggested by figure 2. This effect is also seen in the LDA measurements displayed in figure 4, where the velocity close to the tube is significantly below unity. The RMS values of the axial flow fluctuations is of order $O(1)$ close to the U-turn. As the flow proceeds downstream both the vortices and the RMS values of the velocities are damped by viscosity and at the outlet rig the axial velocity is almost unity, whereas the fluctuations are close to zero.

After the U-turn the circumferential velocities reach values up to 0.1 of the main flow and the normalized RMS values grow to up to 0.4. But, close to the rig outlet the swirl has almost been diminished.

The pressure losses measured are by about 50% lower than those calculated using numerical codes as CFX [1].

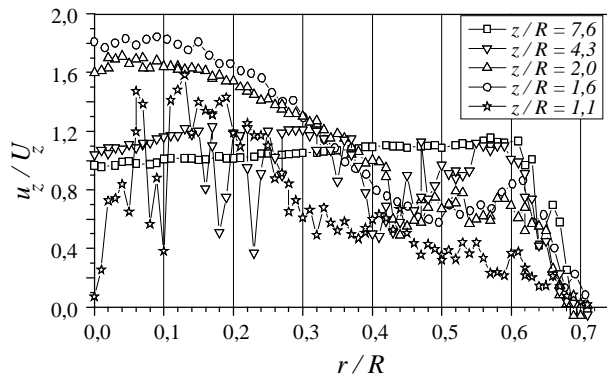


Figure 4: Normalized axial velocity u_z in the riser tube as a function of r/R at different planes z/R for $Re=6 \cdot 10^4$

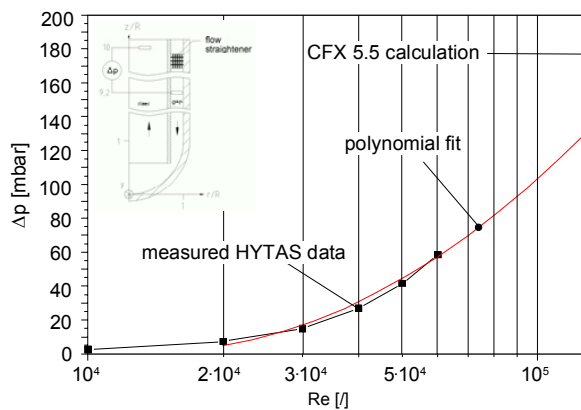


Figure 5: Measured pressure drop in HYTAS for the base case as a function of Re .

MEGAPIE HYTAS BYPASS CONFIGURATIONS

In case of the configuration with bypass necessary to cool the MEGAPIE window adequately the symmetry of the flow gets lost. The figure 6a shows a LLS of the configuration with a 100x2mm bypass of the lower part of the window at a Reynolds number of $Re=6 \cdot 10^4$ and a main to bypass flow ratio of 15. As LLS show the flow loses its symmetry and the stagnation area is shifted in opposite direction of the bypass nozzle. At a main/bypass flow ratio of 15 (as considered in MEGAPIE) the stagnation point, which is more or less steady positioned, is about 32mm away from the centerline. Directly next to the nozzle in the riser tube a recirculation area with a weak mean velocity establishes. The flow unsymmetry caused by the nozzle keeps alive far upstream the riser tube and unsymmetries of the order 0.15 of the main flow are still existent as the flow leaves the test rig at $z/R=7.6$. The swirl induced in the riser tube by the bypass reaches values of 0.2, which is about twice as high as in the base case. Nevertheless, from the momentum transfer point of view this type of flow is capable to cool the MEGAPIE target adequately.

The flow pattern described above remains unchanged for main/bypass flow ratios from 12 to 20, except for the location of the stagnation point and its neighborhood. The stagnation point moves for larger main/bypass flow ratios nearer to the symmetry line. Undergoing a main to bypass flow ratio of 12 the stagnation point start oscillating and below a ratio of 10 a large more or less stagnant fluid domain close to the center line establishes as depicted in photograph 5b. This is caused by a reflection of the bypass jet at the hemispherical walls due to the high momentum of the jet flow. This effect leads in principle to the same pattern as before only the

recirculation area decreases a little. But, the appearance of a stagnation zone at the centerline leads to an uncoolability of the MEGAPIE window and hence has to be avoided in practice.

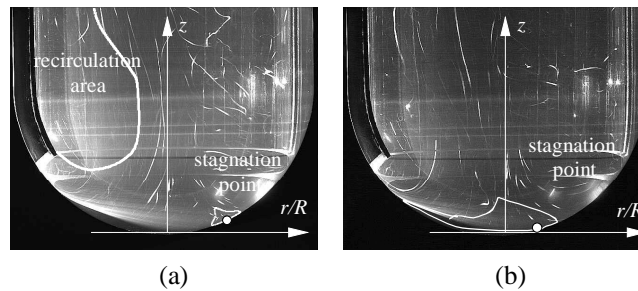


Figure 6: LLS-Photographs at the lower beam window for $Re=6 \cdot 10^4$. (a) $Q_{main}/Q_{bypass}=15$ (b) $Q_{main}/Q_{bypass}=10$. The bypass is black painted on the left side. In both graphs the illumination time is 196ms.

Another possibility for an effective window cooling is to slant the riser tube and additionally rotate the nozzle exit versus the slantation. Such a configuration is depicted in figure 7. For a flow rate ratio $Q_{main}/Q_{bypass}=15$ qualitatively approximately the same flow pattern as in the case discussed above has been obtained and a coolability of the window can be expected. But, superposed to the described flow pattern a strong swirl flow is induced. This swirl flow expressed by the horizontal lines in the LLS of figure 7c reaches magnitudes of 0.5 of the main axial flow and hence leads to a strong mixing of the fluid within the riser.

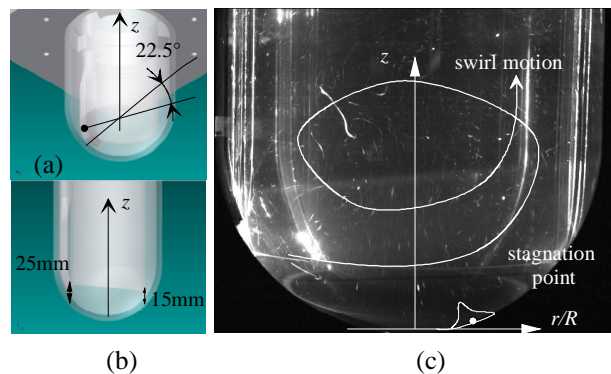


Figure 7: Arrangement of bypass nozzle and slanted riser tube in the MEGAPIE HTAS arrangement (a, b). LLS-Photographs at the lower part of the beam window at $Re=6 \cdot 10^4$ and $Q_{main}/Q_{bypass}=15$. The bypass is black painted on the left hand side. In both graphs the illumination time is 49ms

HEATED JET AND KILOPIE EXPERIMENT

The MEGAPIE window facing the proton beam proton beam produced in the SINQ facility at the Paul-Scherrer Institute has to withstand surface heat fluxes up to $140W/cm^2$ and in case of miscellaneous beam focusing up to $200W/cm^2$. Although this is only a minor part ($<10\%$) of total heat released in the target it represents one of the most critical technically to be solved issues for a liquid metal cooled target. In order to minimize the heat release in the structural material the window itself made of a 2.5mm thin martensitic steel T91 (9Cr-1MoVNb) sheet.

The simulation of a 1:1 heat production scenario as in SINQ is out of the question, since a volumetric heating by means of electric AC fields is in liquid metals due to the magnetohydrodynamic coupling almost impracticable.

Thus, regarding the MEGAPIE test two problems has to be experimentally solved, in order validate CFD codes currently being developed:

The turbulent mixing of cold and hot streams in liquids with low molecular Prandtl number.

Simulation of the coolability of the window at MEGAPIE similar surface heat fluxes.

The first can be easily achieved within the THEADES loop of KALLA by injecting overheated lead bismuth ($\Delta T=120^{\circ}\text{C}$) via the bypass tube into the relatively cold main flow. In this configuration the window hemispheres thickness can be thick. The specific instrumentation for this experiment is the same as for the later on described KILOPIE experiment except for the thermocouple instrumentation in the hemisphere. The instrumentation of the riser tube in both the heated jet and the KILOPIE experiment is the same and shown in figure 8. The thermocouples being used are mantled NiCr-Ni elements with an outer diameter of 0.5mm. This experiment is readily fabricated and will start up in March 2003.

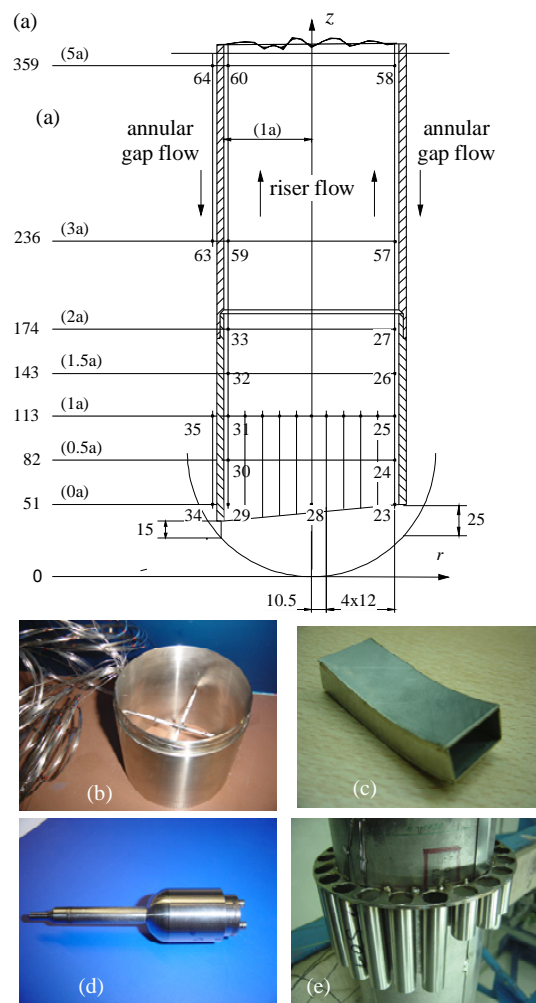


Figure 8: Coordinate system and TE instrumentation in the riser tube of the Heated Jet and KILOPIE experiment in KALLA (dimensions in characteristic length a and mm). (b) lower end of riser tube. (c) Nozzle; (d) Prandtl tube for velocity measurement and (d) flow straightener at the annular gap inlet flow.

In order to simulate a MEGAPIE relevant surface heat flux an electric resistance heating systems has been invented by Patorski et al. [2] which is capable attaining surface heat fluxes up to 140 W/cm^2 . It consists in principle of a $50 \mu\text{m}$ thick nickel foil, which is glued to dish and DC current heated. Attached to the nickel foils are

spring loaded needles, with which local potential differences can be acquired. The measured local potential differences correspond to local heat transfer coefficients α and are thus reflecting the local temperatures.

Using the HETSS heating and acquiring technique different proton beam shapes as they appear in SINQ [3] can be simulated and investigated. A sketch of the HETSS experimental set-up is illustrated in figure 9.

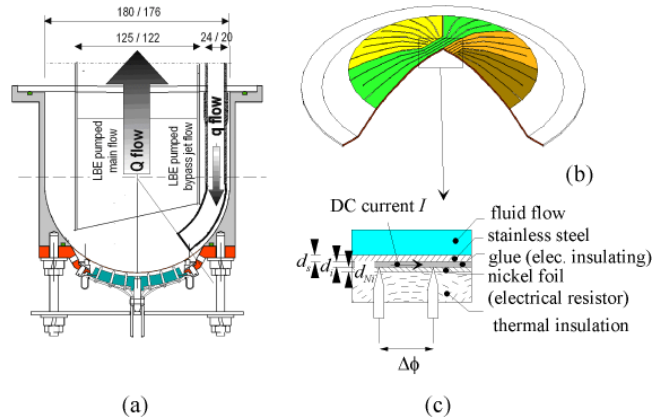


Figure 9: (a) KILOPIE HETSS configuration. (b) Nickel heating foil (from Patorski et al. [2]). (c) cut through a HETSS element.

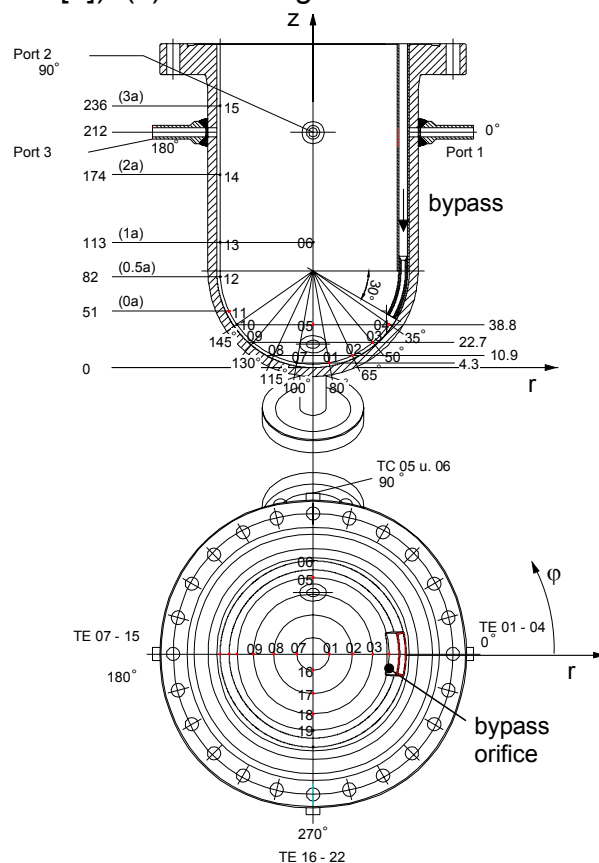


Figure 10: TE instrumentation of the Heated Jet experiment in KALLA.

The exchange of Heated Jet experiment and the KILOPIE experiment can be easily performed by screwing off the lower flange, shown in figure 11 and mounting the KILOPIE test part. The other environment especially regarding the pressure sensors, the velocity sensor and the loop connection are the same. The dimensions of the entire window test module corresponds to the MEGAPIE geometry. Also the instrumentation rod is embedded in the test module. Here, however, instead of a

neutron flux measurement device as foreseen for the real in-pile module, a combined pressure and velocity sensors is installed.

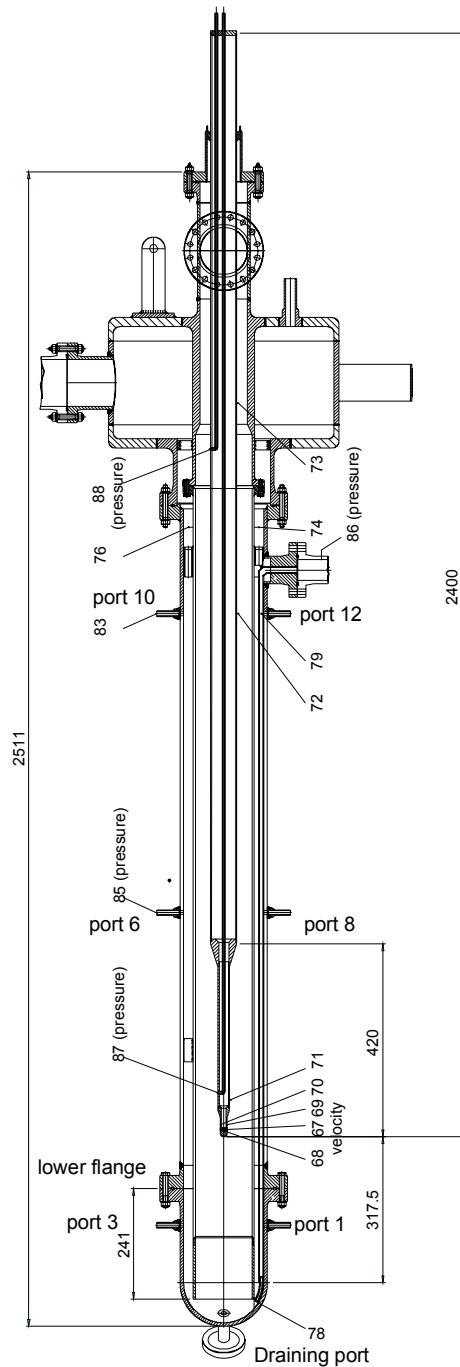


Figure 11: MEGAPIE window test module being set-up in the THEADES loop of the KALLA facility at FZK.

The total instrumentation MEGAPIE module test excluding the HETSS experiment amounts to 96 thermocouples, 4 pressure transducers (resolution ± 3 mbar) and 2 velocity sensors. An experimental campaign of the KILOPIE experiment can also be expected after the Heated Jet experiment in spring 2003.

SYNTHESIS

A set of complementary experiments related to the lead bismuth cooled MEGAPIE target development is currently under investigation at the Forschungszentrum

Karlsruhe. Experiments in a water filled plexiglass module of the MEGAPIE module, in which LDA measurements have been performed, have shown that at window relevant conditions even without a bypass jet no stagnating regions appear. A strong turbulent mixing in the backward riser flow was measured, where the highest volumetric heat is released. In all configurations with MEGAPIE relevant main to bypass flow ratios ($10 \leq Q_{main}/Q_{bypass} \leq 20$) the turbulent momentum exchange is dramatically enhanced. and the flow loses its symmetry. If additionally the riser tube is slanted a swirl motion with significant circumferential velocities is generated. A rotational shift of the nozzle with respect to the slanted riser tube increases this effect. Both of the latter measures very likely lead to a better cooling characteristics of the MEGAPIE beam window.

Simultaneously to the water experiments, in which the kinetic energy exchange and the flow field is investigated a set of heat transfer experiments in lead bismuth at window relevant conditions in a 1:1 geometry is in preparation and will start up in march 2003. The fabrication and instrumentation with thermocouples, pressure sensors and velocity sensors is finished. The THEADES loop of KALLA is commissioned and passed two test runs in november 2002 and february 2003 sucessfully. A security concept for the KILOPIE experiment is already licensed by the authorities.

Acknowledgements

This work is supported by the HGF Strategy Fund Project under the Förderkennzeichen 01SF9926/3.

References

- [1] B. Smith, 2002, Summary of the First CFD Benchmark Study. PSI-Internal Report *MPBE-4-BR-1/0*, 2002.
- [2] J.A. Patorski, G.S. Bauer, I. Platnieks, Y. Takeda, "Experimental estimation of optimum Bypass-jet-flow conditions for the cooling of the window of the SINQ liquid metal target", *PSI Report 2000*, ISSN 1423-7350, Vol. VI, pp.42-44, PSI, CH-5232 Villigen, Switzerland.
- [3] T. Dury, "Best-estimate fit for MEGAPIE Heat Deposition Profile Data of 19.2.01", PSI Memorandum, 22.03.2001, PSI, CH-5232 Villigen, Switzerland.

CFD ANALYSIS OF THE FLOW BEHAVIOUR IN A SPALLATION TARGET

A.Batta, N. I. Tak, G. Grötzbach, X. Cheng, Forschungszentrum Karlsruhe GmbH, Institut für Kern- und Energietechnik, Postfach 3640, 76021 Karlsruhe, Germany

INTRODUCTION

The MEGAPIE spallation target is the first lead-bismuth target worldwide, which will be put into test at the SINQ accelerator of Paul Scherrer Institute [1]. The Forschungszentrum Karlsruhe is strongly involved in the design of the active part of the target. The contribution of the Forschungszentrum Karlsruhe consists of both experimental and numerical studies. Experiments using water and lead-bismuth are being carried out to assess the fluid-dynamic and thermal performance of the target [2].

In addition to the experimental work, numerical analysis is performed using CFD (computational fluid dynamics) codes [3]. In the international community of target design, it is agreed that more reliable physical models, especially turbulence models, are required for the design of a spallation target with liquid metal cooling [4]. Besides some specific problems coupled with the fluid properties of heavy liquid metals, there is still a big deficiency in the experience of the CFD application to the target geometry. The present work is concentrated on the assessment of the applicability of CFD codes on target geometries. The flow in the active part of the target is usually accompanied with recirculation and boundary layer separation. The suitability of standard turbulence models, which are used in commercial codes, needs to be assessed for the proper simulation of this flow and heat transfer behaviour. In addition to the selection of turbulence models, the treatment of the wall boundary layer and the selection of the computational domain are also important issues and have to be assessed.

In the present work, the effect of some of the above mentioned parameters are investigated using the CFD codes CFX 4.4 and CFX 5.5.1 to analyse an adiabatic water experiment. Based on the results achieved so far, recommendations are made for further studies and for generating experimental data for a benchmark exercise.

NUMERICAL ANALYSIS

The MEGAPIE target was considered as the reference target for the following numerical analysis. In the conceptual design phase of the MEGAPIE target, several design concepts were proposed for effective cooling of the window and the target itself [3]. In the first design configuration there is no bypass injection and the guide tube is cut horizontally. The present numerical work is focused on this first configuration. Selection of this configuration enables the coupling of the numerical analysis with the model experiment at the HYTAS facility [5], where the flow field is investigated using laser measurement techniques. This provides in the future the possibility of a comparison of the numerical results with experimental data. A photo of the test section of the HYTAS experiment is given in Figure 1, whereas Figure 2 presents the dimensions of the geometry.

Table 1 summarizes the parameters and their ranges studied in the present work. The flow domain is geometrically axisymmetric. With axisymmetric inlet conditions and boundary conditions, a two-dimensional flow would be expected. To assess the effect of the treatment of the flow domain, three different kinds of computational configurations are selected, i.e. a 2-D axisymmetric, a 3-D half-scale (180°), and a 3-D full-scale (360°) configuration.

Table 1 Studied parameters and their ranges.

Parameter	Ranges
Flow domain	2D axisymmetric, 3-D half-scale (180°), 3-D full-scale (360°)
Mesh effect	Different meshes for 2-D and 3-D flow domains
Turbulence model	$k-\varepsilon$, RNG $k-\varepsilon$ low Re $k-\varepsilon$, $k-\omega$ SST
Reynolds numbers	10,000, 20,000, 40,000, 60,000



Figure 1: Photo of the HYTAS experiment

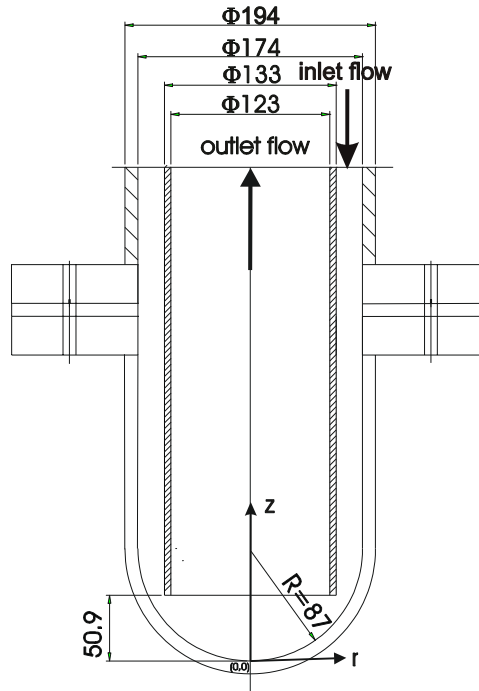


Figure 2: Reference geometry of the target considered

In the present study, five turbulence models are selected to assess their effect on the calculated velocity field, see Table 1. The SST turbulence model (Shear Stress Transport) is a modified version of the $k-\omega$ model in CFX 5.5.1 [6]. Coupled with the turbulence models, the mesh sizes in the near the wall region are adapted adequately. Flow with Reynolds numbers from 10,000 to 60,000 was analysed, where Re is based on the flow parameters in the annular gap. The thermal-physical properties of water at 20 °C were used.

EFFECT OF MESH

A 2D axisymmetric flow domain and the standard $k-\varepsilon$ turbulence model are selected for the investigation of the mesh effect. Five different sizes of meshes are tested, and two kinds of different block structures are generated for the comparison. One block structure uses a nearly overall uniform grid and the other block structure uses a thin block near the window to achieve a constant grid spacing there. The calculations are performed for the flow conditions of $Re=40,000$. For the comparison of the influence of different tested meshes on the flow fields, the axial velocity W along a radial line (ML1) at $z=0.097$ m and along an axial line (ML2) at $r=0$ are presented in Figure 2. Qualitatively, the results widely coincide. Especially, the small recirculation near the window is well recorded in the W -profile by all grids. Quantitatively, the results show deviations of 10-12%.

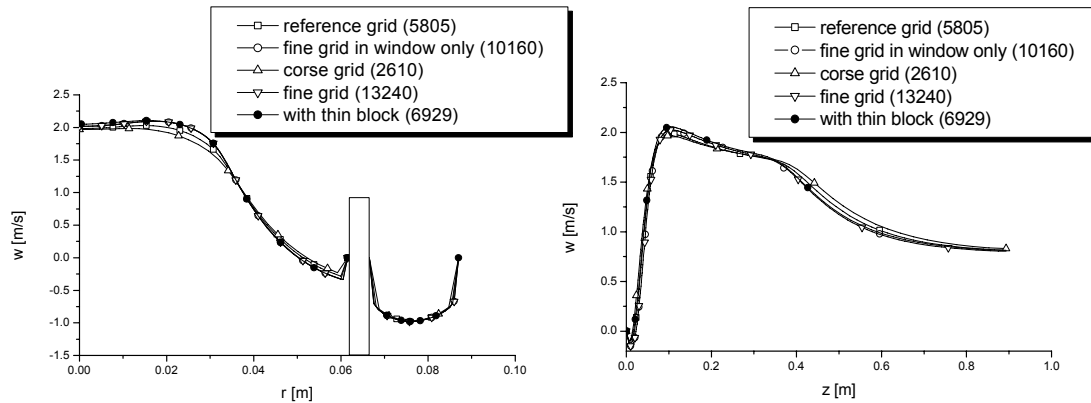


Figure 2. Axial velocities W along ML1 and ML2 with different meshes.

EFFECT OF TURBULENCE MODEL

To study the effect of various turbulence models, the 2D axisymmetrical flow domain is selected. The calculations are done for $Re=10,000$ to minimize the number of grids which are required for application of the low Reynolds number turbulence models. Structured grids are used for both, for CFX 4.4 and CFX 5.5.1. Special care is taken in the preparation of grids to satisfy the turbulence model requirements regarding suitable y^+ values. The predicted W velocities along ML1 and ML2 are given in Figure 3.

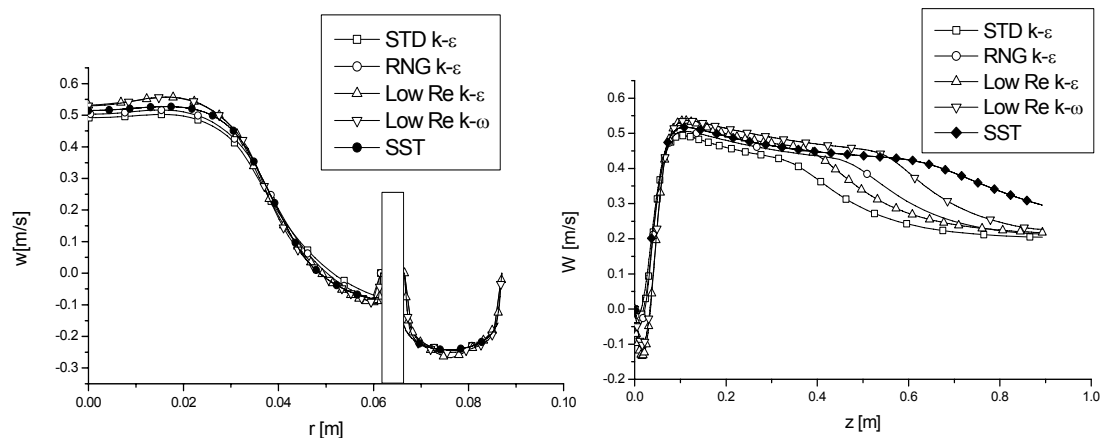


Figure 3. Axial velocities W with different turbulence models at ML1 and ML2.

The maximum W velocity values which are predicted by the five turbulence models differ by about 10%. However, there exist significant qualitative differences in the flow fields near the window centre and in the region down stream of the riser part ($z = \sim 0.6$ m). In the prediction of the flow near the window, the SST turbulence model doesn't predict any recirculation while the other turbulence models do. In the region down stream of the riser part, large differences in the flow fields exist. This result seems to be very important because it shows that experimental data are required for the validation of the turbulence models, especially in certain regions, i.e. between $z=0.4$ and 0.6 m,.

EFFECT OF COMPUTATIONAL DOMAIN

Three types of computational domains are tested using CFX 5.5.1: The 2D axisymmetric flow domain, the 3D half (180°), and the full (360°) model. The same turbulence models and similar sizes of grids are used for the calculations to minimize the unwanted effects. Figure 4 shows the W velocity profiles along ML2 resulting from three different computational domains with the SST model. Locally,

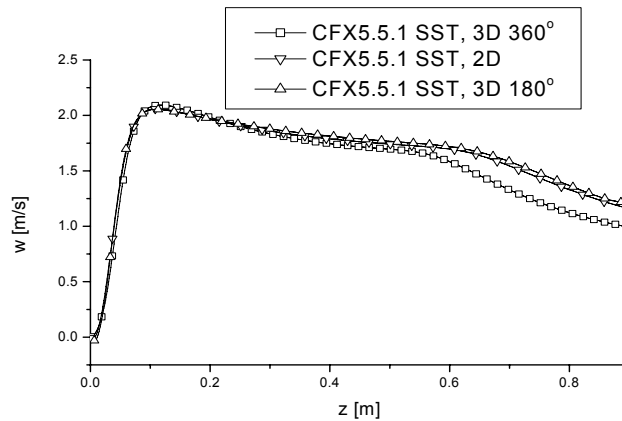


Figure 4: Axial velocity w along ML2 by three different computational domains with the SST model, $Re=40000$.

differences of up to 20 % are observed in the magnitude of the W velocity component.

An other comparison using the standard $k-\epsilon$ turbulence model shows that the results of calculations by three different computational domains are not so sensitive, they are nearly identical.

CONCLUSIONS

Three kinds of modelling effects in the numerical analysis of the adiabatic HYTAS experiments without bypass injection were investigated in the present paper: The effects of different meshes, turbulence models, and computational domains. Among them, the effect of the turbulence models is the most significant one. In other words, the present results strongly support the fact that the suitable selection of a turbulence model is a very important parameter for the design of the flow field in the special MEGAPIE target geometry. Therefore, the ongoing HYTAS experiments are considered to be very important for the validation of numerical models. In addition, it is concluded that measurements of the axial velocity upstream of the riser part in the range of $z \sim 0.6$ m are required to select an adequate turbulence model. Later, the selected model will be used to analyse the target experiments with heat transfer which will be performed in lead-bismuth in the KALLA facility [7].

References

- [1] G. Bauer et al., Description of SINQ and Boundary Conditions for MEGAPIE, 1st MEGAPIE General Meeting, CEA, Cadarache, June 14-15, 2000
- [2] J.U. Knebel et al, Water and Lead-Bismuth Experiments for MEGAPIE, MEGAPIE Technical Review Meeting, ENEA, Bologna , 5.-6., March 2002.
- [3] N. I. Tak, X. Cheng, Wissenschaftliche Berichte, FZKA 6611, June 2001
- [4] Carteciano, L. N., Wörner, M., Grötzbach, G., Erweiterte Turbulenzmodelle für technische Anwendungen von FLUTAN auf Naturkonvektion. Jahrestagung Kerntechnik 1999, INFORUM Bonn 1999, S. 129 - 133
- [5] C. Pettan, et al, HYTAS Water Experiments on Beam Window Design, Wissenschaftliche Berichte, FZKA 6741, pp. 422-424, June 2002
- [6] CFX 5.5.1 manuals, AEA Technology Engineering Software Ltd, 2002
- [7] J.U. Knebel et al, Wissenschaftliche Berichte, FZKA 6618, September 2001

SESSION 4: NUCLEAR ASSESSMENT + MATERIALS & RADIATION DAMAGE

NUCLEAR ASSESSMENT OF THE MEGAPIE TARGET

Y. Foucher

Spallation group, SUBATECH Laboratory, 4 rue Alfred Kastler, BP 20722, 44307 Nantes Cedex 3, France

Abstract

Based on an initiative of PSI (Switzerland), CEA (France) and FZK (Germany), the MEGAPIE (MEGAwatt Pilot Experiment) project [1] was started to design, built, safely operate and decommission an exploratory liquid lead-bismuth spallation target of 1 MW beam power, taking advantage of the existing spallation neutron facility and accelerator complex SINQ, at PSI. One of the goals of the neutronic and nuclear assessment is to give requirements and contributions for design, safety and operation. The present report will summarize the nuclear calculations performed with the FLUKA transport code (power deposition in the structural materials and in the Pb-Bi, nuclide inventory, dpa and gas production (H, He) in the target windows). Many of those results have been compared with the MCNPX code in order to give a first idea of sensitivity of the results as a function of the code used. A first approach of the evaluation of uncertainties will be also given.

Introduction

The study and development of spallation targets, which are complex systems, require multiple numerical simulations in order to:

- optimize the target neutronic (maximize the neutron production and improve the yield),
- answer to special requirements related to the conception, realization and reliability of the target, to the safety studies and to the Post-Irradiation Examination.

Those simulations have been performed with the FLUKA transport code.

The FLUKA Transport code

During the last ten years, researchers of the INFN Milan have developed a code, named FLUKA (FLUctuating KAscades) [2], [3], [4] for particle transport (neutral, charged, γ ...). This code simulates the nucleons-nuclei interactions for a few GeV down to the reaction threshold with the PEANUT (Pre-Equilibrium Approach to NUclear Thermalization) algorithm. This algorithm is based on:

- a Generalized Intranuclear Cascade,
- a Pre-equilibrium model,
- an Evaporation / Fission / Fermi Break up model,
- a Residual nuclei desexcitation model.

The low energy transport is made by a multigroup approach: 72 groups for neutrons transport (from 10^{-5} eV to 19.6 MeV) and 22 groups for gamma transport (from 10^{-5} eV to 20 MeV).

Simulation parameters

Beam profile

The information concerning the beam profile is essential because it will govern the power deposition profiles in the structural beam window materials and the material damages. The beam profile has been calculated in 2001 [5], by inserting in the beam line the 4 cm graphite target E. According to those calculations, the beam profile on SINQ is not completely gaussian. The figure 1 (left) shows the current density profile used for the MEGAPIE target simulations as a function of the X and Y axis (for $Y = 0$ cm and $Y = 0$ cm respectively). The current density is maximum in the center and reach $51.75 \mu\text{A}/\text{cm}^2$ (for a beam intensity of 1.74 mA).

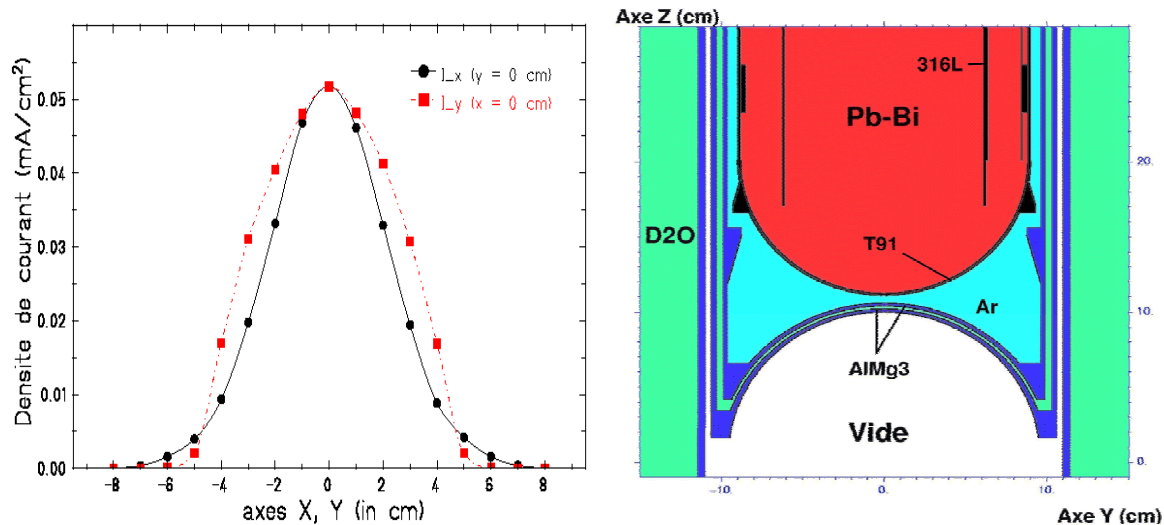


Figure 1 : Current density (mA/cm^2) at the centre as a function of the position X and Y (left). (Y, Z) view of the lower part of the simulated target geometry (right).

Target geometry

The calculations, performed with the FLUKA transport code, are using the geometry describe in the figure 1 (right). It deals with a vertical cut of the lower part of the MEGAPIE target which takes into account the different target windows (AlMg3 and T91), the inner guide tube, the bypass flow guide tube, the catchers which avoid the complete T91 window falling on the AlMg3 target lower enclosures and the central rod tube for instrumentation. Simulations have to be close to the MEGAPIE target design. Nevertheless, by taking into account of the FLUKA limitations in term of surface definition, some simplifications have been done. Indeed, the shape of the double AlMg3 shell cooled with D_2O is not plane in its junction between the target window and the cylindrical part. Those simplifications have no influence on the results (power deposition, residual production, ...).

Target materials

The materials used for the MEGAPIE spallation target, the structural materials are:

- T91 steel for the liquid eutectic Pb-Bi container,
- AlMg3 alloy for the lower target enclosures cooled with D_2O and the moderator vessel,
- A316L stainless steel for the inner guide tube, the bypass guide tube, the spacers and the central rod,
- D_2O between the target lower enclosures (AlMg3) and as a neutron moderator,

- Ar between the T91 container and the internal AlMg3 window,
- Liquid eutectic Pb-Bi for neutron generation.

The table 1 represents the mass fraction of the main elements constituting the target materials as they are used in the calculations. The density of each target material is defined in the table 2.

Material	Pb	Bi	Al	Fe	Cr	Ni	Mg	Mo	Mn	Si	Cu
Pb-Bi	44.5	55.5									
T91				88.57	9.0	0.2		1.0	0.5	0.3	
AlMg3			96.26	0.26	0.042	0.004	2.83		0.39	0.09	0.023
A316L				64.76	17.5	12.5		2.5	1.9	0.4	0.2

Table 1 : Mass fraction (%) of the main elements constituting the Pb-Bi, T91, AlMg3 and A316L.

Material	Density (g/cm ³)
Pb-Bi	10.46
D₂O	1.106
H₂O	1.00
T91	7.76
A316L	7.958
AlMg3	2.66
Ar	1.396E-3

Table 2 : Material density.

Results & discussions

Power deposition in the target

The normal operating conditions are defined by the beam profile represented in figure 1 (left). The table 3 shows a comparison between the predictions of the FLUKA and MCNPX [6], version 2.4., codes concerning the dissipated power in the MEGAPIE target. The agreement between the 2 codes is good within a relative difference less than 5%.

Approximately 85% of the beam power is dissipated in target-moderator system, the rest is dissipated in the surrounding region (shielding). 71% of the beam power is dissipated in the Pb-Bi, 11.4% in the moderator (H₂O and D₂O). Although only 2% of the beam power is dissipated in the structural materials (T91 and AlMg3), a cooling system is required. The table 3 provides only the order of magnitude of the power deposition in the system: a more detailed map of the power deposition in the materials (Pb-Bi, AlMg3, T91 and A316L) is required in order to:

- evaluate the thermal-mechanical constraints on materials,
- optimize the efficiency of the window cooling with parametrical studies in fluid mechanics,
- study the ability to transport the heat from its production zone (in the lower part of the target) to the heat exchanger located in the upper part of the target.

Materials	FLUKA		MCNPX	
	Power (kW)	% of total	Power (kW)	% Of total
Pb-Bi	710.8	71	708.2	70.8
T91	8.603	0.90	8.942	0.90
Spherical	5.56		5.87	
Cylindrical	2.68		2.64	
Catcher	0.363		0.432	
AlMg3 external	4.153	0.42	4.212	0.42
Spherical	2.536		2.646	
Cylindrical	1.617		1.566	
D₂O	3.829	0.38	3.96	0.40
AlMg3 internal	4.478	0.45	4.602	0.46
Spherical	2.593		2.71	
Cylindrical	1.680		1.654	
Catcher	0.205		0.238	
Inner guide tube	5.552	0.56	5.228	0.52
A316L				
Ar	0.012		0.016	
Moderator	114.4	11.4	115.4	11.5
Total	851.8	85.2	850.6	85.1

Table 3 : Power deposition in the MEGAPIE target evaluated with the FLUKA and MCNPX codes.

Power deposition in the structural materials

The figure 2 represents the power deposition profiles in the target windows (AlMg3 and T91) as a function of the X axis (for Y = 0 cm) for a beam intensity of 1.74 mA. The power deposition in the materials follows the same profile. The power is maximum in the center and decrease as a function of the axial position X.

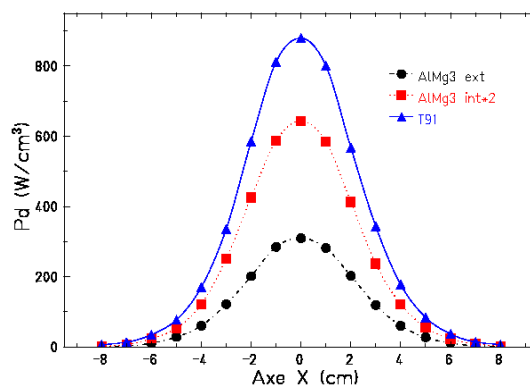


Figure 2 : Power deposition in the target windows (AlMg3 and T91) as a function of the X axis (Y = 0 cm) for a beam intensity of 1.74 mA.

The maximum values of the power deposition in the materials, predicted by FLUKA and MCNPX are given in the table 4. The relative difference between codes results is less than 5%.

Materials	FLUKA	MCNPX	FLUKA/MCNPX
T91	879.5	924.8	0.95
AlMg3 external	309.4	321.1	0.95
AlMg3 internal	321.9	330.4	0.97

Table 4 : Maximum power deposition (W/cm^3) in the structural materials of the MEGAPIE target.

The power deposition distribution in the materials is depending on the beam current density profile. In this case, the current density profile is defined by the position dependant matrix $I(x, y)$. Power deposition and current density are linked by the following relation:

$$P_d(x, y) = \lambda \cdot I(x, y)$$

Materials	T91	AlMg3 external	AlMg3 internal
λ ($\text{W}/\text{cm}/\text{mA}$)	17000	5980	6220

Table 5 : Values of the λ parameter as a function of the material

Power deposition in the Pb-Bi

In order to present the power deposition in the Pb-Bi, we are looking to the dissipated power in the central part of the target and to the evolution of the axial components of the power deposition. The map of the power deposition is represented in the figure 3 (central on the left curve and axial evolution on the right curve). Those 2 curves have been represented as a function of the altitude Z. The beam intensity taking into account for those calculations is 1.74 mA.

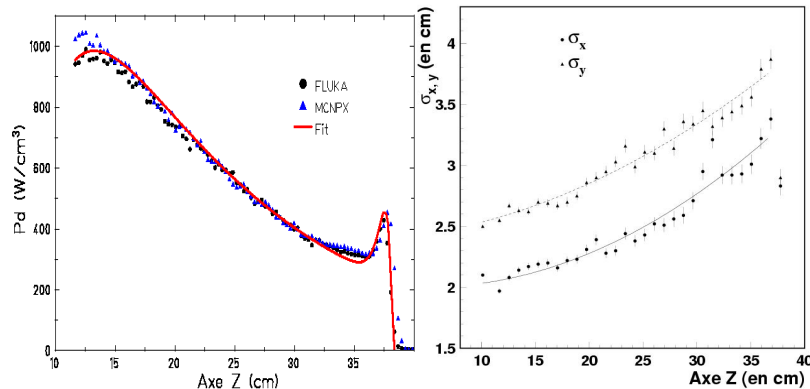


Figure 3 : Dissipated power in the Pb-Bi in the central part of the target ($r < 0.3$ cm, left curve, for FLUKA and MCNPX) and the evolution of the axial components $\sigma_{x, y}$ (right curve only for FLUKA) as a function of the altitude Z for a beam intensity of 1.74 mA

The Pb-Bi begins at $Z = 11.25$ cm. The shape of the figure 3 (left) is characteristic of the power deposition in the central part of a spallation target. The power deposition increase to reach 1 kW/cm^3 at $Z = 13.25$ cm. Then the power deposition decrease until $Z = 35$ cm. Charged particles do not have enough energy to go through the Pb-Bi and loose all their energy in the same region (Bragg Peak around $Z = 37$ cm). The power deposition distribution as a function of the X and Y axis, for a given altitude Z is quasi-gaussian. It is possible to fit each curve and to determine the corresponding σ . The evolution of σ as a function of the altitude Z is quadratic (figure 3: right). The analytical function defining the power deposition in the Pb-Bi is:

$$P_d(x, y, z) = G(z) \cdot D(x, y, z)$$

$$G(z) = A \cdot e^{-\frac{z-11.25}{z_a}} \left[1 - e^{-\frac{z+z_b}{z_c}} \right] \cdot \left[1 + B(z_d - z) \cdot e^{-\frac{|z_d - z|}{z_e}} \right]$$

$$D(x, y, z) = e^{-\frac{1}{2} \left[\left(\frac{x}{\sigma_x(z)} \right)^2 + \left(\frac{y}{\sigma_y(z)} \right)^2 \right]}$$

$$\sigma_{x,y}(z) = a_{x,y} + b_{x,y} \cdot z + c_{x,y} \cdot z^2$$

with :	$A = 1480 \text{ W/cm}^3$	$B = 5.5 \text{ cm}^{-1}$	$Z_a = 14.5 \text{ cm}$
	$Z_b = -6.75 \text{ cm}$	$Z_c = 4.5 \text{ cm}$	$Z_d = 38.05 \text{ cm}$
	$Z_e = 0.45 \text{ cm}$	$a_x = 2.03 \text{ cm}$	$b_x = -1,17 \cdot 10^{-2}$
	$c_x = 1,21 \cdot 10^{-3} \text{ cm}^{-1}$	$a_y = 2.38 \text{ cm}$	$b_y = 6,67 \cdot 10^{-3}$
	$c_y = 8,40 \cdot 10^{-4} \text{ cm}^{-1}$		

The term $G(z)$ is fitting the central part of the power deposition in the Pb-Bi and the term $D(x,y,z)$ is fitting the evolution of the axial components of the power deposition.

The interaction of the proton beam with the structural materials of the target will generate thermal and mechanical constraints on them.

A comparison between the results of the FLUKA and MCNPX codes concerning power deposition in the MEGAPIE target materials shows that the agreement between codes is satisfying. Indeed, the relative difference between codes is less than 5%, which allows to be confident for the future thermo-mechanical and thermo-hydraulical calculations.

The power deposition calculations in the target windows are used as data bases for thermo-mechanical calculations which allows to optimize the target window geometry (thickness and shape).

The study of the T91 window cooling and of the Pb-Bi flow (heat transport) in the target require to know the power deposition in the Pb-Bi and in the structural materials. Those studies are performed with thermo-hydraulical codes.

Spallation residue production

The interaction of the proton beam with the eutectic Pb-Bi generate many elements more or less stable. For many reasons, it is important to study the spallation residues produced:

- change of the physico-chemical behaviour of the liquid Pb-Bi (solid liquid interaction: corrosion phenomena),
- gamma emitter production which will circulate inside the target,
- volatile element production (gas, Hg, ...) and α emitters (Po-210 mainly),
- residual heat production after shutting down the beam.

The production rates are determined using the FLUKA code. Those data are used by ORIHET3 [7] which deals with the time evolution of the production, activity ... After having received 6 A.h (1.25 mA during 200 days), the element production in the MEGAPIE target is represented in the figure 4.

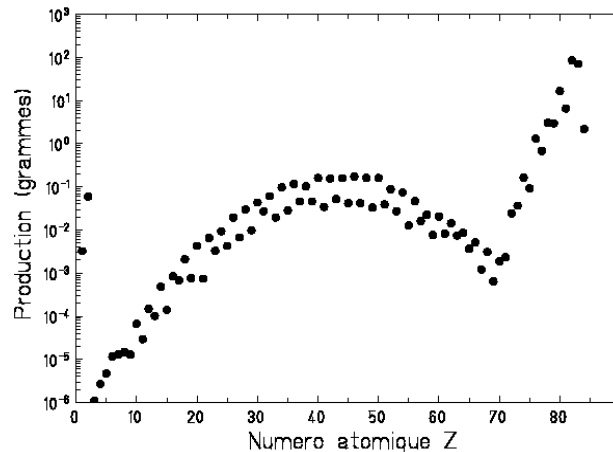


Figure 4 : Element production in the liquid Pb-Bi target for a total charge of 6 A.h (1.25 mA during 200 days).

This spectra is characteristic of the spallation reactions. It is possible to distinguish 4 zones:

- the elements which the atomic number is around the target one ($Z \approx 82.5$): spallation residues,
- the elements which the atomic number is around $Z = 40$. Those elements are produced by fission reactions,
- the light elements (He and H) which are produced during the evaporation and cascade stages,
- the intermediate mass fragments located between the light fragments and the fission zone.

We can notice 2 lines in this figure corresponding to the production of even (superior line) and odd (inferior line) elements due to the ORIHET3 treatment.

In order to give a critical point of view concerning the production of some elements produced during spallation reactions, we have performed a first approach of the uncertainty evaluation. This approach is based on comparisons between data and experiments that have been done in the reference report [8]. It is possible to distinguish 3 uncertainty sources:

- Uncertainties on the residual production cross-sections induced by protons on thin targets. For the spallation region: the ratio between FLUKA and experiments is around a factor of 2-3, and for the fission region this ratio is less than a factor of 10,
- Uncertainties on the residual production cross-sections induced by neutrons on thin targets. For this study, we have assumed the same ratio between FLUKA and experiments (factor of 2-3 for the spallation region and less than a factor of 10 for the fission region),
- Uncertainties on particle transport (neutrons and protons) in thick targets. For this study, a maximum ratio of 2 has been taken into account).

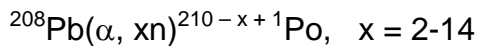
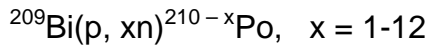
The uncertainties on the FLUKA prediction vary as a function of the region. In the field of the MEGAPIE project, we need to consider the coupling of uncertainties residual production cross-sections induced by protons and neutrons and particle transport. This gives an uncertainty on the FLUKA results of a factor 6 for the spallation region and a factor less than 20 for the fission region.

Among the isotopes produced in the target, only a few will be investigated in detail.

Polonium production

The production of polonium isotopes, mainly α emitters, in the spallation target will not cause any problems during normal operating conditions. Nevertheless, in the case of T91 window break, the polonium will evaporate.

The different production channels of polonium are:



The table 6 representing a comparison between the predictions of FLUKA and MCNPX concerning the polonium production shows the production ratio vary between 0.7 for Po-206 and 1.8 for Po-210. These variations are mainly due to nuclear data bases used by the codes and the particle fluxes (neutrons and protons).

Isotopes	Mass (g)		LiSoR	
	FLUKA	MCNPX	FLUKA/MCNPX	exp/cal
Po-206	0.032	0.043	0.74	2.46
Po-208	0.278	0.329	0.84	1.45
Po-209	0.048	0.047	1.02	
Po-210	2.04	1.15	1.77	18.4

Table 6 : Comparison between FLUKA and MCNPX predictions concerning Po production for a total charge of 6 A.h (1.25 mA during 200 days), and comparison between results from the LiSoR experiment and the FLUKA one.

Previously, we have seen that the uncertainty of the FLUKA code concerning the prediction of the elements of the spallation region was less than a factor of 6. Those

results are confirmed by the results coming from the first LiSoR experiment. As a matter of fact, concerning the production of Po-206 and Po-208, the ratio between experimental results and FLUKA is 2.5 and 1.45 respectively. The spectra of the neutrons emitted in the LiSoR experiment is a “hard” one (high energy neutrons), it is difficult to conclude when talking about FLUKA prediction on Po-210 production. Nevertheless, it will be interesting to use the neutron capture cross-section on Bi-209 measured by the Fioni group at ILL in order to estimate correctly the production of Po-210.

Gas production

Among the isotopes produced in the target, there is a few which will accumulate in the expansion tank. This will generate a pressure increase in the target that needs to be managed. A particular attention should be given to noble gas production (Ar, Kr, Xe ...), to tritium and other radioactive volatile elements. The FLUKA code predicts a He production more important than the H one, which should not be the case. The He production seems to be consistent with other codes (MCNPX), while the H production is underestimated. Indeed, the FLUKA code is not able to evaluate the production of H-1 which is mainly contributing to the production of H in the target. Data provided by FLUKA have not been taken into account for the H and He production. The table 7 represents the gas production (liters) for a total charge of 6 A.h (1.25 mA during 200 days), according to FLUKA and MCNPX.

	H	He	Ne	Ar	Kr	Xe
FLUKA	0.04	0.34	$7,97.10^{-5}$	$1,26.10^{-3}$	$3,36.10^{-2}$	$1,37.10^{-2}$
MCNPX	5.2	1.1	0	$2,9.10^{-10}$	$3,00.10^{-2}$	$1,15.10^{-2}$

Table 7 : Gas production (liters) in the target for a total charge of 6 A.h, in the CNTP conditions.

The hydrogen is main gas produced in the target (5.2 liters) and overpass the volume available for the expansion tank. The gas should be absorbed or vented during operation. The volume of the other gas produced in the target is very small. Nevertheless, some of them are radioactive and constitute a γ source: the upper part of the target should be shielded.

Mercury production

The FLUKA code predicts a production of 16.6 grams of mercury in the target for a total charge of 6 A.h (13.3 grams according to MCNPX [9]). Except the Pb and Bi, the mercury is the most abundantly produced element. The main radioactive isotopes of mercury generated are short lived elements and have a low mass production. Stable isotopes of mercury are the most abundant (see table 8).

Hg	Mass (g)	
	FLUKA	MCNPX
196	1.80	1.32
198	2.53	2.12
199	2.86	1.85
200	3.45	3.07
201	3.86	2.99

Table 8 : Production of the main mercury isotopes calculated with FLUKA and MCNPX for a total charge of 6 A.h (1.25 mA during 200 days).

The mercury concentration does not allow to modify the Pb-Bi characteristics, neither to influence the neutronic performances of the target. Nevertheless, the mercury will concentrate in the expansion tank as vapor. At 340°C, for example, with a vapor pressure of 7.10^4 Pa, the mercury do not condense on the expansion tank surfaces. A particular cold trap is now investigated in order to condense the mercury.

Damages in structural materials

The interaction of the protons beam with the MEGAPIE target will generate power deposition and nuclear reactions in the structural materials. This gives displacement per atom (dpa) and gas production (H and He) in the target windows.

Damages caused to structural materials are mainly due to protons and neutrons generated by spallation reactions. The knowledge of the spatial and energetic particle distributions is required in order to estimate dpa and gas production. These data answer to specific requirements related to:

- The conception: the figure 5 represents the evolution of the mechanical properties of the AlMg3 as a function of the irradiation conditions (dpa) [10]. The strain and stress curve shows that the more the dose (dpa) is important, the more the sample harden and brittle: for a non irradiated sample, the break is at an elongation of 22% and a constraint of 200 Mpa while for 2.5 dpa, the break is at an elongation of 8% and a constraint of 300 Mpa.
- The Post-Irradiation Examination of the target (PIE).

We are particularly interested in the target windows (AlMg3 and T91), critical elements for safety, directly exposed to the proton beam and to the generated neutrons.

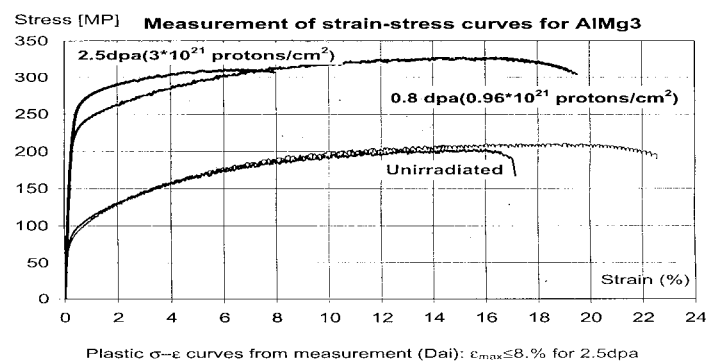


Figure 5 : Evolution of the mechanical properties of the AlMg3 as a function of the irradiated conditions (dpa).

Dpa evaluation

The number of displacement per atom (dpa) generated in the target windows (AlMg3 and T91) could be calculated from the following equation:

$$dpa = I \cdot T_{irr} \sum_{n,p} \sum_{E_{min}}^{E_{max}} \phi_{n,p}(E) \sigma_{n,p}(E)$$

For each particle (protons and neutrons), the flux must be multiply by the corresponding damage cross-section. The damage cross-sections are provided by Barnett and al [11]. They are varying as a function of the material (AlMg3 and T91) and as a function of the particle (protons and neutrons). The dpa distribution is represented on the figure 6 as a function of the X axis (Y = 0 cm) for the target windows made of AlMg3 and T91.

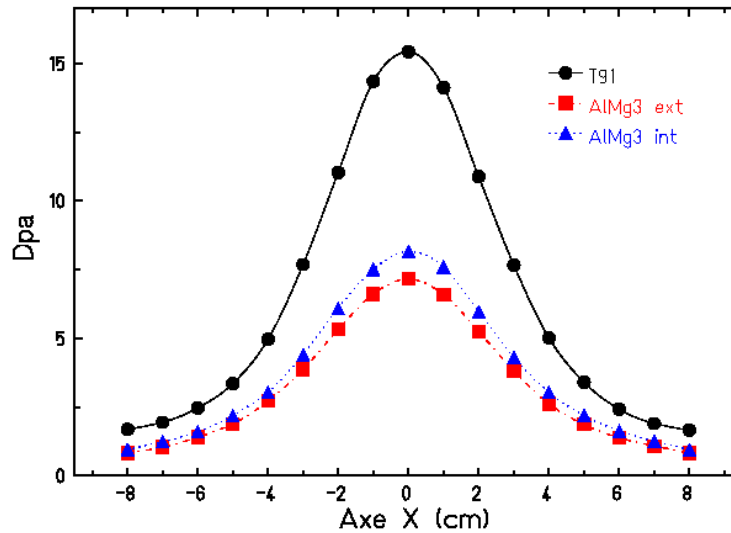


Figure 6 : Dpa distribution in the AlMg3 and T91 windows as a function of the X axis (Y = 0 cm) for a total charge of 6 A.h.

The dpa number is maximum at the centre of the target and reaches:

- 15.4 dpa in the T91 window,
- 7.2 dpa in the AlMg3 external window,
- 7.5 dpa in the AlMg3 internal window.

H & He production

The gas (H and He) production in the structural materials is calculated in the same

$$P(H, He) = 10^6 \cdot I \cdot T_{irr} \sum_{n,p} \sum_{E_{min}}^{E_{max}} \phi_{n,p}(E) \sigma_{n,p}(E)$$

way:

For each particle (p, n), the flux is multiplied by the corresponding cross-section. The cross-section are provided by Barnett and al [11].

The figure 7 shows the hydrogen (left curve) and helium (right curve) production distributions as a function of the X axis (Y = 0 cm) for a total charge of 6 A.h.

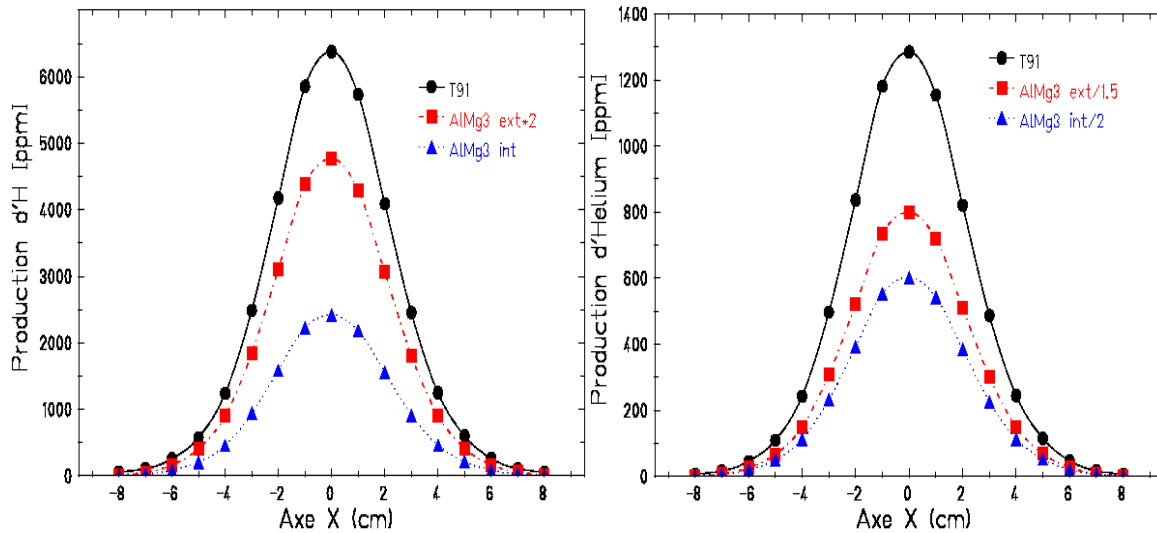


Figure 7 : H and He production distributions as a function of the X axis (Y = 0 cm) in the target windows for a total charge of 6 A.h.

The table 9 represents the maximum H and He production (appm) for the structural materials (T91 and AIMg3).

Materials	H (appm)	He (appm)
T91	6400	1285
AIMg3	2400	1200

Table 9 : Maximum H and He production (appm) in the T91 and AIMg3 windows.

Conclusion

The study and develop a liquid Pb-Bi spallation target requires numerical simulations in order to provide data bases. Power deposition in the structural materials are useful for conception, realization and reliability of the target (thermo-mechanical constraints evaluation) and for safety studies (cooling of the T91 container, extraction and transport of the heat). The evaluation of the spallation residues is needed for the Pb-Bi management after irradiation and for safety studies in case of T91 break. Finally damage evaluation is required for conception, realization (evolution of the mechanical properties under irradiation, thermo-mechanical calculations) and for the Post-Irradiation Examination of the target. Many other calculations have been performed with the FLUKA code concerning the MEGAPIE spallation target and are referred in [8]. Nevertheless, an important effort is still required in order to evaluate the calculation uncertainties.

References:

- [1] G. Bauer, "MEGAPIE Baseline Summary Report", Paul Scherrer Institut (2000).
- [2] A. Ferrari and P.R. Sala, "The Physics of High Energy Reactions", Workshop on Nuclear Reaction Data and Nuclear Reactors: Physics, Design and Safety, Trieste (1996).
- [3] A. Ferrari and al, "FLUKA: Status and Prospective for Hadronic Applications", Proceedings of the Monte-Carlo 2000 Conference, Lisbonne (2000); Springer Verlag, Berlin p 159-164 (2001).
- [4] A. Fasso and al, "Electron-Photon Transport in FLUKA: Status", Proceedings of the Monte-Carlo 2000 Conference, Lisbonne (2000); Springer Verlag, Berlin p 159-164 (2001).

- [5] U. Rohrer, "p-Strahlbreiten und Profil-Formen beim SING-Target mit und ohne Target E (4 cm graphit)", internal report PSI (2001).
- [6] L.S. Waters, "MCNPX User's Manual", Los Alamos National Laboratory (2002).
- [7] F. Atchison, "ORIHET3-version 2.12: A guide for Users", PSI (2000).
- [8] Y. Foucher, "Etude et Développement d'une Cible de Spallation", Ph-D thesis report, Nantes University (2002).
- [9] E. Pitcher, "Summary Report on Neutronics Work in Support of MEGAPIE", internal report PSI (2002).
- [10] Y. Dai, "Preliminary Examination of the Safety Hull of SING Target MARK II", PSI Scientific and Technical Report 2000, vol VI p-33 (2000).
- [11] M.H. Barnett and al, "Proceedings of the Third International Topical Meeting on Nuclear Applications of Accelerator Technology (ACCAPP99), p555 (1999).

FISSION CHAMBERS FOR NEUTRON FLUX MEASUREMENTS: STATUS REPORT

A. Letourneau, M. Fadil, F. Marie, D. Ridikas, J.C. Toussaint, C. Veyssière, CEA/DSM/DAPNIA
Ch. Blandin, CEA/DEN/SPEX/LPE

Introduction

Since one year, the possibility to measure the neutron flux inside the MEGAPIE target has been studied into detail by CEA/DSM/DAPNIA [1]. In order to determine thermal, epithermal and fast components of the neutron flux and to follow their time and space variations, 8 fission micro-chambers [2] (fig. 1) will be inserted in the central rod of the target at distances range from 32 cm to 82 cm from the target window.



Figure 8: Photography of a fission micro-chamber.

These neutron detectors will allow getting access to the neutronic performances of this unique 1MW liquid Pb-Bi spallation target, in terms of flux intensities and minor actinide transmutation capability.

Measurements of the neutron flux components

The thermal component will be measured with ^{235}U deposit fission micro-chambers. Thanks to the high thermal fission cross section of this element, the signal measured in the detector is proportional to only the thermal flux component. Due to the relatively low neutron flux, the burn-up of ^{235}U is sufficiently low ($< 0.01\%$ per hour) to monitor the neutron fluctuations with a relative time precision of 1% (precision requested for the current measurement), and high enough (10% per month) to get a calibration of the chambers (with a precision of less than 5%) with the procedure already used at ILL [3].

The epithermal component (from 1 eV to 1 MeV) will be measured with a ^{235}U deposit fission micro-chamber filtered with a 300 μm Gd envelope. The filter will reduce the thermal contribution by a factor 10^5 so that the signal will be essentially created by the epithermal neutrons. After 20 days the envelope will be burned out and the signal will be created by the thermal neutrons. In order to keep the full dynamic of the signal (with the shielding and without) a very sensible electronic is required and, in parallel, a measurement of the background signal with a no-deposit fission chamber.

The fast energy part and the transmutation capability of the spallation target will be measured with minor-actinide deposit fission chambers: ^{242}Pu and ^{241}Am , ^{237}Np , respectively. These actinides present the particularity of threshold fission (in particular ^{242}Pu) with a sharp increasing of the fission cross section above 1 MeV. It

is then possible to get access to the high energy spectrum region. The low signal (below 400 nA for ^{242}Pu) that we will obtain from these chambers requires a very precise electronic for the current measurement. In addition to the fission chambers, monitors with energy threshold reactions will be irradiated and analyzed off-line by spectroscopy. These monitors will be placed as references for the integrated neutron flux.

Proton and gamma background, including Bremsstrahlung and radiative capture processes, have been calculated with MCNPX code and compared to the neutron flux for various positions of the detectors from the target entrance. These results show a ratio, between the neutron flux and proton or gamma fluxes, of respectively 17 and 1850 at a distance of 32 cm from the target entrance. Taking into account these numbers, the impact of the protons in the fission chambers should be negligible. Concerning the gamma flux, these predictions have been compared to the same simulation and shown a ratio neutron over gamma of at least 3 for 7.10^{13} n/cm²/s. From our experience of ILL background currents, we can estimate a signal over background ratio larger than 1 within the MEGAPIE experimental conditions. In addition, the background will be corrected properly with the “no deposit” reference chambers.

Detector geometry and layout

The implantation of the neutron detectors has been carefully studied in particular with respect to the geometrical constraints of place, airtight passage, pressure and thermo mechanical properties. The proposed layout consists on a cylindrical container which will be inserted in the lower part of the central rod of the target. In order to be able to measure, at the same position, both signal and background, the inner diameter of the central rod has been enlarged from 10 mm to 13 mm. 8 micro fission chambers ($\phi=4.7$ mm) will be disposed in the container. The positions of the neutron detectors within the container and the nature of the active deposits have been determined to allow simultaneous measurements of thermal, epithermal, and fast components of the flux at different distances from the target window (fig. 2):

- 32 cm: 300 μm Gd-filter (60 μg ^{235}U deposit and no deposit) fission chambers to get epithermal component. After few days of irradiation, this chamber will be sensible only to thermal flux.
- 39 cm: 400 μg of ^{242}Pu and 200 μg of ^{241}Am deposit fission chambers to access the fast component and to probe the incineration and transmutation potential of these elements.
- 46 cm: flux monitor for off-line measurements to get the fast component and to crosscheck the validity of previous fission chambers.
- 47 cm: 40 μg ^{235}U and 200 μg ^{237}Np deposit fission chamber to get thermal component at middle position and transmutation studies.
- 77 cm: 40 μg of ^{235}U deposit (and no deposit) fission chamber to get thermal component at high position.

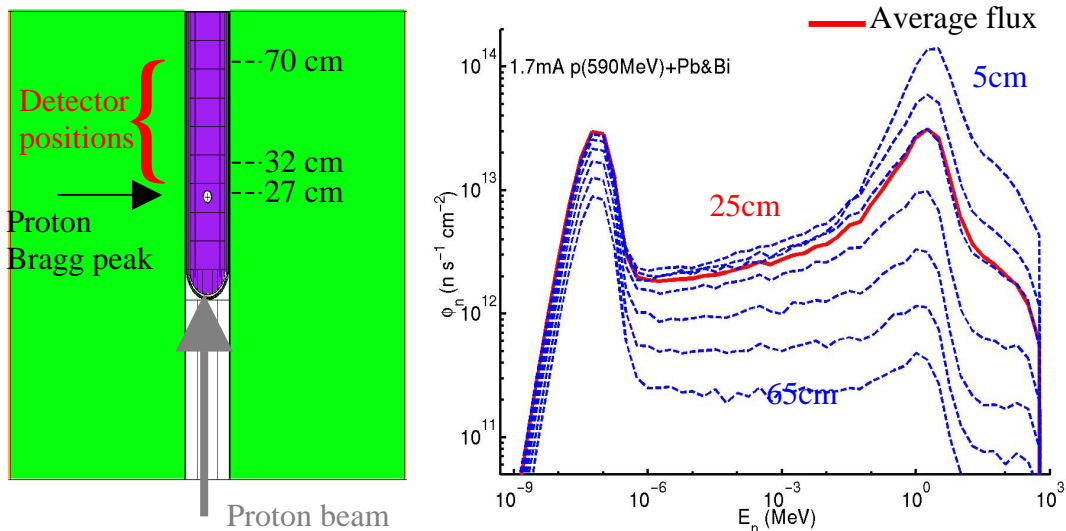


Figure 9 : Positions of the fission micro-chambers in the target and the neutron fluxes calculated with MCNPX and corresponding to different distances from the window.

The 8 chambers will be connected to 15m long mineral Thermocoax cables ($\phi=1$ mm). The container will be inserted in the target via a 4.5 m long steel pole of handling, which will remain in place as shielding during the irradiation of the target.

Experimental constraints

The experimental constraints in the MEGAPIE target are slightly different from the experience encountered at ILL: the running temperature and the low current measurement.

The running temperature conditions range from 350 to 450° C with frequent variations of 100°C in a few seconds every 20 mn approximately. Moreover, after the insertion of the detectors in the central rod, the temperature will rise up to 600° C. We are now developing fission chambers with a special device in order to absorb differential dilatations due to temperature. Moreover 4 fission chambers (2 with ^{235}U as deposit and 2 without deposit) will be constructed and irradiated this year at ILL. Before irradiation, one of these would have follow heating cycles in 700°C oven and mechanical and electrical inspection, in order to check the resistance of these new fission chambers to temperature variations.

The other point that requires dedicated studies is the new high precision acquisition system that will allow to measure currents from 100 nA to 100 μA (fig. 3) with a relative uncertainty of 1%. This high accuracy electronic will measure sequentially the current in the 8 detectors keeping their polarization stable. Two modules will be tested this year at ILL.

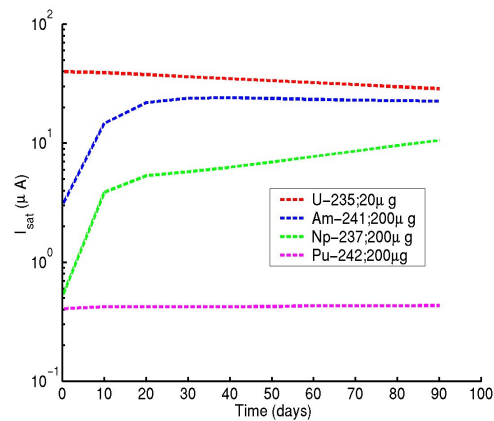


Figure 10: Estimation of the current expected from the fission micro-chambers with different deposit.

Conclusions

This project offers the unique possibility to measure on-line the neutronic performances and transmutation capabilities of the first liquid Pb-Bi spallation target. The results will define the next generation targets for the future ADS. The space and time variation of the thermal and fast components of the neutron flux will provide a wide set of data to improve the reliability of the neutron generation models and transport codes in spallation targets. Taken into account all the constraints, these measurements are challenging, but the promising results obtained with the same detectors at IL, make this goal achievable.

- [1] F. Marie et al., *Measurement of the neutron flux at MEGAPIE*, proposal at the CSTS, DAPNIA-report 16/12/2002.
- [2] M. Fadil et al., *Feasibility study of new microscopic fission chambers dedicated for ADS*, Proceeding of the 7th Information Exchange Meeting on Actinide and Fission Product P&T, Jeju, Korea, 14-16 October, 2002.
- [3] M. Fadil et al., *Development of fission micro-chambers for nuclear waste incineration studies*, NIM A476 (2002) 313.

TRIPLE ION BEAM IRRADIATION TESTS ON WINDOW MATERIALS OF SPALLATION TARGETS

M.Futakawa¹, Y.Kurata¹, J. Henry², I. Ioka³, S. Saito¹, A. Naito³

¹Center for Proton Accelerator Facilities, JAERI

²CEA/Saclay

³Department of Nuclear Energy System, JAERI

Introduction

The high-energy protons induce displacement damage and produce transmutation products, particularly hydrogen and helium in beam window materials of liquid metal targets. It is important to estimate the radiation damage for design of high-power liquid metal targets. In order to study helium effect, tensile tests and microstructure examinations were performed on 9Cr-1Mo steels implanted to 0.5 at % helium ion [1]. Furthermore, synergistic effect of displacement damage and gas atoms of hydrogen and helium should be taken into consideration. A triple ion beam facility at JAERI can be used to simulate the spallation neutron environment [2]. Triple ion beam irradiation tests on window materials of spallation targets have been conducted using TIARA (T_{akasaki} I_{on} A_{ccelerators} for A_{dvanced} R_{adiation} A_{pplication}) facility of JAERI. In this presentation, results of triple ion beam irradiation tests conducted on T91 under MEGAPIE condition are described.

Experimental Specimens

The material tested in this experiment was T91 supplied from CEA. Table 1 shows chemical composition and heat treatment of T91. Specimens used in ion irradiation tests were transmission electron microscopy (TEM) specimen discs of 3mm in diameter with 0.2mm thickness. The disks were polished electrochemically before irradiation.

Ion irradiation

Ion irradiation experiments were performed using single, dual and triple beams. Condition of beam window of MEGAPIE target is the following: 1400appm He, 10000appm H, displacement damage of 15dpa, temperature of 320°C. Table 2 shows aim irradiation condition of T91 specimens. Not only Fe³⁺ ions but also Ni³⁺ ions were used in triple beam irradiation. Fig.1 shows a triple beam target irradiated by beams from 3MV tandem accelerator, 3MV single end accelerator and 400kV ion implanter. The schematic configuration and beam condition are shown in Fig.2. 10.5MeV Fe³⁺ ions, 12MeV Ni³⁺ ions, 1.1MeV He⁺ ions and 0.38MeV H⁺ ions were used in the experiments. The damage peak of Fe³⁺ ions and Ni³⁺ ions was 1.7 – 1.8 μm, and the irradiation of helium and hydrogen ions was controlled to implant in depth ranges from 1.0 to 1.5μm. The SRIM97 code formerly known as TRIM [3] was used to compute depth profiles of implanted ions and displacement damage.

Fig.3 shows schematic diagram showing procedure to study irradiation effect using ion beam irradiation and an indentation technique. After the irradiation, load versus depth curves were obtained using a testing machine, DUH-200 (Shimadzu Co.). Birkovich indenter with $A_p/h^2=24.5$ (A_p and h are the projected area and the apex angle from the surface) was used with maximum load of 98mN.

Results and discussion

Fig.4 shows the effect of ion irradiation on load versus depth curves of T91specimens. As shown in this figure, the slope of the load-depth curve increases and the maximum depth decreases with change from single(He⁺, Fe) to dual, triple ion irradiation. Hardness can be calculated from the following two methods: Universal

hardness can be calculated from the maximum depth and the shape of the indenter tip and apparent hardness can also be calculated from the slope of a load/depth-depth curve obtained in microindentation tests. In this report, the result of the former is shown. Fig.5 indicates the effect of ion irradiation on universal hardness of T91 specimen. Each hardness datum point was calculated from ten measurements of the microindentation test. The hardness of T91 as received was about 2.5GPa at room temperature. Radiation-hardening was observed after ion irradiation at 320°C. The hardness increased after Fe³⁺ ion irradiation to 15 dpa. The effect of He⁺ ion irradiation on the hardness was small. According to the results of triple ion irradiation(Fe+He⁺+H⁺, Ni+He⁺+H⁺), it seems that there is a little effect of simultaneous He⁺ and H⁺ ion implantation on the hardness under MEGAPIE condition at 320°C.

Although the application has not been completed for T91 data yet, finite element modeling of microindentation for determining mechanical characterization of ion implanted layer has been attempted[4]. Fig.6 shows a schematic diagram showing procedure to identify material constants from indentation tests and inverse analysis. In step 1, the constitutive equation was assumed as follows:

$$\sigma = E\varepsilon, \quad \sigma \leq \sigma_y \quad (1)$$

$$\sigma = C(\varepsilon_0 + \varepsilon)^n, \quad \varepsilon_0 = (\sigma_y/C)^{1/n} - (\sigma_y/E), \quad \sigma > \sigma_y \quad (2)$$

where E is Young's modulus and σ_y is yield stress, and C and n are material constants.

In step 2, inverse analysis is conducted to obtain suitable fitting between experimental and analytical results for load-depth curves. The inverse analysis was performed using an explicit FEM code, DYNA. In step 3, tensile stress-strain curves can be drawn using material constants obtained from the inverse analysis. Fig. 7 shows examples of results of inverse analysis on load-depth curves of Inconel600 and A5056 specimens. The stress-strain curves calculated using constants estimated by inverse analysis gave a good agreement with the experimental results of tensile tests. Similar approach will be carried out for ion irradiated T91specimens.

Summary and future work

Triple ion beam irradiation tests on T91specimens were conducted under MEGAPIE condition at 320°C using TIARA facility at JAERI. The aim condition of triple ion beam irradiation was the following: 15dpa by Fe³⁺ ions or Ni³⁺ ions, 1400appm He and 10000appm H. Results of triple ion beam irradiation were compared with those of single beam irradiation (Fe³⁺, He⁺) and dual beam irradiation (Fe³⁺+He⁺). Indentation tests were performed at room temperature. Radiation-hardening was observed after ion irradiation at 320°C. Hardness increase of T91 was mainly attributed to displacement damage by Fe³⁺ or Ni³⁺ ions. There seems to be a little effect of simultaneous He⁺ and H⁺ ion implantation on the hardness under MEGAPIE condition at 320°C.

TEM observation of T91 specimens after ion beam irradiation will be performed at CEA/Saclay. Analysis of microindentation results for determining mechanical characterization of ion irradiated layer will be conducted at JAERI.

References

- [1] J.Henry et al., J.Phys.IV France 12(2002)Pr8-103.
- [2] M.S. Wechsler et al., Proc. of Symp. on Materials for Spallation Neutron Sources, Florida, 23(1997).

- [3] J.F.Ziegler et al., "The Stopping and Range of Ion in Solids", vol.1, Pergamon Press, New York(1985).
- [4] I.Ioka et al., JAERI-Review 1999-025(1999)140.

Table 1 Chemical composition of T91 specimen used for irradiation (wt %)

	C	Cr	Mo	V	Nb	Ni	Mn	P	Si
T91	0.105	8.26	0.95	0.2	0.075	0.13	0.38	0.009	0.43

Heat treatment: 1050C for 45 min + 760C for 45 min.

Table 2 Aim irradiation condition of T91for triple beam ion irradiation at TIARA facility

Temperature (C)	He (appm)	H (appm)	dpa (by Fe ³⁺ irradiation)	dpa (by Ni ³⁺ irradiation)
320	1400	-	-	-
320	-	-	15	-
320	1400	-	15	-
320	1400	10000	15	-
320	1400	10000	-	15

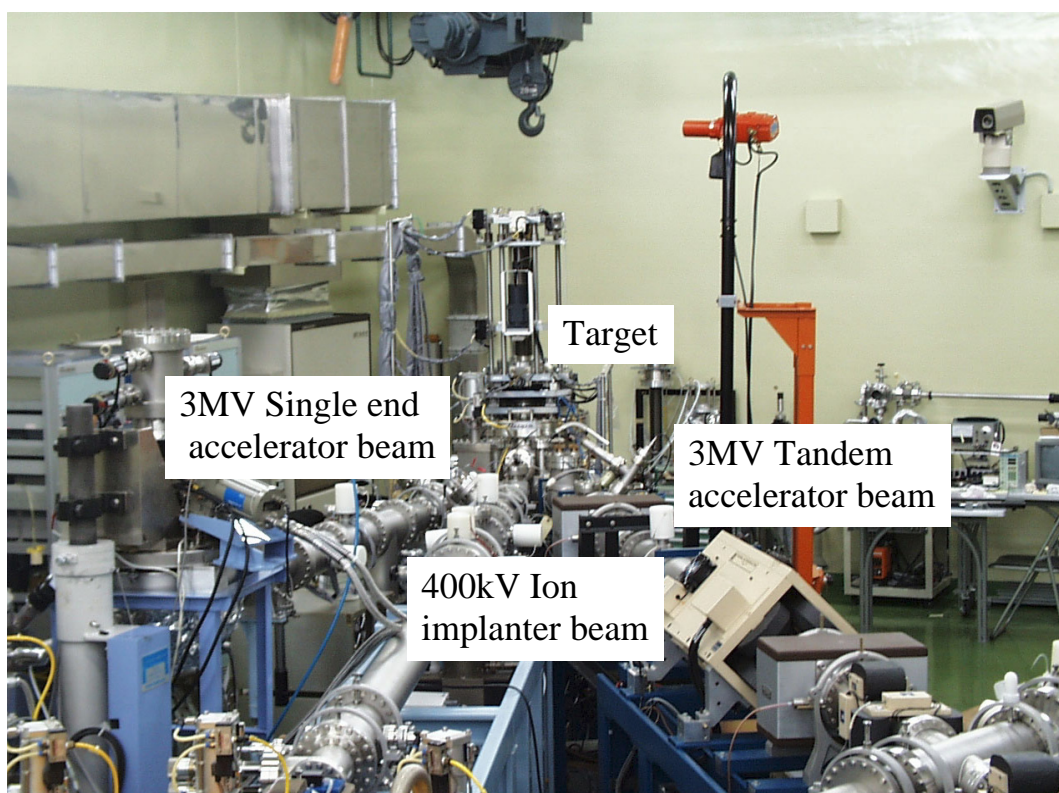


Fig.1 Triple ion beam target of TIARA(Takasaki Ion Accelerators for Advanced Radiation Application) facility at JAERI

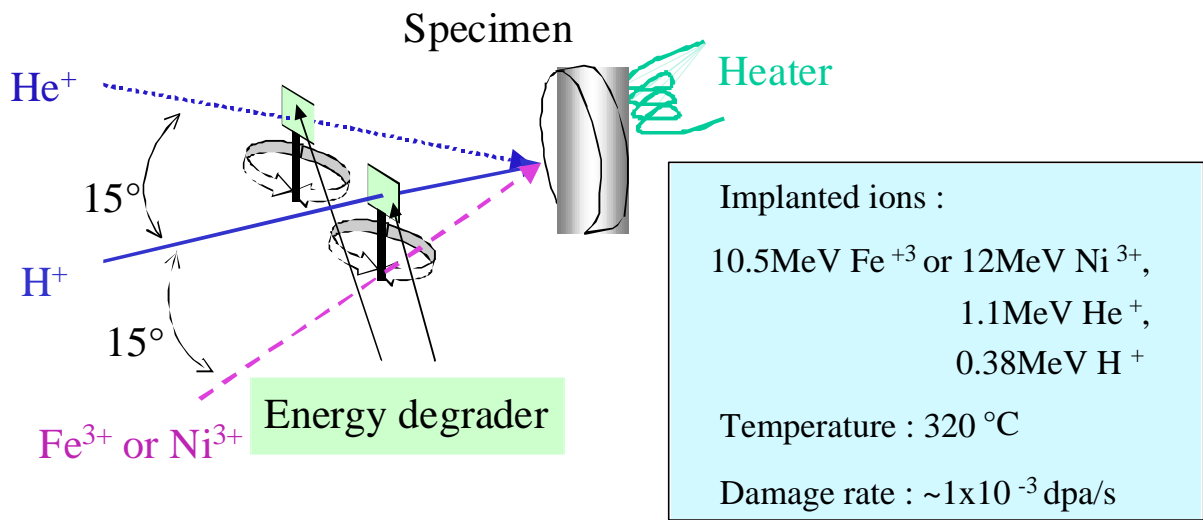


Fig. 2 Schematic configuration and beam condition of triple ion beam irradiation

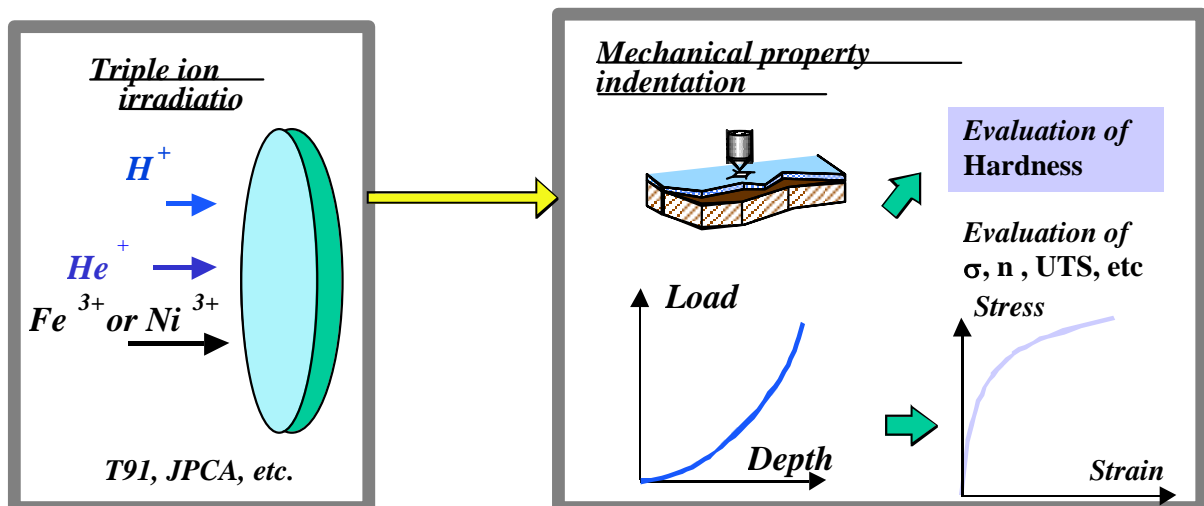


Fig.3 Schematic diagram showing procedure to study irradiation effect using ion beam irradiation and indentation technique

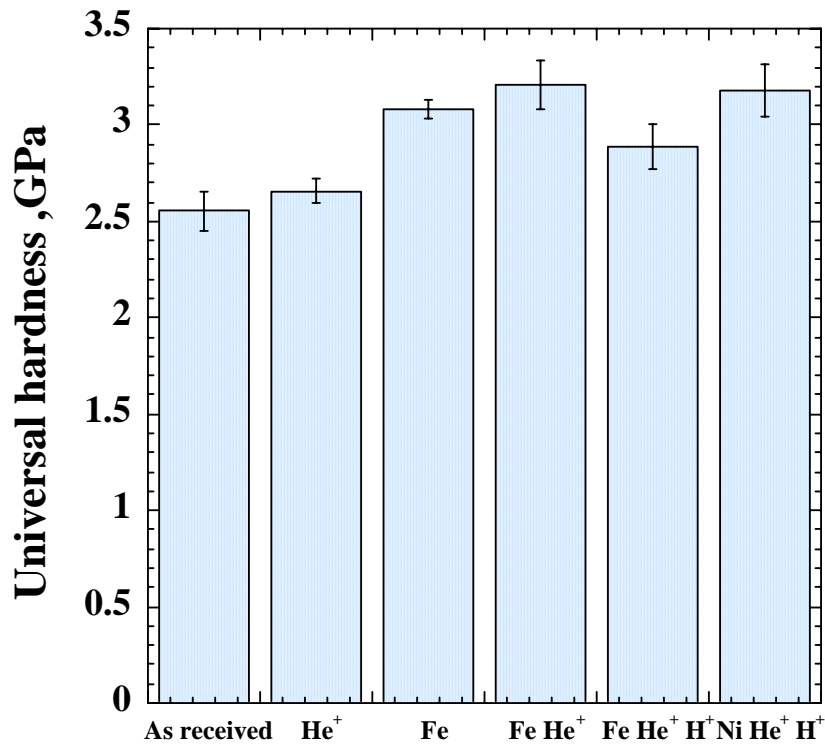


Fig.4 Effect of ion irradiation on load versus depth curves of T91 specimen

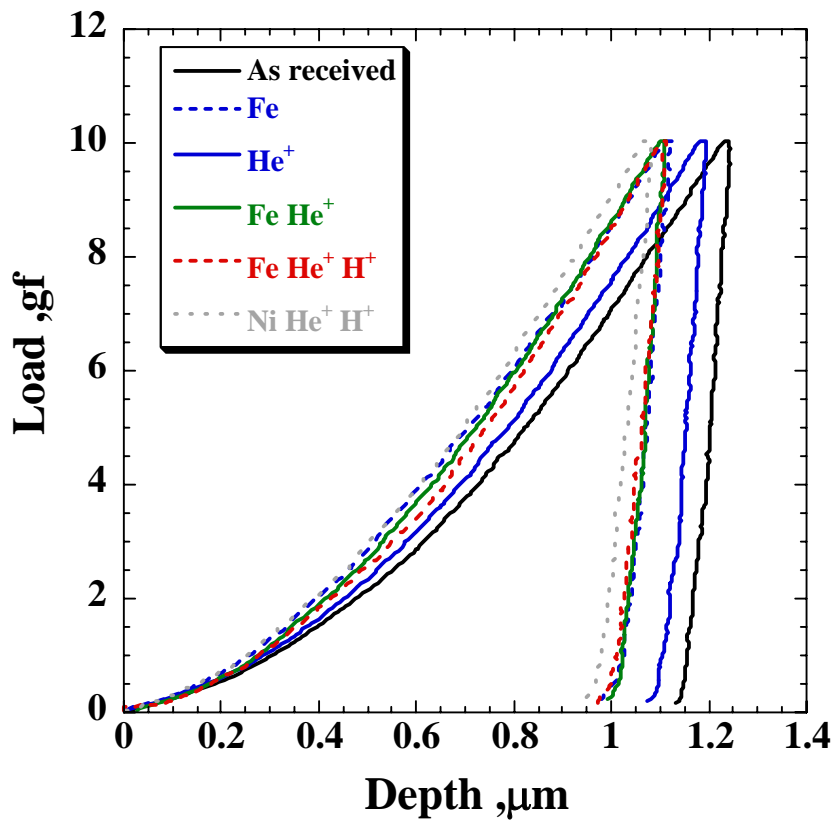


Fig.5 Effect of ion irradiation on hardness of T91 specimen. The hardness was estimated by using a microindentation technique.

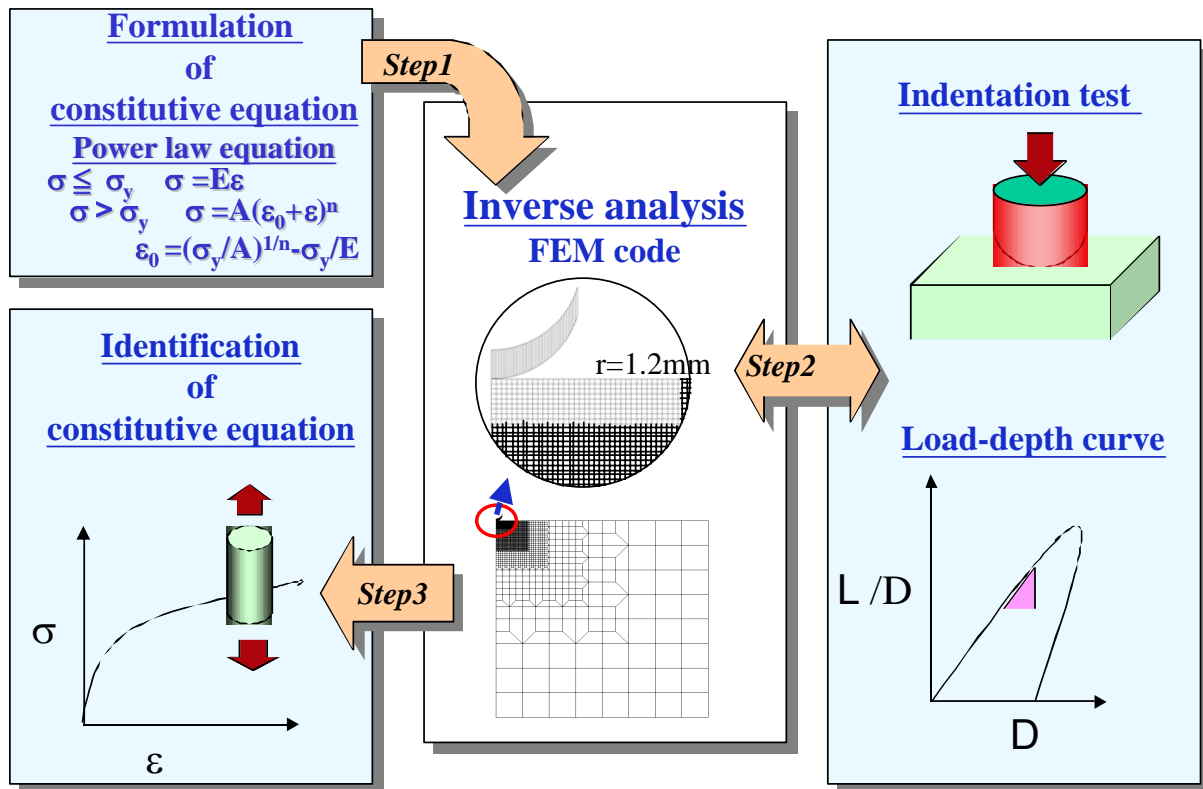
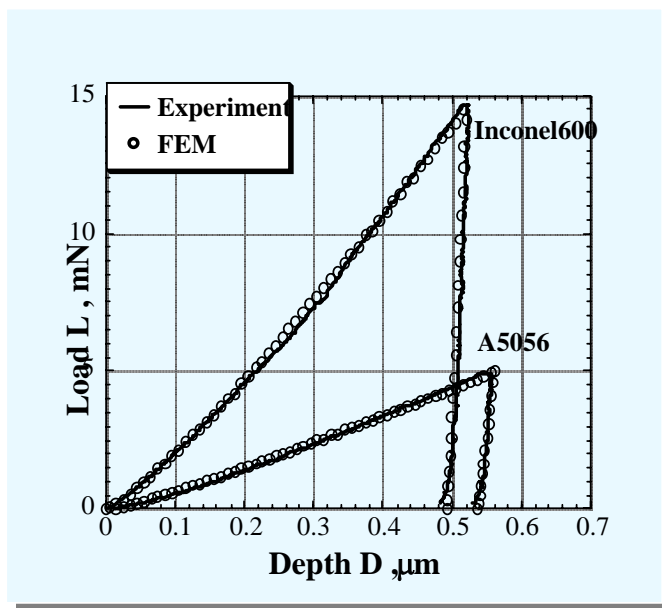


Fig.6 Schematic diagram showing procedure to identify material constants from indentation test and inverse analysis.



Estimated constants by inverse analysis

	A5056	Inco.600
E, GPa	73	170
σ_y, MPa	77	263
A, MPa	322	1425
n, MPa	0.126	0.293

Fig.7 Results of inverse analyses on L-D curves for estimation of materials constants of the power law equation of stress-strain curves.

DISCUSSION ON THE LIFETIME OF THE TARGET BASED ON PRELIMINARY STIP RESULTS

Yong Dai

Paul Scherrer Institut, 5232 Villigen PSI, Switzerland

Abstract

In the first SINQ target irradiation program (STIP-I) a number of martensitic steels were irradiated at temperatures up to 360°C to a maximum dose of 12 dpa (displacement per atom) and 1100 appm He. Small punch (SP) and Charpy impact samples of T91 steel were irradiated up to 9.4 dpa at 275°C and below. Small punch tests and Charpy impact tests have been performed to evaluate the ductile-brittle transition temperature (DBTT) of T91 steel. The results show that the DBTT of T91 at unirradiated condition is about -55°C and increases significantly after irradiation, e.g. to about 245°C at 9.4 dpa. The results also demonstrate the strong effects of helium on the DBTT shift. The temperature at the beam window of the T91 container of MEGAPIE target will be generally below 350°C at 1.4mA proton beam current. The neutron irradiation data indicate that DBTT can increase substantially if the irradiation temperature is below about 400°C. This means that the DBTT of the T91 material of the beam window, especially at the center position may increase to an unacceptable level, above the operation temperature. This level could be taken as a limit for the further operation of the target.

Introduction

For the safety and reliability study of the Megapie target it is necessary to know, at least to estimate the lifetime of the beam window of the liquid Pb-Bi container. This was not possible until recently some mechanical data were obtained from T91 samples irradiated in the first SINQ target irradiation program (STIP-I). However, it can be seen in the following sections that a definite conclusion can still not be made from the limited data.

A brief overview of STIP-I results

Mechanical properties and microstructure of T91 and other martensitic steels such as F82H, Optifer have been studied after irradiation in SINQ Target-3 in 1998 and 1999.

Detailed transmission electron microscopy investigations have been performed on T91 and F82H samples [1, 2]. The results show that high-density helium bubbles of size about 1 nm formed in T91 and F82H samples irradiated at temperatures above about 200 °C to about 10 dpa with 550 appm He. The size of bubbles increases with the increasing of irradiation temperature, but the density remains almost constant. Similar to our previous observations on different martensitic steels irradiated in LANSCE [3, 4], it demonstrates that irradiation introduced also small defect clusters or dislocations loops. The size increases while the density drops rapidly with irradiation temperature above about 250 °C. In addition, the amorphization of $M_{23}C_6$ precipitates was observed again in both T91 and F82 samples irradiated at 220 °C and below. Fig. 1 to 3 show the features of helium bubbles, defect clusters and precipitate amorphization in both T91 and F82H, respectively.

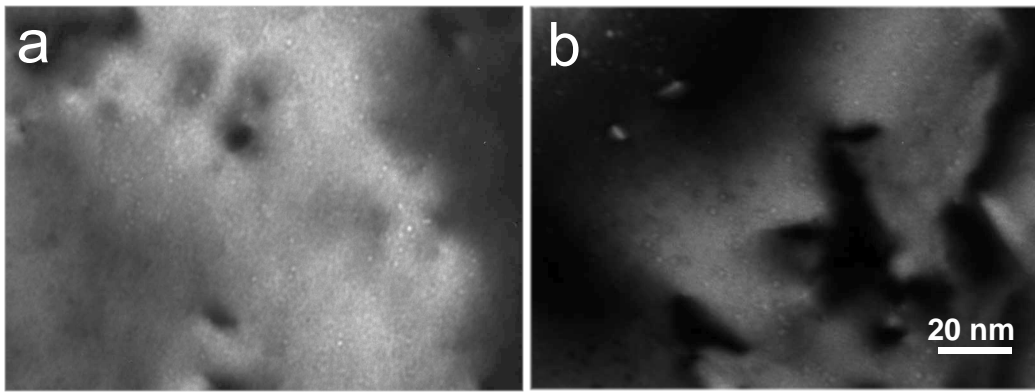


Figure 1: High-density helium bubbles in (a) F82H irradiated to 9.7 dpa and (b) T91 irradiated to 10.1 dpa at 295°C [2].

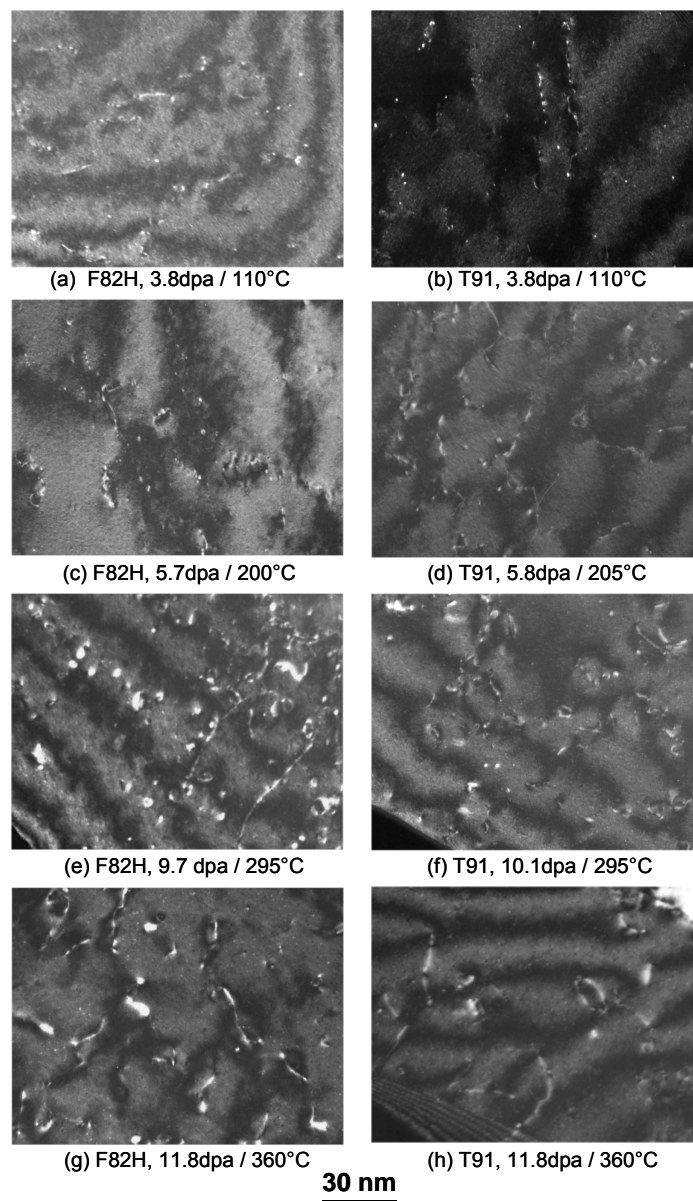


Figure 2: Defect cluster structure of irradiated F82H (left column) and T91 (right column) samples. The irradiation conditions are indicated below the micrographs. The scale for all the micrographs is the same as indicated at the bottom [2].

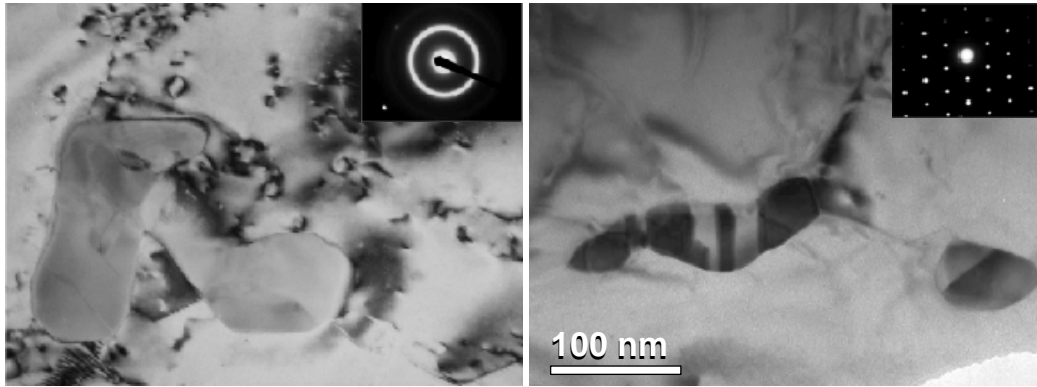


Figure 3: TEM BF images showing the amorphization of precipitates in T91 steel, left: 5.8 dpa / 205°C, right: 8.3 dpa / 250°C [2].

Mechanical tests performed are tensile, small punch (SP) and Charpy impact tests. Fig. 3 illustrates the tensile strain-stress curves of the T91 samples tested at 22, 250 and 350°C [5]. The tensile test results demonstrate that the irradiation hardening increases with dose. The uniform elongation falls to less than 1%, while the total elongation is greater than 5% in all cases. All the tensile samples broke in a ductile fracture mode, as can be seen from pictures in Fig. 5 for samples at unirradiated condition and irradiated to 9.8 dpa tested at 250°C.

Systematic SP tests have been conducted on T91, F82H and Optimax samples in a temperature range from -185 to 100°C [5, 6]. Fig. 6 presents, as an example, the displacement-load curves of T91 samples at unirradiated condition and irradiated to 9.4 dpa at 275°C. It can be seen that at unirradiated condition (Fig. 6a) the material becomes brittle when the test temperature drops to about -160°C, while for the 9.4 dpa case (Fig. 6b) this transition temperature is about -30°C. Fig.7 illustrates the temperature dependence of the energy to break the discs irradiated to different doses. It demonstrates clearly that the temperature - energy curve shifts to higher temperatures as a result of irradiation. The ductile-brittle transition temperature (DBTT_{SP}) is taken to be the point at which the energy reaches half of the maximum upper shelf energy (USE_{SP}). Fig. 8 shows the dose dependencies of the DBTT_{SP} and EUS_{SP} for the three steels. It indicates that the DBTT_{SP} of T91 steel increases strongly from about -153 °C for the unirradiated condition to about -35 °C after irradiation to 9.4 dpa, whereas the USE_{SP} decreases gradually with increasing dose. In addition, it shows also that the DBTT increases more rapidly at doses above about 6 dpa.

Charpy impact test using V-notched bar specimens is the standard method for evaluating the DBTT of martensitic steels and other alloys. Four steels, T91, F82H, Optifer and Optimax have been tested [7]. As an example, Figure 9 shows curves of absorbed energy as a function of testing temperature for T91 steel samples in conditions of unirradiated and irradiated to 4.6 and 6.8 dpa. The figure demonstrates that the DBTT of T91 in the as-received condition is about -54°C. After irradiation to 4.6 and 6.8 dpa, the DBTT increases to 54 and 165°C, respectively. Meanwhile the upper shelf energy (USE) decreases after irradiation.

The DBTT obtained from Charpy impact (DBTT_{CVN}) and SP-test can be correlated with an empirical expression [8]:

$$DBTT_{SP} = 0.4 \times DBTT_{CVN} \quad (1)$$

Figure 10 presents all the data of the increase of DBTT (Δ DBTT) after irradiation obtained from both Charpy and SP tests plotted as a function of helium concentration. It can be seen that the data of Charpy and SP tests are consistent with each other, and more important, the Δ DBTT increases more or less linearly with helium concentration.

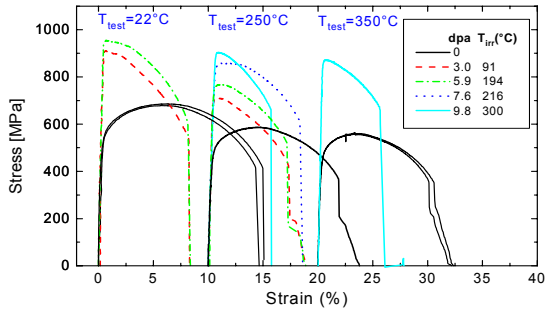


Figure 4: Engineering tensile stress-strain curves of T91 irradiated at SINQ Target-3 and tested at 22, 250 and 350 °C [5].

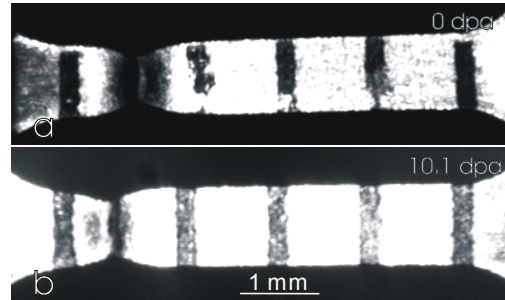


Figure 5: Pictures of samples tested at 250 °C (a) unirradiated and (b) irradiated to 9.8 dpa. The black lines on the surfaces of the specimens were used for measuring elongation with a video-extensometer [5].

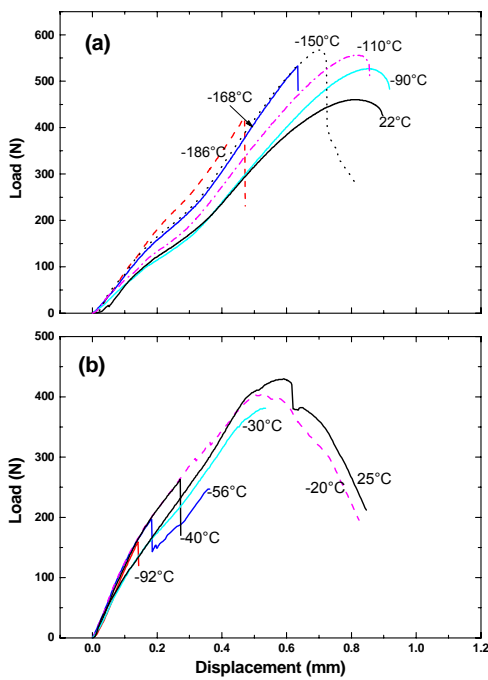


Figure 6: The load – displacement curves for SP tests of (a) unirradiated specimens and (b) specimens irradiated to 9.4 dpa. Test temperatures are shown on the curves [5,7].

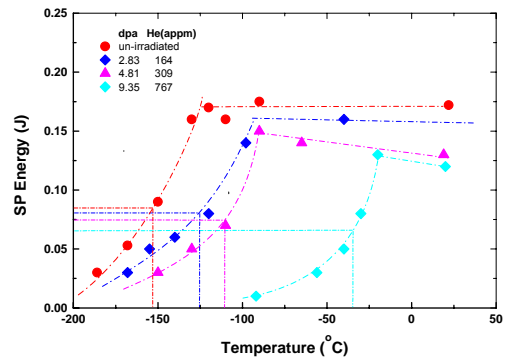


Figure 7: Test temperature dependence of the SP energy for specimens of different irradiation doses [5,7].

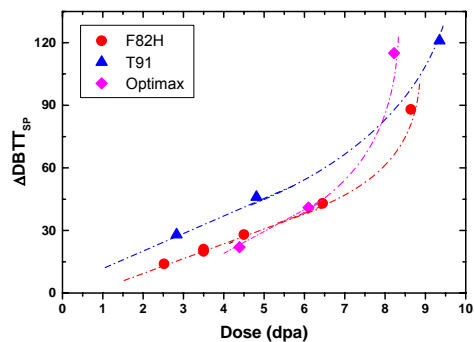


Figure 8: Δ DBTT_{SP} as a function of irradiation doses [7].

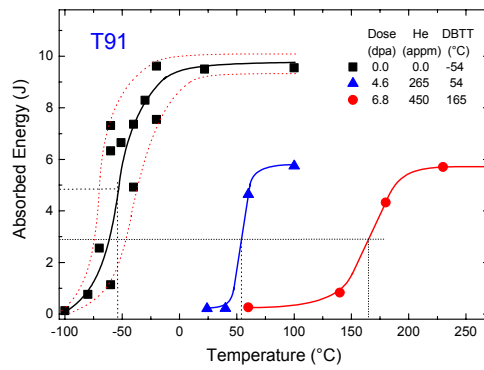


Figure 9: Charpy impact properties of T91 steel in the as-received condition and after irradiation to 4.6 and 6.8 dpa [7].

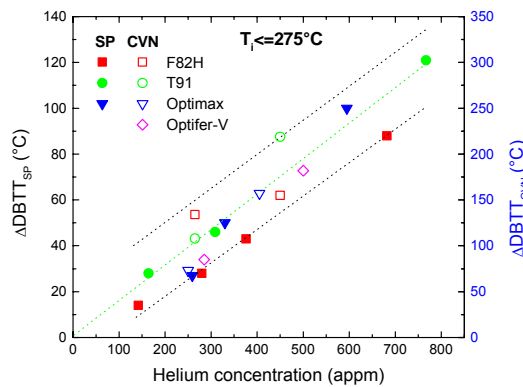


Figure 10: The helium concentration dependence of DBTT obtained from Charpy impact and SP tests [8].

DBTT of martensitic steels after neutron irradiation

The effects of neutron irradiation on the DBTT of martensitic steels have been studied for several decades already. The main features are: 1) different steels show very different Δ DBTT after irradiation in low temperature regime; 2) Δ DBTT increases with dose at low doses and saturates at 5 dpa and below; 3) little or no DBTT shift after irradiation at temperatures above 400°C; 4) helium may have significant effects on DBTT shift.

Figure 11 presents the data of six kinds of steels irradiated in the Petten High Flux Reactor (HFR) at 300°C up to 2.5 dpa [9]. The results demonstrate clearly that there are significant differences among different steels. However, the Δ DBTT saturates at a dose of about 1 dpa for all the steels. The reason for such a dose dependency is believed to be mainly an effect of helium generated by different levels of boron. It can be seen that the burn-up of boron has nearly the same dose dependence as DBTT increases towards saturation. It is also interesting to see that the Δ DBTT do increase with the boron contents in the steels, which gives nearly a linear helium concentration dependence of Δ DBTT, as shown in Fig. 12 for another set of data obtained from the same series of irradiation [10]. The helium effect on Δ DBTT was observed in many cases even before these experiments. One example demonstrates that T91 (9Cr-

1MoVNb) and HT9 (12Cr-1MoVNb) irradiated in HFIR at 400°C to 40 dpa have much higher DBTT shift than those irradiated in EBR-II at 390°C to 13 and 26 dpa (far above the saturation dose) [11]. The difference is attributed to the helium production is much higher for the irradiation in HFIR than in EBR-II for these two steels. The irradiation temperature effect on DBTT shift is illustrated in Fig. 13 which includes data of different steels irradiated in fast or mixed neutron spectra to different doses [12-19]. Although different steels show different behaviors, it is clear the DBTT shift increases significantly when the irradiation temperature is below 400°C.

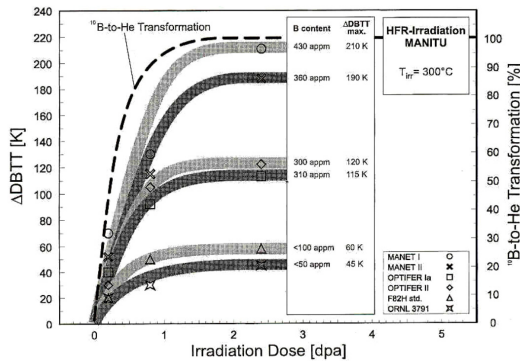


Figure 11: Dose dependence of Δ DBTT and ^{10}B -to-He transformation of different martensitic steels after irradiation in HFR at 300°C [9].

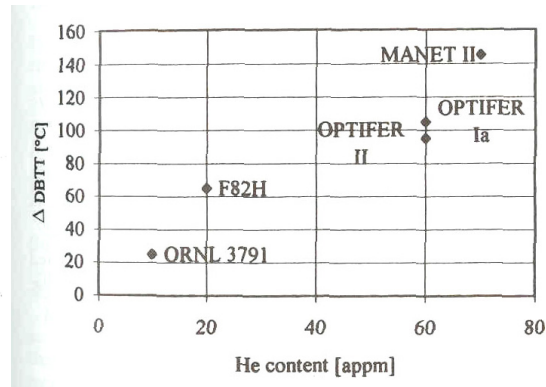


Figure 12: The Δ DBTT as a function of helium concentration of different martensitic steels after irradiation in HFR at 250°C to 0.8 dpa [10].

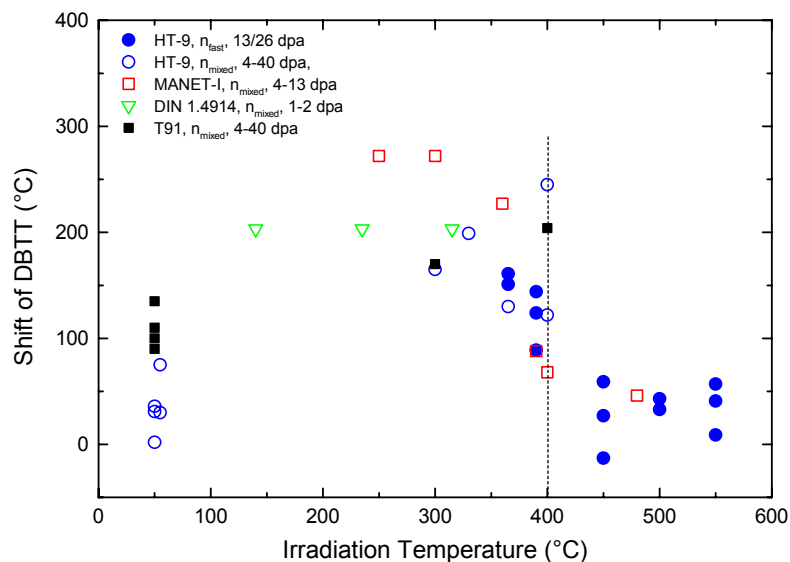


Figure 13: Temperature dependence of Δ DBTT of different martensitic steels after neutron irradiation. Data are from [11-19].

Irradiation of the beam window of T91 LBE container

Detailed neutronic calculations [20] have been performed using a practical proton beam profile from measurements [21]. Fig. 14 shows the distributions of the radiation damage and helium production along the short beam axis at the beam window of the T91 LBE container and the AlMg₃ safety-hull after the target receiving 6 Ah proton charge. From these data it can be derived that the peak damage and helium production rates (namely at the central position) at the beam window of the T91 container are 2.6 dpa / Ah and 215 appm He / Ah, respectively.

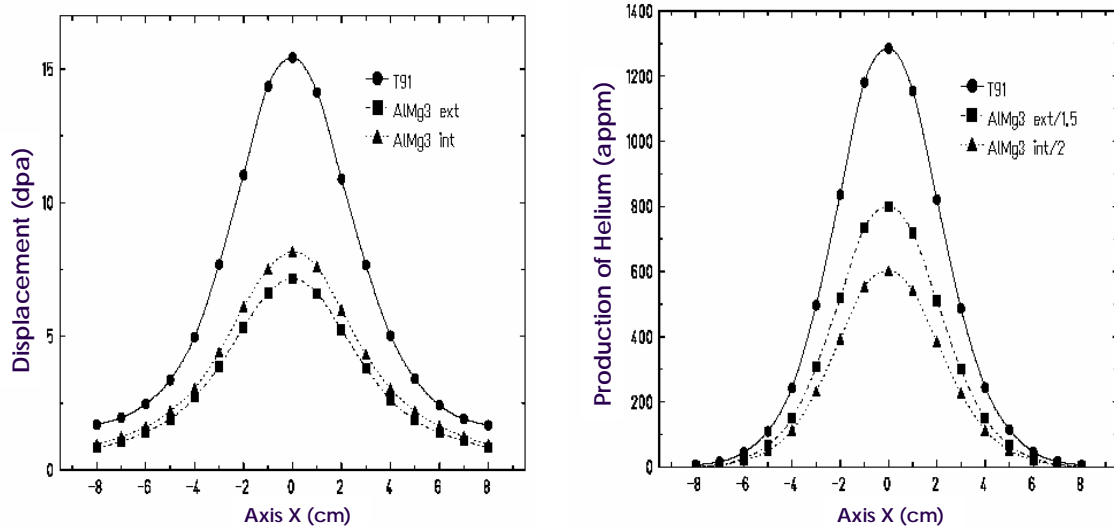


Figure 14: Radiation damage and helium production distributions along the short beam axis at the beam window of the T91 LBE container and the AlMg₃ safety-hull after the target receiving 6 Ah proton charge [20].

Temperature distribution at the normal operation condition

The temperature distribution at the beam window of the T91 container depends on the several parameters such as the temperature of inlet LBE flow, proton beam intensity profile, beam current, main LBE flow and by-pass LBE flow. The calculation has been performed using the heat deposition data which calculated for the practical proton beam profile at a beam current of 1.74 mA. The inlet temperature is 230°C. The main flow is 37.5 kg/s and the by-pass flow is 2.5 kg/s. Two different cases, the by-pass flow parallel to the long beam-axis [22] and the by-pass flow perpendicular to the long beam-axis [23], have been studied.

Case 1: the by-pass flow parallel to the long beam-axis

Figure 14 shows the temperature distributions of the outer surface (left) and inner surface (right) of the beam window. At the proton beam current of 1.74 mA, the maximum temperature is about 370°C at the outer surface and about 335°C at the inner surface [22]. Therefore the temperature gradient across the wall is about 35°C. The by-pass flow brings the position of the peak temperature about 1.3 cm away from the beam center or the geometry centre of the window, as shown in the figure.

Case 2: the by-pass flow perpendicular to the long beam-axis

In this case the profile of the temperature distribution looks different from that of Case 1, as can be seen in Fig. 15. However, the maximum temperature is close to that in Case 1. Again the position of the peak temperature is about 1.2 cm away from the geometry centre along the direction of the by-pass jet flow.

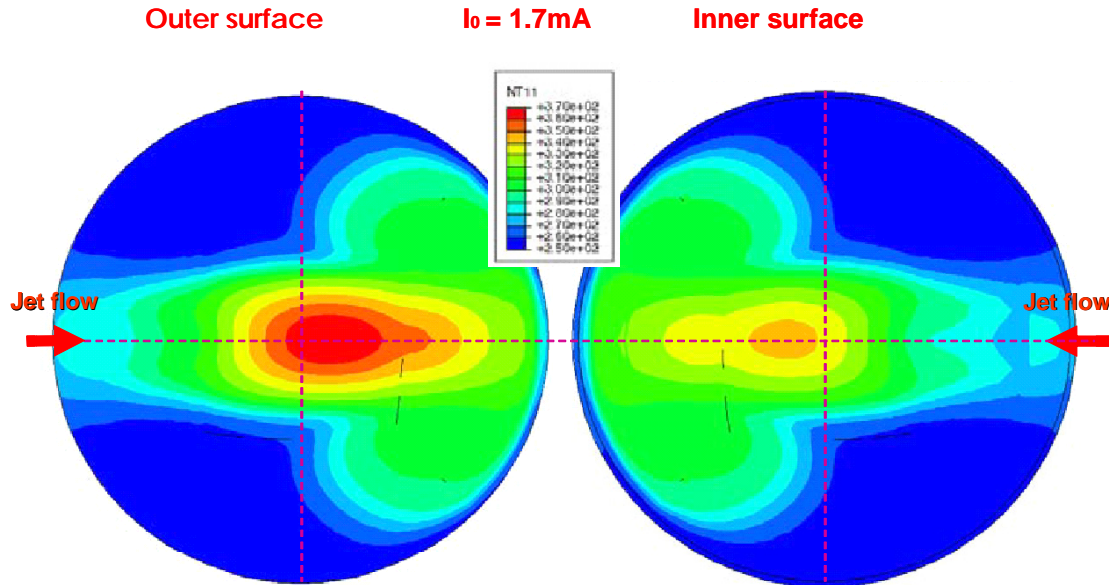


Figure 14: Temperature distributions of the outer surface (left) and inner surface (right) of the beam window in the case of the by-pass flow parallel to the long axis of the beam [21, 22].

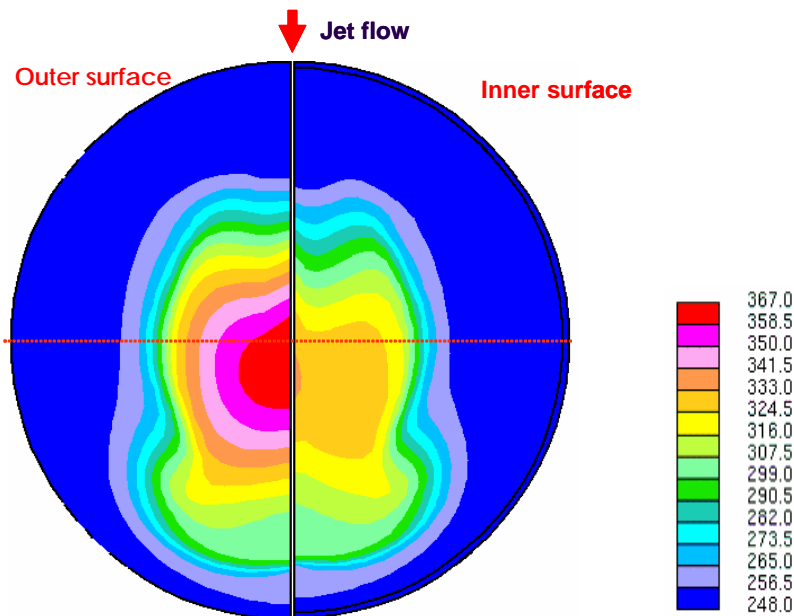


Figure 15: Temperature distributions of the outer surface (left) and inner surface (right) of the beam window in the case of the by-pass flow perpendicular to the long axis of the beam [23].

Mechanical load at the beam window of the T91 container

Using the data of above temperature calculations, the thermal mechanical load distribution in the beam window area has been calculated [24]. The calculation indicates that the maximum Van-Mises stress is generally below 50 MPa.

Discussion and conclusion

1. DBTT shift of the material in the beam window area

The results of STIP-I indicate that DBTT of T91 increases about 295°C after irradiated at 275°C to 9.4 dpa / 770 appm He. Furthermore, the DBTT shift does not saturate in the dose range below 10 dpa as it is normally shown by neutron irradiation. This indicates that the high helium concentration promotes the DBTT shift. It is believed that the DBTT of T91 and other martensitic steels will increase with irradiation dose and helium concentration. However, it is difficult to predict to which extend the DBTT can increase to. This question will be answered by the experiments on STIP-II samples with about doubled doses and helium concentrations. Since the neutron irradiation showed the DBTT of T91 can still increase significantly when irradiated at 400°C, the DBTT of the material in the beam area of the T91 window will certainly increase substantially, and very likely to above 300°C at a high dose of around 15 dpa.

The STIP-I results demonstrate that the Δ DBTT has a linear dependence of helium concentration. Although the mechanism is not well understood yet, the data provide a guideline for predicting the DBTT increase in the Megapie case since the irradiation conditions in STIP are almost the same as that at the beam window of the T91 container. From the data of SP and Charpy tests, it can easily derive that the DBTT of martensitic steels will increase about 100°C per 250 appm He, corresponding to 3 dpa roughly.

2. Temperature at the beam window

The inlet LBE temperature, 230°C, will be the lowest temperature at the beam window during the beam-off time, which includes the beam-trips and service time and is about 10% of the total target operation time.

The proton beam current at Megapie target is expected to be 1.4 mA rather than 1.74 mA in 2005. Therefore the calculated temperatures shown above have to be scaled down. For a rough calculation an expression:

$$T_{1.4} = (T_{1.74} - T_{in})/1.74 \times 1.4 + T_{in} \quad (2)$$

where $T_{1.4}$, $T_{1.74}$ and T_{in} are temperatures at 1.4 mA, 1.74 mA and inlet flow, respectively, can be used. It gives that the maximum temperature at outer surface is about 343°C and 315°C at the inner surface.

3. The lifetime of the beam window

One of the criteria for judging the lifetime of the T91 beam window can be that the DBTT of the materials should not exceed the operation temperature in any case. This means that the DBTT of the material in the beam area should be lower than 230°C. From the data given above it obtains that the DBTT will be 230°C after the peak dose reaching 8.6 dpa and helium concentration reaching 720 appm. At this time the target will receive about 3.4 Ah of proton charge. Therefore, the proton charge of 3.4 Ah

can be taken as a critical limit for the operation. The theoretical beam time to get 3.4 Ah is 2428 hours at 1.4 mA. However, even during normal operation there is a service time of about 14 hours each week for the accelerator. In addition, there are about 50 beam trips of few minutes on average each day. All together gives about 10% of “beam-off” time. On the other hand the beam current is not constant. This will increase also the time to reach 3.4 Ah. AS an example, in year 2000 the beam current should be 1.2 mA at the SINQ target since the 4 cm Target-E was used through the whole year. The average proton charge per week obtained during the middle 39 weeks (good operation period) was 0.14 Ah. Supposing the operation situation in 2005 be the same as that in 2000 (very likely), it will get 0.164 Ah per week with the higher beam current of 1.4 mA. Hence, it will take about 21 weeks to reach 3.4 Ah, which can be considered as the lifetime of the window.

During the beam-on time, the center area of the window will be around 300°C or above. In this case the temperature at the inner surface is lower and therefore, concerned. Fig. 16 presents the temperature distribution after the beam current scaled down to 1.4 mA, in addition the distributions of dose and DBTT are also plotted for the situation when the peak dose reaches 11 dpa. It can be seen that the DBTT reaches 311°C at the beam center, which is the temperature at this point in the normal operation condition. However, except the very small area at the centre, the DBTT is lower than the normal operation temperature. Nevertheless, the dose of 11 dpa can be considered as the limit for the normal operation condition, which gives the lifetime of the target of about 26 weeks.

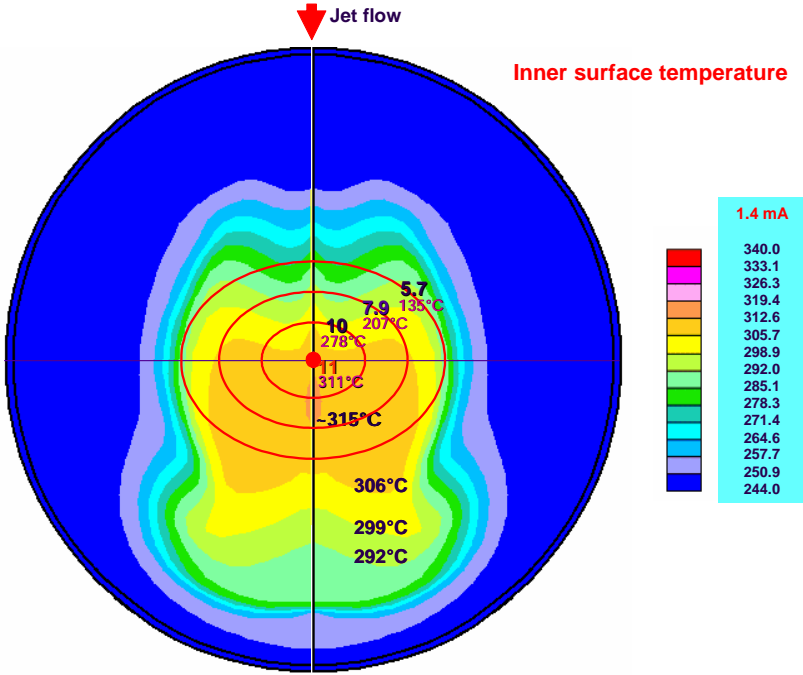


Figure 16: Temperature distribution at 1.4 mA, and the distributions of dose and DBTT when the peak dose reaches 11 dpa.

The above discussion is only from the radiation damage point of view. The effects LBE embrittlement should not be excluded, though which is little understood yet. This

means the lifetime of the target window should be considered shorter than what given above. Meanwhile the safety-margin (e.g. 20%) has to be considered.

To extend the lifetime time, one may think about using the 6cm Target-E. There are two obvious advantages to use the 6 cm Target-E. Firstly, it will reduce the possibility of the over-focused beam due to part of the proton beam by-pass the Target-E [25], which is of greatly concerned. Secondly, the peak proton flux will decrease about 30%, which will increase the time to reach a critical dose by 40%.

The new results of the temperature calculation shown by P. Roubin [26] demonstrate that the temperature in the central area of the beam window can increase to 400 to 430°C if the bypass flow rate reduced to 1 kg/s. In this case the high DBTT shift could be significant reduced to an acceptable level for 9-month operation. Further detailed studies in this direction will be carried out soon.

The present discussion may suffer to two folds limitations. Firstly, the DBTT data of T91 irradiated at right temperature range, 300 – 350°C to higher doses are still missing. This question will be at least partly answered by STIP-II results at doses up to 18 - 20 dpa. Secondly, whether the DBTT can be taken as criterion is not so sure. This needs some discussion with engineering design experts.

References

- [1] X. Jia, Y. Dai and M. Victoria, *J. Nucl. Mater.* 305 (2002) 1.
- [2] X. Jia and Y. Dai, *J. Nucl. Mater.*, in press.
- [3] Y. Dai, F. Carsughi, W.F. Sommer, G.S. Bauer, H. Ullmaier, *J. Nucl. Mater.* 276 (2000) 289.
- [4] Y. Dai, S. A. Maloy, G.S. Bauer and W.F. Sommer, *J. Nucl. Mater.*, 283-287 (2000) 513.
- [5] Y. Dai, X.J. Jia, K. Farrell, *J. Nucl. Mater.*, in press
- [6] X. Jia and Y. Dai, to be published in *J. Nucl. Mater.*
- [7] Y. Dai, R. Thermer and P. Marmy, PSI Scientific and Technical Report 2002, in press; to be published in *J. Nucl. Mater.*, too.
- [8] X. Mao, H. Takahashi, *J. Mater. Sci.* 27(1992) 983.
- [9] M. Rieth, B. Dafferner, H. D. Roehrig, *J. Nucl. Mater.* 258-263 (1998) 1147.
- [10] E. I. Materna-Morris, M. Rieth and K. Ehrlich, in *Effects of Radiation on Materials: 19th Inter. Sym.*, (ASTM STP 1366, 2000), p. 597.
- [11] R. L. Kluch and D. J. Alexander, *J. Nucl. Mater.* 187 (1992) 60.
- [12] R.L. Klueh and D.J. Alexander, in *Effects of Radiation on Materials: 16th Inter. Sym.*, (ASTM STP 1125, 1992), p. 1256.
- [13] C. Wassilew, M. Rieth and B. Dafferner, in *Proc. IEA Workshop on Ferritic-Martensitic Steels*, (Tokyo, 1992), p. 295.
- [14] R.L. Klueh, J.M. Vitek, W.R. Corwin and D.J. Alexander, *J. Nucl. Mater.* 155-157 (1988) 973.

- [15] W.L. Hu and D.S. Gelles, in Influence of Radiation on Material Properties: 13th Inter. Sym., (ASTM STP 965, 1987), p. 83.
- [16] W.L. Hu and D.S. Gelles, in Effects of Radiation on Materials: 14th Inter. Sym., (ASTM STP 1046, 1990), p. 453.
- [17] R.L. Klueh and D.J. Alexander, J. Nucl. Mater. 212-215 (1994) 736.
- [18] M.B. Toloczko, F.A. Garner and C.E. Eiholzer, J. Nucl. Mater. 212-215 (1994) 604.
- [19] R. L. Kluch and D. J. Alexander, J. Nucl. Mater. 218 (1995) 151.
- [20] Y. Foucher, PhD thesis, Subatech, 2002.
- [21] U. Rohrer, unpublished data.
- [22] T. Dury, this meeting
- [23] P. Coubin, CEA document, STH/LTA/2003-03 (Draft)
- [24] A. Zuccini, ENEA report, RTI/FIS/MET/2002/1
- [25] U. Rohrer, Megapie PCG meeting.
- [26] P. Roubin, this meeting.

RISK OF BRITTLE FAILURE OF THE PB-BI CONTAINER WINDOW : A TENTATIVE ASSESSMENT

J. Henry, P. Lamagnère
CEA - France

Introduction

Irradiation in a spallation spectrum at low temperature (around 300°C or below) will induce significant hardening and ductility loss of the window material as shown by the results of tensile tests carried out on specimens irradiated in SINQ Target-3 [1,2]. Also, a large shift of the so-called Ductile-to-brittle Transition Temperature (DBTT) will occur as a result of irradiation : based on impact tests performed on a limited number of sub-sized Charpy specimens, this shift was evaluated to be larger than 200°C in the case of mod. 9Cr-1Mo (T91) irradiated to about 7 dpa (450 appm He) in SINQ target-3 [3]. Although the value of the DBTT shift clearly indicates a drastic irradiation-induced embrittlement, this parameter must be used with caution when evaluating the window life-time or for design purposes. Indeed it is well known that the DBTT is not an intrinsic material property, but can vary to a large extent depending on specimen geometry/size and test parameters, as pointed out by numerous authors (see for instance [4], [5]). Hence the purpose of the present report is not to discuss the possible service time of the window based on measured DBTT values as a function of irradiation dose, but rather to evaluate the risk of brittle failure in the presence of a defect (a surface crack) assuming a drastic toughness reduction due to irradiation.

II Risk of failure in the presence of a surface crack

Surface cracks may exist in a structural component as a result of fabrication (welding cracks, machining-induced cracks/grooves) or can be generated during operation (fatigue cracks). In the following, we will evaluate the failure risk for normal operating conditions in the presence of a surface crack as a function of crack geometry and depth. This evaluation will be done in the framework of the linear elastic fracture mechanics (LEFM), which is only valid under restrictive conditions such as the so-called "Small scale yielding " (SSY) condition (which means that the plastic zone ahead of the crack tip must be small compared to crack and component dimensions). This point is discussed below. As a first step for this evaluation, the stress-intensity factor K_I is computed as described in the following.

II.1 Stress intensity factor for a surface crack

The stress-intensity factor (mode I loading) K_I for a surface crack was computed using an empirical equation derived by Newman and Radju [6], based on stress-intensity factors obtained from a finite-element analysis of semi-elliptical surface cracks in finite elastic plates subjected to tension and/or bending loads. FEM stress analyses of the beam window for normal operating conditions were performed both at PSI [7] and ENEA [8]. They showed that the maximum value of the equivalent von Mises stress is about 45-50 MPa. The window loading is due both to beam heating (thermal stresses) and Pb-Bi pressure. We have used as input values for the stress-intensity factor calculations a bending stress of 40 MPa and a tensile stress of 10 MPa.

The crack geometry and loading conditions are shown in Figure 1a and 1b, respectively. The crack width was assumed to be small with respect to plate width ($c/b \approx 0$). We have investigated two cases : the large shallow crack ($a \ll c$) and the semi-circular crack ($a/c=1$). The corresponding stress-intensity factors are plotted in figures 2 and 3, respectively.

II.2 Evaluation of the failure risk

As mentioned above, LEFM can be used to evaluate the risk of brittle fracture provided the SSY condition is met. The plastic zone size R_p calculated using Irwin's approach [9] is plotted in Figure 4, which shows that R_p is at most equal to a few percent of the crack length. The use of LEFM is therefore justified. In the framework of LEFM, the stress/strain state in the vicinity of the crack tip is characterized by the stress intensity factor K_I and brittle failure occurs at a critical value K_{Ic} (fracture toughness of the material). In principle a plastic zone correction should be applied, i.e. K_I values should be calculated for effective cracks of depth $a+R_p$, but in the present case, this correction would only marginally modify the calculated stress intensity factors.

The failure risk can now be assessed based on the comparison of calculated stress intensity factors and fracture toughness data for irradiated T91. Unfortunately toughness data for T91 irradiated in a spallation spectrum are relatively scarce. Figure 5 shows the results of toughness tests carried out at irradiation temperature by Maloy et al. [10, 11] on T91 specimens irradiated at 50-160°C up to about 4 dpa. While significant drop in toughness occurs with increasing irradiation dose, toughness values remain above 50 MPa m^{1/2}. Limited toughness data are also available for T91 irradiated in fission reactors at low temperatures. Toughness values of more than 100 MPa m^{1/2} were measured at irradiation temperature by Huang and Hamilton [12] for T91 irradiated at 55°C to 5 dpa in HFIR. The toughness of T91 was also evaluated by Horsten et al. [13] following irradiation in HFR at 300°C. The toughness measured at room temperature was above 50 MPa m^{1/2} and close to 300 MPa m^{1/2} at 100°C.

Hence the available data, however limited, show that the toughness of irradiated T91 remains above 50 MPa m^{1/2}, which is approximately the lower shelf toughness for this material in the unirradiated condition. If one assumes that the fracture toughness following irradiation in a spallation spectrum at doses higher than 4-5 dpa will not drop below the lower shelf value for unirradiated T91, then Figures 2 and 3 demonstrate that a surface crack cannot trigger brittle fracture of the window under normal operating conditions. Of course spallation products such as helium might induce a further decrease in toughness. However, it is very unlikely that the toughness could become as low as the values plotted in Figures 2 and 3.

Conclusion

The simple LEFM analysis described above shows that the presence of a surface crack will not lead to sudden brittle failure of the window under normal operation conditions, since the window material should retain sufficient toughness even following several months of irradiation in a spallation spectrum.

However this analysis does not take into account possible effects of liquid Pb-Bi. The Megapie window will be submitted to cyclic loading as a result of beam trips. Recent low cycle fatigue tests conducted both in air and in liquid Pb-Bi have shown that the presence of the liquid metal induced a reduction in fatigue life, which decreased below the total number of cycle expected for the Megapie window [14]. Of course, the total strain range for these tests (0.3 %) was much higher than the strain amplitude in the Megapie window (0.03%). Nevertheless, the risk of fatigue crack initiation and propagation leading to window leakage and/or failure should be investigated. To this end, it would be useful to carry out high cycle fatigue tests in Pb-Bi as well as measurements of crack propagation rates.

References

- [1] Y. Dai et al., IWSMT, Charleston, SC, May 2002
- [2] J. Henry et al., IWSMT, Charleston, SC, May 2002
- [3] Y. Dai, this Technical meeting
- [4] K. Edsinger, G.R. Odette, G.E. Lucas, J.W. Sheckherd, J. Nucl. Mater. 233-237 (1996) 342
- [5] P. Jung, A. Hishinuma, G.E. Lucas, H. Ullmaier, J. Nucl. Mater. 232 (1996) 186
- [6] J.C. Newman and I.S. Raju, Engng Fracture Mech. 15 (1981) 185
- [7] Y. Dai and L-P. Ni, KA Seminar, PSI, January 2002
- [8] A. Zucchini, Megapie Technical Meeting, Bologna, March 2002
- [9] G.R. Irwin, App. Mater. Res. 3 (1964) 65
- [10] S.A. Maloy, M.R. James, G. Willcutt, W.F. Sommer, M. Sokolov, L.L. Snead, M.L. Hamilton, F. Garner, J. Nucl. Mater. 296 (2001) 119
- [11] AAA Materials Handbook, Rev. 3, Chapter 19, p. 53
- [12] F-H. Huang and M.L. Hamilton, J. Nucl. Mater. 187 (1992) 278
- [13] M.G. Horsten, E.V. van Osch, D.S. Gelles, M.L. Hamilton, 19th ERM, ASTM STP 1366 (2000) 579
- [14] M. Grosse and D. Kalkhof, Megapie Technical Meeting, Bologna, March 2002

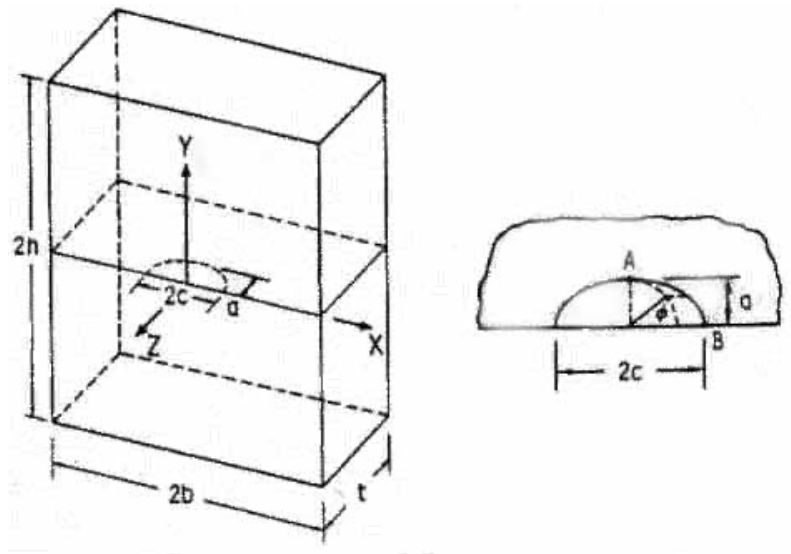


Figure 1a : Surface crack in a plate [6]

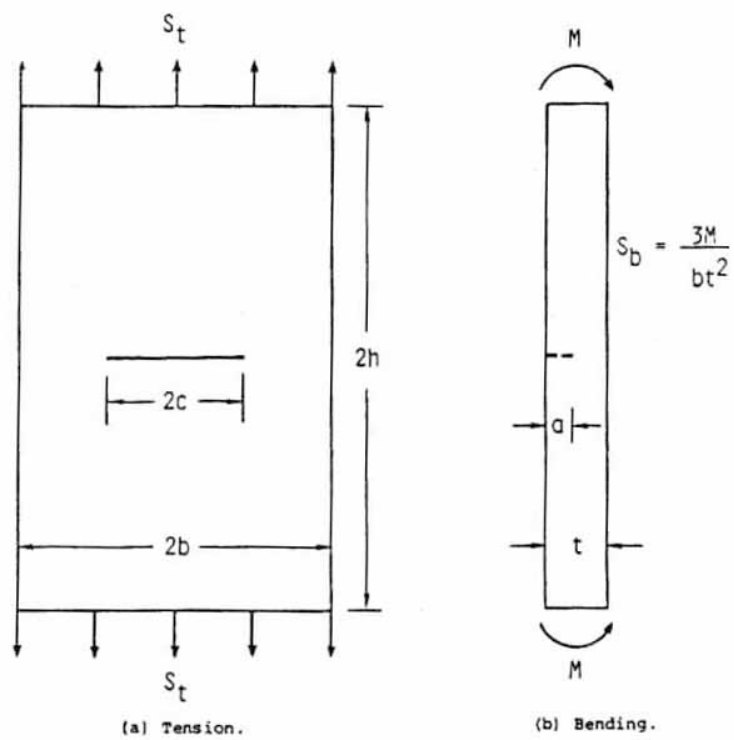


Figure 1b : Surface-cracked plate subjected to tension and/or bending loads [6]

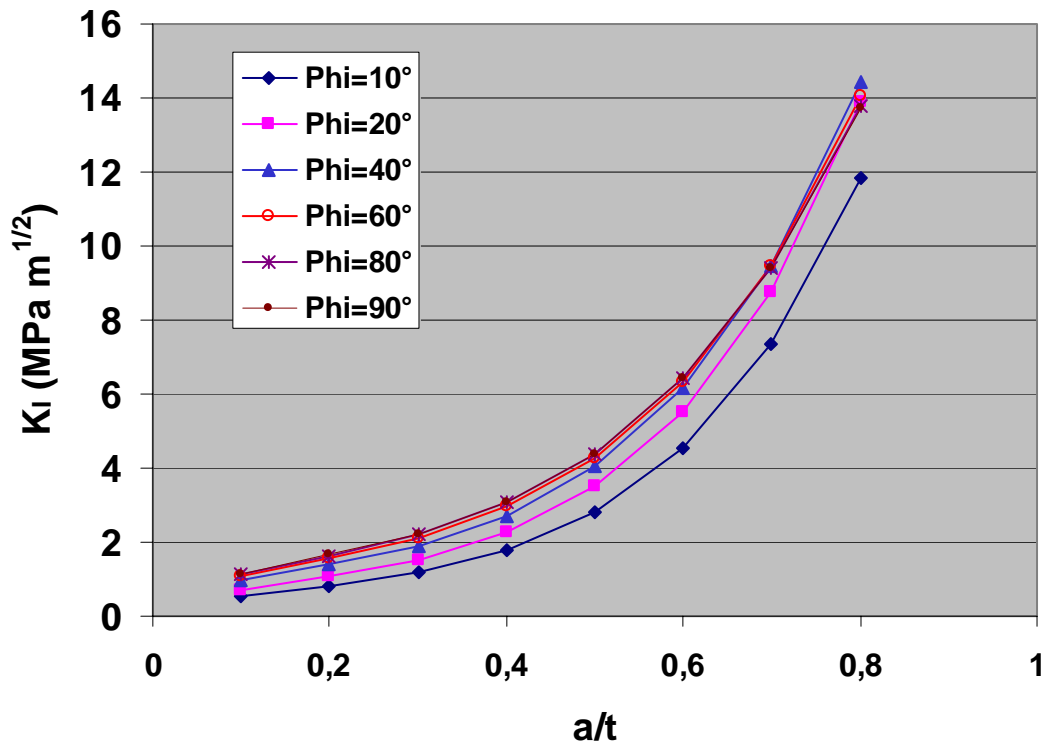


Figure 2 : Calculated stress intensity factors for a surface crack with $a \ll c$ in a plate of thickness $t=1.5$ mm as a function of crack depth and parametric angle \square .

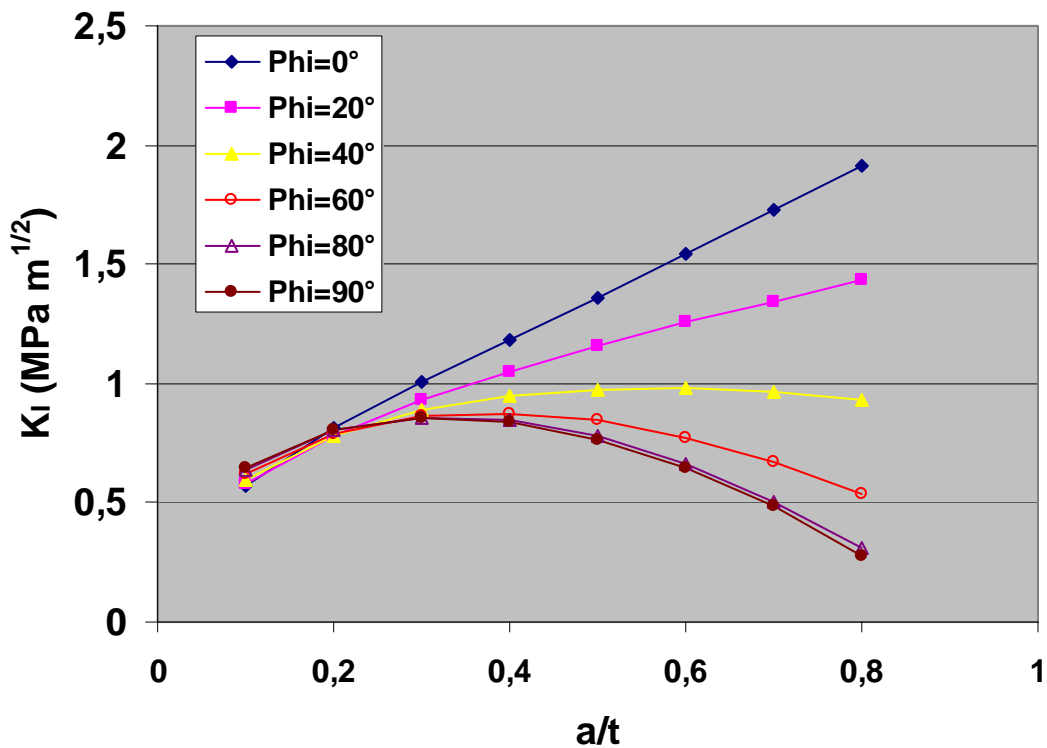


Figure 3 : Calculated stress intensity factors for a semi-circular surface crack ($a/c=1$) in a plate of thickness $t=1.5$ mm as a function of crack depth and parametric angle \square .

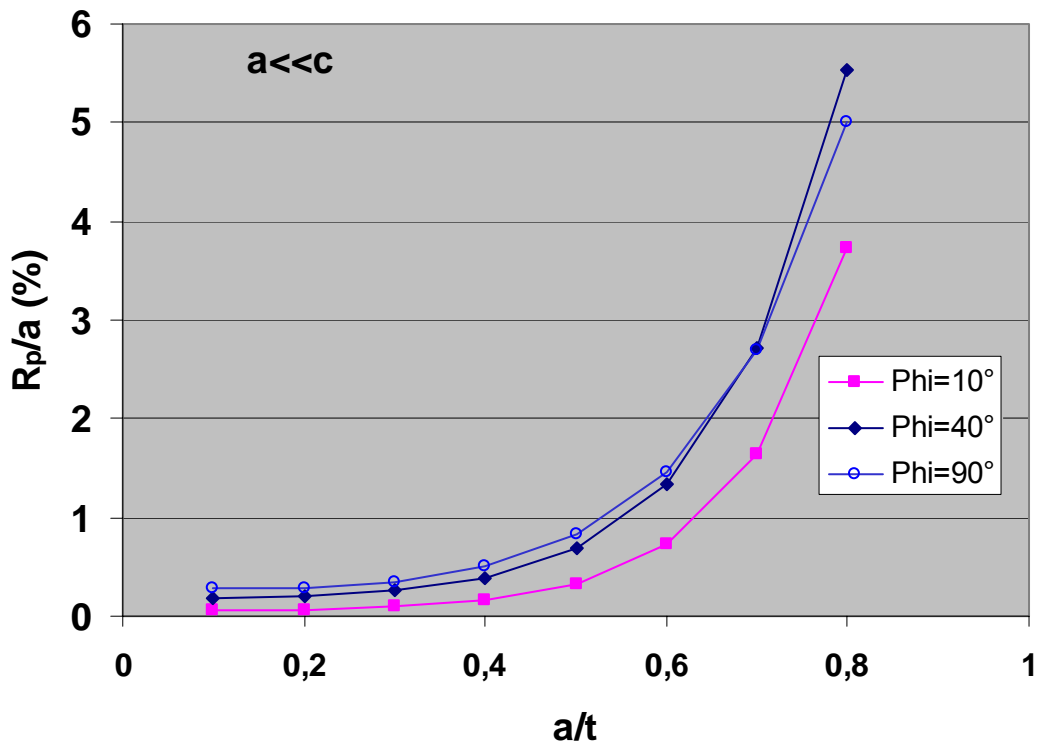


Figure 4 : Plastic zone size R_p calculated using Irwin's model : $R_p = 1/2 \sqrt{(K_I/\sigma_y)^2}$ where σ_y is the yield stress. We have used for irradiated T91 $\sigma_y = 1000$ MPa.

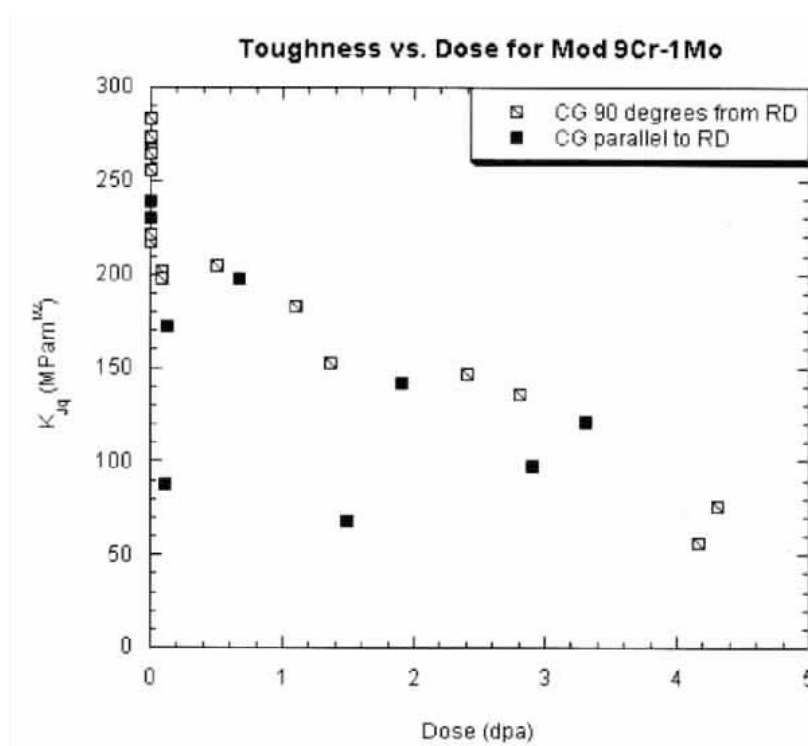


Figure 5 : Fracture toughness as a function of dose for T91 irradiated in a spallation spectrum ($T_{irr} = T_{test} = 50-160^\circ\text{C}$)

SESSION 5: LM TECHNOLOGY + SOLID LIQUID INTERFACE

MAIN RESULTS OF STATIC AND DYNAMIC CORROSION TESTS IN OXYGEN-SATURATED LIQUID LEAD-BISMUTH

Y. Kurata, K. Kikuchi, S. Saito, M. Futakawa and T. Sasa
Center for Proton Accelerator Facilities,
Japan Atomic Energy Research Institute

Introduction

A series of corrosion tests in liquid Pb-Bi have been conducted at JAERI to investigate applicability of metallic materials for an accelerator driven system which is currently being developed for transmutation of long-lived nuclear wastes[1]. Two static corrosion tests in oxygen-saturated liquid Pb-Bi were performed using various specimens with and without aluminum surface-treatments. Furthermore, two dynamic corrosion tests in oxygen-saturated liquid Pb-Bi were performed using type 316ss specimen. In this presentation, main results of static and dynamic corrosion tests in liquid Pb-Bi conducted at JAERI are described.

Static Corrosion Tests

First static corrosion test

Fig.1 shows the static corrosion test equipment in liquid Pb-Bi and experimental conditions. Materials used in the first static corrosion test were 2.25Cr-1Mo steel, F82H (8Cr-2W steel), Mod.9Cr-1Mo steel, JPCA (14Cr-16Ni-2Mo steel), type 410ss, type 430ss, pure iron and pure Mo. 2.25Cr-1Mo steel, F82H, Mod.9Cr-1Mo steel, JPCA, type 410ss, type 430ss with Al surface-treatments were also tested in a pot. Two kinds of Al surface-treatments were employed: a gas diffusion method followed by heating at 1100C for 10h and a melt dipping method followed by heating at 703C. The static corrosion test was performed in oxygen-saturated Pb-Bi at 450 and 550C for 3000h.

Effect of Al surface-treatments on corrosion properties in liquid Pb-Bi is shown. Corrosion behavior of specimens without Al surface-treatments is also described shortly. Fig. 2 shows optical micrographs of cross sections of Al surface-treated specimens(JPCA) after the corrosion test at 450 and 550C for 3000h. Al surface-treated layer produced by a gas diffusion method has corrosion resistance. However, Al surface-treated layer produced by a melt dipping method suffers a severe corrosion attack and a reaction layer is formed in liquid Pb-Bi as indicated in Fig.2. The result of EDX analysis shows that Al dissolves and that Pb and Bi penetrate into the reaction layer(Fig.3). The Al surface-treated layer produced by a melt dipping method almost becomes the reaction layer at 550C. Compounds with high Al ratio such as Fe_4Al_{13} and Fe_2Al_5 produced by a melt dipping method disappeared during the corrosion at 550C. Al_2O_3 , FeAl, $FeAl_2$ and $AlCr_2$ exhibited corrosion resistance to liquid Pb-Bi. Oxides were formed at 450C on steels without Al surface treatment. On the other hand, FeAl was formed at 550C on some steels without Al surface treatments. The FeAl layer seemed to prevent further progress of corrosion.

Second static corrosion test

In the second static corrosion test, specimens were changed: Steels with Al surface treatments were not tested. Austenitic steels such as type 316ss and SX(18Cr-19Ni-4Si) were added. Other experimental conditions in the second static corrosion test were the same as those in the first one.

Fig.4 shows optical micrographs of cross sections of Mod.9Cr-1Mo steel and JPCA specimens after the second corrosion test in liquid Pb-Bi at 450 and 550C for 3000h.

In the case of Mod.9Cr-1Mo steel, only increase in thickness of a corrosion film is recognized at 550C in comparison with the result at 450C. On the other hand, it is characteristic that a thick ferrite layer is formed in the surface region of JPCA at 550C. The difference in behavior between Mod.9Cr-1Mo steel and JPCA is shown in Figs. 5 and 6. The ferrite layer is formed under the oxide film of JPCA. The contents of Ni and Cr decrease significantly and Pb and Bi penetrate into the ferrite layer. The oxide film on JPCA is porous at 550C and cannot have protective function. Significant corrosion was not observed at 450C on Mod.9Cr-1Mo steel and JPCA.

Dynamic Corrosion Tests

First dynamic corrosion test

Fig.7 shows the liquid Pb-Bi loop(JLBL-1) used for the dynamic corrosion test and experimental conditions. The condition of the first dynamic corrosion test was the following: The temperatures of high and low temperature parts of the loop were 450C and 400C, respectively, and the flow rate of liquid Pb-Bi at the test section was about 1m/sec. The first dynamic corrosion test was performed for about 3000h(3126h). Argon gas of 99.995% purity was used as a cover gas of expansion and dump tanks. A tube of type 316ss (inner diameter of 9.8mm and tube thickness of 2mm) was used as a specimen as shown in Fig.8(a). Fig.8 (b) and (c) shows a transverse section of the tube and SEM micrograph of an inner surface of the tube, respectively. The final treatment of the tube produced by a normal method was cleaning with hot acid. This treatment produced deeply dug grain boundaries as indicated in this figure.

Corrosion/erosion at the test section is shown in Fig. 9. The following contrast is characteristic; rough interface at the initial surface and smooth interface at the bottom of the corroded hollow. A grain boundary fissure is also recognized at the rough interface. Pits or hollows observed over wide range on the inner surface of the tube were produced by corrosion/erosion in flowing Pb-Bi. The corrosion depth of type 316ss at the high temperature part was estimated to be about 100 μ m after the test for 3000h. Considering the fact that the initial inner surface had deeply dug grain boundaries, it is considered that this rough surface with deeply dug grain boundaries accelerates corrosion/erosion by flowing Pb-Bi. We also experienced decrease in flow rate of liquid Pb-Bi with increasing corrosion time during the first dynamic corrosion test. It was remarkable when the corrosion test was restarted after draining of Pb-Bi. Therefore, the narrow passage of liquid Pb-Bi in electro-magnetic pump(EMP) system was inspected after the first dynamic corrosion test. Fig. 10 shows an appearance of a shaft of the EMP and the result of EDX analysis of deposits on the shaft. Gray and thick deposits are formed in the narrow passage of the EMP. As shown in Fig.10, it is found that the deposits consist of Pb/Bi and grains of Fe-Cr ferrite.

Second dynamic corrosion test

In the second dynamic corrosion test, modification of JLBL-1 and the tube specimen was carried out. Metallic filters and the test section at a low temperature part were set in JLBL-1as shown in Fig.11. The passage of liquid Pb-Bi in the EMP system was made wider. Although an oxygen control system and an oxygen sensor were also set in the loop, they were not used in the second dynamic corrosion test. Inner surface of type 316ss tube specimen was mechanically polished before testing. Other experimental conditions in the second dynamic corrosion test were the same as those in the first one.

Decrease in Pb-Bi flow was not observed up to 3000h in the second dynamic corrosion test. It is considered that addition of metallic filters to JLBL-1 and

modification of the EMP system gave a good effect on operation of the Pb-Bi loop system. Fig.12 shows the cross section of a high temperature tube(450C) of type 316ss after the second dynamic corrosion test in oxygen-saturated Pb-Bi. As can be seen in Figs.9 and 12, corrosion/erosion in the second loop test was reduced. Corrosion depth in Fig.12 was small (about 10 μ m), while it was about 100 μ m in the first loop test. It is considered that polishing inner surface of a high temperature tube and attaching metallic filters to the loop brought about the reduction of corrosion/erosion at a high temperature tube.

Conclusions

The following conclusions were drawn from the static and dynamic corrosion experiments in liquid Pb-Bi:

- 1) Al surface-treated layer produced by the gas diffusion method exhibited corrosion resistance to liquid Pb-Bi, while Al surface-treated layer produced by the melt dipping method suffered a severe corrosion attack.
- 2) In the first static corrosion test using both steels with and without Al surface treatments, oxides were formed on most steels, while FeAl was formed at 550C on some steels without Al surface treatments.
- 3) Significant corrosion was not observed at 450C on Mod.9Cr-1Mo steel and austenitic stainless steel, JPCA, while a thick ferrite layer was formed in the surface region of JPCA at 550C. The contents of Ni and Cr decreased significantly and Pb and Bi penetrated into the ferrite layer.
- 4) Corrosion/erosion at the high temperature part and deposition of Fe-Cr steel at the low temperature part occurred in the first dynamic corrosion test. The deposition of Pb oxide and Fe-Cr alloy in the narrow passage in electro-magnetic pump system caused plugging and decrease in Pb-Bi flow.
- 5) The modification of the loop system such as adoption of metallic filters and a wide passage of liquid Pb-Bi in the EMP system, and the use of an inner-polished 316ss tube brought about a good effect on operation of the Pb-Bi loop.

References

- [1] Y. Kurata, M. Futakawa, K. Kikuchi, S. Saito and T. Osugi, J. Nucl. Mater., 301(2002)28.

- Materials
F82H steel, Mod.9Cr-1Mo steel, JPCA(14Cr-16Ni-2Mo), 410 ss, 430 ss, 2.25Cr-1Mo steel, (316ss)
pure Fe, pure Mo,
(Al surface-treated steels)
- Temperature, Time
450°C, 3000h
550°C, 3000h
- Pb-Bi(45Pb-55Bi)
Oxygen-saturated Pb-Bi
Formation of PbO on the liquid Pb-Bi surface

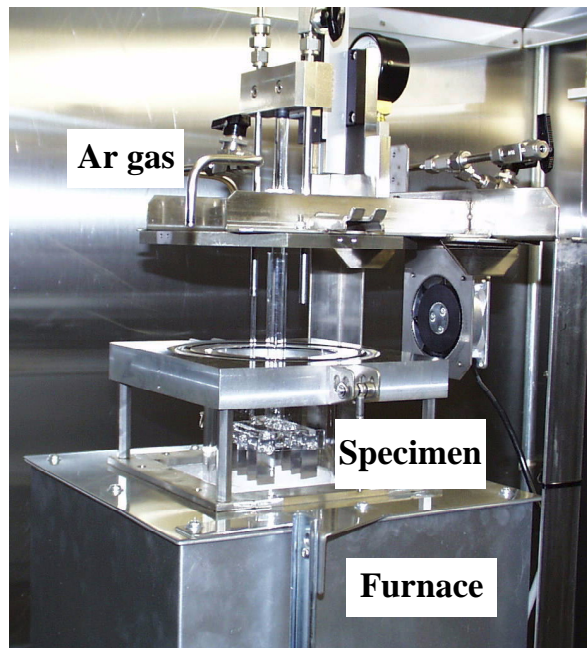


Fig.1 Static corrosion equipment in liquid Pb-Bi.

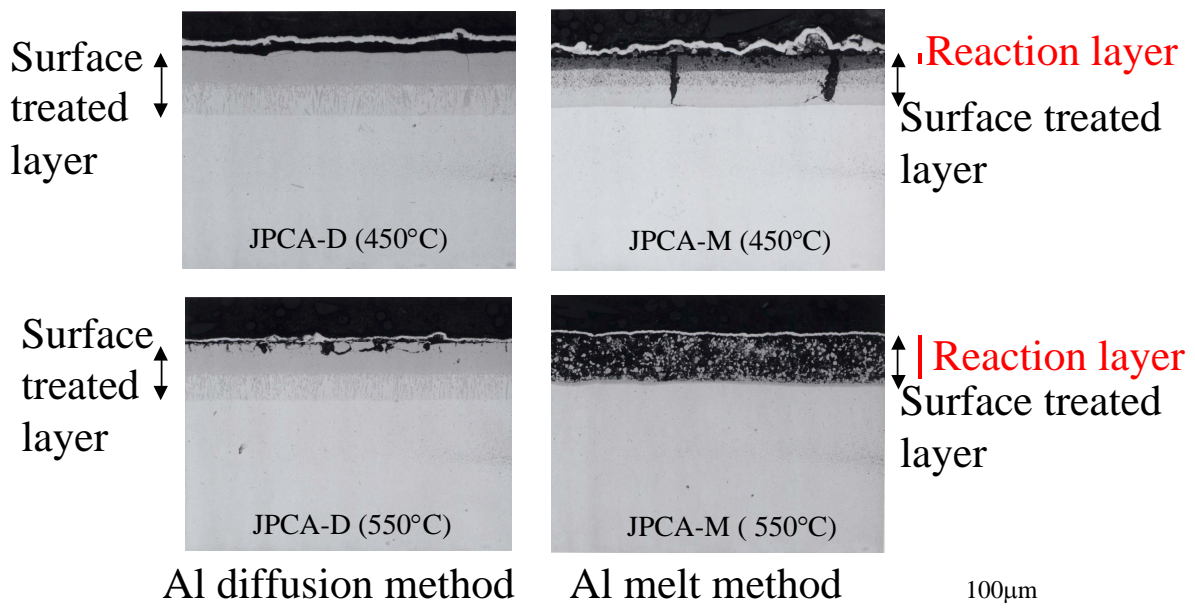


Fig.2 Optical micrographs of cross sections of Al surface-treated specimens (JPCA-D and JPCA-M) after the first corrosion test in liquid Pb-Bi at 450 and 550°C for 3000h.

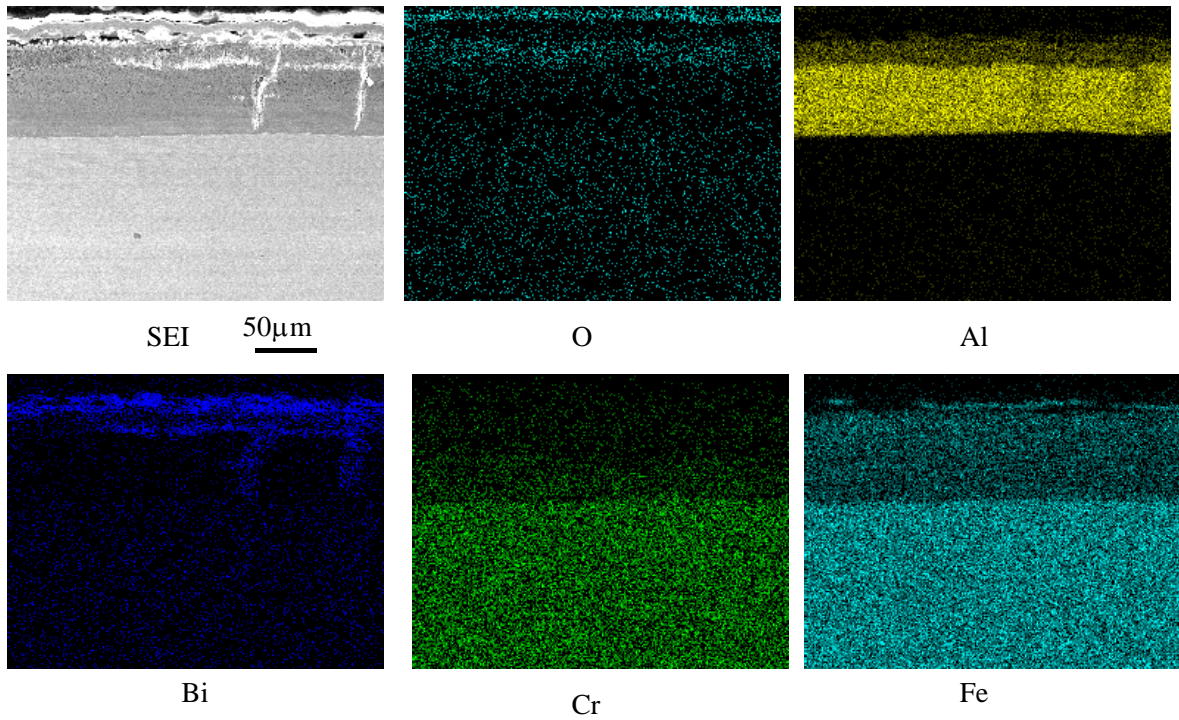


Fig.3 EDX analysis of cross sections of Al melt dipping-treated specimen (JPCA-M) after the first corrosion test in liquid Pb-Bi at 450°C for 3000h.

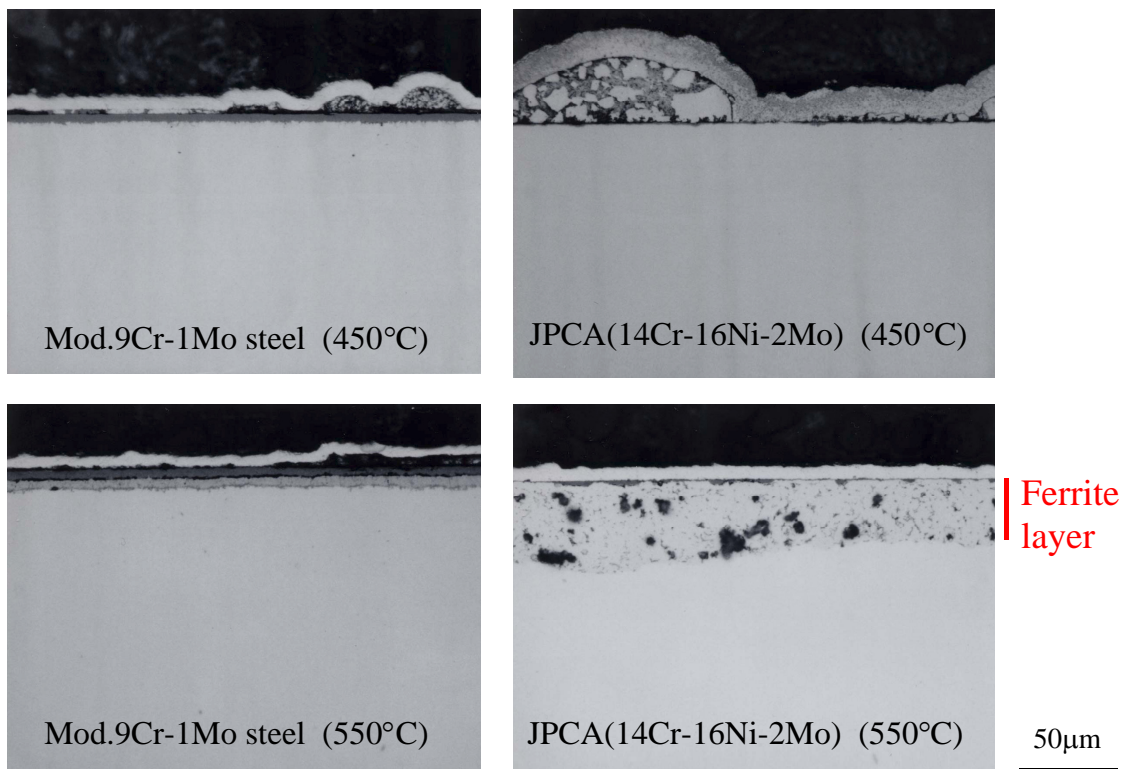


Fig4 Optical micrographs of cross sections of Mod.9Cr-1Mo steel and JPCA specimens after the second corrosion test in liquid Pb-Bi at 450 and 550°C for 3000h.

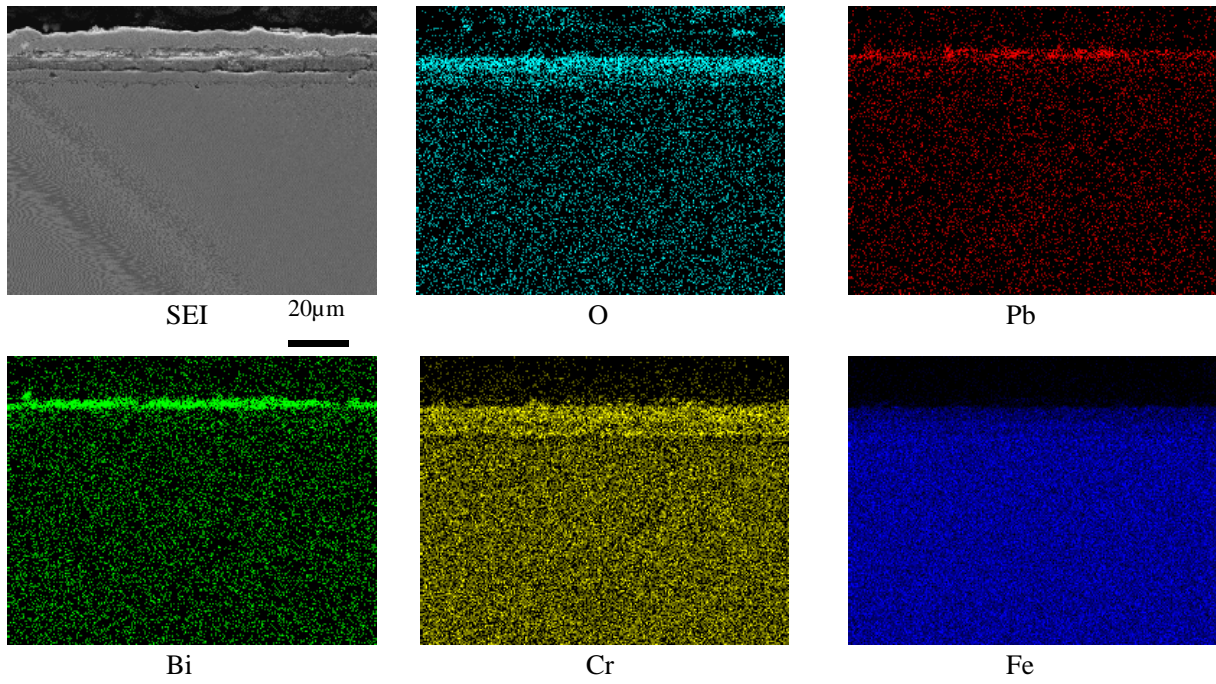


Fig.5 EDX analysis of cross section of Mod.9Cr-1Mo steel specimen after the second corrosion test in liquid Pb- Bi at 550°C for 3000h.

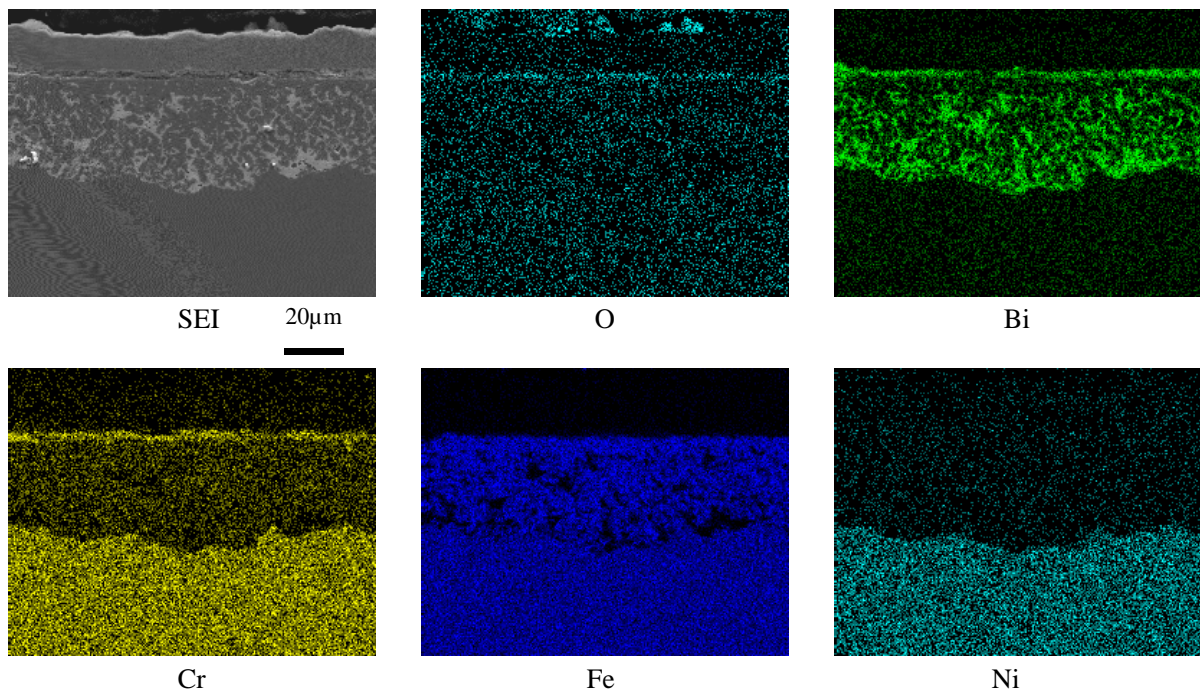


Fig.6 EDX analysis of cross section of JPCA(14Cr-16Ni-2Mo) specimen after the second corrosion test in liquid Pb- Bi at 550°C for 3000h.

Test temperature : 450°C

(High temperature part)

Temperature difference :

50°C (up to 100°C)

EMP power : 5 L/min

Velocity at test section : 1m/sec

Flow meter : Electromagnetic type

Pb-Bi inventory : 0.018m³

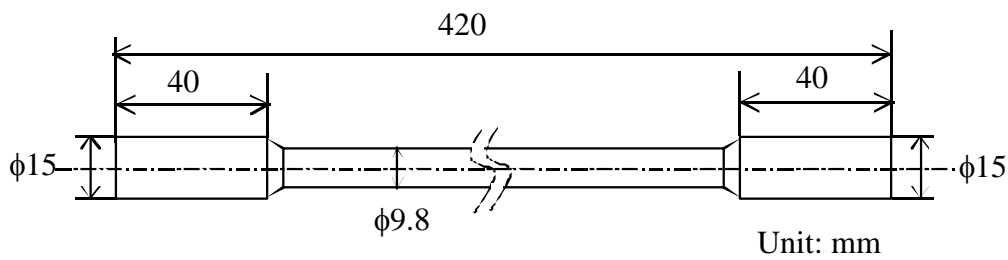
Material of components and specimen : type 316ss

Cover gas : 99.995% Ar

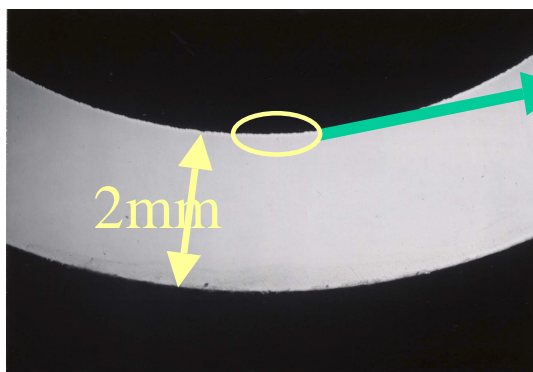
Testing time: ~3000h



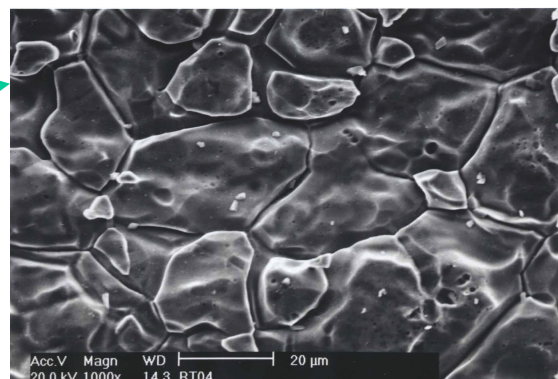
Fig. 7 Liquid Pb-Bi loop(JLBL-1) at JAERI.



(a) Shape and size of type 316ss tube specimen



(b) Transverse section of tube



(c) SEM micrograph of inner surface of tube

Fig.8 Shape, cross section and inner surface of the type 316ss tube specimen of liquid Pb-Bi loop.

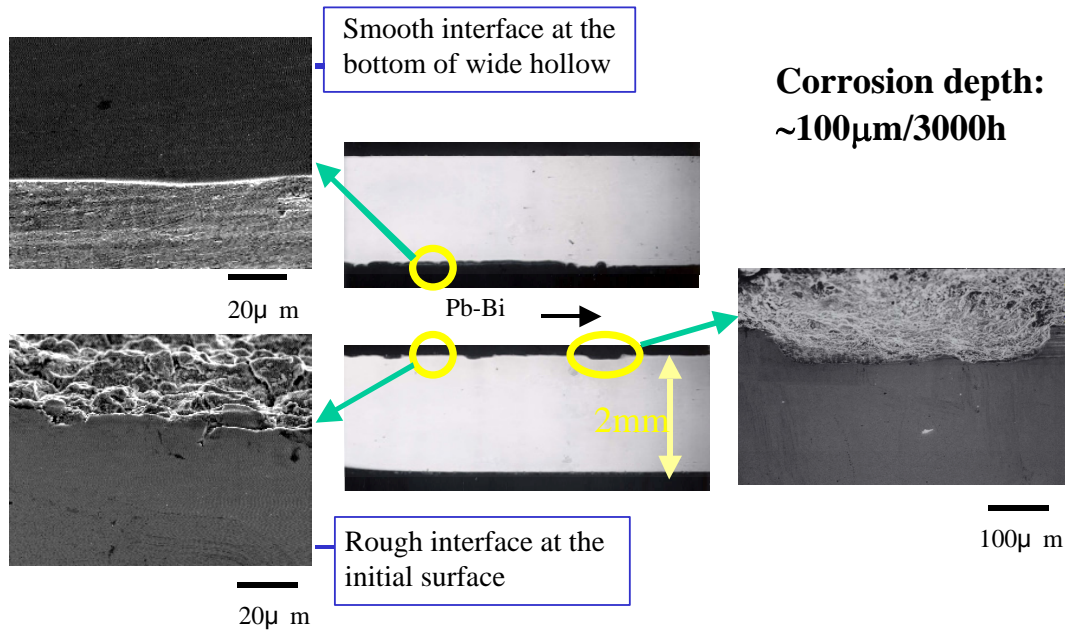


Fig.9 Corrosion/erosion of the type316ss tube specimen after the first dynamic corrosion test in liquid Pb-Bi loop.

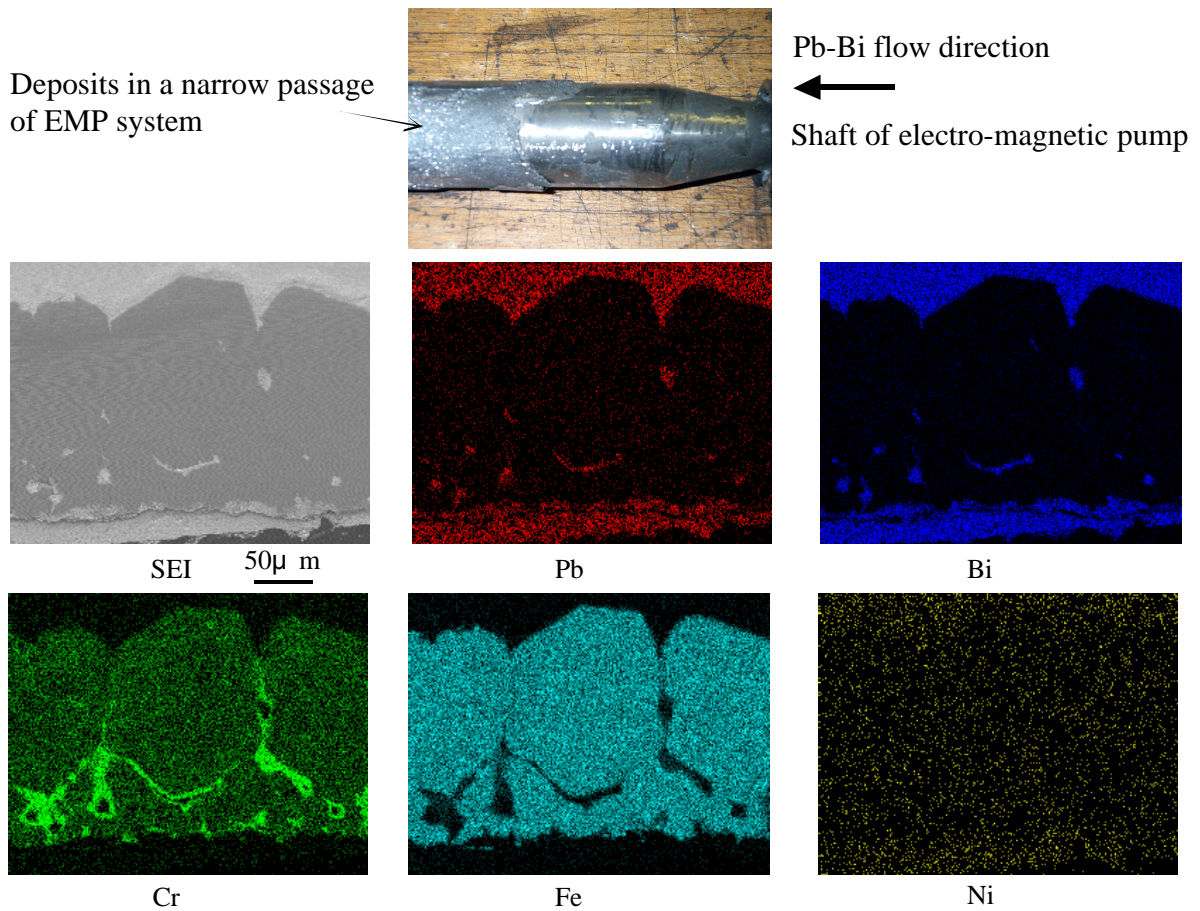


Fig.10 Analysis of deposits in a narrow passage of electro-magnetic system: EDX analysis of cross section of deposits.

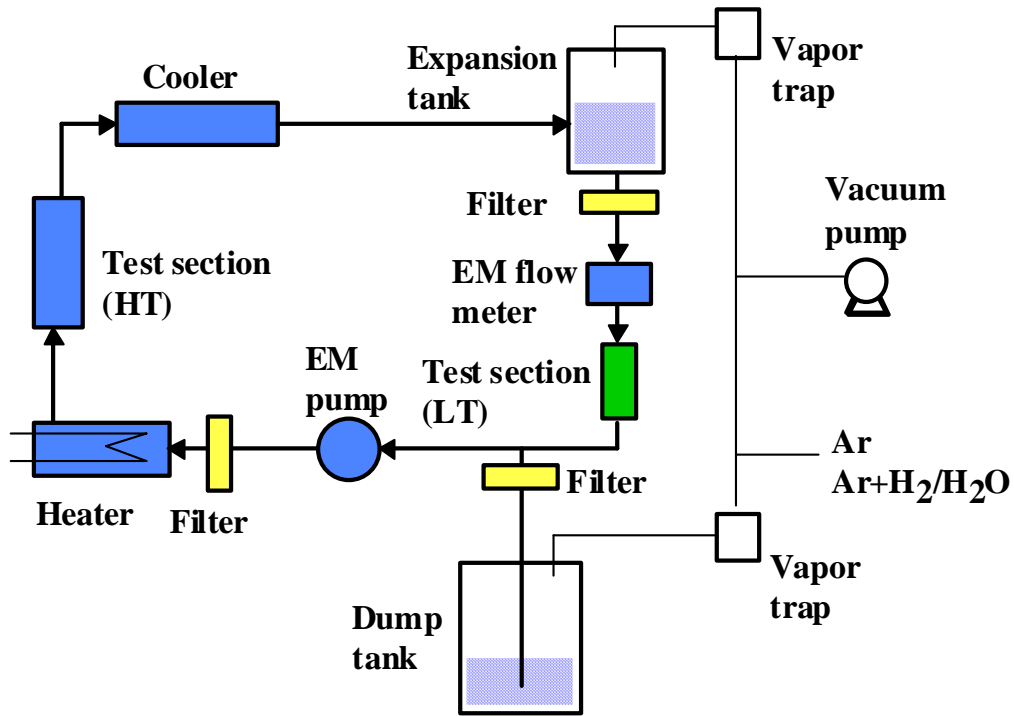


Fig.11 Flow diagram of modified liquid Pb-Bi loop(JLBL-1): three filters and a lower temperature test section were installed and a passage for liquid Pb-Bi in EMP system was made wider.

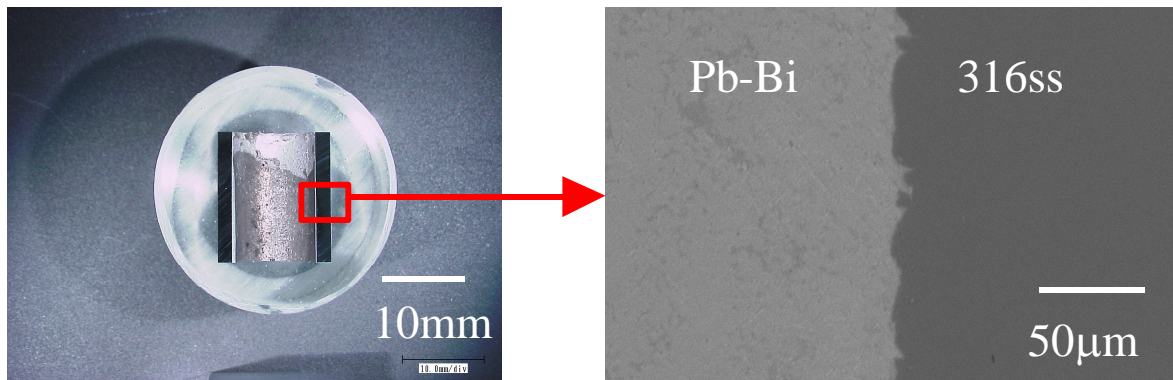


Fig.12 Cross section of high temperature tube(450°C) of type 316ss after the second dynamic corrosion test in liquid Pb-Bi loop.

CORROSION BEHAVIOR OF STEELS AND REFRACTORY METALS IN FLOWING Pb-Bi

B.Long^{2**}, G.Scaddozzo³, C.Fazio^{1***}, M.Agostini¹, A.Aiello¹, G.Benamati¹

1. ENEA C.R. Brasimone, 40032 (BO), Italy

2. China Institute of Atomic Energy, 102413 Beijing, China

3. Politecnico di Torino, Corso Duca degli Abruzzi 24, I-10129 Torino, Italy

***Presently at Forschungszentrum Karlsruhe

Abstract

An experimental activity was started in ENEA Brasimone centre to investigate the compatibility of selected materials in flowing Pb-Bi. The aim of the experiments was to evaluate the corrosion behaviour, in terms of corrosion mechanism and rates, of austenitic and martensitic steels as well as refractory metals (W, Mo and Ta). In addition the possible mechanical degradation of the steels, due to the exposition to the liquid metal, was evaluated by performing tensile tests on corroded specimens. The compatibility tests were performed in the LECOR (LEad CORrosion loop) designed and constructed for these purposes. The tests were performed at 673 K and with an oxygen content in the liquid metal in the range of 3.1×10^{-10} ~ 7.3×10^{-8} wt.%. Every 1500 h of loop operation, specimens were taken out of the test section and analysed. In this report the results of the corrosion investigation and tensile tests performed on the specimens exposed to the liquid metal for 1500 h and 4500 h are discussed. The metallurgical investigations showed that all corroded specimens, except Ta, exhibited a weight loss. Further, the evaluated weight change rates show that the refractory metals (W, Mo and Ta) present a higher corrosion resistance to Pb-Bi than steels. Concerning the tensile properties, it could be observed that the tensile behaviour of the austenitic steel was not affected by corrosion, while the martensitic steel exhibited a decrease in the elongation and the area reduction factors and the morphology of the fracture surface was mixed brittle-ductile.

Introduction

Accelerator Driven Systems (ADS) are proposed for the transmutation of nuclear waste^[1,2] in order to reduce its radioactive inventory and the associated radiotoxicity. ADSs consist of an accelerator for high-energy proton generator, a spallation target where the proton beam will impinge to produce neutrons, and a sub-critical blanket. Therefore, the demonstrations of ADSs cover high intensity proton accelerators, spallation targets of high power (~ 1 MW, like MEGAPIE) and their effective coupling with a subcritical core. Thus, the Megawatt pilot experiment (MEGAPIE), an international initiative, which was launched in 1999 in order to design, build, operate and explore a liquid lead-bismuth spallation target for 1 MW of beam power^[3] represents in the ADS roadmap a key experiment.

In this context, the compatibility of structural materials with the liquid metal was considered and compatibility tests of steels, coated steel and refractory metals with lead and lead bismuth eutectic were performed in recent years in stagnant conditions^[4-11].

The aim of the experimental activities performed with the LECOR loop was to describe corrosion mechanism and to estimate corrosion rates of AISI 316L austenitic steel, T91 martensitic steel, W, Mo and Ta exposed to flowing Pb-Bi with low oxygen activity. Moreover the tensile behaviour of corroded AISI 316L and T91 steel was also investigated. The results are relevant for the MEGAPIE project, since the chosen test parameters are very close to the real conditions of the window of the MEGAPIE target.

Facility

The LECOR loop, reported in figure 1, is a non-isothermal corrosion loop, consisting of feed tank (S2), mechanical pump (P), heat exchanger (EX), heater (H), three test sections (TS), air cooler (C), storage tank (S1), oxygen sensor and etc, where a detailed description of the loop is given in reference^[18]. In Table.1 the main characteristics of the loop are given.

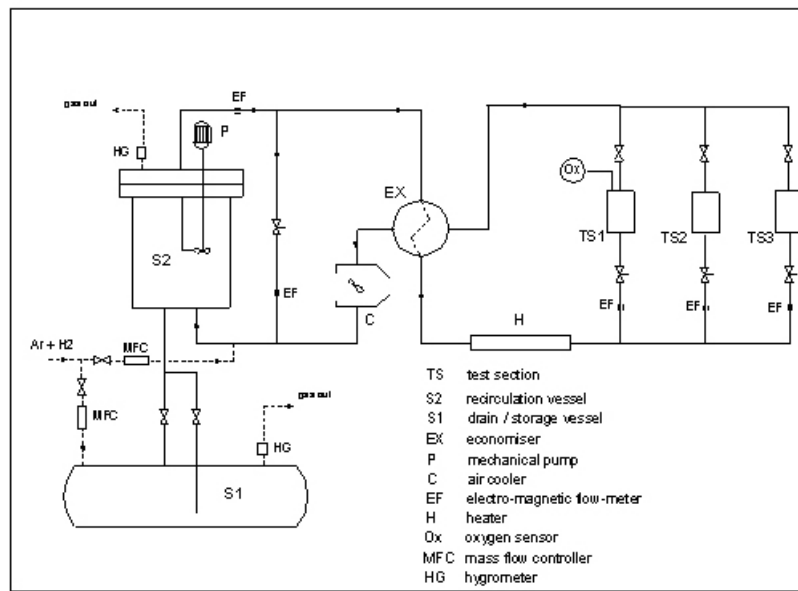


Fig.1 Flow scheme of LECOR loop

A detailed description of the oxygen control and monitoring in the LECOR loop is given elsewhere^[18], here it is recalled that for guarantying a low oxygen concentration in the liquid metal, the Pb-Bi was treated with H₂ gas in the storage tank at 603K, following the indications of the work reported in reference^[12] and 80 wppm of pure Mg were added to the liquid eutectic. During operation, the oxygen content in Pb-Bi was monitored by an electrochemical oxygen sensor (Ox), which was placed in the hot part of the loop, close to one of the test sections. The EMF recorded during the test and the corresponding oxygen activity both are given in the diagram of Fig.2. As shown in this diagram the oxygen activity was between 2.3×10^{-6} and 5.5×10^{-4} , corresponding to 3.1×10^{-10} and 7.3×10^{-8} wt.% of oxygen concentration in liquid Pb-Bi.

Table.1 Main parameters of the LECOR loop

Maximum temperature in the test section (°C)	550
Maximum Pb-Bi flow rate in the pump delivery line (m ³ /h)	4
Total installed electrical power (kW)	150
Maximum heating power of heater H (kW)	82
Maximum heat exchange power in EX (kW)	240
Inventory of Pb-Bi (m ³)	0.6
Design pressure (bar)	4

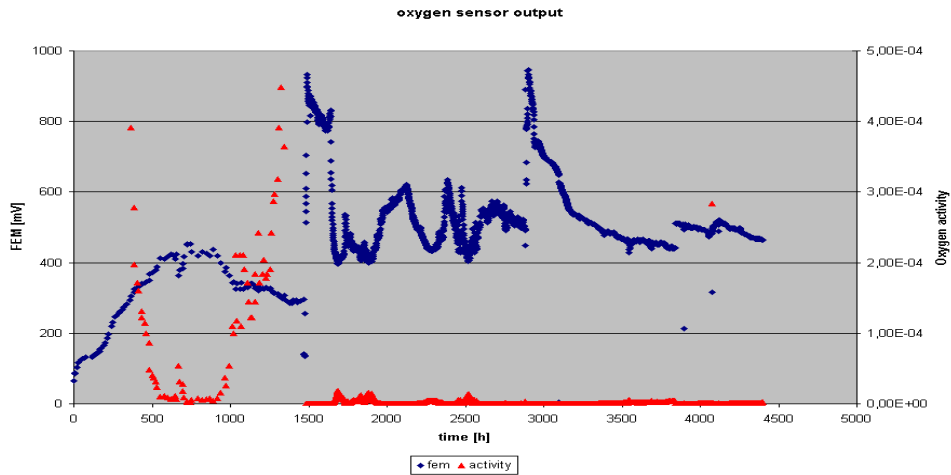


Fig.2 Electromotive force and oxygen activity in the liquid metal recorded during test period

Experimental

Materials

The materials investigated were the following:

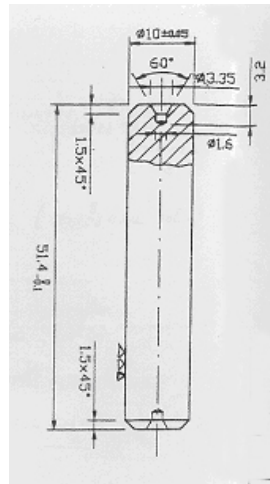
- a. Austenitic steel AISI 316L and martensitic steel T91 (corrosion and tensile tests), the chemical composition of the steels are given in Table.2.
- b. Refractory metals:
 - a. Pure molybdenum Mo (purity about 99.95%, sintering), (corrosion tests).
 - b. Pure tungsten W (purity about 99.9%, sintering), (corrosion tests).
 - c. Pure tantalum Ta (purity about 99.9%), (corrosion tests).

The specimens include two kinds of shape:

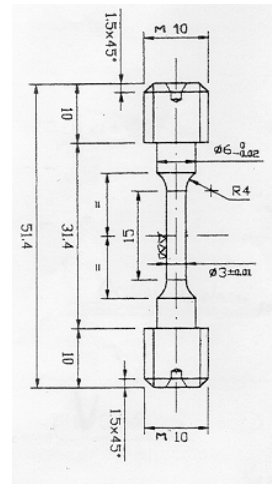
- a. Cylindrical machined specimens, $\Phi 10 \times 50$ mm (see Fig.3a), for the evaluation of the corrosion rate and mechanism.
- b. Cylindrical tensile specimens with 3mm diameter and a gauge length of 10mm (see Fig.3b)

Table. 2 Chemical composition of steels (wt.%, balance Fe)

Element	Cr	Ni	Mo	Mn	V	Nb	Si	C
AISI 316L	17.3	12.1	2.31	1.8	----	----	0.35	0.02
T91	8.26	0.13	0.95	0.38	0.20	0.075	0.43	0.105



a. specimen for corrosion test



b. specimen for tension test

Fig.3 Dimensions of the test specimens

Test procedure

Before locating the specimens in the test sections of the LECOR loop, they were degreased, weighed and their diameters were measured. As described in the previous paragraphs the Pb-Bi was treated with hydrogen in the drain tank and afterwards the loop was filled with the liquid metal. During the test, the temperature in the test sections was set at 673 K, in the cold part of the loop the temperature was 573 K and the liquid metal velocity in the test sections was 1 m/s. In table 3 the loop parameters set for the tests, were summarised. After 1500 h and 4500 h of exposure to the liquid alloy, two corrosion specimens for each material tested and four tensile specimens of AISI 316L and T91 steels were taken out from test sections. One corrosion specimen for each type of material was immersed in a fresh solution of CH₃COOH, H₂O₂, C₂H₅OH in a ratio of 1:1:1 in order to remove the adhering Pb-Bi. Specimen's surfaces were then washed and dried, and the procedures of weighting and measuring were repeated until the weight of specimens remained constant. Each second corrosion specimen without cleaning was studied by optical microscopy (OM), scanning electron microscopy (SEM) and electron probe microanalysis (EPMA). The EPMA measurements were carried out by the energy dispersive X-ray spectroscopy (EDX), which was used to evaluate the chemical composition of the corroded layers and bulk materials.

Table. 3 The parameters of corrosion test in LECOR loop

Temperature in the test section	400°C (673K)
Temperature in the cold part	300°C (573K)
Test time	1500h, 3000h, 4500h
Velocity in the test section	1m/s
Oxygen concentration	3.1x10 ⁻¹⁰ wt.% ~ 7.3x10 ⁻⁸ wt%

Tensile test on AISI 316L and T91 were carried in SYNTECH test machine at 673 K and under Ar atmosphere, with an extension rate of 2mm/min, corresponding to an

initial strain rate of 3×10^{-3} /s. After tensile test, SEM examination of the fracture surfaces of specimens was performed.

Results

Austenitic steel AISI 316L

Corrosion: The weight measurement of AISI 316L specimens after 1500 h and 4500 h exposure to the liquid metal indicated that they exhibited a weight loss. The measured weight variations ($\Delta W/\text{mm}^2$) are reported in Table 4. In Figs 4a and 4b the optical micrographs of the cross section of the 1500 h and 4500 h corroded specimens are reported. As can be observed in Fig 4a, after 1500h the AISI 316L steel exhibited a very limited attack while the 4500 h sample (Fig 4b) exhibited a more evident corrosive attack. Moreover, it was observed, on both samples, that the deepness of the liquid metal attack was not uniform on the entire surface of the specimen. Indeed, as can be seen in Fig. 4b, the morphology of the corrosive attack is for some extend similar to that of a pitting corrosion mechanism. In order to reveal the microstructure of the corroded layer, the cross section was etched with a solution of oxalic acid, see SEM micrograph of Fig.5a. As shown in this figure a corroded layer was detected and the EDX analysis performed on this layer showed that there is a Ni and Cr depletion (see Fig.5b). Thus, the corrosion of the AISI 316L steel occurred through the leaching of Ni and the consequently formation of a ferrite layer. This assumption might be explained by the high solubility of Ni in Pb-Bi, which is at 673 K about 16000 wppm ($T=673\text{K}$)^[9].

Table.4. Weight variation of AISI 316L exposed in LECOR

Test time (h)	0	1500	4500
Weight loss (mg/mm^2)	0	0.022	0.124

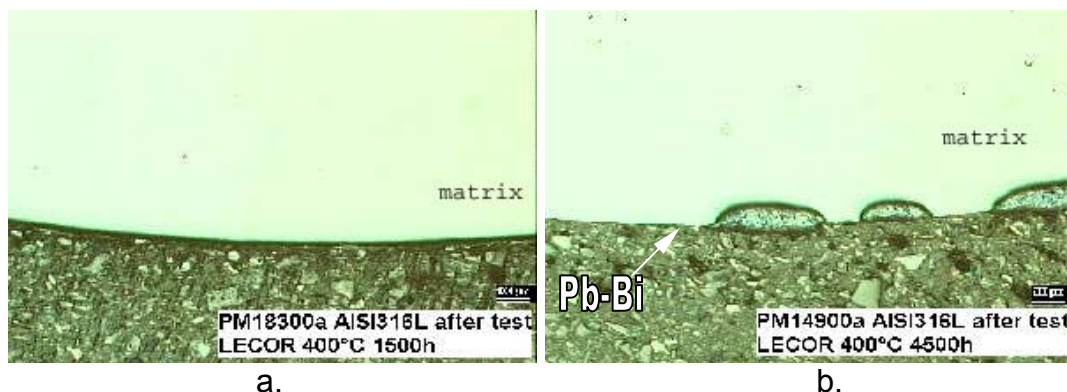


Fig.4 Optical micrographs of AISI 316L specimens after exposed in LECOR (x50) (a. 1500h, b. 4500h, both without etch)

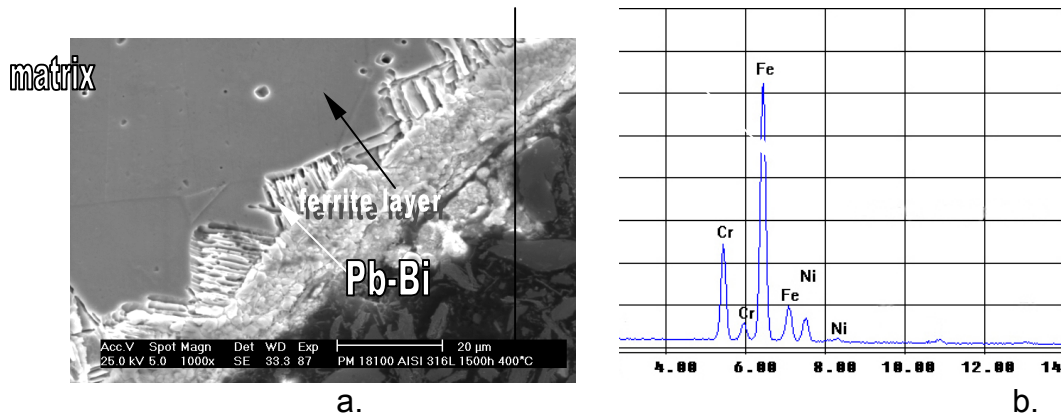


Fig.5 a SEM micrograph of the 1500h tested AISI 316L specimens; 5b EDX pattern on the ferrite layer of AISI 316L specimen (Fe: 76.55wt.%; Cr: 15.79wt.% Ni: 7.66wt.%)

Tensile Tests. The results obtained from the tensile test of AISI 316L before and after corrosion are reported in Table.5, where the average values of the yield strength (R(0.2%)), ultimate tensile strength (UTS), elongation percent (A%) and area reduction (Z%) are given. In Fig.7 selected engineering stress-strain curves are reported.

Table.5 The tension test result of AISI 316 steel

	Yield strength (YS) R(0.2%) MPa	Ultimate Tensile Strength (UTS) σ_b MPa	Percent Elongation A%	Reduction of Area Z%
As received	165±34	455±40	69±3	72±3
1500h	185±25	475±9	68±3	68±1
4500h	185±19	455±5	57±14	66±1

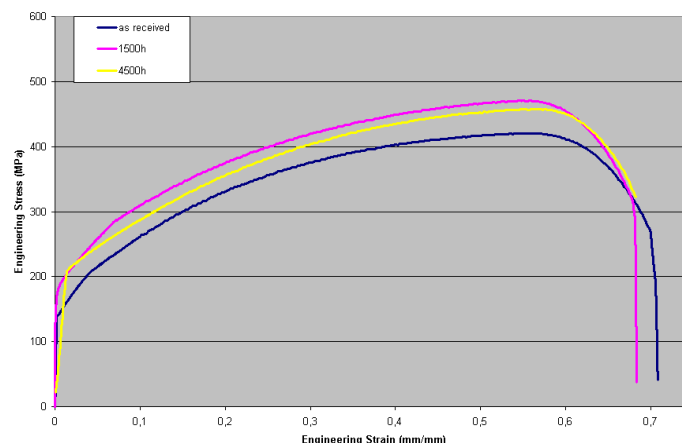


Fig.7 Engineering stress-strain plots of AISI 316L

Comparing tensile behaviors of as-received specimens with that of corroded specimens, both the strength parameters (yield strength YS and ultimate tensile strength UTS) and the ductility parameters (percent of elongation A% and area reduction Z%) don't change significantly and the corrosion seems not to affect the

tensile properties. The fractographic analyses performed on the 1500 h and 4500 h tested samples showed that the fracture surface had a dimpled morphology, which is typical of a ductile fracture.

Martensitic steel T91

Corrosion: The weight measurements of martensitic steel after tests exhibited, as for the austenitic steel, a weight loss. In table.6 the values of the weight changes versus test time are reported. Metallurgical analyses are given in Fig.9 and Fig.10. From the optical micrograph it could be observed that, differently from AISI 316 L, the liquid metal corrosion occurred uniformly. The SEM micrographs of the two T91 corroded specimens shows that a transgranular and intergranular attack occurred, where lead and bismuth penetrated into the matrix along the intergranular or pierced through the grain.

Table.6. Weight variation of martensitic steel T91 exposed in LECOR

Test time (h)	0	1500	4500
Weight loss (mg/mm ²)	0	0.027	0.184

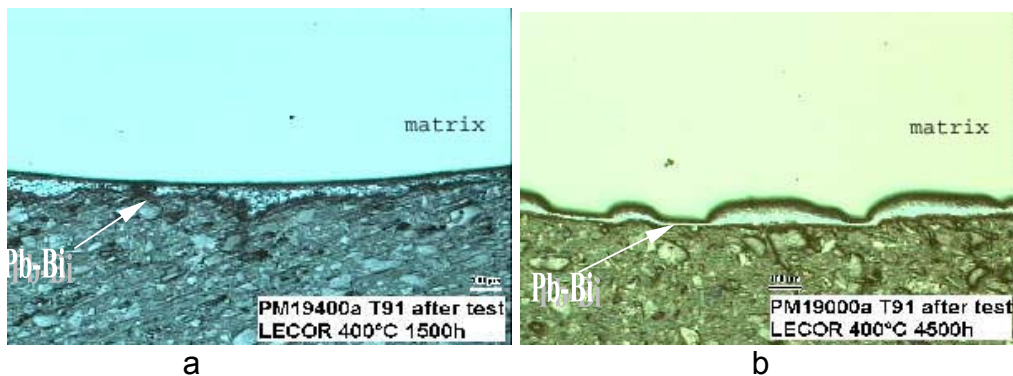


Fig.9 Optical micrographs of T91 specimens after exposed in LECOR (x50) (a. 1500h b. 4500h, both without etch)

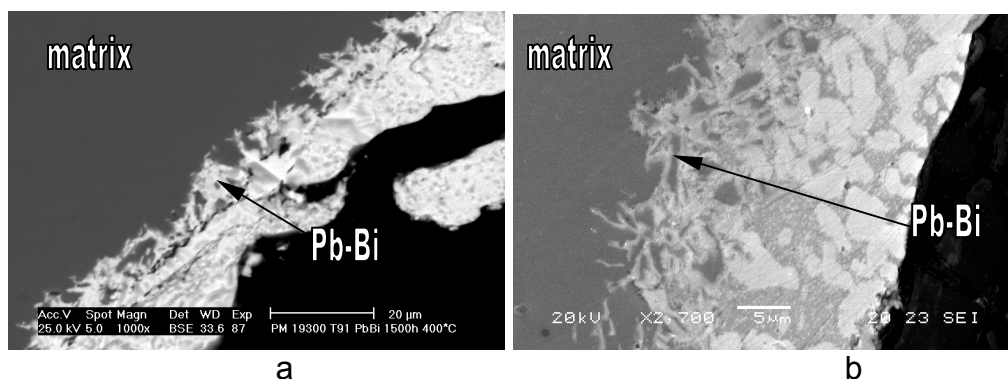


Fig.10 SEM micrograph of AISI 316L specimens after exposed in LECOR (a. 1500h b. 4500h, both without etch)

Tensile properties: Fracture surfaces of the corroded specimens are reported in Figs.11. As shown in those figures a loss of ductility can be observed at the peripheral part of the samples, which exhibited a flat morphology. Contrary, the central region of the fracture surface showed a ductile behaviour (see Figs.11 a2, b2.). Selected engineering stress-strain plots are reproduced in Fig.12, and the main

results of the tensile tests are listed in Table.7. Comparing the results of as-received specimen and corroded specimens (immersion in flowing Pb-Bi for 1500h and 4500h), it shows that the elongation percent (A%) and area reduction (Z%) of corroded specimens (both of 1500h and 4500h) are significant lower than that of uncorroded specimen. Comparing the tensile properties between the specimens of 1500h and the specimens of 4500h, it is also possible to notice a detrimental effect by the increasing of corrosion time. This tensile behaviours of corroded T91 steel is quite different to the similar past works performed on martensitic steel exposed to Pb-17Li^[14, 16], where the liquid metal had little or no effect on the tensile properties. Moreover, the liquid metal embrittlement test performed in Pb^[15] have shown that there was no influence on the mechanical behaviour of normal heat-treated martensitic steel.

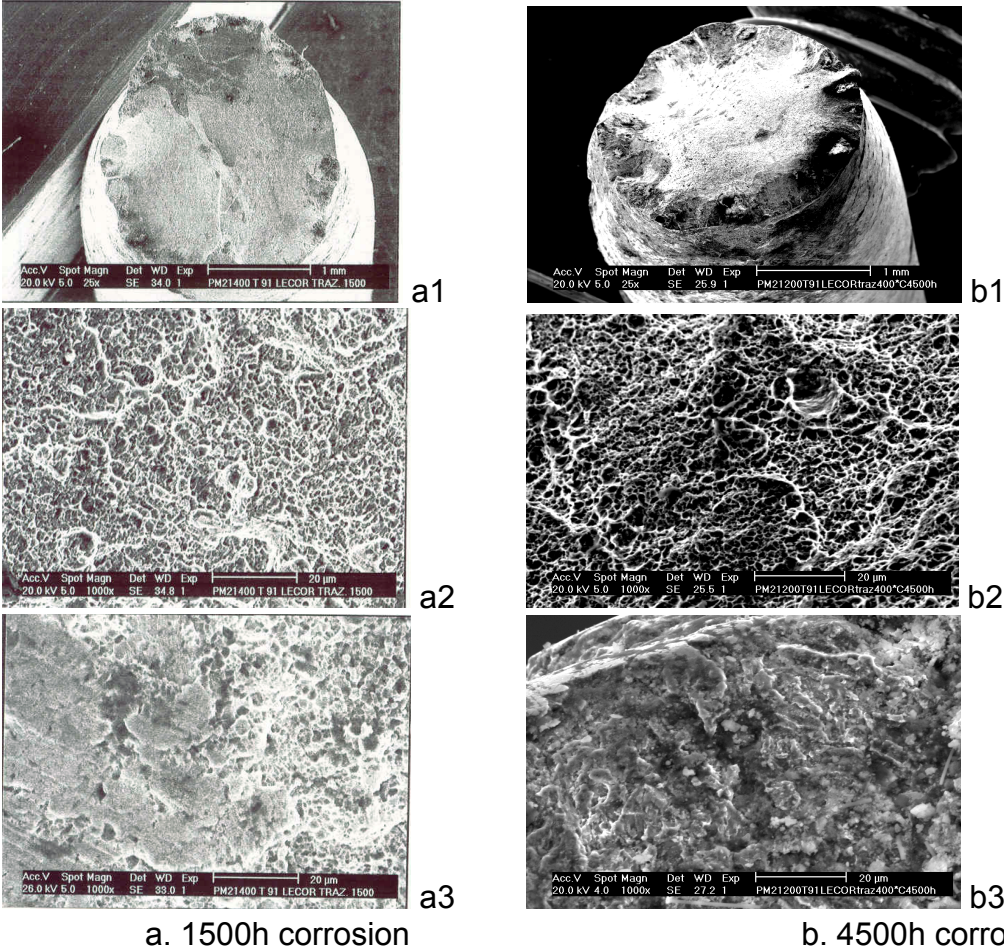


Fig.11 SEM micrographs of martensitic steel T91 fracture surfaces (a1,b1: full morphology of fracture surface; a2,b2: the center of the fracture surface; a3,b3: at the periphery of fracture surface)

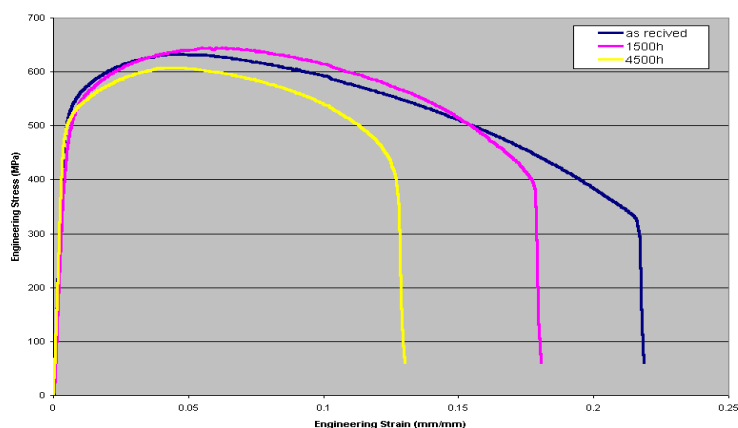


Fig.12 Engineering stress-strain plots of martensitic steel T91

Table.7 The tension test result of T91 steel

	Yield strength (YS) R(0.2%) MPa	Ultimate Tensile Strength (UTS) σ_b MPa	Percent Elongation A%	Reduction of Area Z%
As received	535±42	645±26	22±1	72±2
1500h	535±10	640±14	18±1	42±8
4500h	515±7	625±15	16±3	32±12

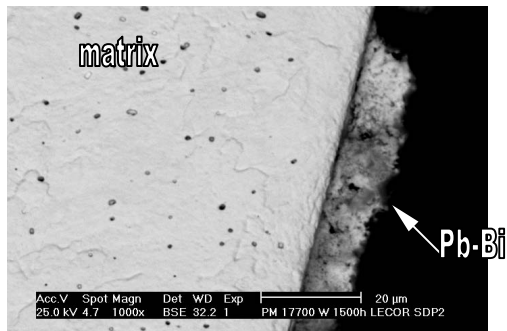
Refractory metals

Visual examination of all refractory specimens (Mo, W and Ta) did not show evident attacks by liquid Pb-Bi eutectic. The weight change measurements of the specimens corroded in the LECOR loop at different time were reported in Table.8. It should be noted that Ta exhibited a weight gain, which is different from other materials (W, Mo and steels). In Fig.13 the OM-micrographs of the corroded refractory metals are reported and it evident that these metals exhibit still a smooth surface, even after 4500 h of exposition to the flowing liquid metal. For pure W and Mo, the weight loss could be associated with the uniform dissolution and the low solubility of W and Mo in lead-bismuth eutectic at 673K. For pure Ta, it can be assumed that a very thin and stable oxide layer was formed on the surface even if it is not detectable with the analytical techniques used. This assumption can be reported considering the free energy of formation of the oxides. As reported in Figure.14, the weight gain of the Ta samples can be explained by considering that the oxygen potential needed to form Ta oxide is much lower than for the other refractory metals and for Fe. Concerning the morphology of the Ta oxide, more analysis will be necessary to clarify the nature and the dimension of this oxide.

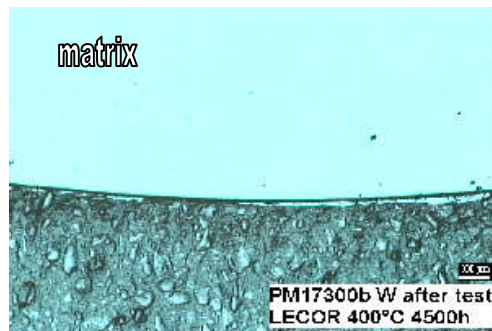
Table.8 Weight variation of refractory metals exposed in LECOR

Metal	W		Mo		Ta	
	1500	4500	1500	4500	1500	3000
Test time (h)	1500	4500	1500	4500	1500	3000
Weight loss (mg/mm ²)	1.36x10 ⁻³	1.54x10 ⁻³	1.08x10 ⁻³	4.5x10 ⁻³	-0.80x10 ^{-3*}	-1.37x10 ^{-3*}

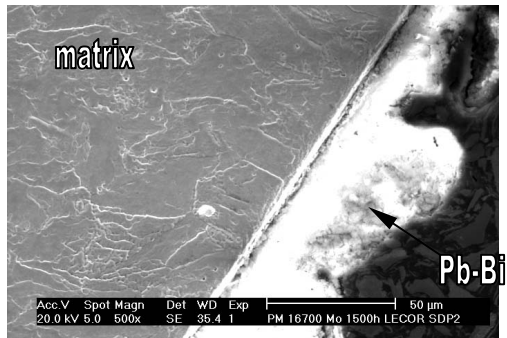
* minus sign means weight gain.



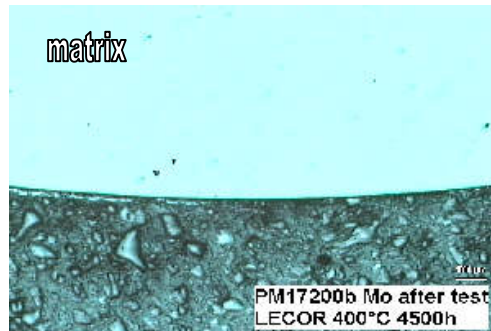
a1. W



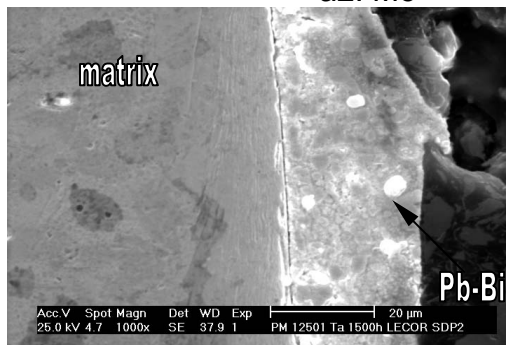
b1. W



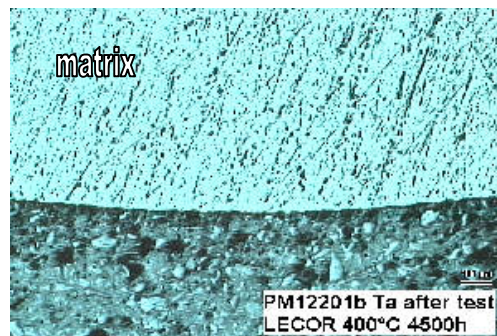
a2. Mo



b2. Mo



a3. Ta



b3. Ta

(x50)

a. 1500h SEM

b. 4500h (b3 is 3000h) OM

Fig.13 metallurgical micrographs of refractory metals (LECOR, T = 673K)

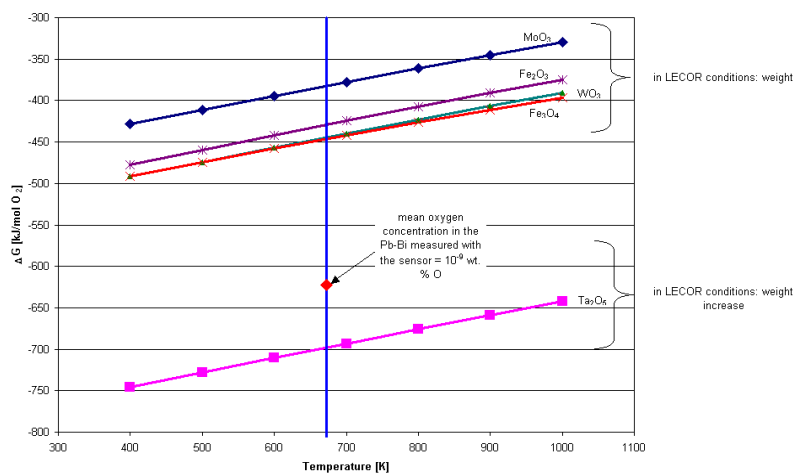


Fig. 14 Comparison of the oxidation potential of W, Mo, Ta and Fe with the mean oxidation potential in the LECOR loop.

Preliminary conclusion

Considering that the whole test plan is not finished yet, hereafter only preliminary conclusions are given:

- 1) The low oxygen activity was achieved by adding Mg, which acts as oxygen getter, and by pre-treatment the liquid Pb-Bi eutectic with Ar + 3% H₂. The oxygen activity was successfully monitored during the corrosion test with an oxygen probe, which is installed on the hot part of LECOR.
- 2) All the materials exhibited a weight loss after 1500h and 4500h exposure in LECOR conditions except of Ta. It can be seen that the weight loss of refractory metals is two orders of magnitude smaller than that of steels.
- 3) The corrosion behavior of austenitic steel AISI 316L exhibited mainly a Ni depletion and consequently a ferritic layer was formed on the surface of specimen. As expected the corrosion behavior of martensitic steel T91 shows a elemental dissolution and transgranular and intergranular attacks were found on the steel surface accompanied by liquid metal penetration into the matrix. The thickness of penetration increased with the increasing of exposure time. A fundamental role of the natural surface oxides could be envisaged in the evolution of the corrosion of the two steels. A larger and uniform attack on the whole specimens has been evidenced for T91 while not uniform attack has been observed in AISI 316 L also after 4500 h.
- 4) The tensile behaviour of austenitic steel AISI 316L seems to be unaffected by corrosion in flowing Pb-Bi, while the martensitic steel T91 exhibited a decrease of ductility property and the surface fracture showed a mixed ductile-brittle morphology. The different behaviour between austenitic and martensitic steels could be explained also on the basis of the different corrosion behaviour of the two steels.

References

- [1] C.Rubbia, J.A.Rubio, S.Buono, F.Carmianti, N.fietier, J.Galvez, C.Geles, Y.K adi, R.Klapish, P.Mandrillioni, J.P.Revol, C.Roche, European Organisation for Nuclear Research, CERN report AT/95-44 (ET), 1995.
- [2] H.Conde Kalmar (Ed.), Proceedings of 2nd International Conference on Accelerator-Driven Transmutation Technologies and Applications, Uppsala University, 1997.
- [3] G.S. Bauer, M.Salvatores, G. Heusener, J. Nucl. Mater. 296 (2001) 17-33
- [4] G.Benamati, P.Buttol, V.Imbeni, C.Martini, J. Nucl. Mater. 279 (2000) 308-316
- [5] G.Mueller, G. Schumacher, F. Zimmermann, J. Nucl. Mater. 278 (2000) 85
- [6] C.Fazio, G. Benamati, C.Martini, G.Palombarini, J. Nucl. Mater. 296 (2001) 243
- [7] F. Barbier, A. Rusanov, J. Nucl. Mater. 296 (2001) 231-236
- [8] H. Glasbrenner, J. Konys, G. Mueller, A. Rusanov, J. Nucl. Mater. 296 (2001) 237-242
- [9] X. He, N.Li, M. Mineev, J. Nucl. Mater. 297 (2001) 214-219
- [10] G. Benamati, C.Fazio, H. Piankova, A. Rusanov, J. Nucl. Mater. 301 (2002) 23-27
- [11] Y. Kurata, M. Futakawa, K.Kikuchi, S.Saito, T. Osugi, J. Nucl. Mater. 301 (2002) 28-24
- [12] I. Ricipito, C.Fazio, G.Benamati, J. Nucl. Mater. 301 (2002) 60
- [13] O.Kubaschewski, C.B. Alock, P.J. Spencer, Materials Thermo-chemistry, 6th Ed., Pergamon, Oxford, 1993.

- [14] O.K Chopra, D.L. Smith, J. Nucl. Mater. 596 (1986) 141-143.
- [15] G. Nicaise, A. Legris, J.B. Vogt, J.Foct, J. Nucl. Mater. 296(2001) 256
- [16] G. Benamati, C. Fazio, I. Ricapito, J. Nucl. Mater., Vol. 307-311, (2002) 1391-1395.
- [17] Kubaschewski and Alocolok, Materials Thermo-Chemistry, program press, 1993
- [18] C. Fazio, I. Ricapito, G. Scaddozzo, G. Benamati "Corrosion behaviour of steels and refractory metals and tensile features of steels exposed to flowing PbBi in the LECOR loop" to be published on Journal of Nuclear Materials.

INFLUENCE OF HYDRODYNAMICS ON THE CORROSION OF MARTENSITIC STEEL T91 IN LIQUID Pb-Bi COMPARISON BETWEEN EXPERIMENTS AND THEORETICAL CALCULATIONS

F. Balbaud-Célérier, C. Delisle, A. Terlain, Service de la Corrosion et du Comportement des Matériaux dans leur Environnement CEA/Saclay – 91191 Gif sur Yvette Cedex - France

Abstract

Corrosion tests were performed in the CICLAD device at 400 °C on martensitic steel T91 and on pure iron for low oxygen concentrations (around 10^{-11} - 10^{-12} wt %) and for different rotating speeds of the cylindrical specimens varying from 500 rpm to 3000 rpm. For this oxygen concentration range, dissolution is expected and if the dissolution process is controlled by the diffusion of dissolved iron from the solid/liquid interface to the Pb-Bi bulk, it is possible by using previously established equations expressing the mass transfer coefficient, to calculate the corrosion rates [1].

The different experiments performed show quite heterogeneous results from one tests to another but also for different samples during the same test. In all the cases when dissolution is observed, increasing the fluid velocity leads to an increase of the corrosion rate. Moreover, a linear variation of the corrosion rate with the rotating speed at a power of 0.7 can be represented which confirms the diffusion control of the dissolution process. However, more results would be needed to ascertain this conclusion.

Finally, these results show that the corrosion behaviour is strongly dependent on local parameters like the Pb-Bi hydrodynamics, the local oxygen content, the surface state of the samples and that a very fine and local control of all these parameters is necessary to anticipate corrosion.

Introduction

For practical evaluation of the Pb-Bi velocity effect on the corrosion of steels, an experimental device, CICLAD (Corrosion Induced by the Circulation of a LeAD alloy) has been built in the laboratory, which consists in a rotating cylinder operating under controlled hydrodynamic conditions.

Previous tests performed in this device at 470 °C showed an important dissolution of martensitic steel T91 for a low oxygen concentration (10^{-11} - 10^{-12} wt %) and for two flow configurations: pipe flow and rotating cylinder. An important position effect of the samples was also observed: for both hydrodynamic configurations, the downstream sample was much more corroded than the upstream sample. Moreover, an influence of the liquid alloy hydrodynamics was observed by comparing corrosion rates measured in both flow configurations [2].

In this paper, results of tests performed on martensitic steel T91 and on pure iron at 400 °C for a low oxygen concentration and for various cylinder rotating speeds are presented and discussed. A comparison is made with the corrosion rates calculated using the equations expressing the mass transfer coefficients.

Experimental data

The CICLAD device

The CICLAD device (Figure 1) has already been presented in previous CEA reports. It consists mainly of a pot containing the rotating cylinder system which is fixed at the bottom of a glove box (which allows to manipulate the corrosion samples in a controlled atmosphere without draining the device) and of a liquid metal circuit which allows the purification of the liquid metal by using a cold trap.

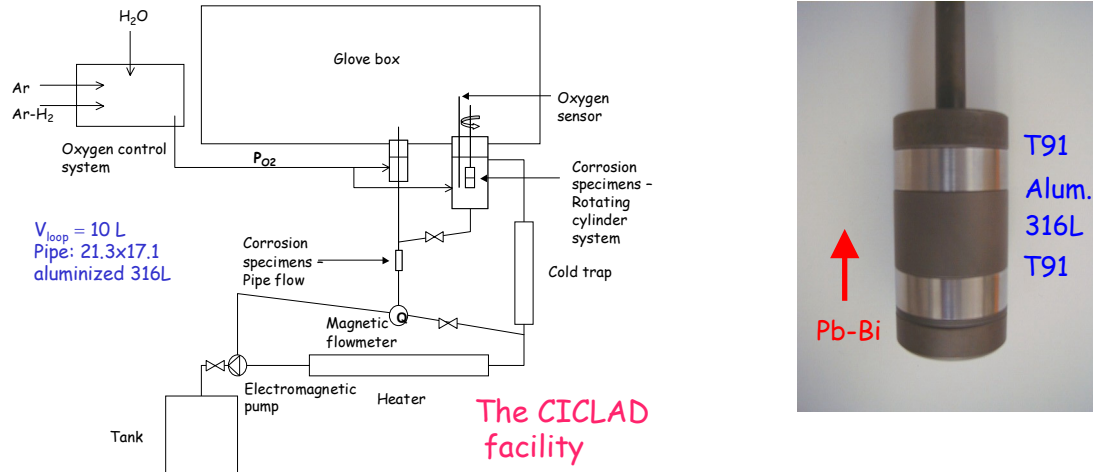


Figure 1. The CICLAD device. Figure 2. Rotating cylinder sample (one of the configurations with two T91 samples and an aluminized steel 316L cross-piece).

All the tests were performed at low oxygen concentrations (10^{-10} - 10^{-12} wt %). This concentration was maintained by imposing a constant pressure of 1 bar of an Ar-4 % H₂ mixture in the testing pot. The oxygen concentration in the testing pot was continuously measured (except for the last test) with an oxygen sensor (ref. Bi/Bi₂O₃ or In/In₂O₃) designed and built by DEN/DER/STR in CEA/Cadarache. For the last tests, zinc was also added to Pb-Bi (\approx 100 wppm) in order to ensure a constant low oxygen concentration. In previous static tests, it was shown that the addition of zinc in the liquid melt had no influence on the corrosion results [3]. In some tests, a prewetting step was also performed ($T = 480$ °C, $t = 16$ h) to ensure a satisfying wetting of the steels surface.

For the series of tests performed at 400 °C, the cold trap was not used due to a plugging of the electromagnetic pump. Therefore, in order to avoid the accumulation of corrosion products in the pot, a cold point was fixed at the bottom of the pot acting as a cold trap. Regular analyses of Pb-Bi samples showed no increase of the corrosion products (Fe, Cr, Ni) content in the pot. However, the iron solubility limit in Pb-Bi at 400 °C being around 0.3 wppm, and as the analytical techniques used do not allow a determination below 1 wppm, there is no certainty that the iron concentration had not reached the solubility limit. However, as for chromium (which solubility limit is close to 4 wppm at 400 °C), no increase is observed, we assume that the dissolved species concentration remains low.

Corrosion tests

Corrosion tests were performed on martensitic steel T91 and on pure iron. The composition of T91 is given in Table 1.

Table 1. Chemical composition of martensitic steel T91 (wt %)

Material	Cr	Ni	Mo	Mn	V	Nb	W	Ti	Si	C
T91	8.98	0.125	0.962	0.393	0.190	0.075			0.351	0.086

Specimens were cylinders of diameter 30 mm and lengths of 10 mm or 20 mm (Figure 2). Depending on the test, two or four specimens were placed on the holder. In all cases, the samples were separated by aluminized steel 316L cross-pieces. No specific treatment of the samples was performed after machining.

The total duration of the tests varied from 150 h to 512 h.

After the corrosion tests, the Pb-Bi alloy adhering to the steel surfaces was removed by an immersion in a 180 °C hot glycerine bath. Samples were cleaned in acetone and alcohol and dried for visual examination and weight measurement. Finally, pieces were cut and polished for cross section or longitudinal section examination by optical microscopy and scanning electron microscopy. Chemical analyses were performed by means of energy dispersive spectrometry (EDS).

Results

Several tests have been performed which are summarized in Table 2. In this table, the experimental conditions of each test are presented. The values of the rotating speed and of the oxygen concentration are the mean values calculated for all the test duration. The corrosion rate is given for each sample from the upper part of the holder (which is situated downstream) to the lower part (Figure 2). The Pb-Bi velocity in a pipe geometry corresponding to the cylinder rotating speed is calculated with the mass transfer coefficients expressed with the Eisenberg equation for the rotating cylinder and with the Berger and Hau equation for the pipe flow [1].

Table 2. Experimental conditions of the tests

Test	t (h)	Rotating speed (rpm)	C _{O2} (wt %)	V _{corrosion} (µm.yr ⁻¹)	V _{Pb-Bi} equiv. (m.s ⁻¹)
1	282	540	8.5×10 ⁻¹⁰	T91 51 (upper sample) 66 (lower sample)	0.58
2	375	529	7.6×10 ⁻¹⁰ (with an increase up to 10 ⁻⁸ wt % for 2 days)	T91 8 (upper sample) 2 1 3 (lower sample)	0.57
3	512	2714	6.85×10 ⁻¹² (prewetting + 100 ppm Zn)	T91 86 (upper sample) 2.5 (lower sample)	2.20
4	435	870	1.60×10 ⁻¹¹ (prewetting + 50 ppm Zn)	Pure Fe 75 (upper sample)	0.86
5	339	2845	No measurement (prewetting + 50 ppm Zn)	Pure Fe 359 (upper sample) ≈ 0 (lower sample)	2.25

Experiments performed on martensitic steel T91

For the first test, quite important weight losses were measured. In this test, no major difference of the weight losses was observed between the different samples. However, the Pb-Bi removal was not completely performed leading to an under evaluation of the corrosion rates.

Observations of the samples showed that the surface of steels was attacked with penetrations around 5 μm deep. An electrochemical attack in an oxalic acid bath showed that these penetrations are both intergranular and transgranular (Figure 3a). Some observations showed also cavities (about 10 μm wide) at the surface of the steel (Figure 3b).

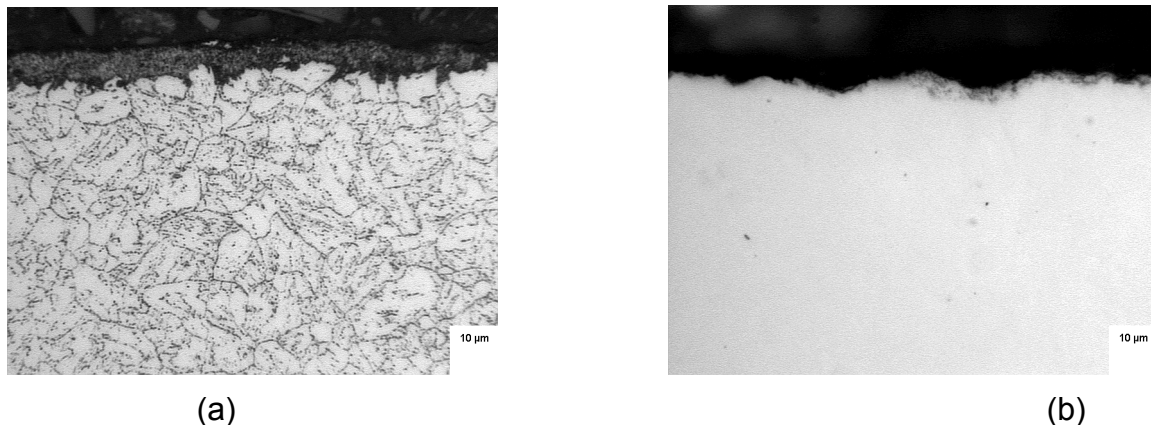


Figure 3. Microscopical observation of a cross section of T91 after an attack in an oxalic acid bath (a) and a longitudinal section (b) exposed to Pb-Bi at 400 °C after 282 h of testing at a rotating speed of 540 rpm ($C_{O_2} = 8.5 \times 10^{-10}$ wt %).

During the second corrosion test performed in the same conditions as the first one, an increase of the oxygen concentration from 10^{-10} wt % to approximately 10^{-8} wt % (which is above the formation of magnetite at 400 °C) occurred during the test. Very small weight losses were obtained and the observation of the samples showed no apparent attack of the surface of the material. With the usual observation techniques, no oxide layer was detected: its thickness must be lower than 1 μm . Moreover, wetting concerns occurred during this test especially for the lower sample probably due to the existence of a thin oxide layer at the steel surface.

Therefore, in order to ensure a very low oxygen concentration, zinc was added to the liquid melt (about 50-100 μm) and to improve the wetting of the samples, a pre-wetting step was performed (immersion of the samples in Pb-Bi at 480 °C during 16 hours).

For the third test, the oxygen concentration was below 10^{-11} wt %. In this test performed at a rotating speed of 2714 rpm, an important weight loss was obtained for the upper sample and a very small weight loss was obtained for the lower sample. This extremely different behaviour is quite surprising as theoretically both samples are surrounded by the same environment. The weight loss obtained on the upper sample was higher than that of the upper sample of the first test which was performed at a lower rotating speed (540 rpm) showing that increasing the rotating speed leads to an increase of the corrosion rate.

The observations of the upper sample showed an attack of the surface of the steels with penetrations both intergranular and transgranular around 5 μm deep. The observations of the lower sample showed no apparent damages of the surface and no oxide layer was detected with the observation techniques used.

The last two corrosion tests were performed on pure iron in order to determine if the extremely different behaviour obtained on the different samples during a same test could be attributed to a local protection of the samples by a very thin chromium oxide layer. This layer could form on the lower sample (which is situated upstream) with the oxygen dissolved in Pb-Bi and as the oxygen content in Pb-Bi is extremely low, no oxygen would be available for the upper sample which could therefore be attacked by the liquid lead alloy.

For the fourth test performed on pure iron at a rotating speed of 870 rpm, only one sample (the upper sample) was available for the weight loss measurement. The weight loss measured corresponded approximately to what was obtained in close experimental conditions for martensitic steel T91. Observation of the samples showed an attack of the material surface and an electrochemical attack in an oxalic acid bath showed that some penetrations initiated at the grain boundaries and other were transgranular (Figure 4).

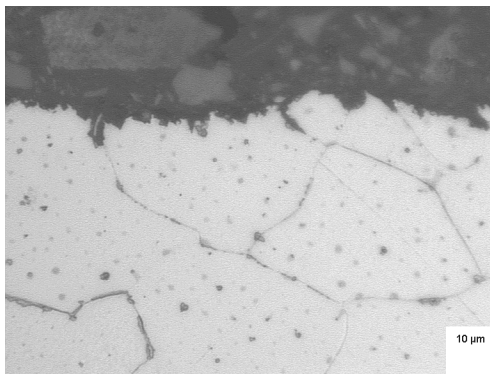


Figure 4. Microscopical observation of a cross section of iron after an attack in an oxalic acid bath exposed to Pb-Bi at 400 °C after 435 h of testing at a rotating speed of 870 rpm ($C_{O_2} = 1.6 \times 10^{-11}$ wt %).

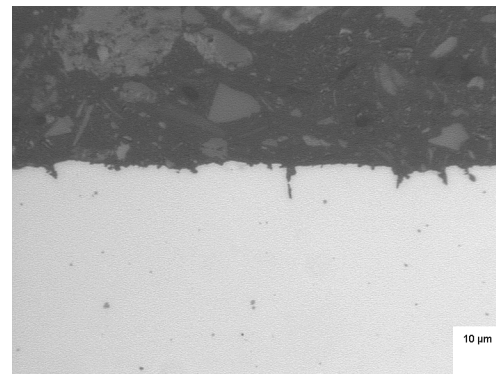


Figure 5. Microscopical observation of a cross section of iron after an attack in an oxalic acid bath exposed to Pb-Bi at 400 °C after 339 h of testing at a rotating speed of 2845 rpm (C_{O_2} : no measurement).

The last test was performed on pure iron at a higher rotating speed (2845 rpm). The results showed that the upper sample had undergone a very severe dissolution leading to a corrosion rate around $360 \mu\text{m} \cdot \text{yr}^{-1}$. No weight loss was measured for the lower sample. Observations of the samples showed for the upper sample the same behaviour as it was previously described with an attack of the material surface (Figure 5). The observations of the lower sample did not show any attack of the metal surface.

Discussion

All these experiments performed for low oxygen concentrations show a quite heterogeneous behaviour for the martensitic steel T91 samples as well as for the pure iron samples.

The first point is that for an equivalent oxygen concentration quite different results can be obtained for different experiments with in some cases an important dissolution of the samples and in other cases a lower corrosion rate probably due to the existence of a very thin oxide layer at the surface of the steel (native ?) which causes also wetting concerns. However, this layer could no be observed with the usual observation techniques and other examinations are planned.

The second point is the position effect which is observed for the samples of a same test. Different explanations can be considered:

- An oxygen effect: the upstream sample could use the oxygen present in Pb-Bi to form a protective chromium or spinel oxide layer (which is stable at the oxygen concentrations tested here) and due to the very low oxygen concentration in Pb-Bi, the downstream sample would not have enough oxygen available to form such a layer leading to high corrosion rates. However, this hypothesis could explain what is observed for T91 but not for pure iron.
- An hydrodynamic effect: a specific hydrodynamic configuration could lead for the downstream sample to very high turbulent conditions which could cause high corrosion rates. To eliminate this hypothesis a specific analysis of the flow around the rotating cylinder is performed at the CNRS/LEGI in Grenoble.
- A surface state effect: the corrosion rate could strongly depend on the initial surface state (no treatment is performed on the samples after machining) i.e. presence of an initial oxide layer, roughness,... In order to be sure of the surface state, tests are going to be performed on electropolished samples.

For the moment, none of these hypotheses can clearly explain the behaviour observed. Moreover, there could be several of these explanations which could together lead to the great heterogeneity of the corrosion rates.

Finally, if we consider the influence of the rotating cylinder speed on the corrosion rate, we observe that for T91 as well as for pure iron increasing the cylinder rotating speed leads to an increase of the corrosion rate. However, the analysis of the results must be performed with great care given the uncertainties of the results: wetting concerns, presence of a protective oxide layer,...

Theoretically, if we assume that the corrosion process of T91 is controlled by the diffusion of dissolved iron from the solid/liquid interface to the bulk, it is possible to estimate the corrosion rate of the cylinders by using the expression of the mass transfer coefficient [1]. Moreover, in that case the corrosion rate of pure iron samples should be very close to what is obtained for T91 as the controlling step is the same. In fact, the corrosion rate obtained for the fourth test on pure iron seems to be close to what was obtained on T91 in close conditions. However, the fifth test performed on pure iron leads to a very high corrosion rate which is much higher than what was obtained on T91.

As a matter of fact, if the controlling step of the corrosion process is assumed to be the transport of dissolved iron by convective diffusion, the corrosion rate can be expressed according to:

$$v_{\text{corrosion}} = K(c_s - c_0), \text{ where}$$

K: mass transfer coefficient ($\text{m}\cdot\text{s}^{-1}$),

c_s : solid-liquid interface iron concentration, which is considered to be equal to the saturation concentration as the interface reaction is assumed to be at the equilibrium ($\text{g}\cdot\text{m}^{-3}$),

c_0 : iron bulk concentration, ($\text{g}\cdot\text{m}^{-3}$).

The mass transfer coefficient is expressed with the Eisenberg equation [4]:

$$K_{\text{Eisenberg}} = 0.0487 \omega^{0.70} d_{\text{cylinder}}^{0.4} \nu^{-0.344} D^{0.644}, \text{ where}$$

ω : cylinder rotating speed ($\text{rad}\cdot\text{s}^{-1}$),

d_{cylinder} : cylinder external diameter (m),

ν : Pb-Bi kinematic viscosity ($\text{m}^2\cdot\text{s}^{-1}$),

D : iron diffusion coefficient in Pb-Bi ($\text{m}^2\cdot\text{s}^{-1}$).

The mass transfer coefficient can be calculated considering the following data:

- $T = 400\text{ }^\circ\text{C}$,
- $d_{\text{cylinder}} = 0.03\text{ m}$,
- $\nu = 1.488 \times 10^{-7}\text{ m}^2\cdot\text{s}^{-1}$ [5],
- $D_{\text{Fe} \rightarrow \text{Pb-Bi}} = 1.93 \times 10^{-10}\text{ m}^2\cdot\text{s}^{-1}$ (as no data is available yet, the diffusion coefficient is assumed to be equal to the one measured in pure lead [6]).

At $400\text{ }^\circ\text{C}$, the iron solubility limit is $c_s = 3.24\text{ g}\cdot\text{m}^{-3}$ and c_0 is assumed to be negligible due to the cold point at the bottom of the pot.

Figure 6 represents the variation of the experimental corrosion rate for the upper iron samples and also the upper T91 samples with the rotating speed at a power 0.7. The calculated corrosion rate is also represented.

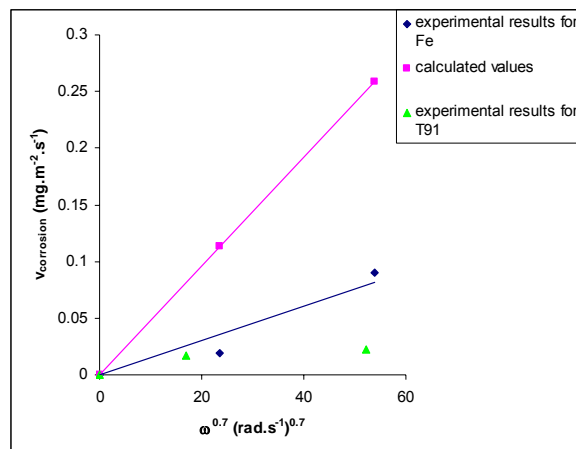


Figure 6. Comparison between the variation of the experimental corrosion rates measured for pure iron immersed in Pb-Bi at $400\text{ }^\circ\text{C}$ as a function of the rotating speed and the calculated ones.

On this figure, a linear variation can be represented for pure iron but more points would be necessary to confirm this result. For T91, a linear variation can also be represented, however, the corrosion rates measured appear to be lower (especially for the higher rotating speed) than what was obtained for pure iron. This could be explained by the existence of a thin chromium oxide layer on the T91 surface which reduces the corrosion rate. Moreover, we observe also that the experimental results appear to be much lower than the calculated values. In fact, this could be attributed first to an uncertainty on the value of the iron concentration in solution (c_0) but also on the value of the iron diffusion coefficient in Pb-Bi which is not known.

In fact, if we consider the experimental slope obtained for pure iron to determine the value of a diffusion coefficient, as this data is not known in Pb-Bi but only in pure lead, we obtain at 400 °C:

$$D_{\text{Fe} \rightarrow \text{Pb-Bi}} = 3.2 \times 10^{-11} \text{ m}^2 \cdot \text{s}^{-1}.$$

This value appears to be realistic if we compare it for example to the data available for chromium in Pb-17Li for which we obtain $D_{\text{Cr} \rightarrow \text{Pb-17Li}} = 6 \times 10^{-12} - 4 \times 10^{-11} \text{ m}^2 \cdot \text{s}^{-1}$ at 500 °C [7].

However, as it was already said before many uncertainties remain and concerning the determination of the iron diffusion coefficient, a specific study is performed at the moment at the laboratory by using electrochemical techniques in a molten salt medium.

Conclusion

Finally, all these tests show that for a low oxygen concentration, dissolution of the martensitic steel T91 and of iron is generally observed. The observations of the materials show an attack of the surface of the materials with intergranular as well as transgranular penetrations and locally the formation of larger cavities.

Moreover, increasing the rotating speed of the cylinder leads to an increase of the corrosion rate. This result could show that the dissolution process is controlled by the transport of dissolved iron from the solid/liquid interface to the bulk.

However, many uncertainties remain and it appears that controlling precisely the physico-chemistry of the Pb-Bi medium is quite complex.

As a matter of fact, uncertainties remain on the existence (prior to the test or which could form during the corrosion test) of a chromium oxide layer on the T91 surface which would lead to wetting concerns and to a decrease of the corrosion rate. This could explain the lower corrosion rate obtained on T91 compared to pure iron and also sometimes between two T91 samples. Moreover, the exact configuration of the hydrodynamic regime has to be determined to ensure that no major difference exists in the flow configuration around the samples. Finally, if we assume a corrosion process controlled by the diffusion of iron apart from the uncertainties concerning the corrosion process, other interrogations remain concerning the iron diffusion coefficient and the iron concentration in solution.

References

- [1] F. Balbaud-Célérier, F. Barbier, Journal of Nuclear Materials 289 (2001) 227-242.
- [2] F. Balbaud-Célérier, C. Delisle, F. Herbert, C. Blanc, RT SCCME 591 (Décembre 2001).
- [3] Ph. Deloffre, C. Delisle, F. Herbert, RT SCCME 610 (Décembre 2002).
- [4] M. Eisenberg, C. W. Tobias, C. R. Wilke, Journal of the Electrochemical Society 101 (1954) 306-319.
- [5] R. R. Miller, Liquid Metals Handbook, R. N. Lyon (Ed.), US government printing office, Washington, 1954, 40-43.
- [6] W. M. Robertson, Transactions of the Metallurgical Society of AIME 221 (1961) 271-275.
- [7] N. Simon, PhD thesis, Paris VI University, 1992.

STATIC Pb-Bi CORROSION TEST OF 316LN AND FERRITIC/MARTENSITIC STEELS *

* This work has been supported by the Korea Ministry of Science and Technology (MOST)

T. Y. Song, J. E. Cha, C. H. Cho, Korea Atomic Energy Research Institute, P.O. Box 105 Yuseong, Daejeon, 305-600 Korea

G. Mueller, A. Heinzl, Forschungszentrum Karlsruhe GmbH, Institut fuer Hochleistungsimpuls- und Mikrowellentechnik, Postfach 3640, 76021, Karlsruhe, Germany

J. Konys, Forschungszentrum Karlsruhe GmbH, Institut fuer Materialforschung III, Postfach 3640, 76021, Karlsruhe, Germany

Abstract

KAERI plans to build a static Pb-Bi corrosion test facility and perform experiments using it in 2003. KAERI will also start constructing a corrosion loop in 2003 and finish the construction in 2004. While we are building our own facilities, we performed static corrosion tests using FZK's facility COSTA. The test materials are 316LN and some ferritic/martensitic steels such as HT-9, HT-9M, HT-9MN, 9Cr-2WVTa and 9Cr-1Mo. The temperatures of the experiment are 350, 500 and 650°C. The experiment was performed under both reduced and oxygen-controlled atmospheres. Oxygen concentration was controlled by adjusting H₂ and H₂O vapor ratio.

Introduction

KAERI plans to build a static Pb-Bi corrosion test facility and perform experiments using it in 2003. KAERI will also start constructing a corrosion loop in 2003. Figure 1 is the simplified schematic diagram of KAERI's loop.

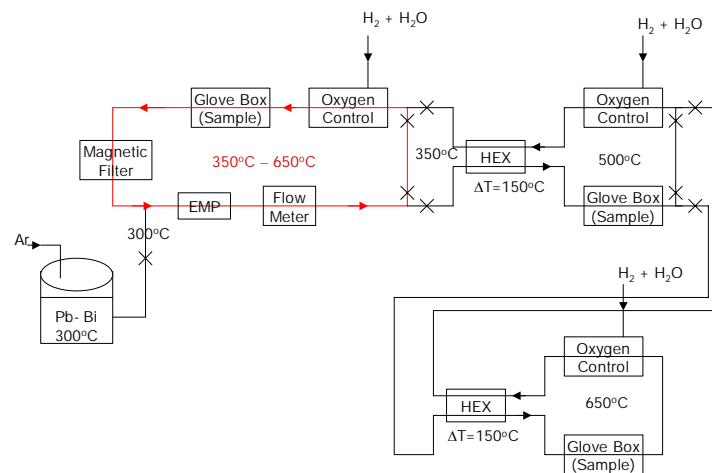


Figure 1. The schematic drawing of KAERI Pb-Bi loop

The main characteristic of KAERI loop is to investigate samples at 3 different temperatures at the same time. KAERI loop is designed to have 350, 500, 650°C temperature zones. The oxygen content is controlled by one of 3 control systems located at different temperature regions to study the controllability of oxygen content at each temperature zone. Oxygen control is performed by flowing Ar/H₂ gas mixed with H₂O vapor. The maximum available velocity of Pb-Bi will be 2 m/s.

The loop will be built step by step. Once the first isothermal loop is built, we will start running the loop and testing materials while building additional second and third

isothermal loops. The design of the first isothermal loop was finished in 2002 and the construction will be finished in 2004. Figure 2 is the design of the first isothermal loop.

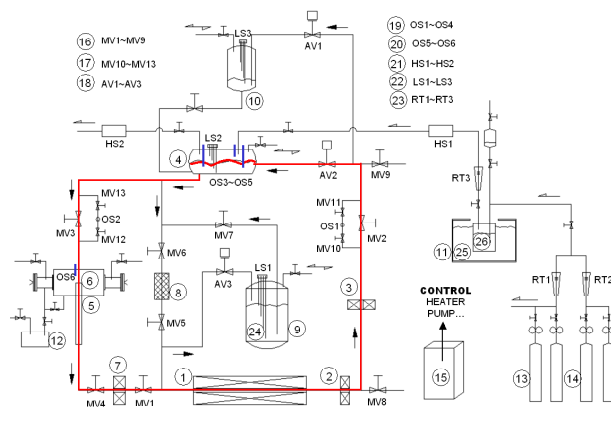


Figure 2. The design of the first isothermal loop

Until KAERI has its own corrosion test facilities, we will use the facilities of foreign institutes for the test of materials. As the first step, we have been using FZK's stagnant corrosion test facility, COSTA [1]. The test materials are 316LN and some ferritic/martensitic steels such as HT-9, HT-9M, HT-9MN, 9Cr-2WVTa and 9Cr-1Mo. Table 1 shows the components of the samples. The samples are 2mm thick and the heat treatment was done at 1050°C for 1 hour and 750°C for 2 hours except 9Cr-2WVTa. In case of 9Cr-2WVTa, the heat treatment was done at 1050°C for 15 minutes and 750°C for 1 hour. The temperatures of the experiment are 350, 500 and 650°C. The experiment was performed under both reduced and oxygen-controlled atmospheres. Oxygen concentration was controlled by adjusting H₂ and H₂O vapor ratio. In this paper, we show the results of 316LN, HT-9 and 9Cr-1Mo at the temperatures of 500 and 650 °C.

Table 1. Components of samples (atomic %)

	C	Si	Mn	Ni	Cr	Mo	V	Nb	W	P	S	N
9Cr-1Mo	0.099	0.32	0.42	0.10	9.03	0.96	0.22	0.094	-	<0.003	0.003	0.032
HT9M	0.145	0.1	0.45	0.46	9.79	1.23	0.2	0.18	-	<0.003	<0.003	0.02
HT9MN	0.15	0.072	0.49	0.50	10.0	1.28	0.205	0.204	-	0.002	0.004	>0.02
HT9	0.19	0.36	0.59	0.53	11.79	0.99	0.31	0.02	0.49	0.019	0.006	<0.01
316LN	0.022	0.53	0.87	10.6	17.69	2.61	-	-	-	0.02	0.001	>316SS
9Cr-2WVTa	0.11	0.21	0.44	<0.01	8.90	0.01	0.23	-	2.01	0.015	0.008	0.0215

Experiment Procedure

Figure 3 shows the layout of FZK's Pb-Bi corrosion test facility. When a reduced atmosphere is needed, Ar5%H₂ gas is forced to flow with the rate of 35 cm³/sec for 3 days. Then samples are put into the Pb-Bi for corrosion test.

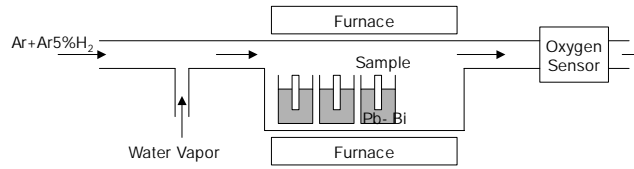


Figure 3. Schematic layout of the FZK stagnant corrosion test facility COSTA

Ar, Ar5%H₂ and H₂O vapor are mixed to produce a certain oxygen content. Equation 1 is used to calculate the corresponding oxygen partial pressure. Then Equation 2 is used to determine the pressure ratio of H₂ and H₂O. The H₂O pressure is set to be 15.94mbar. Ar gas is forced to flow with the rate of 100 cm³/sec and the corresponding rate of Ar5%H₂ gas is also forced to flow.

$$\frac{C}{C_s} = \left(\frac{P_{O_2}}{P_{O_{2,S}}} \right)^{\frac{1}{2}} \quad (1)$$

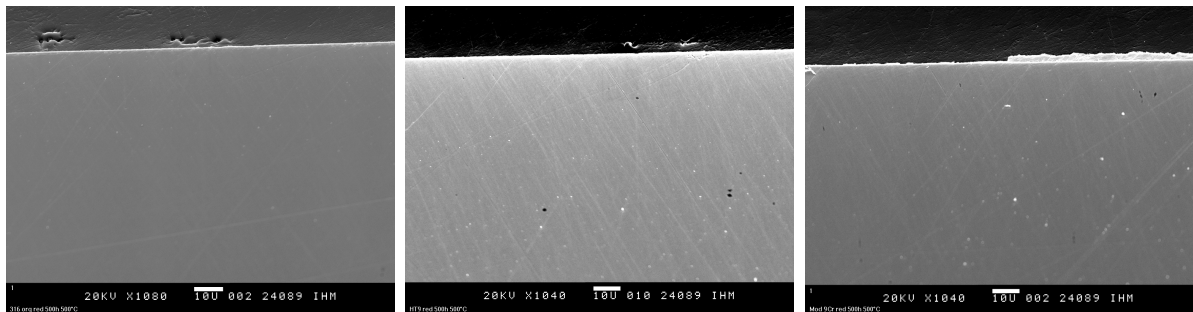
$$P_{O_2} = \frac{P_{H_2O}^2}{P_{H_2}^2} \exp\left(\frac{2\Delta G_{H_2O}}{RT}\right) \quad (2)$$

, where C_S is the solubility of oxygen in Pb-Bi [2].

Results and Discussion

1) Temperature 500°C, oxygen content < 10⁻⁸ wt%

Figure 4 shows SEM results of 316LN, HT-9 and 9Cr-1Mo exposed to Pb-Bi at 500°C with reduced oxygen for 500 h. The oxygen meter shows that the oxygen content in the flowing gas is less than 10⁻²⁷ bar, which means the oxygen content in the Pb-Bi is less than 10⁻⁸ wt%. No dissolution attack was shown and oxygen layer was not detected. The experiment is still being performed and will last until the total exposure time reaches 2000 h.



(a) 316LN

(b) HT-9

(c) 9Cr-

1Mo

Figure 4. 316LN, HT-9 and 9Cr-1Mo at 500 °C with oxygen content <10⁻⁸ wt% (500h)

2) Temperature 500°C, oxygen content 10⁻⁶ wt%

Figure 5 is the result of HT-9 exposed to Pb-Bi at 500°C with the oxygen of 10⁻⁶ wt% for 500 h. The oxide layer consists of magnetite scale and spinel zone as expected. Atomic percent of Fe varies from 40% to 60% and oxygen from 30% to 40% in the magnetite scale. In the spinel zone, Cr content is measured to be 13-16 atomic percent in addition to Fe and oxygen.

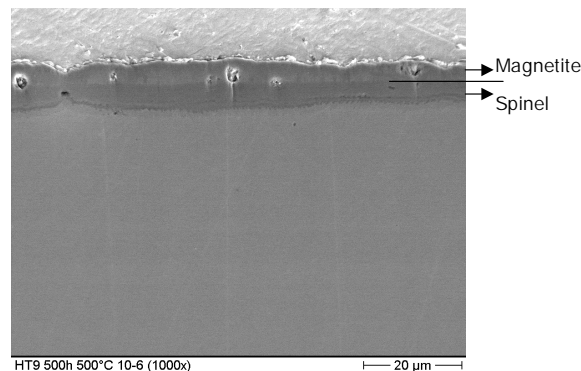


Figure 5. HT-9 at 500 °C with oxygen content of 10⁻⁶ wt% (500h)

3) Temperature 650 °C, oxygen content < 10⁻⁸ wt%

Figure 6 is the result of 316LN exposed to Pb-Bi at 650°C with reduced oxygen(<10⁻⁸ wt%) for 500 h. Dissolution attack is clear for the 316LN sample and the corrosion pattern is homogeneous through the sample surface. The maximum depth of dissolution is about 40μm. EDX analysis was done for a part of the sample. Table 2 shows the atomic % of main elements of the sample, Pb, Bi and O for each point of investigation.

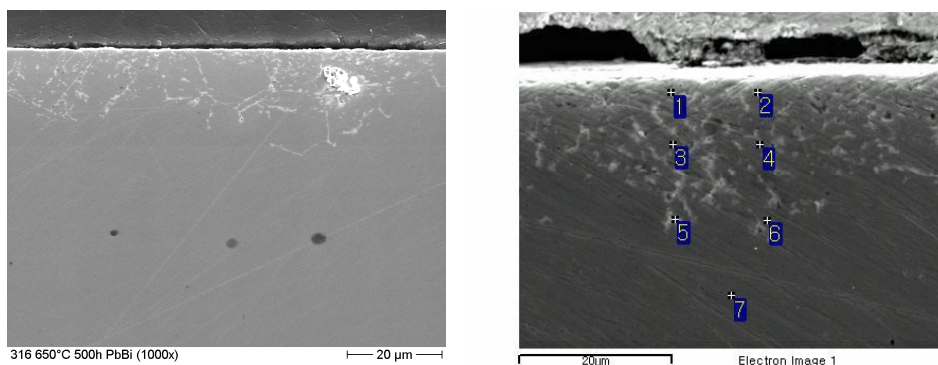


Figure 6. SEM results of 316LN sample at 650 °C with reduced oxygen(500h)

Pont 7 in Figure 6 is located inside the sample, so it is not affected by Pb-Bi corrosion. Point 1 and 2 are located just below the surface and there is no Ni content in those regions. A small amount of oxygen is detected at point 1, the source of which is not quite clear yet. It should not happen if the oxygen reduction is perfect.

Table 2. EDX results of 316LN at points described in Figure 6 (at. %)

	Fe	Cr	Ni	Pb	Bi	O
1	52	19			21	8
2	73	27				
3	70	20	9		1	
4	69	18	11		2	
5	73	19	8			
6	78	15	2	2	3	
7	69	20	11			
Original	70	19	11			

Figure 7 is the result of HT-9 and 9Cr-1Mo at 650 °C with reduced oxygen. The exposure time is 1000h. The corrosion attack can be seen, but the pattern is different from 316LN. In these cases, the corrosion pattern is rather inhomogeneous. EDX analysis was performed on the surface where there seems no corrosion attack, but the result shows that small amount of Cr is dissolved near the surface.

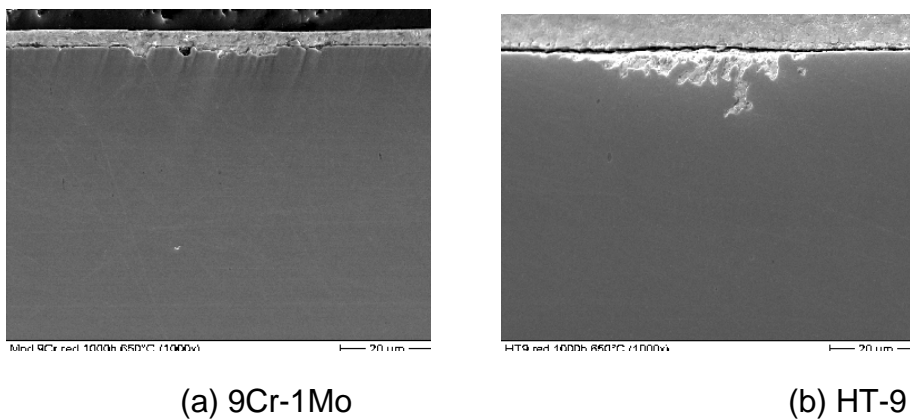


Figure 7. HT-9 and 9Cr-1Mo at 650 °C with reduced oxygen(1000h)

4) Temperature 650°C, oxygen content 10⁻⁶ wt%

Since the corrosion of steels is severe at 650°C, the prevention of corrosion is needed. Therefore we investigated the corrosion at 650°C with controlled oxygen. Figure 8 is the SEM pictures of 316LN exposed to 650°C Pb-Bi for 500 h with 10⁻⁶ wt% of oxygen.

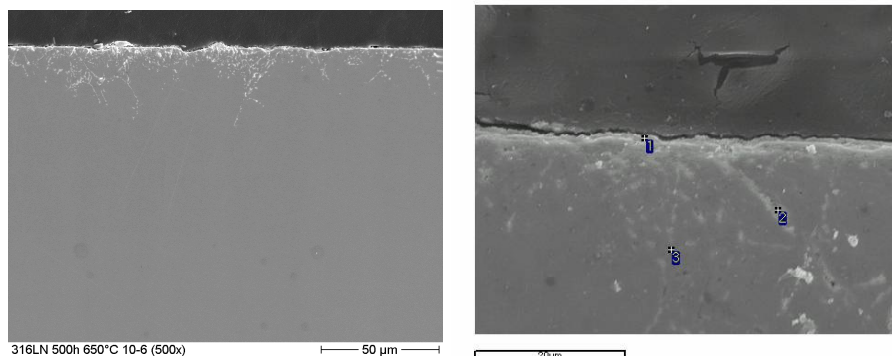


Figure 8. SEM results of 316LN at 650°C with 10^{-6} wt% of oxygen(500h)

In case of 316LN, a stable oxide layer was not formed with 10^{-6} wt% of oxygen. The corrosion pattern is similar to the case of reduced atmosphere. The difference between reduced atmosphere case and 10^{-6} wt% case is that a high oxygen atomic % is detected at some regions of the sample. Table 3 shows the atomic % of the main elements at points described by numbers in Figure 8. We can see that an oxide layer is formed at point 1, but the layer is not firm enough to prevent the corrosion. There is Pb-Bi penetration at point 2.

Table 3. EDX results of 316LN at points described in Figure 8 (at. %)

	Fe	Cr	Ni	Pb	Bi	O
1	30	8		9		53
2	59	11		2	10	18
3	87	13				

Figure 9 is the SEM of HT-9 with the oxygen content of 10^{-6} wt%, which does not show any sign of firm oxide layer. Figure 9(a) is the pattern which can be seen most frequently. But there are some regions attacked deeply by Pb-Bi, which are shown in Figure 9(b). The largest depth is about 120μm and most of Cr is depleted in that region.

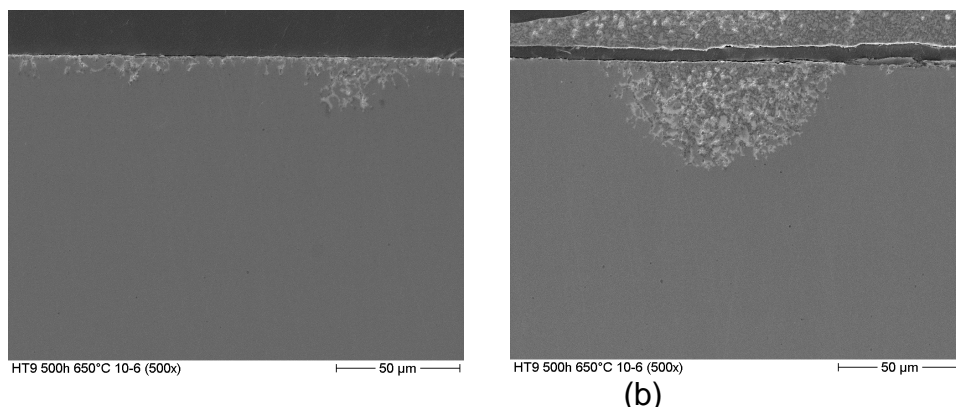


Figure 9. HT-9 at 650°C with 10^{-6} wt% of oxygen(500h)

Summary

KAERI plans to build a Pb-Bi loop for corrosion study. The design of the 1st stage of Pb-Bi loop was finished. The construction will start in 2003. At the same time, a stagnant Pb-Bi corrosion test facility will be built. Until KAERI has its own corrosion

test facilities, we will use test facilities operated by foreign institutes. As the first step, we performed experiments using FZK's stagnant corrosion test facility COSTA. Three different temperatures of 350, 500 and 650°C are chosen. The experiment was performed under both reduced and oxygen-controlled atmospheres. Oxygen concentration was controlled by adjusting H₂ and H₂O vapor ratio. In this paper, we showed the results of 316LN, HT-9 and 9Cr-1Mo at temperatures of 500 and 650°C. When the test was performed with a reduced atmosphere, no corrosion was shown for 500h, 500°C samples. But dissolution attack was clear for 650°C samples although the corrosion pattern of 316LN is different from HT-9 and 9Cr-1Mo. The oxygen content was changed to 10⁻⁶ wt% for 650°C samples, but no firm oxide layer was formed.

References

- [1] G. Mueller et al., J. of Nuclear Materials, 278(2000) 85-95
- [2] Yu. I. Orlov et al., "The Problems of Technology of the Heavy Liquid Metal Coolants (Lead-Bismuth, Lead)", Heavy Liquid Metal Coolant Conference, 1998

CORROSION OF A WELDED T91 SPECIMEN IN Pb-Bi RESULTS OF A CORROSION TEST IN THE CICLAD DEVICE

A. Terlain, F. Balbaud-Célérier, C. Delisle

Service de la Corrosion et du Comportement des Matériaux dans leur Environnement
CEA/Saclay – 91191 Gif sur Yvette Cedex - France

Abstract

A corrosion test was performed in the CICLAD device during 446 hours at 400 °C on welded martensitic steel T91 for a low oxygen concentration ($c_{O_2} = 1.5 \times 10^{-11}$ wt %) and for a rotating speed of the cylinder of 2970 rpm. This speed corresponds to a velocity in pipe of 2.3 m.s^{-1} for a hydraulic diameter of 0.011 m (which is the hydraulic diameter in the CICLAD device). In the same experimental conditions, dissolution of non welded martensitic steel T91 was previously observed with a maximum corrosion rate of $86 \text{ }\mu\text{m.yr}^{-1}$. For the welded specimen, dissolution is observed leading to an irregular interface with intergranular penetrations as well as transgranular penetrations. The same results were obtained on non welded specimens. No specific attack of the welded zone was observed compared to the rest of the sample. The corrosion rate of the welded specimen was $96 \text{ }\mu\text{m.yr}^{-1}$ which is quite close to what was previously obtained for non welded specimens. Therefore, no specific damage of the material is observed on the welded zone.

Introduction

A specific test was performed in the CICLAD device to evaluate the sensitivity to corrosion by Pb-Bi in circulation of a welded martensitic steel T91 specimen. This specific sample was supplied by PSI.

Experimental conditions

The CICLAD device has already been described in previous CEA reports and in a previous presentation in this meeting [1]. It consists mainly of a rotating cylinder which allows to work in controlled hydrodynamic conditions and of a liquid metal circuit which allows to purify the liquid metal by using a cold trap.

Two cylindrical T91 samples of diameter 30 mm and length 10 mm were tested in the CICLAD device. The disposition of the samples is shown on Figure 1 (the T91 plate is used to determine the weight loss during the prewetting step). On the external surface of the upper sample, a piece of welded T91 was inserted as shown on Figure 2.



Figure 1. Disposition of the samples.

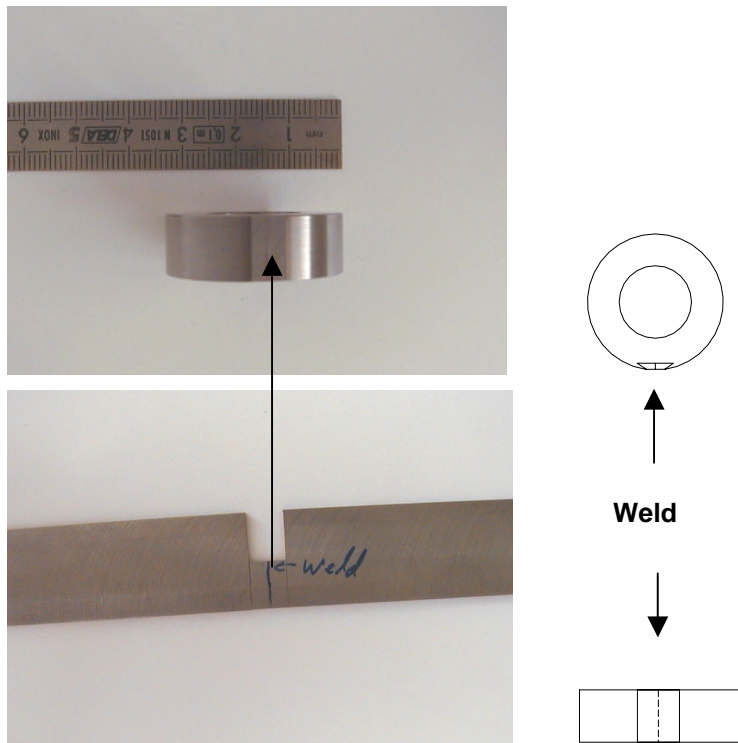


Figure 2. Insertion of the welded zone on the cylindrical T91 sample.

This test was performed at a low oxygen concentration (1.5×10^{-11} wt %). This concentration was maintained by imposing a constant pressure of 1 bar of an Ar-4 % H_2 mixture in the testing pot. The oxygen concentration in the testing pot was continuously measured with an oxygen sensor (ref. In/ In_2O_3) designed and built by DEN/DER/STR in CEA/Cadarache. Zinc was also added to Pb-Bi (≈ 70 wppm) in order to ensure a constant low oxygen concentration and also to improve the wetting. In previous static tests, it was shown that the addition of zinc in the liquid melt had no influence on the corrosion results [2]. A prewetting step was also performed ($T = 480$ °C, $t = 16$ h) to ensure a satisfying wetting of the steels surface.

As it was said in the previous presentation [1], the cold trap was not used due to a plugging of the electromagnetic pump. Therefore, in order to avoid the accumulation of corrosion products in the pot, a cold point was fixed at the bottom of the pot acting as a clod trap. Regular analyses of Pb-Bi samples showed no increase of the corrosion products (Fe, Cr, Ni) content in the pot. However, the iron solubility limit in Pb-Bi at 400 °C being around 0.3 wppm, and as the analytical techniques used do not allow a determination below 1 wppm, there is no certainty that the iron concentration had not reached the solubility limit. However, as for chromium (which solubility limit is close to 4 wppm at 400 °C), no increase is observed, we assume that the dissolved species concentration remains low.

After the corrosion test, the Pb-Bi alloy adhering to the steel surfaces was removed by an immersion in a 180 °C hot glycerine bath. Samples were cleaned in acetone and alcohol and dried for visual examination and weight measurement. Finally, pieces were cut and polished for cross section or longitudinal section examination by optical microscopy and scanning electron microscopy.

For this test, the conditions were:

$T = 400\text{ }^{\circ}\text{C}$

$t = 445\text{ h}$

$\omega = 2972\text{ rpm}$

$C_{\text{O}_2} = 1.5 \times 10^{-11}\text{ wt \%}$

Results and discussion

The results obtained are :

- For the T91 sample with the welded zone: $v_{\text{corrosion}} = 96\text{ }\mu\text{m.yr}^{-1}$ (upper sample)
- For the T91 sample without the welded zone: $v_{\text{corrosion}} = 31\text{ }\mu\text{m.yr}^{-1}$ (lower sample)

The observations show for both samples an attack of the steel surface with penetrations about $5\text{ }\mu\text{m}$ deep (Figure 3). The results obtained are quite similar for both samples.

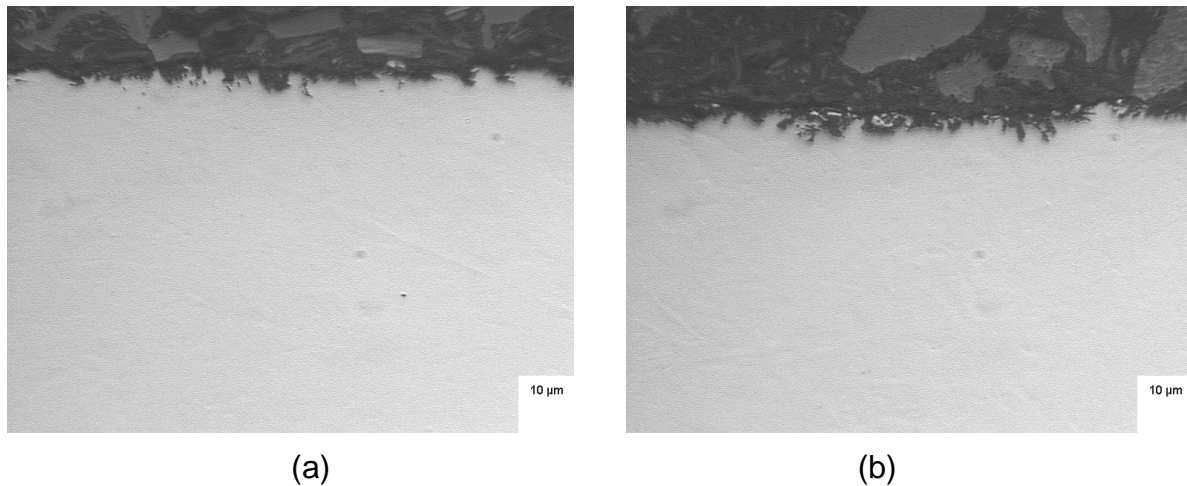


Figure 3. Microscopic observation of the longitudinal section of the upper sample (out of the welded zone) (a) and of the lower sample (b) exposed to Pb-Bi at $400\text{ }^{\circ}\text{C}$ after 446 h of testing for a rotating speed of 2972 rpm ($C_{\text{O}_2} = 1.5 \times 10^{-11}\text{ wt \%}$).

The specific observation of the welded zone after an electrochemical attack with an oxalic acid bath showed no specific attack in this zone (Figure 4).

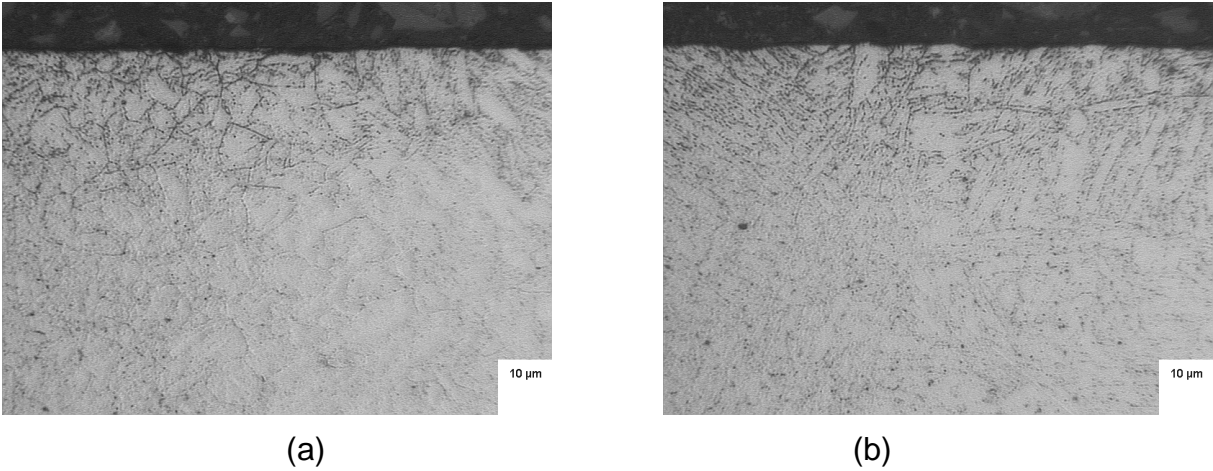


Figure 4. Microscopic observation of the cross section of the upper T91 sample in the welded zone (a) and out of the welded zone (b) exposed to Pb-Bi at 400 °C after 446 h of testing for a rotating speed of 2972 rpm ($C_{O_2} = 1.5 \times 10^{-11}$ wt %).

Dimension measurements were also performed in and out of the welded zone. No difference was observed.

Finally a chromium concentration profile was performed by microprobe analysis before and after the test in the welded zone and out of the welded zone. No modification of this profile was observed (Figure 5).

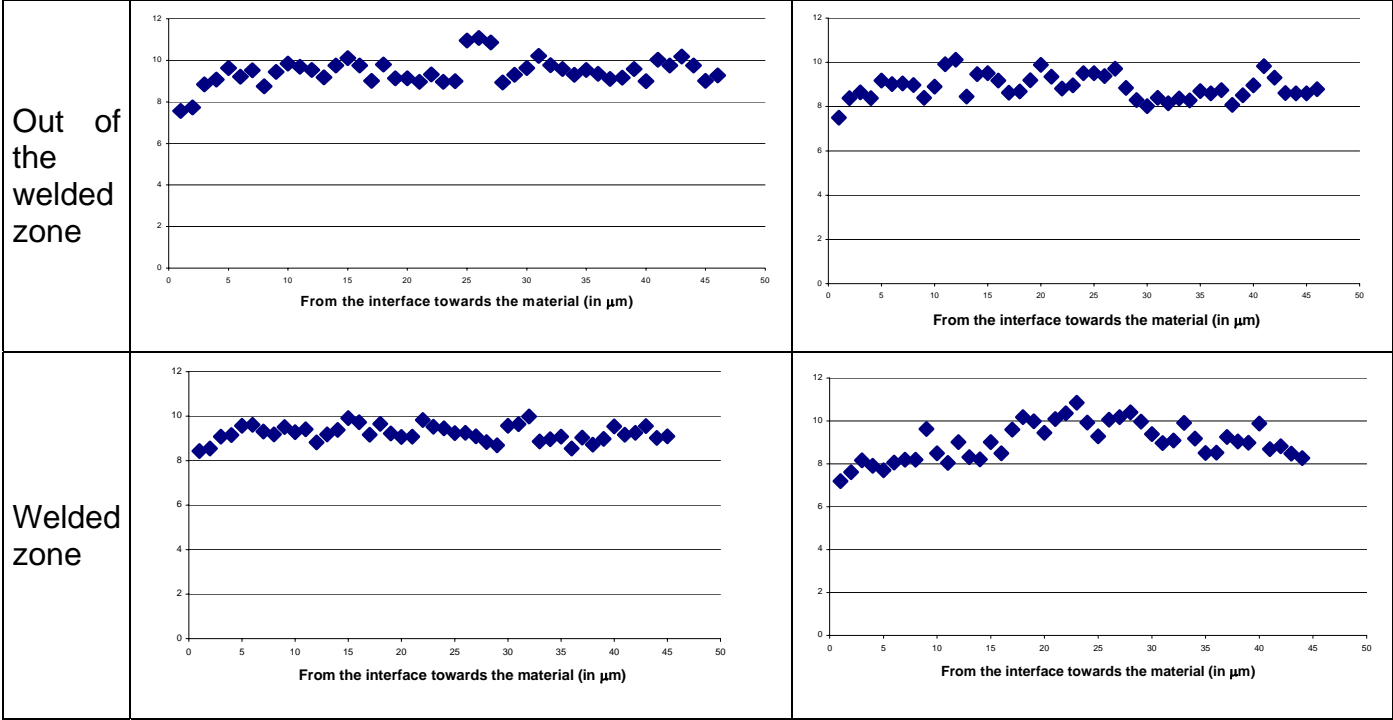


Figure 5. Chromium concentration profile before and after immersion in Pb-Bi in and out of the welded zone.

All the observations performed on the welded zone of the T91 specimen showed no specific behaviour or damage of this zone. The only difference is the higher corrosion rate obtained for the upper sample (with the weld) compared to the lower sample. However this behaviour is observed systematically in the CICLAD device and was already discussed in the previous CEA presentation [1].

Conclusion

Finally, the specific test performed in the CICLAD device at 400 °C for a low oxygen concentration (1.5×10^{-11} wt %) and a rotating speed of 2972 rpm during 446 hours showed no specific damage of the weld inserted in the martensitic steel T91 sample. The observations performed showed the same behaviour as "classical" T91 samples that is a dissolution of the specimen with penetrations at the surface of the steel. The value of the corrosion rate of the upper sample of $96 \mu\text{m}\cdot\text{yr}^{-1}$ (which contains the weld) can be compared with the value previously obtained for a T91 sample with no weld placed in the upper part of the rotating cylinder system which was $86 \mu\text{m}\cdot\text{yr}^{-1}$.

References

- [1] F. Balbaud-Célérier, C. Delisle, A. Terlain, Influence of hydrodynamics on the corrosion of martensitic steel T91 in liquid Pb-Bi (this meeting).
- [2] Ph. Deloffre, C. Delisle, F. Herbert, RT SCCME 610 (Décembre 2002).

INSPECTION OF THE FIRST LISOR TEST SECTION

H. Glasbrenner, R. Brütsch, F. Gröschel
Paul Scherrer Institut, 5232 Villigen PSI, Switzerland

Introduction

LiSoR loop, an experimental liquid metal loop, was developed to investigate the influence of Pb-Bi on possible structural materials under static load and irradiation. The first test section of LiSoR was manufactured of the austenitic steel 316L and the steel MANET II (MARTensitic for NET). Altogether the operation time of the loop during commissioning accounted about 2000 h for this test section at LBE temperatures between 180 and 350 °C. Some short testing was as well performed in Ar atmosphere at temperatures up to 250 °C. A short irradiation experiment of 1 h was performed after the successful commissioning phase.

The results revealed by EDX and SEM on the inner surfaces of the MANET II and 316L tubes are shown. Additionally the T91 tensile specimens, fractured with and without beam, were analytically investigated by optical microscopy, SEM and EDX and the results observed are presented.

Experimental

Materials

The test section was fabricated by the company ATEA, France, whereby special jobs were given to subcontractors. T91 steel was not available during the manufacturing phase of the first test section hence the unit that should be made of T91 was fabricated out of MANET II steel (material number 1.4914).

After irradiation the test section was disassembled in the hot cells of PSI. The activity of the MANET II tube beside the irradiated zone was 0.8 Sv/h in a distance of 10 cm and 2 Sv/h in contact, the activity of the MANET II tube in the irradiated zone was 106 Sv/h in a distance of 10 cm and 4 mSv/h in contact.

The tensile specimens were prepared of T91 steel with the following dimensions: thickness 1 mm, gauge length 20 mm, width 5 and 35 mm distance between the shoulders by means of EDS wire cutting. The surface of the specimens was mechanically polished in the reduced area. The degreased specimens using ethanol were assembled into the LiSoR loop. After the experiment the activity of the tip of the fractured specimen was 120 Sv/h in a distance of 10 cm and 4 mSv/h in contact.

Loop conditions

The LiSoR loop was operated in the commissioning phase up to about 2000 h, mostly at LBE temperature of around 200 °C in the test section. For investigating the influence of LBE temperatures to different loop parameters LiSoR was operated from time to time between 180 to 350 °C. Additionally tensile tests were performed at different temperatures. Hence the LiSoR loop was filled and drained more than 20 times altogether.

Tensile tests

Two mechanical testing were performed on T91 tensile specimens with and without beam in order to see whether the irradiation has an influence to the mechanical properties of the steel. The flow velocity in the test section was 0.9 m/s by a turbulent

flow regime. The tensile tests were planned at a constant cross head speed of 10^{-4} mm/s using a machine with a pneumatic jack that is regulated by an electromagnetic pressure valve. The specimens were exposed about 24 h to flowing LBE at 300 °C before the fracture tests were started. In addition the tensile specimen to be fractured in the beam was irradiated for about one hour before the tensile test was started. Due to the breakdown of the data transfer from the load and extension amplifiers during the tensile test under irradiation, the test specimen was fractured uncontrolled and no data were recorded. The experiment was therefore stopped immediately.

Results and Discussion

Steel MANET II beside the irradiated zone

The visual inspection revealed on the inner surface of the MANET II tube an oxide layer which varies in thickness between app. 3 and 7 μ m. Additionally the examination of the MANET II tube showed an uneven surface structure and many micro cracks up to a length of 15 μ m were detected. In Figure 1 a the areas are marked by numbers to show where EDX point analyses were carried out. The corresponding EDX results are summarised in Table 1. The content of Pb is relatively high in the oxide layer. The element Bi is as well present in this layer but compared to the ratio in the LBE it is downgraded (ratio in LBE: Pb/Bi = 0.8, in the oxide layer: Pb/Bi = 4.4). Probably Pb diffuses preferred into the oxide layer compared to Bi.

For better understanding the results, the content of the steel elements in the oxide layer was calculated without consideration of Bi and Pb (see Figure 1 b). In the oxide layer the steel elements Cr, Si, Mn and Ni are enriched compared to the composition in the steel whereas Fe is downgraded in this layer. It is well-known that the oxide layer formed on steels has a two-layered structure. The outer layer mainly consists of the compound Fe_3O_4 , the oxide layer staying in contact with the basic material is formed by the spinel type $Fe(Fe_{1-x}Cr_x)_2O_4$. Due to the quite thin oxide layer it is probably that the analysis was not carried out on the most outer area of the oxide layer consisting of the magnetite Fe_3O_4 . This measurement has to be made up in the near future. Just beneath the oxide layer the composition of the steel is reached. The element Bi is not found in the steel. The content of Pb detected in the steel matrix just below the oxide layer is very little. Hence it is not clear if it is a home made effect due to preparation or if Pb diffuses real into the steel or only into the oxide layer.

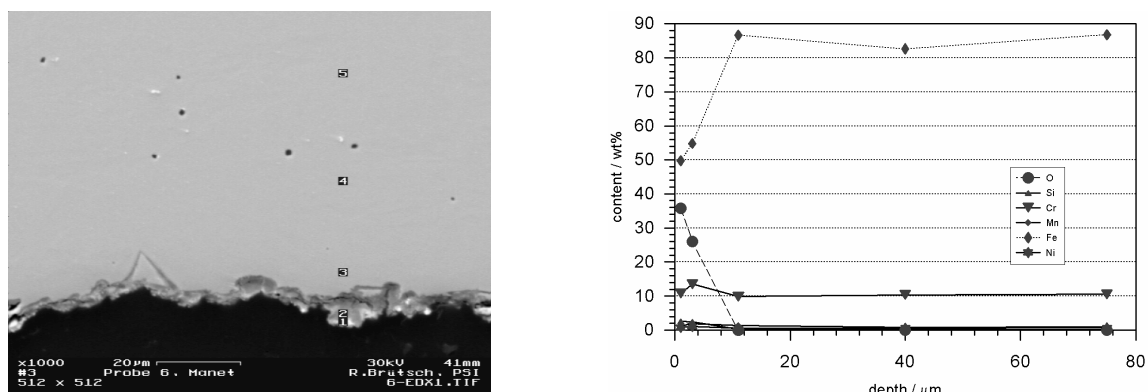


Figure 1: SEM image (a: left) showing the areas where EDX point analyses were performed. The corresponding depth profile is plotted on the right side (b).

Table 1: Results of the EDX point analysis.

Wt%	Point 1 (1 m)	Point 2 (3 m)	Point 3 (11 m)	Point 4 (40 m)	Point 5 (75 m)
O	16.29	16.62	0	0	0
Si	1.22	1.61	0.33	0.3	0.22
Cr	5.05	8.66	9.89	10.34	10.57
Mn	0.6	1.24	1.38	0.8	0.93
Fe	23.23	35.15	86.67	82.66	86.76
Pb	41.99	29.64	0.54	0	0
Ni	0.38	0.75	0.59	0.61	0.67
Bi	9.57	4.39	0	0	0
Zr	0	0	0	4.23	0.28

Steel MANET II directly in the irradiated zone

The cross section of the inner surface of the MANET tube which was located directly in the beam is shown in Figure 2. The optical inspection obtained an oxide layer having a thickness between 3 to 7 μm . The surface is not uniform and many micro cracks parallel and perpendicular to the surface are visible. The same result was obtained for the MANET II tube that was not in the irradiated zone. Hence it can be concluded that the short irradiation time of about 1 h has no visible influence to the surface structure. Probably the roughness of the surface and the cracks are produced during fabrication.

Due to the still quite high activity (4 mSv/h in contact) it was not possible to examine the specimen by means of EDX. But we do not expect a different result as for the MANET II specimen beside the irradiated zone.

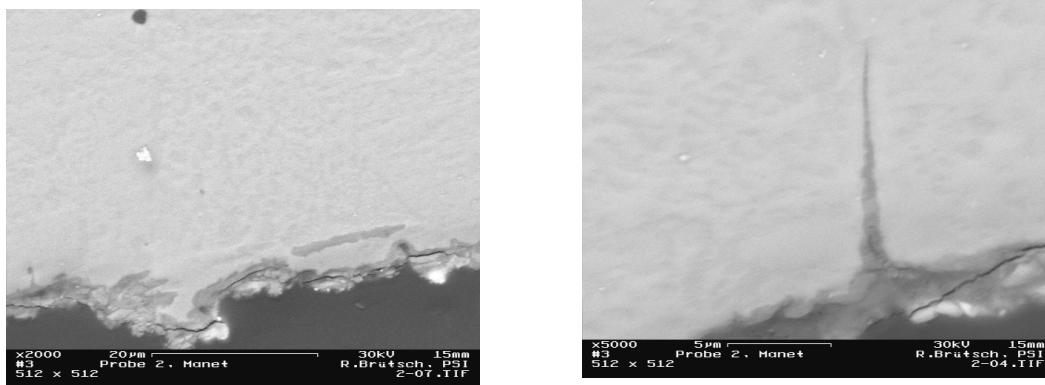


Figure 2: Cross section of the MANET II tube which was located directly in the beam.

3.3 Non-irradiated T91 tensile specimens

Adherent LBE was detected on the fractured face of the T91 specimen so that the SEM inspection of the covered surface did not give any result. After removing the adherent LBE from the fractured face SEM micrographs show spherical dimples characteristic for a ductile fracture (Figure 3).

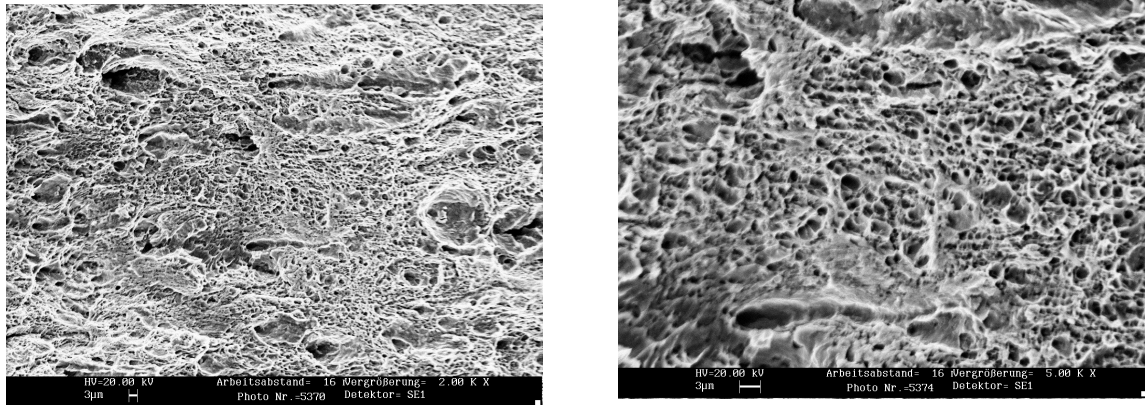


Figure 3: Ductile fracture of T91 tested in LBE at 300 °C.

For cross section examination one omitted to remove the adherent LBE from the specimen. Even so only a little amount of solidified LBE is observed on the fractured surface and no penetration of Pb or Bi into the base material is visible by means of metallurgical examination. The fracture obtained after tensile testing is quite rough and some micro cracks are visible. Optical inspection of the etched cross section reveals a martensitic structure for the steel after testing.

The examined cross section of the tensile specimen investigated by SEM shows a rough surface but neither Pb nor Bi penetration can be observed into the micro cracks of the base material. The element Bi is enriched in the tiny amount of adherent LBE detected on the surface by means of EDX.

Irradiated T91 tensile specimens

The activity of the embedded specimen was 4 mSv/h measured in contact just before the examination was started. Hence EDX measurements could not be carried out due to the high activity. The SEM inspection of the complete specimen shows a necking which is the normal fracture behaviour of ductile materials. Solidified LBE is observed on some areas of the fractured surface of the specimen but no penetration of Pb and / or Bi into the structural material is visible.

The fractured face of the correspondent of the embedded tensile specimen was examined by means of SEM to analyse the fracture mode. Therefore the adherent LBE had to be removed using the solution made of CH₃COOH, H₂O₂ and C₂H₅OH in a ratio of 1:1:1. The procedure was repeated 3 times over 4 days. Before cleaning the activity of the specimen was 60 Sv/h measured in a distance of 10 cm and 2.5 mSv/h directly in contact. The activity revealed after removing the LBE is 55 Sv/h measured in a distance of 10 cm and 2.2 mSv/h directly in contact. The decrease of activity shows that LBE was adherent to the specimen. The fractured face analysed by SEM showed a ductile structure with the typical large and smooth facets (Figure 4). Although the cleaning procedure was carried out accurately and over a few days, LBE droplets can still be found on the fractured face. This was not the case for the tensile specimen that was tested without beam under the same conditions. The temperature of the tensile specimen in the beam was higher than in the non-irradiated specimen. The wetting behaviour of steel with LBE is dependent on the temperature; hence it is clear that irradiated tensile specimen is better wetted than the non-irradiated one.

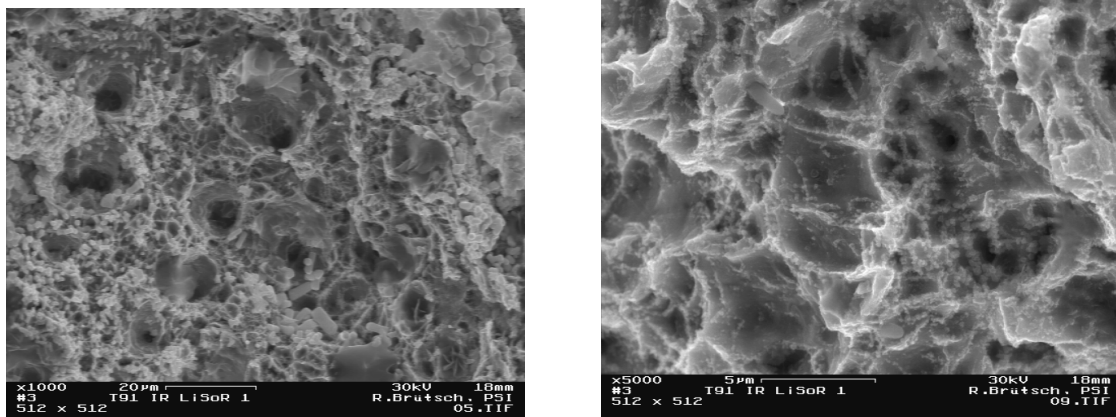


Figure 4: Fractured face of T19 ruptured in LBE under irradiation.

Conclusion

In general it can be said that the operation of the LiSoR loop with test section 1 (made of MANET II steel), the assembling and disassembling of this test section, the transport into the PSI hot cells, the dismantling and the analysis of different specimens could be performed without any problems.

A corrosion attack on the steels MANET II by LBE cannot be observed after about 2000 h of operation time at LBE temperatures between 180 and 350 °C. Thin non-uniform oxide layers and cracks perpendicular and parallel to the surface are observed on the inner surface of the MANET II test section tube which are probably formed during the manufacturing procedure and not by interaction of LBE and / or irradiation. In the oxide layer an enrichment of Pb opposite to Bi was analysed whereas the amount of Bi in the Pb-Bi melt near the steel surface is higher than in the LBE.

The tensile tests were performed with and without beam on T91 specimens. After testing both specimens showed a ductile fractured face and no influence of the beam

to the steel was visible.

Acknowledgement

The assistance of Mr. T. Rebac and Mr. H. Zimmermann (FZK) for metallurgical examination is gratefully acknowledged. The authors especially wish to express their thanks to Mr. V. Boutellier for his support by cutting out and preparing the specimens. The work has been performed in the framework of the MEGAPIE project and is partly supported by the BBW within the 5th EU frame work program.

Summary for Solid-Liquid Interface of Session 5

J. Konys
Forschungszentrum Karlsruhe

Within the session of Solid-Liquid Interface, seven presentations were given, dealing with the most important issues for a safe and reliable operation of the MEGAPIE target module:

- **Corrosion** behavior of bare, coated and welded steels in flowing LBE
- Investigations on the corrosion behavior of steels at different **oxygen contents** in LBE
- Investigations on the influence of **hydrodynamic** conditions on corrosion of T91 steel by LBE
- Comparison of experimental corrosion results with theoretical **modeling**
- Investigations on fatigue of T91 steel in LBE at low temperature
- Resistance of T91 steel to liquid metal corrosion (**LMC**) and liquid metal embrittlement (**LME**) by LBE
- First results of the **LiSoR** test campaign

The major outcome of the presentations and the discussion is as follows:

- The results at JAERI and ENEA with austenitic and martensitic steels in oxygen saturated and low-oxygen conditions at temperatures ranging from 400 to 550°C confirmed that “pure” LMC is not a serious problem for e.g. AISI 316L or T91 steel. The corrosion proceeds by elemental dissolution and/or trans- resp. intergranular penetration. For low-oxygen conditions, a corrosion rate was found to around 25 µm/year from the LECOR results. If a perfect filtering of dissolved corrosion products is applied, loops even at high-oxygen conditions can be operated safely. Furthermore, the CEA results gave no indication of preferred corrosion of T91 welds, compared to unaffected material.
- The results from the CICLAD low-oxygen experiments at CEA revealed a significant influence of the existence of surface oxides and the position of the samples along the LBE flow direction on the corrosion rate. Under nominal similar conditions, a reduction by a factor of about 10 was achieved if no wetting occurred. Many reasons for this pronounced effect were discussed, but no clear explanation could be given at the moment. Further tests with samples with well-defined surface states have to prove the presented hypotheses. The comparison of experimental results with corrosion modeling under the assumption, that the transport of dissolved iron by convective diffusion has shown, that much too high corrosion rates were predicted. The reason for this discrepancy was maybe due to the use of incorrect diffusion data for iron in LBE. From literature, only iron in pure lead is available ($\approx 10^{-10} \text{ m}^2\text{s}^{-1}$), whereas from the slope of pure iron in LBE a value of about $3 \cdot 10^{-11} \text{ m}^2\text{s}^{-1}$ could be calculated. This is a strong indication that more materials data are necessary for a correct modeling of LBE corrosion processes.
- “High-cycle” fatigue seems not to be a problem for T91 steel. A sensitivity to this damage was only seen when notches were evident

- and special hardening heat treatments were applied. Without notches and standard heat treatment, no sensitivity between 260 and 400°C was found at the Univ. of Lille.
- If T91 steel is in its standard metallurgical state, the probability for LME at 350°C is quite low, as shown by the CNRS experiments. But all measures, which improve the contact of T91 by LBE, are also increasing the probability for liquid metal embrittlement.
- The inspection of the first LiSoR test section has not shown any negative influence due to the short (1 h) “beam-on” conditions. All T91 specimens failed by ductile fractures. The observed cracks on the inner wall of the test section were attributed to the manufacturing process (EDM) and not to the LBE/mechanical load/proton beam condition.

Future recommendations

- Continuation of the corrosion testing in flowing LBE under MEGAPIE-relevant conditions. The soon starting of CORRIDA of FZK can contribute to the materials evaluation for the MEGAPIE target module.
- To bring the corrosion modeling in LBE on a more solid basis, joint activities between CEA, FZK and DoE/Los Alamos should be performed under, but not only, MEGAPIE-relevant conditions. It is also obvious, that the focus has to be made on the establishing of missing materials data, e.g. diffusion coefficient of Fe in LBE, too.
- Due to the operating conditions of the MEGAPIE target, low- instead of medium- or high-cycle fatigue tests are absolute necessary. A relevant frequency is around 0.1 instead 10 Hz, as used by the Lille group.
- The results regarding LME of T91 are still not clear enough to exclude LME. Therefore, the next work has to be focused on the influence of surface state of T91 steel, the LBE chemistry (oxygen, metallic impurities) and the temperature range where LME can occur.

EXPERIMENTAL RESULTS FROM DTHT-LBE INTERACTION EXPERIMENTS AND DTHT IRRADIATION TESTS

Waihung Leung¹, Eyke Wagner¹, Keith Woloshun²

¹Paul Scherrer Institute - CH

²Los Alamos National Laboratory - USA

Abstract

Both short-term (2 hr) and long-term (1 week) experiments were conducted to investigate and measure any interactions between the MEGAPIE coolant, DTHT, and LBE. Experiments are conducted at 350°C, assumed to be an upper bound temperature for a DTHT-LBE mixture in the event of a THX leak. There was no observable result during short-term tests, but in 1 week there was measurable pressure rise, apparently due to gas generation resulting from pyrolytic decomposition of the DTHT. A control experiment with DTHT only (Ar cover gas) resulted in comparable but higher total gas generation, including possibly a condensable component. Post-test gas samples taken after both DTHT-only and DTHT-LBE experiments will be analyzed. DTHT decomposition rates are compared to information provided by the manufacturer (Bayer). Additionally, a sample of DTHT was gamma-irradiated to a dose of 10⁷ Gray. No material or property change in the form of solids or increased viscosity was observable.

Introduction

The MEGAPIE spallation neutron target uses as a coolant the oil Diphyl THT (DTHT), produced by Bayer AG, to cool the molten lead-bismuth eutectic (LBE) target. In the event of a heat exchanger leak, higher pressure DTHT will enter the lower pressure LBE. Chemical or thermal interactions between the DTHT and the LBE could result in unsafe conditions, most particularly an unacceptable pressure rise or an exothermic reaction causing rapid temperature increases. Also of concern are the possible negative effects of a long-term exposure of the DTHT to the full temperature of the LBE, as high as 350°C.

Additionally, radiation to the DTHT from the activated LBE could cause physical changes in the DTHT that would degrade its performance as a coolant. Of particular concern would be an increase in viscosity, which would change the flow characteristics of the fluid, or the production of solids, which could cause blockage in the fluid loop, most likely in the Intermediate Heat Exchanger (DTHT-to-water).

To address these concerns, a set of experiments was conducted to examine the result of heating the DTHT to 350°C with and without the presence of LBE. Independently, a sample of the DTHT was exposed to a source of gamma radiation for a cumulative dose of 10⁷ Gray. These experiments and results are described below.

Experiment Description: DTHT-LBE Interactions

1-liter autoclave was used as a heated vessel to conduct time-at-temperature experiments. The autoclave vessel was heated by internal radiant heaters. The control temperature was that of the DTHT. The autoclave is shown in Figure 1. Note that the top of the 1-liter vessel is uninsulated. Because of this, the average gas temperature was estimated from the initial pressure response. A midlevel gas temperature sensor gave an approximate measure of gas temperature. From access ports in the top of the autoclave vessel it was possible to evacuate and fill the gas portion, measure pressure, and take gas samples.

Tests were conducted first with DTHT only (118.05 g DTHT) and then with a DTHT-LBE (132.90 g DTHT, 1278.1 g LBE) mixture. To conduct an experiment, first the DTHT or DTHT-plus-LBE was placed in the autoclave vessel. This was fitted into the autoclave furnace along with instrumentation and gas lines. Air was removed by a 5-cycle pump-and-purge routine with argon. The gas sample bottle was also purged in this manner. The vessel was then backfilled with 0.5 bar argon at room temperature, to a gage pressure of -0.5 Bar.

The vessel was then heated with a set point of 350°C . Heating resulted in an increase in pressure to 0.2 Bar, gage, due to heating of the Ar and to the vapor pressure of the DTHT at this temperature. DTHT vapor pressure is shown in Figure 2. This temperature condition was then held for 168 hrs (7 days). Pressure and temperature were measured for the duration of the experiment.

At the end of the test, gas samples were taken by once again evacuating the sample bottle, isolating the system from the vacuum system, then exposing the sample bottle to the gas.



Figure 1. Photo of the DTHT-LBE interaction experimental set-up.

Results

The temperature control cycle during the first few cycles for the DTHT-LBE run is shown in Figure 3. After a higher initial overshoot caused by the thermal inertia of the autoclave, the temperature oscillated steadily between 361 and 245 C. The DTHT-only temperature oscillations were similar, but because of the lower mass of

the system, the maximum and minimum temperatures were a bit more extreme: 365 and 240 C, respectively.

Figure 4 shows the resulting pressure rise as a function of time for both runs. Most noteworthy is the striking difference between rate of increase in pressure between the 2 curves. Clearly, some net gas production is evident in the DTHT-only case that is not observed in the DTHT-LBE system.

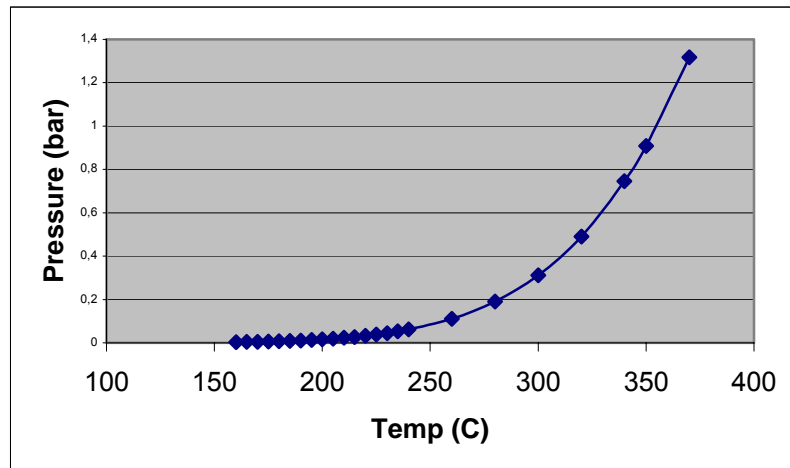


Figure 2. DTHT vapor pressure curve.

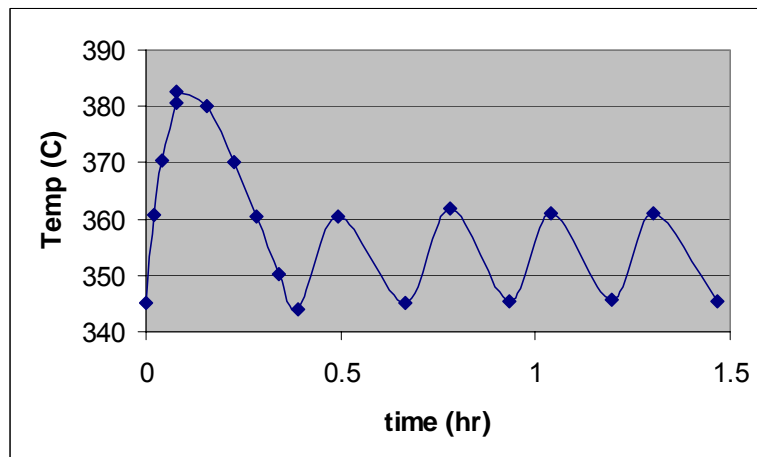


Figure 3. Temperature history of the DTHT during the early part of the mixed DTHT-LBE experiment. After the initial overshoot, temperature oscillated steadily for the remainder of the 168-hr run.

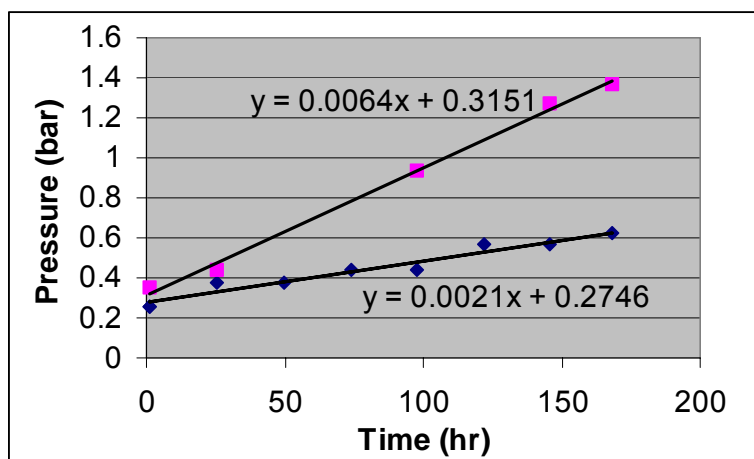


Figure 4. Pressure vs. time for DTHT-only and DTHT-LBE mixture. Indicated pressures are measured at 360°C, near the peak in the temperature cycle curve.

Most important to MEGAPIE is any rapid interactions resulting from a leak event. The initial pressure response on heating was an increase to nominally 0.3 bar in both cases, indicating a pressure rise from room temperature of 0.8 bar. Although the DTHT temperature is measured directly and is well known, the average gas temperature is uncertain, due to gradients within the vessel and the difficulty of direct measurement. Assuming no initial gas production due to some material interactions, the 0.8 bar pressure increase is due to a sum of the vapor pressure of the DTHT (Figure 2) at the gas temperature and the expansion of the Ar cover gas,

$$P(T) = P_0(T/T_0) + P_v \quad (1)$$

$$P_v = 3 \times 10^{-19} T^{7.2727} \quad (2)$$

from a curve fit to the vapor pressure data provided by Bayer (T in °C). The effective gas temperature can be found by iteration to be 300°C, consistent with expectations and a mid-level measurement. One can conclude that the initial response of the system was consistent with the temperature rise alone, and not affected by a chemical reaction resulting in gas production.

From Figure 4, it is evident that the gas pressure rise in the DTHT-only case is about 3 times higher than in the mixed DTHT-LBE case. Since the mass of DTHT in the latter case is 13% more than in the former, one would expect a slightly higher gas generation in the mixed DTHT-LBE case. The possibility of a gas leak was minimized by leak rate checks. These checks were conducted at test temperature, but with Ar only in a previous assembly (closure of vessel). It is not possible to leak check the actual assembly leak rate at temperature because gas is being generated at an unknown rate. The linearity of the data would suggest no or very low leak rates. Most significantly, the final (room temperature) pressure changes, relative to initial pressure, were nearly identical in the 2 cases; 0.27 bar. This suggests that the additional gas pressure was generated by a condensable species in the DTHT-only experiment.

Bayer, the supplier of the DTHT, provided thermal degradation data at 350°C. They report 54% per year decomposition, of which 20-30% is gas, of which 93% is H₂ and 7% is CH₄. The results of this experiment and comparisons with the Bayer data are

shown in Table 1. Measured gas production is dramatically less than expected, as per the information provided by Bayer. The gas samples taken from each test have yet to be analyzed.

Table 1. Experimental data summary and comparison with Bayer data.

	DTHT Only	DTHT-LBE Mixture
As measured at 300°C gas temp.		
dP/dt	650 Pa/hr	210 Pa/hr
dP/dt-g _{DTHT}	5.5 Pa/hr/g	1.6 Pa/hr/g
dP/dt-g _{DTHT} -I _{gas}	6.2 Pa/hr/g/l	2.2 Pa/hr/g/l
dP/dt-g _{DTHT} -I _{gas} Bayer	42.7 Pa/hr/g/l	42.7 Pa/hr/g/l
Room Temperature		
Pressure rise after 168 hr	27000 Pa	26000 Pa
H ₂ per g _{DTHT} per hour (1)	1.0 X 10 ⁻⁶ g/g _{DTHT} -hr	
H ₂ per g _{DTHT} per hour (Bayer)	14.3 X 10 ⁻⁶ g/g _{DTHT} -hr	
CH ₄ per g _{DTHT} per hour (2)	0.07 X 10 ⁻⁶ g/g _{DTHT} -hr	
CH ₄ per g _{DTHT} per hour (Bayer)	1.1 X 10 ⁻⁶ g/g _{DTHT} -hr	

(1) Assumes H₂ is 93% by weight of the gas produced.

(2) Assumes CH₄ is 7% by weight of the gas produced.

Radiation effects on DTHT

DTHT was exposed to a gamma irradiation dose of 10⁷ Gray. The expected dose during 6 A/hr at 560 MeV in SINQ is 7.2 X10⁵ Gray, as predicted by E. Pitcher using MCNPX. The qualitative result was no visible solids and no apparent change in DTHT viscosity.

Conclusions

The conclusions are as follows:

- There is no chemical reaction between DTHT and LBE that results in an initial increase in temperature or pressure that would be of consequence to MEGAPIE.
- There is a significant difference between apparent gas production rates for the DTHT than for the DTHT-LBE mixture at elevated temperature, but the net gas production as measured at room temperature was virtually identical for the DTHT-only and the DTHT cases. This suggests the production of a condensable gas in the DTHT-only experiment.
- The gas production rates predicted from the information provided by Bayer is as much as 14 times higher than measured.
- Irradiation dose in the range expected during the MEGAPIE experiment will cause no significant change in DTHT.

The gas samples taken during these tests have yet to be analyzed.

Pb-Bi EUTECTIC RECRYSTALLIZATION STUDIES FOR MEGAPIE TARGET.

Alberto Zucchini, ENEA FIS MET
Pietro Agostani, ENEA FIS ING
Elio Baicchi, ENEA FIS MET

Abstract

In the present work, the LBE (Lead Bismuth Eutectic alloy) expansion behaviour after freezing is described according to the reported theory [1]. The issue of vessel resistance, after LBE recrystallization, was dealt with by experimental and numerical studies performed in ENEA in the frame of the Megapie Project [2]. We have identified the important elements which, in case of LBE solidification inside the Megapie target, play a role in the reduction of the possible vessel over-stressing; among them, the LBE yield strength has been tested in significant experimental conditions.

The resulting suggestions can also be related to the design and the freezing procedures of other LBE technology facilities.

Introduction.

In 2001, in ENEA, the necessity of performing in-depth studies to face recrystallization problems to be referred to the Megapie Project was envisaged.

For these reasons a bibliographic research has been followed by related experimental tests and numerical modelling. Different experimental studies have been, in parallel, performed by PSI [3, 4 & 5].

Chemistry of the phenomenon

Recrystallization is, as reported in Russian bibliography [1], an atomic level phenomenon which tends to an equilibrium state. Also in our case, different phases are segregated in adjacent grains and form crystal cells with different inter-atomic distances. With varying temperature, atoms can migrate through grain boundaries and pass from one to the other crystalline forms. In particular, LBE presents, after solidification, a mixture of two phases:

- a β phase (inter-metallic compound),
- a γ phase (solid solution of Pb in Bi).

With time, at a constant temperature, the excess γ phase precipitates. This gives rise to a volume increase, as that phase is richer in Bismuth which tends to increase the atomic distances when passing from the liquid to the solid phase.

At each temperature the precipitation of γ phase continues until the equilibrium condition is asymptotically reached. The equilibrium condition is essentially determined by the position, in the phase diagram, of the boundary line between the β and $\beta+\gamma$ regions (fig.1). The temperature effect accelerates the process. This process corresponds to a volume increase that has been measured by several researchers. Considering all the cooling modalities up to now tested, the maximum observed asymptotic value of volume rise was over 1% [1 & 3].



Stress analysis of LBE expansion

The main concern about the freezing of LBE inside a vessel after an experiment, such as in the Megapie Project, is related to the risk of a rupture of the target hull, when the frozen LBE will start to expand by recrystallization.

A study of the parameters affecting the stress level in the vessel, produced by the expansion of the solidified LBE, has been required. The stress analysis of the target,

during possible freezing procedures, have been performed with the FEM code ABAQUS. The lower part of the target including the internal guide tube, which separates the upward flow in the center of the target from the downward flow in the outer annulus, and the central instrumentation rod have been simulated in the 2-D axial-symmetric FE model shown in Fig. 2. The stress analysis is based on full elastic-plastic FEM simulations, which produce the stress distributions in the model as a function of LBE expansion (ΔV). The model for the behaviour of the LBE-structures interfaces is a no slip (perfect bond) contact. This approach is conservative, because any constraint to axial LBE expansion, such as higher shear stresses at the interfaces, will increase its radial expansion and consequently the stress state in the containment structures.

The stress analysis shows that the field of stresses in the Megapie target vessel is mainly affected by the height of the solid LBE level, by the expansion extent of the contained alloy, by the LBE yield stress and by the presence of internals.

The height of each solid LBE layer (Fig.3) in the container resulted to be a significant parameter which needs to be accurately chosen to avoid over-stresses of the vessel. We assume that the liquid volume, resting above the level of the solid substrate, is free to expand toward the top of the vessel without any constraint. It was proposed, in case of high containers, to complete the freezing of LBE by subsequent batches of appropriate height. This procedure was numerically simulated too. In the case of Megapie target it has been found that, assuming 1MPa of LBE yield strength, by increasing the solid LBE height in the 1st expansion step from 350 mm to 500 mm, the maximum stress at the bottom of the target varies from 230 MPa to 300 MPa. This is shown in Fig.3,  here are the plots of the Mises stresses vs. ΔV  reported in differently stressed positions of the Megapie Target

The expansion extent of the recrystallization process depends on its duration and temperature. It is evident, from Takeda experiments [3], that a first period of faster expansion, which ranges from two hours (110 °C) to three months (20°C), is followed by a second period of lower expansion rate. In any case the final volume expansion hardly exceeds 1.3 % in one year. In the numerical study reported in Fig.3, for the case of Megapie Target, the assumed volume expansion was 1.2%. It has been found also that if the final expansion is 1.5% instead of 1.2%, the maximum stress of Megapie window would increase about 15%.

The LBE yield strength, considered in the next paragraph, turned out to be a very important parameter. In Fig.4 the cases of $\sigma_{y=0.2} = 1MPa$ and $\sigma_{y=0.2} = 2MPa$ are compared. The maximum calculated stress increases of 33%. A higher yield stress means that the internal forces needed to axially extrude the material in a plastic flow are higher, with a consequent increase of the load on the containment structures. According to Takeda's experimental tests [3] the LBE free strain rate is affected by temperature, while Dai [5] has found that the LBE yield stress is a function of temperature and strain rate. The LBE yield stress could therefore provide a means for reducing the stress level in the walls by temperature control of the solidified LBE. Such possibility has suggested further numerical and experimental research work, whose results are presented in the section below.

The presence of internals, such as the central instrumentation load, which interrupt the extrusion flow path clearly results in a wall stress increase, as verified with the stress analysis simulation.

Further considerations involve the shrinkage and the thermal expansion. During the transition from liquid to solid, a significant shrinkage takes place (5%); unfortunately the voids are concentrated in the centre of the free surface and do not allow a significant volume recovery during the recrystallization. The expansion coefficient of LBE is $21 \times 10^{-6} \text{ 1/}^\circ\text{C}$, while that of stainless steel is $16 \times 10^{-6} \text{ 1/}^\circ\text{C}$; this means that, as the cooling takes place, the contraction of LBE is larger than that of its container and a 0.15 % of volume becomes available after reaching the room temperature. Such a value is about one tenth of volume expansion due to recrystallization.

Experimental tests

The numerical observation about this parameter can be explained considering that when the LBE is very “soft” (lower yield stress), its plastic flow toward the free surface is facilitated and takes place without exerting large forces on the walls.

On the contrary, when the LBE is “hard” (higher yield stress) its flow toward the top requires large internal forces. These forces can definitely damage the vessel.

For this reason it would be useful to deal with “soft” LBE during freezing – de-freezing operations.

Some compression tests were performed for two reasons:

- better connotation of the results, since the LBE is compressed in the actual case
- easier procedure of specimen fabrication, controlling and testing.

The interface between specimens and testing machine was refurbished following the ASTM standard E 9-81 for compression tests.

Each specimen was a little cylinder of LBE, the diameter of each specimen was 26 mm, the height 20 mm.

During each test the LBE specimen was maintained immersed in diathermic oil, whose temperature was continuously followed by thermocouples.

The comparison test parameter was the 0.2% yield strength recorded as average value of 5 valid tests in each case.

Experiments have shown, as expected, that the chosen parameter is strongly influenced by the test temperature, as reported in Fig.5.

The second parameter affecting the LBE yield strength is the strain rate. When this parameter is combined with high temperatures, close to the melting point, there is a complex microphysical phenomenology involving relaxation, phase segregation, matrix deformation and grain boundary sliding. The net result is a positive strain rate sensitivity of the material which is clearly shown in Table 1.

It should be noted that for the LBE eutectic the importance of creep increases dramatically with temperature: according to Russian bibliography [9] the creep extent over 70°C results about 4 orders of magnitude higher than at 0°C.

Table 1

Strain -Rate	Temperature	Yield Strength 0.2%
5 E-6 1/s	90°C	6.1 MPa
5 E-6 1/s	110°C	3.3 MPa
1 E-4 1/s	86°C	11 MPa
1 E-4 1/s	104°C	8.8 MPa

The velocity of stress application, in the actual case, is close to the strain rate of the LBE free expansion. The maximum LBE expansion rate resulted, after Takeda experiments, 5 E-6 1/s @ 110°C. Since, up to now, the strain rate effect of a constrained expansion has not yet been studied, we assume the former figure as the most realistic strain-rate for laboratory compression tests.

The third parameter, whose influence was evidenced, is the ageing time after solidification. Two different sets of compression specimens were tested at 5 E-6 1/s strain-rate and 110°C and 90°C. The first set of specimens had been produced three months before testing; the second set had been produced less than five hours before testing. The comparison between 'fresh' and 'aged' samples, evidences a yield stress reduction of up to 18% for the 'fresh' LBE. It has to be noticed that the case of freshly frozen samples is the most representative of the actual situation, where the expansion takes place immediately after the solidification.

The yield stress reduction observed on the 'fresh' samples is due to the lack of γ phase segregation, while in 'aged' alloy it constitutes a significant resistance to the relative motion of dislocations. The most favourable situation, in terms of low yield stress, is the case with 'fresh' LBE expanding at high temperature and low strain-rate. It can be reached when maintaining the containing vessel at 110°C for about one week after solidification. During this time period, more than 80% of the total expected volume expansion is asymptotically reached, closely approaching to saturation [3].

Conclusions:

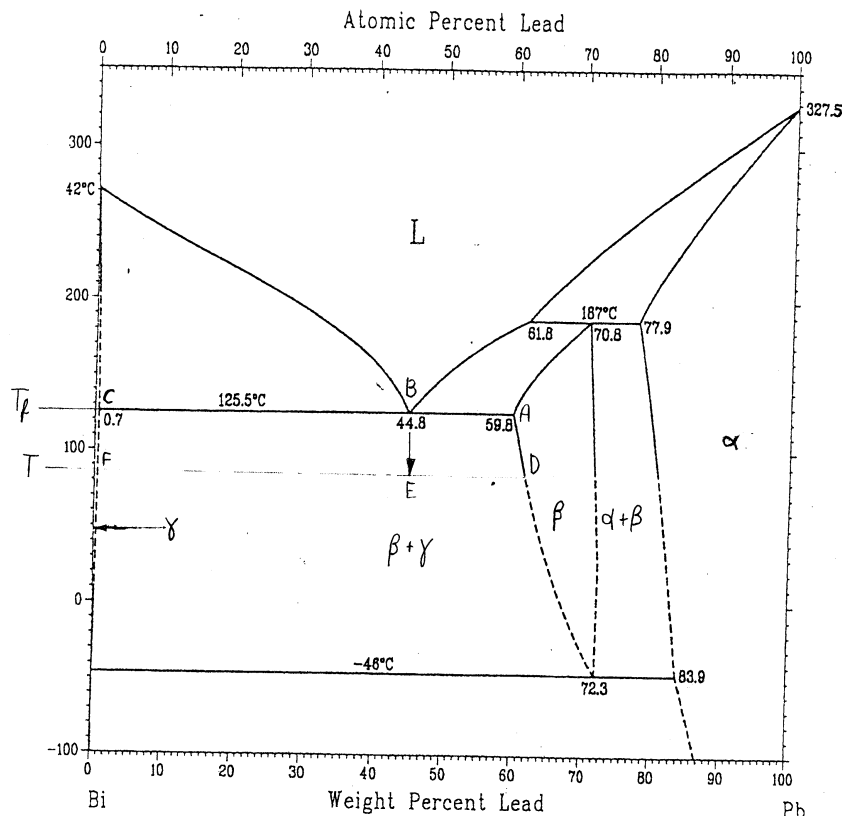
The numerical and experimental studies described in this paper show that the over-stressing, due to LBE recrystallization and expansion in containment vessels, such as in the Megapie Target, has to be considered during the design phase of the containment structures and can be faced by means of engineering rules. To avoid over-stressing of structures it is necessary to reduce:

- the height of each solid LBE layer,
- the presence of internals,
- the LBE yield strength.

The reduction of LBE yield strength can be attained raising the temperature at which the recrystallization takes place. The height of expanding LBE can be reduced by an appropriate freezing procedure, where the vessel is solidified in subsequent steps from bottom to top. Two other important factors, significantly affecting the yield stress, are the strain-rate and the degree of γ phase precipitation. It has been shown that a realistic combination of the former effects can lead to a significant reduction of the LBE yield strength. Further steps have to be done to compare the numerical approach with a validating experience and to formulate specific indications for design.

References:

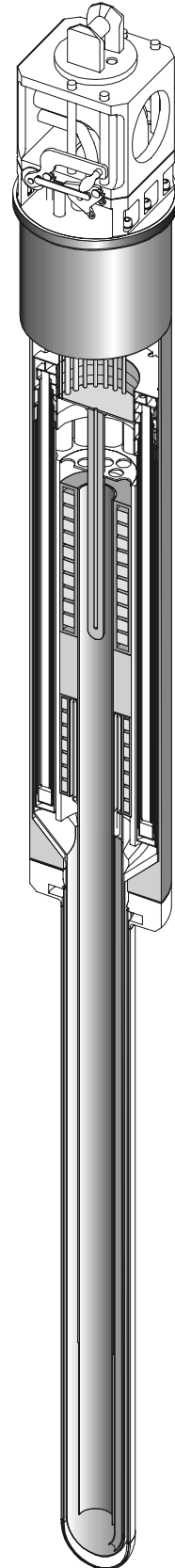
- [1] "Heavy Liquid Metal Coolants in Nuclear Technology", HLMC-98 Conference, Obninsk.;
- [2] G.S. Bauer, M. Salvatores and G. Heusener, J. Nucl. Mater. 296 (2001), 17;
- [3] Y.Takeda, "Volume change of LBE after solidification", internal document PSI n°TM-87-02-01;
- [4] J.A.Patorsky, "Influence of freezing-defreezing of Lead-Bismuth Eutectic (LBE) on an experimental strain distribution for the model of the Megapie target container", Megapie Project Co-ordination Group (PCG) Meeting , PSI 16/01/02;
- [5] Y.Dai et al., "Compression Tests on PbBi at Different Temperatures and Strain-rates", Megapie presentation held at PCG meeting on 03/09/02;
- [6] ASTM Standards E 9-81, "Standard Methods of Compression Testing of Metallic Materials at Room Temperature";
- [7] "Metals' Handbook" edited by the American Society for Metals;
- [8] Perry and Chilton, "Chemical Engineers' Handbook", Fifth Edition, McGraw-Hill;
- [9] Pylchenkov, "The Issue of Freezing-Defreezing Lead-Bismuth Liquid Metal Coolant in Reactor Facilities Circuits", in [1].



Pb-Bi phase diagram as reported by the ASM Handbook (1992)¹¹.

Figure 1: Phase Diagram of the Lead – Bismuth Alloy.

Figure 2a :
Sketch of a Preliminary Design
of the MEGAPIE Spallation Target



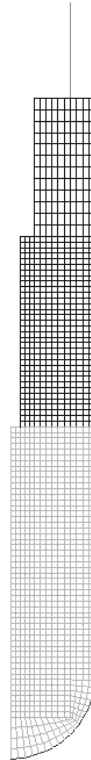


Figure 2b: FEM Mesh of MEGAPIE Lower Target
The two solidification layers are shown in different grey levels; the presence of
internals can be deduced from different meshes.

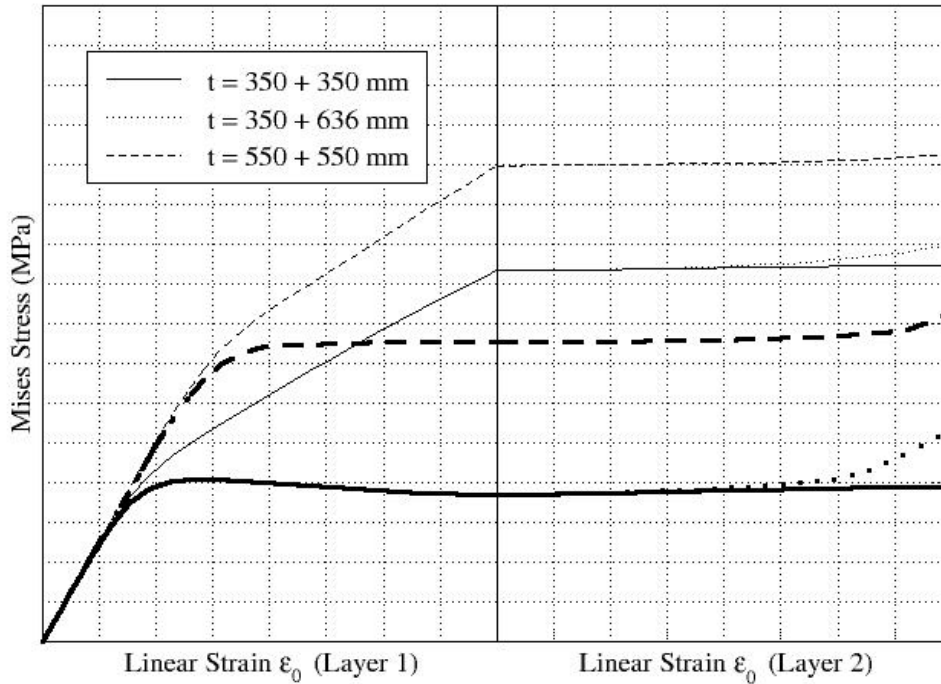


Figure 3: Influence of the Solid LBE Height.

$$\sigma_y = 1 \text{ MPa} , \epsilon_0 = 0.4\% ;$$

Where: h_1 and h_2 are the heights of two LBE layers frozen and solidified in sequence from bottom to top; σ_y is the LBE yield strength; ϵ_0 is the linear expansion ($\epsilon_0 = 0.4\%$ corresponding to 1.2% volume expansion).

Thin lines are referring to the junction between cylindrical and emispherical vessel parts.

Thick lines are referring to the centre of the emispherical shell.

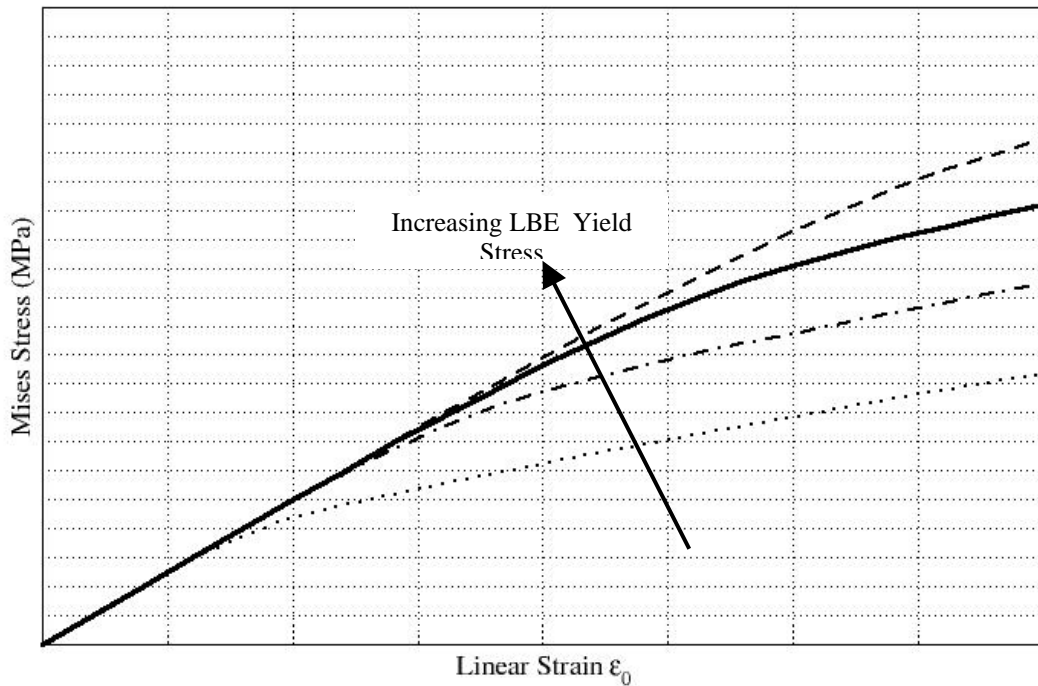


Figure 4a: Influence of the yield stress.

Stress at the junction between cylindrical and emispherical vessel parts with $h_1 = 350\text{mm}$, $\varepsilon_0 = 0.4\%$, where: h_1 is the height of the bottom LBE layer; σ_y is the LBE yield strength; ε_0 is the linear expansion ($\varepsilon_0 = 0.4\%$ corresponding to 1.2% volume expansion).

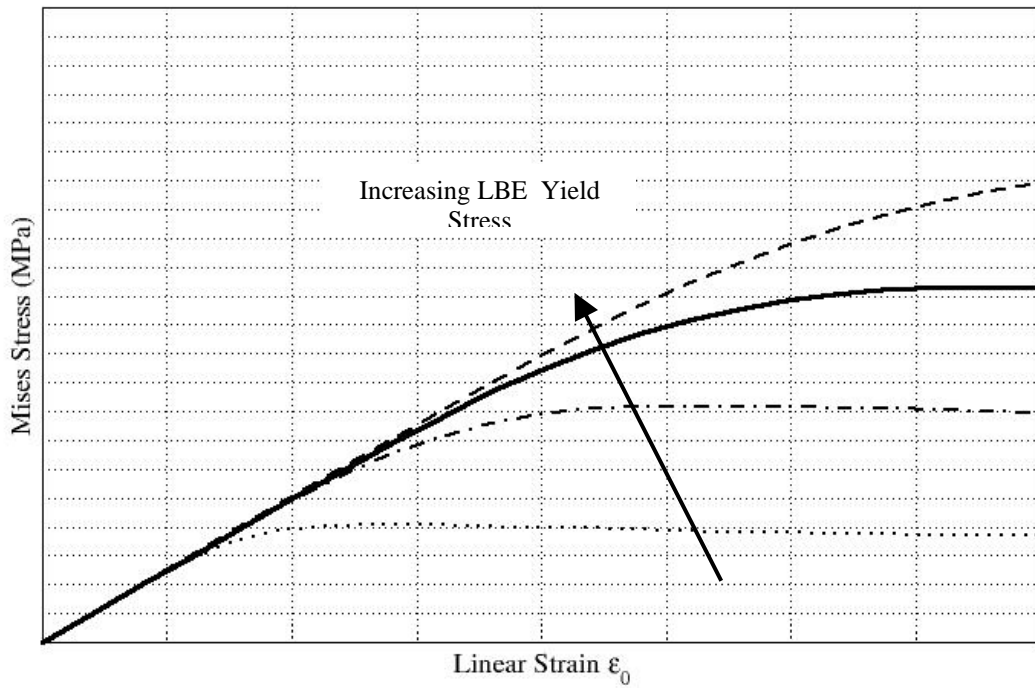


Figure 4b: Influence of the yield stress.

Stress in the center of the emispherical shell with $h_1 = 350\text{mm}$, $\varepsilon_0 = 0.4\%$, where: h_1 is the height of the bottom LBE layer; σ_y is the LBE yield strength; ε_0 is the linear expansion ($\varepsilon_0 = 0.4\%$ corresponding to 1.2% volume expansion).

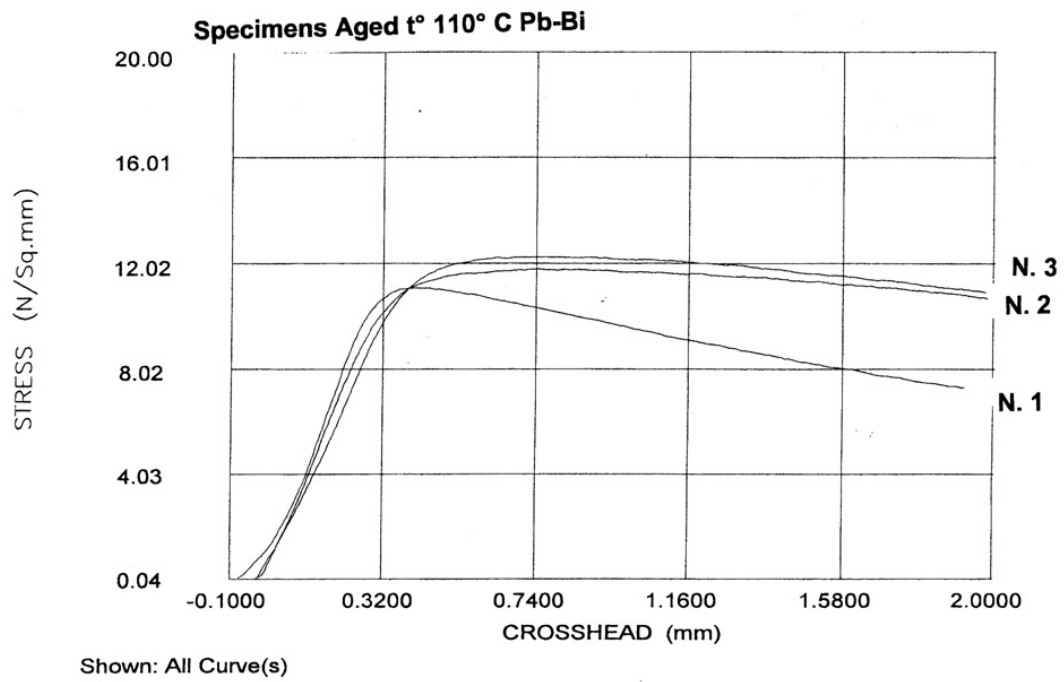


Figure 5: Influence of temperature in the stress-strain diagram of PbBi

Diagram n°1 was obtained at 110°C;
 Diagram n°2 was obtained at 100°C;
 Diagram n°3 was obtained at 90°C.

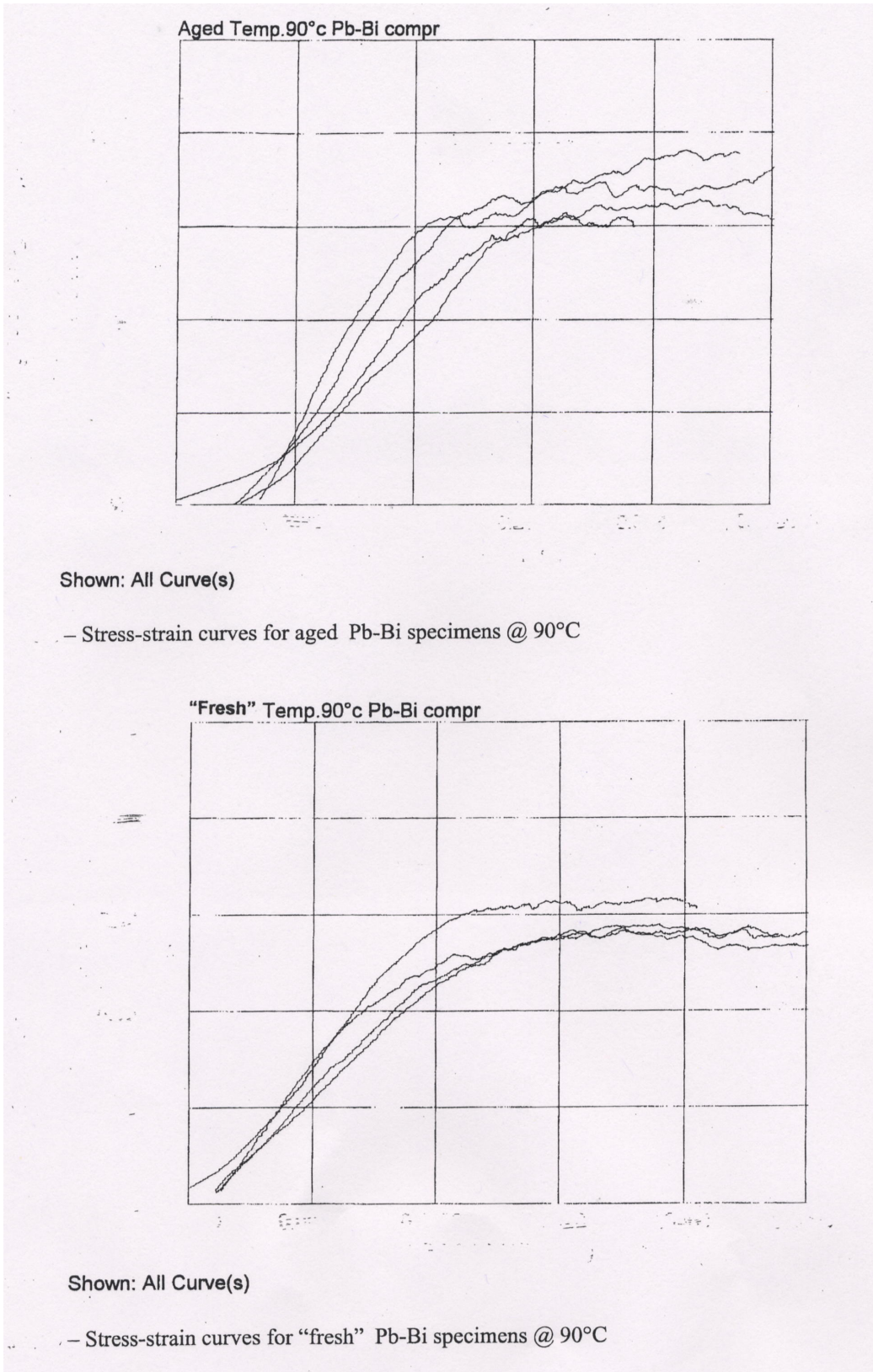
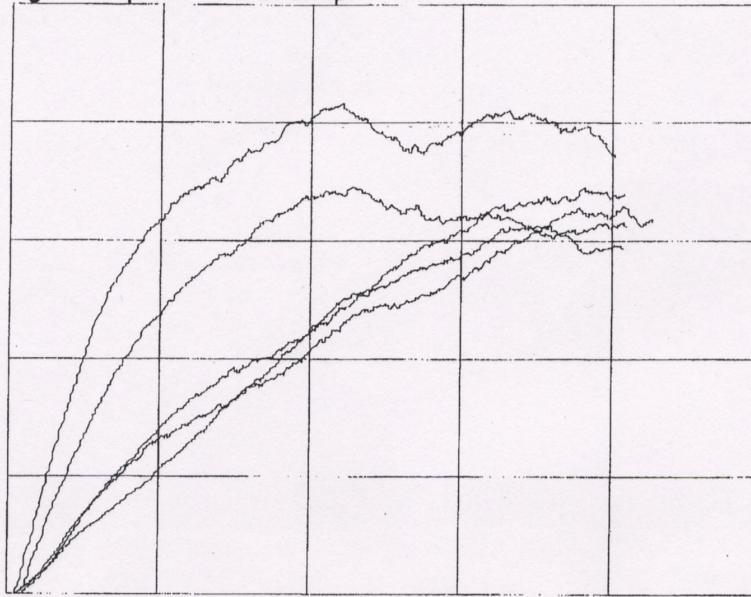


Figure 6.a: Stress-strain curves for aged Pb-Bi specimens @ 90°C
 Figure 6.b: Stress-strain curves for "fresh" Pb-Bi specimens @ 90°C

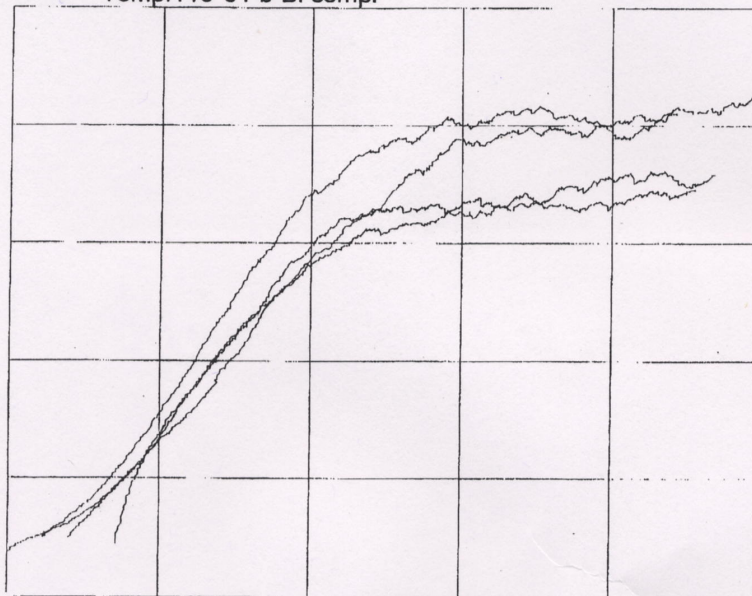
Aged Temp. 110°c Pb-Bi compr



Shown: All Curve(s)

- Stress-strain curves for aged Pb-Bi specimens @ 110° C

"Fresh" Temp. 110°c Pb-Bi compr



Shown: All Curve(s)

- Stress-strain curves for "fresh" Pb-Bi specimens @ 110°C

Figure 7.a: Stress-strain curves for aged Pb-Bi specimens @ 110° C
Figure 7.b: Stress-strain curves for "fresh" Pb-Bi specimens @ 110°C

ANNEXES



MEGAPIE Design Concerns

John Herczeg (DOE-NE)

Frank Goldner (DOE-NE)

Kemal O. Pasamehmetoglu (LANL)

Advanced Fuel Cycle Initiative

Presented at the MEGAPIE Technical Review Meeting

March 18-19, 2003 (Paris, FRANCE)



A successful completion of the test is important to DOE program



- We are concerned that some of the design decisions and recent design simplifications made to accommodate the tight schedule demands may jeopardize the successful conclusion of the test.
- Our first priority is to start the test when we have a high confidence of success.
- We question the value of meeting the schedule but completing either an inconclusive or, worse, an unsuccessful test.
- We are equally concerned with the status of the design in reference to remaining essential design activities.



We disagree with the decision to remove the drain system



- The removal of drain capability may result in a premature termination of the tests with possible interpretation of technology failure!
- The implications of a frozen target on PIE results are uncertain.

- Evaluate the impact of maintaining the drain capability on the schedule and cost of the project.
- Evaluate and document the implications of this decision in reference to test objectives.
- Evaluate the possibility of moving the target to hot cell while molten and of draining it without freezing in place.



We are concerned about the window lifetime and catastrophic failure during testing.



- The low operating temperature may not be the best choice concerning irradiation induced ductility.
- The decision not to use oxygen control must be better justified in reference to liquid metal embrittlement and corrosion control issues.
- Cyclic thermal stress effects (compounded with the above issues) must be addressed.

- At this point, we would like a careful assessment of these issues while specifically addressing the failure risks in reference to test objectives.
- There may still be room for further design optimization with respect to temperature and stress issues.
- We strongly urge the project to re-evaluate the need for active oxygen control.



The behavior of the safety hull following a sudden window failure is a concern.



- This is primarily an internal safety issue for PSI but may have negative impacts on the technology:
 - The safety authorities may not allow the test to go forward
 - Alternatively, a serious accident will result in a serious negative press on the technology.
- Thus, it is important for all partners to understand the risk.

- Given that there are a lot of uncertainties on window performance, safety hull must be evaluated as the single containment.
- Proper peer review of the analyses based on conservative, worst-case assumptions is strongly recommended.
- We also strongly recommend an experimental verification of the analyses.



The possibility of a leak at the flange between the lower and upper target is serious.



- We are concerned about the possibility of a leak at the flange connection between T91 and 316 SS components.
 - Flange joint between two materials with different CTE !
 - Irradiation assisted bolt relaxation !
 - What is the initial preload ? How will it be measured ? What is the load requirement at the end of life ?
 - What is the effect of thermal transients?
 - Given that there is no inspection possibility, how will the design be validated ?

- We strongly recommend that the option of welding this joint after the integral test be evaluated.
 - Redesign of the joint
 - Or weld around the existing flange and bolts.



What is the status of the heat exchanger design and testing?



- The new heat exchanger design is complex and unconventional.
- We are concerned about the status of the stress analyses on this design.

- As a minimum, an independent stress analysis could be performed in consultation with the manufacturer.
- A dedicated test program would be advisable but may not be possible given the schedule constraints.
- The Integral Test plan should include specific tests to address both the mechanical and thermal-hydraulic performance of the heat exchanger.



What are the plans to address the issues associated with the pump and the flowmeter ?



- How are the issues being addressed?
 - Radiation effects
 - Operating temperature
 - Mechanical robustness
 - Transient stresses
 - Electrical noise
 - Flowmeter calibration and failure

- A comprehensive test plan is essential
- We recommend the test be performed at PSI by the same personnel who will conduct the Integral test and SINQ operations.



Looking forward to a clear path forward prior to the Steering Committee meeting in June



- We request that the issues raised in this presentation be addressed prior to and during the upcoming Steering Committee meeting, in parallel to
 - Carefully reviewing the MEGAPIE test objectives
 - Developing the Integral Test plan
 - Developing detailed separate effect test plans in areas recommended in this presentation
- The failure risk of achieving test objectives must be carefully evaluated and communicated to the partners.
- We would like to offer our assistance in resolving these issues when requested within the limitations of our resources.



Fatigue experiments on T91 steel in Pb-Bi

J.- B. Vogt, A. Legris, A. Verleene, G. Guittier and I. Serre
Université des Sciences et Technologies de Lille
Laboratoire de Métallurgie Physique et Génie des Matériaux UMR CNRS 8517
Bâtiment C6
59655 VILLENEUVE d'ASCQ cedex France

Introduction

The objective of our work is to study the mechanical behaviour of the T91 steel for the window. Since this component will be exposed to severe environment, a loss of ductility or an early fracture is possible. In a previous work we have shown that under monotonic loading the presence of a liquid metal could lead to a ductile to brittle transition if the alloy was in a hard condition and if very sharp microcracks forms in the liquid metal. It is now of interest to study the effect of a liquid metal on the cyclic behaviour of the T91 steel.

Material and experimental procedure

The chemical composition of the T91 steel supplied by Creusot Loire Industries is given in Table 1.

TABLE I : Chemical composition of the T91 steel

Element	Cr	Mo	V	Mn	Si	Ni	C	Nb	Fe
Wt %	8.80	1.00	0.25	0.38	0.41	0.17	0.11	0.07	bal

The alloy was air quenched from 1050°C and then tempered at 500°C for 1 hour, leading to a fully martensitic structure and an average grain size of 20µm.

Fatigue testing was carried out on cylindrical notched specimens with a gauge length of 10mm and a reduced diameter 3 mm. All the tests were performed under load control , using a sinusoidal waveform, a frequency of 10Hz and a stress ratio $R = 0.5$. Tests were conducted at 260°C in air and in a liquid lead bismuth eutectic bath.

Results and comments

The fatigue resistance is reported in Figure 1 where the fatigue lives are plotted against the maximum stress value. Here the stress is the ratio between the applied load and the specimen area at the notch without taking into account the notch factor. As can be seen, the fatigue lives do not depend very much on the environment except for the lowest stress value where the fatigue lifetime is much higher in air than in the lead bismuth bath.

The fracture surfaces have been examined by scanning electron microscopy. All the fracture surface consist in two zones :a “pure” fatigue fracture area and a final monotonic fracture area. The figure 2 is relative to the specimen failed at 260°C in air at the highest stress value. The final fracture is located at the centre of the specimen surrounded by the fatigue zone.

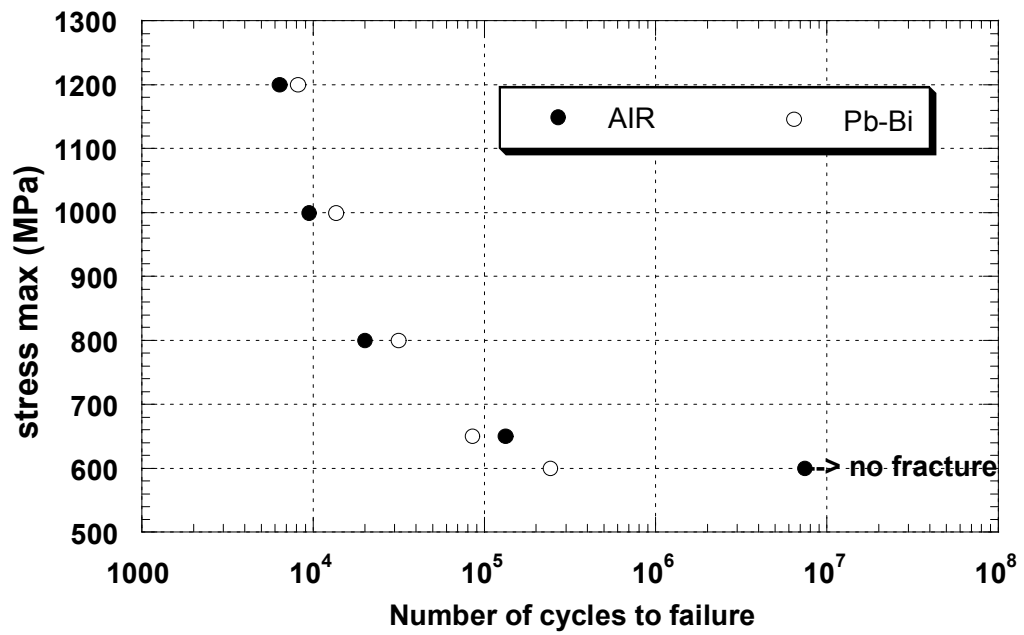


Figure 1 : fatigue resistance at 260°C of the T91 steel in air and liquid Pb-Bi bath

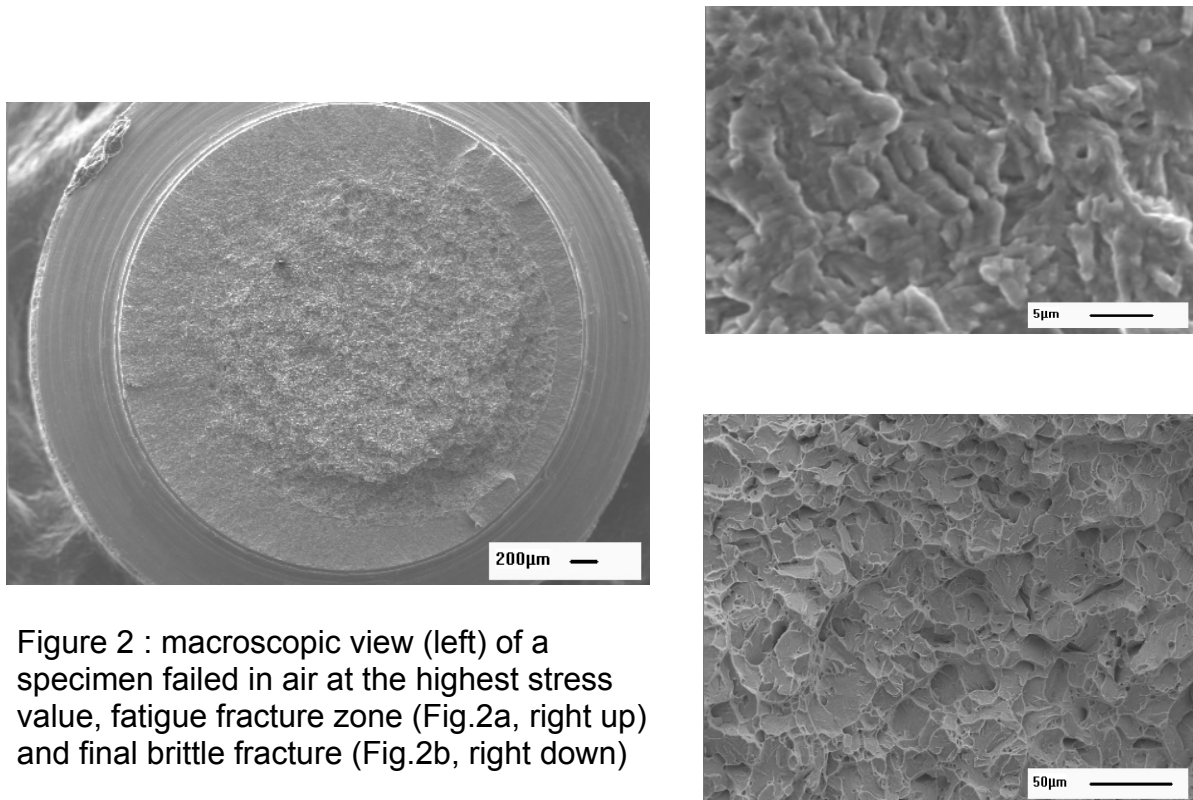


Figure 2 : macroscopic view (left) of a specimen failed in air at the highest stress value, fatigue fracture zone (Fig.2a, right up) and final brittle fracture (Fig.2b, right down)

The fatigue fracture zone exhibited fatigue striations which could be observed with some difficulty (Fig.2a). In the final fracture zone, a fully brittle transgranular fracture was unambiguously identified (Fig.2b). Decreasing the stress value of the fatigue test led to move progressively from a mixed brittle-ductile to a fully ductile fracture in the final fracture zone.

Cycling in the lead-bismuth bath resulted in a change in the fractography of the final fracture zone while fatigue striations were still observed in the fatigue fracture zone (Fig. 3a).

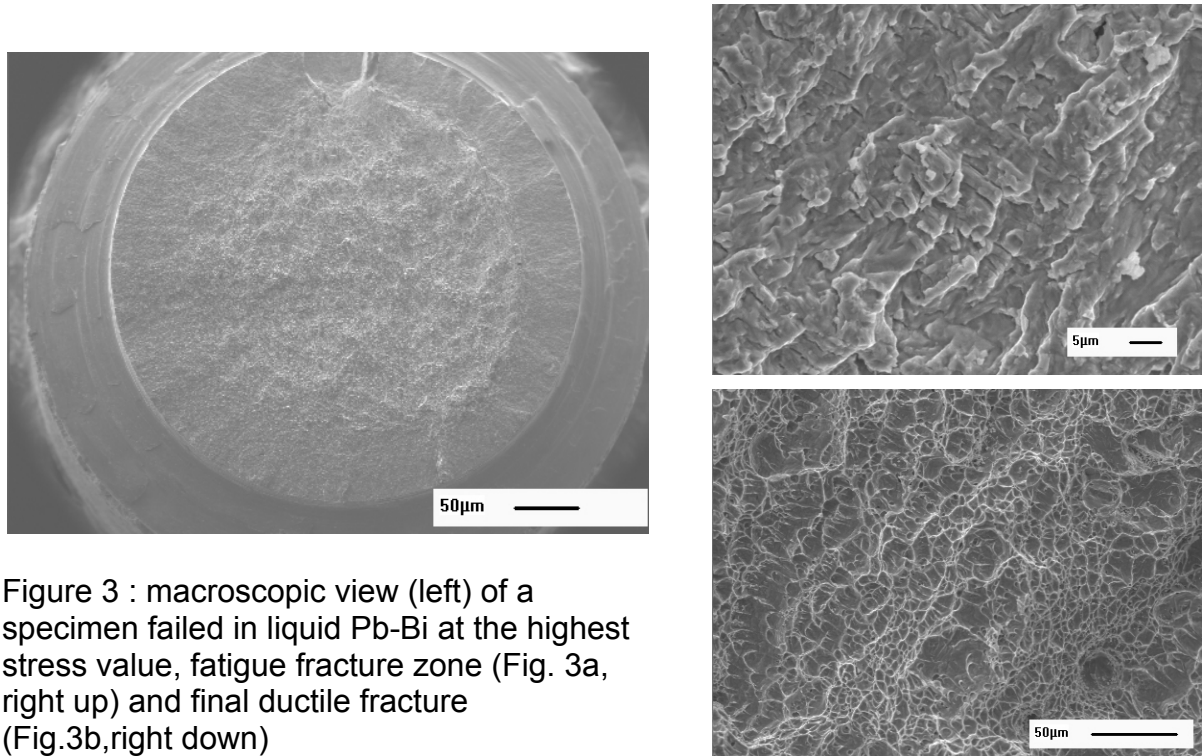
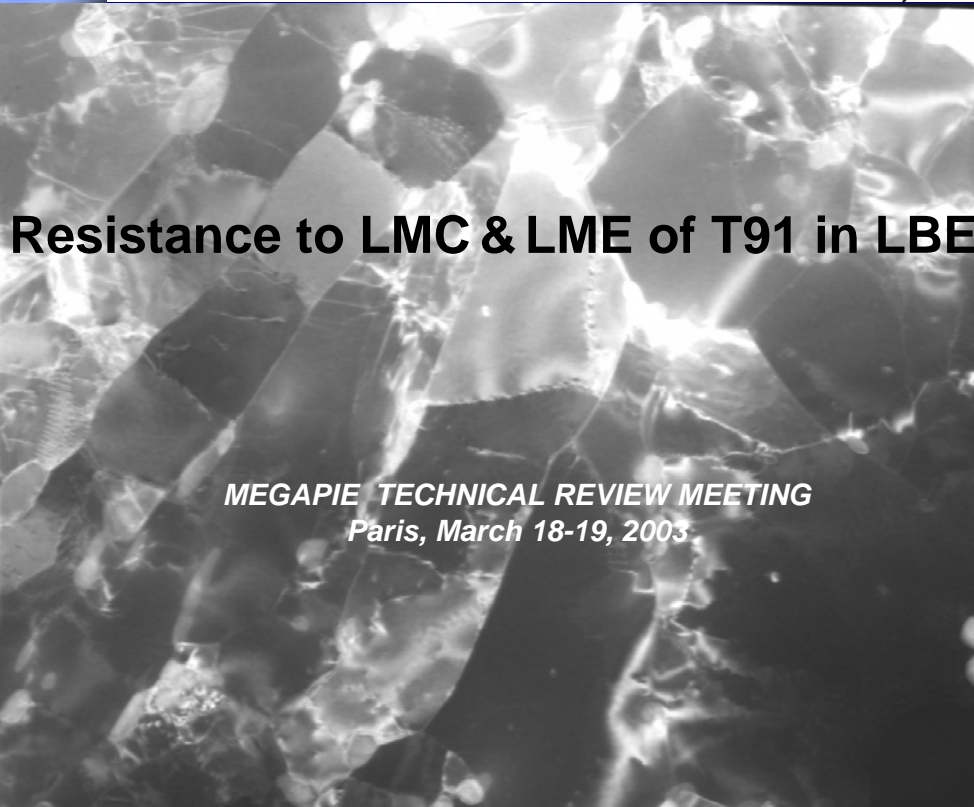


Figure 3 : macroscopic view (left) of a specimen failed in liquid Pb-Bi at the highest stress value, fatigue fracture zone (Fig. 3a, right up) and final ductile fracture (Fig.3b,right down)

A ductile fracture surface was observed in the final fracture zone in the liquid lead-bismuth bath whatever the cyclic load (Fig.3b).

The present results suggest that crack initiation is not influenced by the environment when the cyclic stress is high or when the test duration is short. The liquid metal could therefore contribute to assist the growth of short cracks, the latter being stable in air but unstable in liquid metal. Additional tests are therefore necessary to confirm the data (to appreciate the scattering) and to study if a decrease in the threshold of the stress intensity factor by the liquid metal is possible. The second information concerns the effect of the liquid metal on the fatigue propagation of the crack in the bulk of the metal. Indeed, the occurrence in the final fracture zone of a ductile fracture in liquid lead-bismuth instead of a brittle fracture suggest that the stress triaxiality at the crack notch is relaxed by the liquid metal. In other words, this should indicate that a cyclic softening of the plastic zone ahead the crack occurs by the liquid metal and promotes crack growth. This preliminary study indicates that the mechanical resistance of T91 in liquid metal under cyclic loading cannot be predicted easily from the monotonic and requires a special attention.



OUTLINE

1. Corrosion behaviour of «T91 - LBE», «T91 - Lead»

- * corrosion effects
- * a side effect : cavitation

2. Mechanical behaviour of «T91 - LBE», «T91 - Lead»

- * resistance to LME : intimate contact ?
- * Tensile tests
- * Relaxation tests

3. Possibility of monitoring a LBE bath ?

4. Concluding remarks & perspectives

5. Recommendations

1. Corrosion behaviour of «T91 - LBE», «T91 - Lead»

*The Protectiveness of the oxide film on T91 is related to:

- surface conditions of the steel
- initial oxide formation kinetics before immersion in LM bath
- *and* oxygen content once into contact with LM bath

*Corrosion kinetics

• In reducing conditions

flowing H₂ [1.5 10⁻¹⁰ wt.% oxygen in lead, at 525° C]

- slow oxide growth, thin oxide film (~ μm after 1 month)
- Localized & Generalized Corrosion delayed

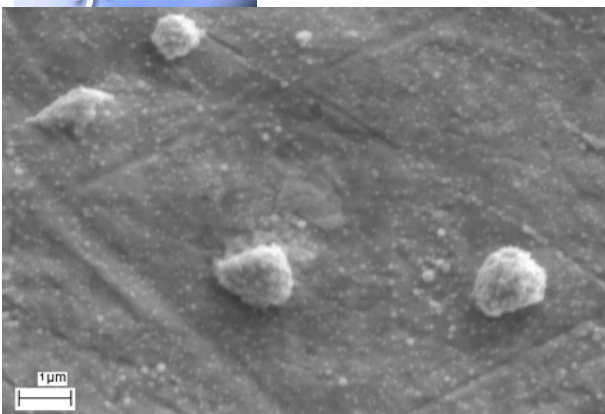
flowing hydrogenated helium

→ Accelerated oxide growth

corrosive attack of oxide film takes less than 1 day!

CNRS-CECM & CNRS-LTPCM

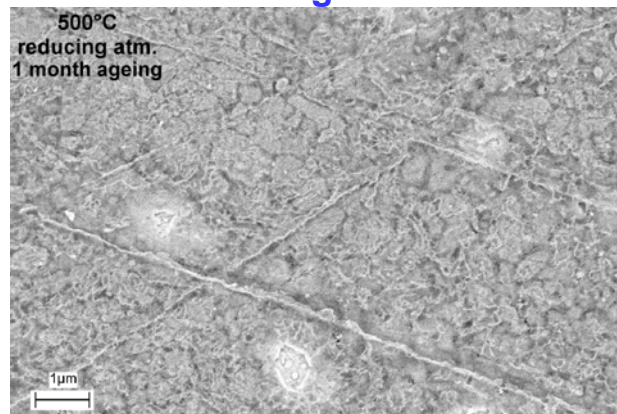
«T91-Pb»: slow corrosion kinetics in reducing conditions



10 days: homogeneous film
few scattered nodules

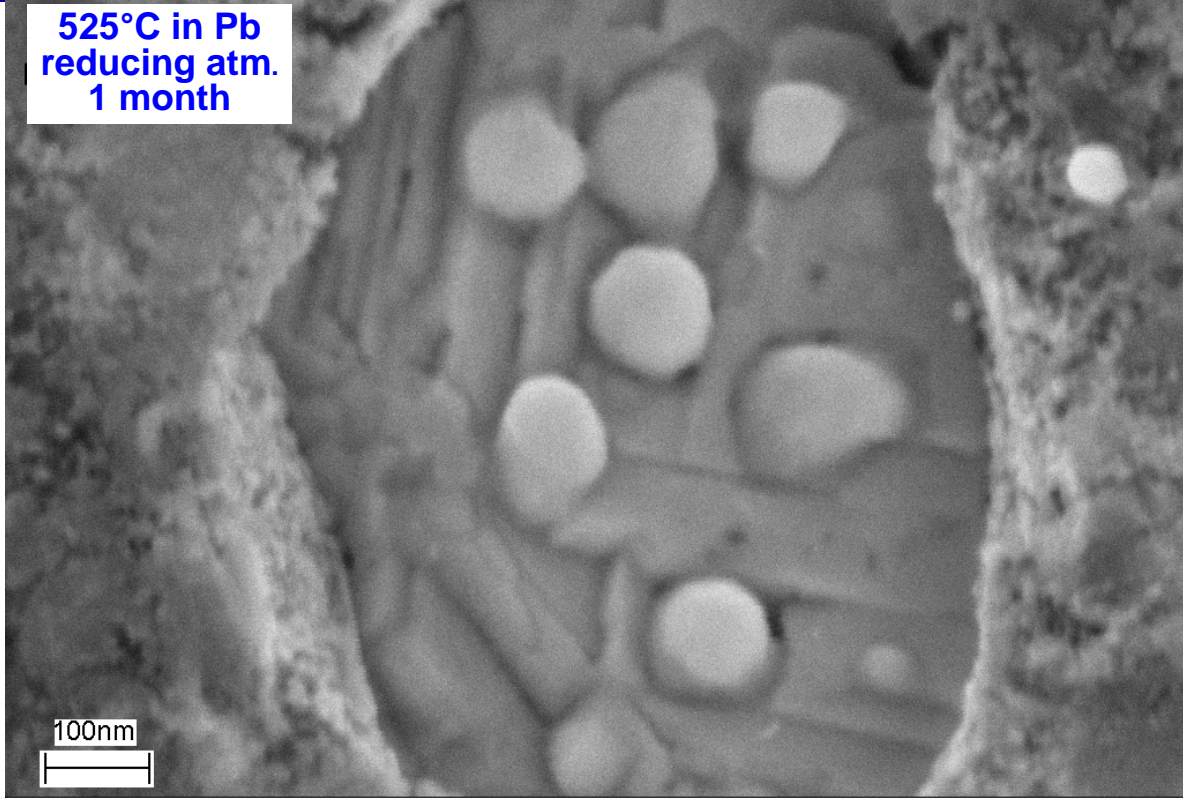


31 days: porous oxide, pits
generalized cor.



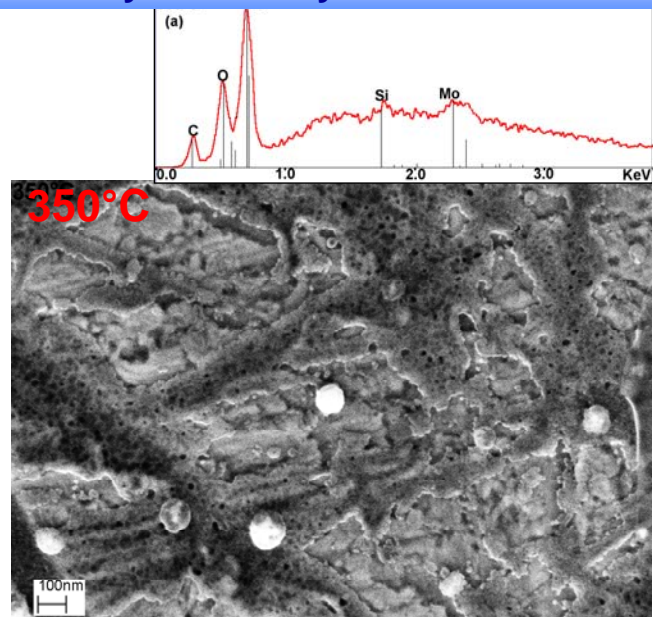
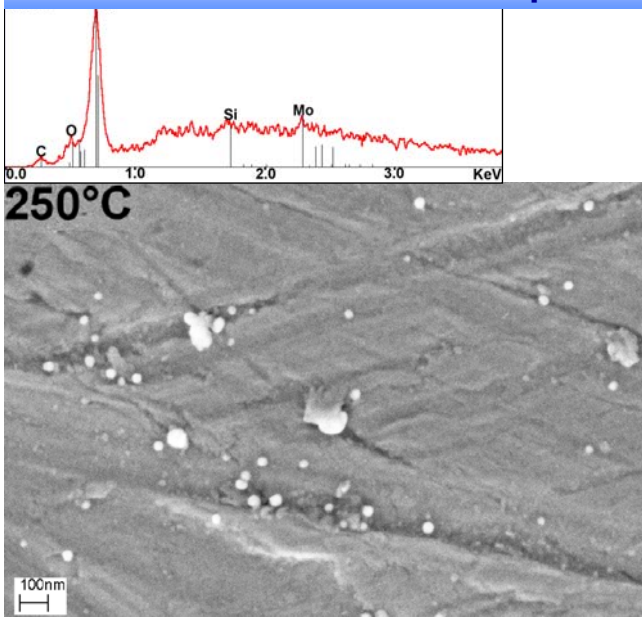
500°C
reducing atm.
1 month ageing

**525°C in Pb
reducing atm.
1 month**



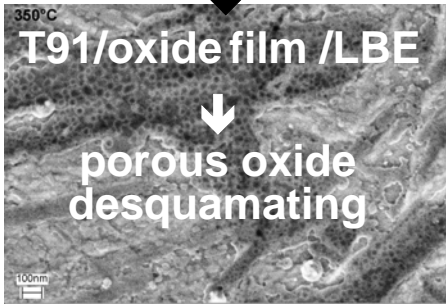
CNRS-CECM & CNRS-LTPCM

**«T91-LBE» after 12 hours in flowing He-4%H₂: fast corrosion kinetics
with delamination of porous oxide layers already at 350°C**



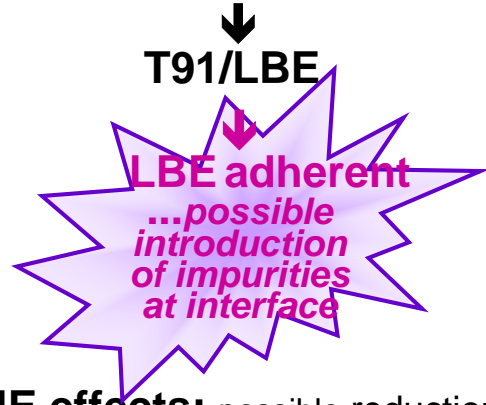
2. Mechanical behaviour of «T91 - LBE», «T91 - Lead»
* resistance to LME : intimate contact ?

(I) by optimizing the environmental conditions (\pm active oxygen control, temperature, LM chemistry) (example: LBE+flowing He-4%H₂)



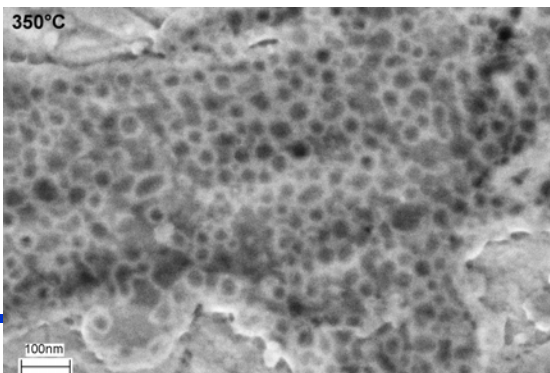
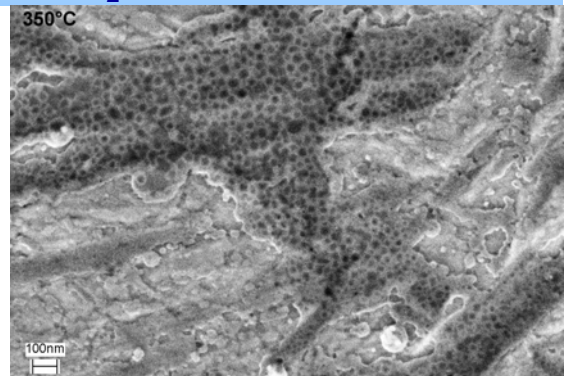
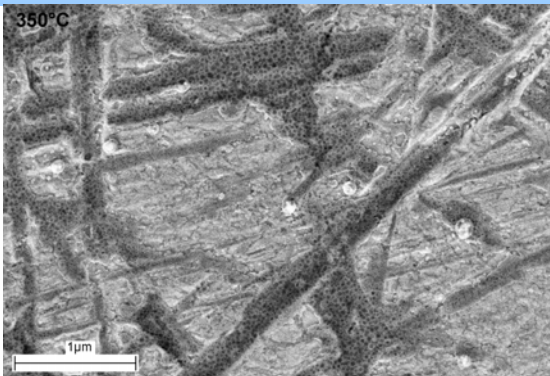
LME effects: reduction of energy to rupture, ductility, UTS on smooth & **notched** specimens

(II) by pretreating chemically, electrochemically specimens "and" LM (i.e. pretinning...)



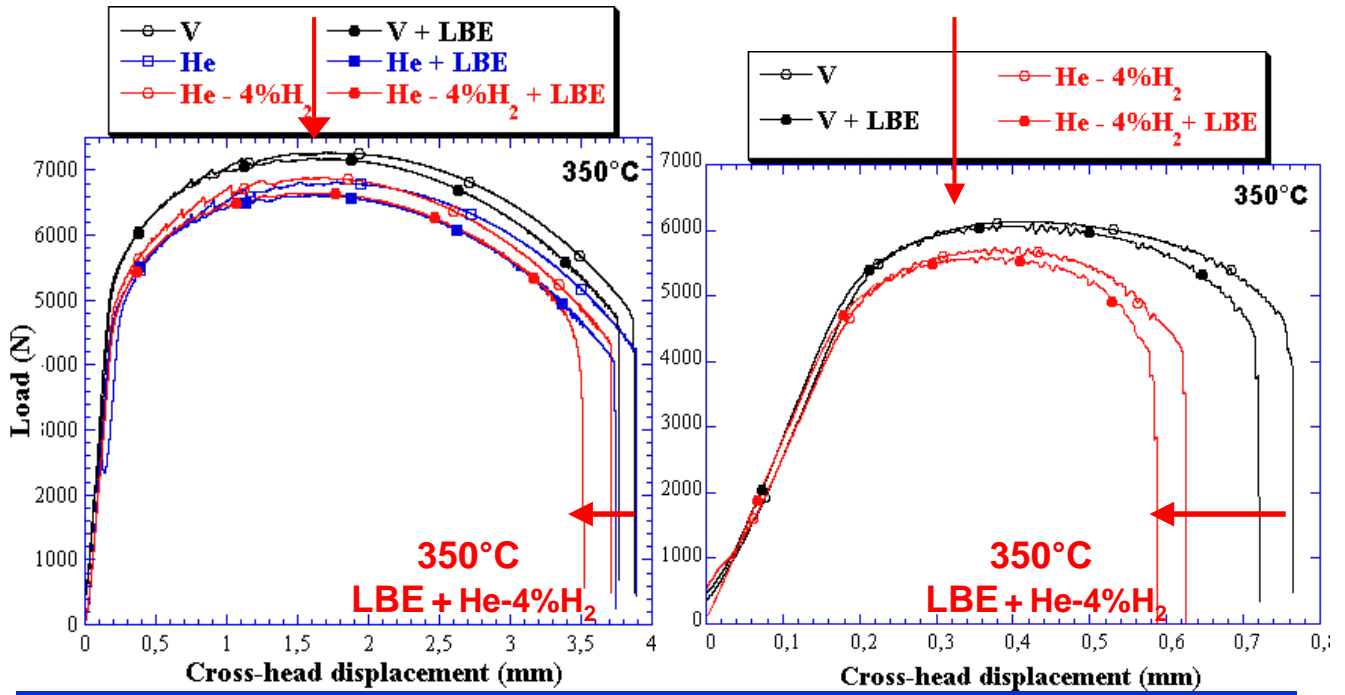
LME effects: possible reduction of ductility, UTS... brittle failure of smooth specimens

LMC : already significant after 12 h exposure to LBE at 350°C under flowing He-4%H₂



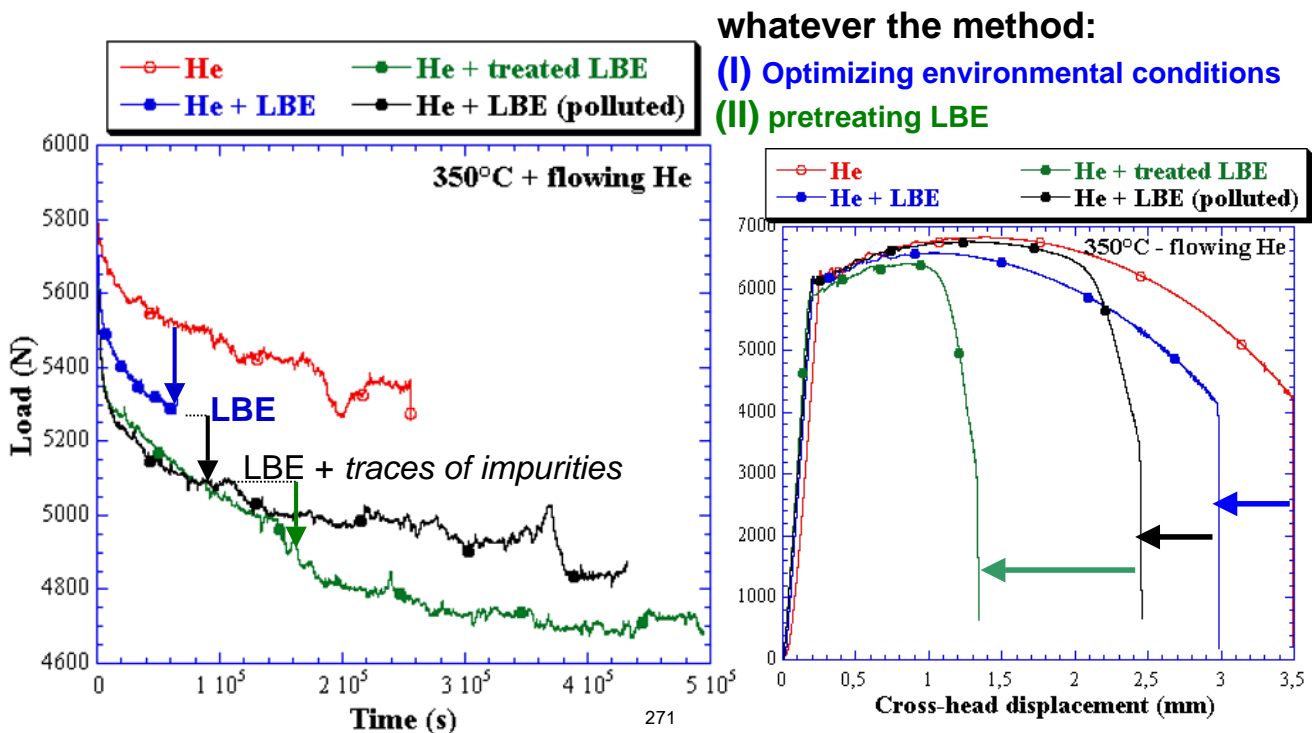
with delamination of porous oxide layers
→ **LME**

2. Resistance to LME of «T91-LBE»: tensile tests with smooth specimens, increased with notched specimens



CNRS-CECM & CNRS-LTPCM

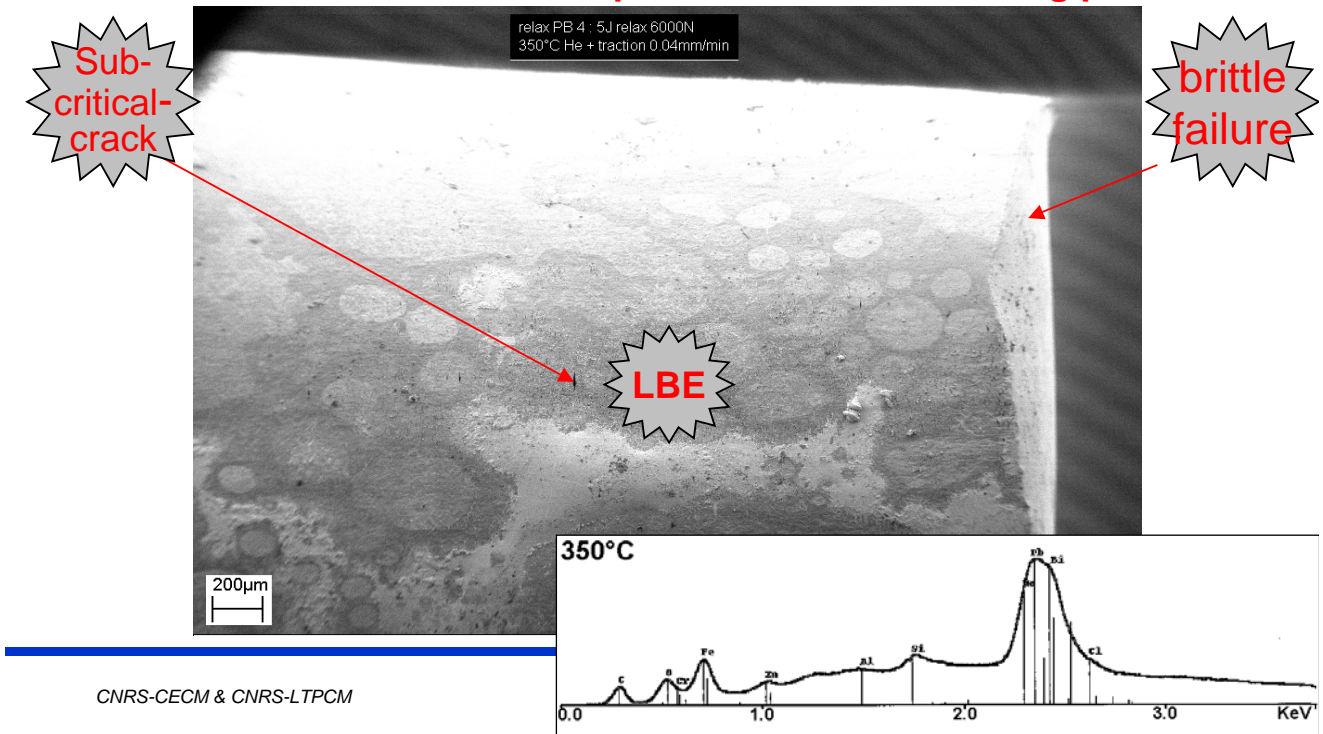
2. Mechanical behaviour of «T91-LBE»: stress relaxation kinetics are accelerated by contact with LBE



Brittle failure of T91

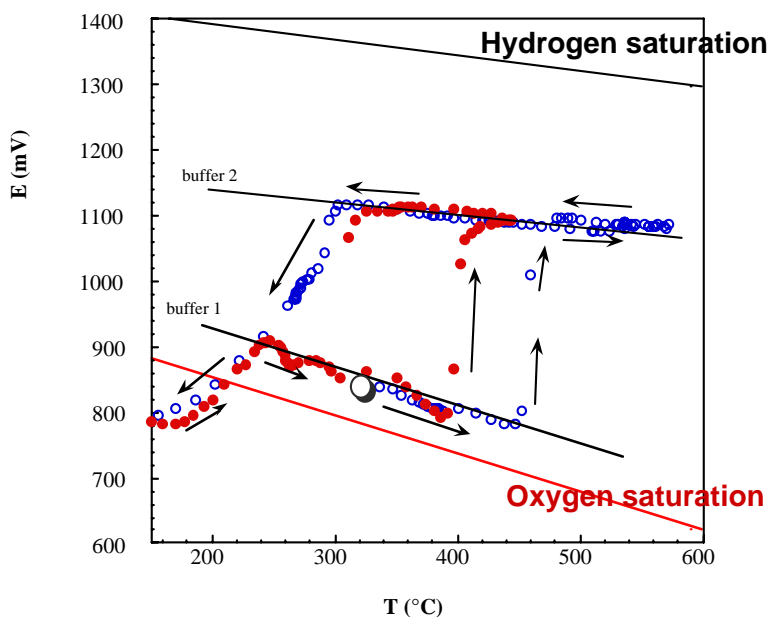
due to improved contact with LBE thanks to pretreatment of LBE

Or due to impurities introduced during pretreatment



3. Possibility of monitoring a LBE bath ?

Air reference sensor



Thermodynamically, e.m.f signal varying between the two limits;

Under specific conditions, like leakage or impurities in LBE...

the oxygen content is controlled by buffering phenomena...

Conclusions & perspectives

Until now, compatibility of T91 steel in standard metallurgical state with LBE, without pollution by metallic or metalloid species can be considered satisfying

1. Corrosion behaviour of «T91 - LBE»

1.1 The importance of the initial surface conditions and initial oxidation conditions is emphasized in order to retard localized & generalized corrosion

1.2 To regulate the corrosion kinetics and prevent sudden oxidation/dissolution fluctuations, it would be reasonable to introduce oxygen sensors conveniently located; if not, over the whole temperature range of interest (200°C-400°C), it will be difficult to guarantee the integrity of the structure for long durations.

1.3 LBE is known corrosive, lead is corrosive too ; the corrosion effects are identical, but with the advantage of a significant time delay...in favour of lead! (in otherwise identical oxygen contents and temperature)

CNRS-CECM & CNRS-LTPCM

Conclusions & perspectives

2. Mechanical behaviour of «T91 - LBE»

2.1 Is «T91-LBE» an embrittling couple ?

Limited embrittling effects are detected until now by means of tensile tests, when the steel is in its as received metallurgical state

2.2 Except if one forces the intimate contact between T91 and LBE

- using appropriate thermochemical conditions (HT, low PO₂, long duration)
- using adapted chemical or electrochemical pre-treatments

in such case, brittle failure is not excluded

2.3 In spite of LBE induced cavitation, good cavitation tolerance of T91 steel that could limit acceleration of creep or stress relaxation in LBE at long term.

Recommendations for MEGAPIE

- good contact «T91-LBE» must be avoided.
- **It would be** important to follow the oxygen content during operation, at least using an ancillary system
- Another point remaining to study:
the impurities level acceptable in the LM target,
with respect to both LMC and LME
either induced by spallation reactions or initially present,
or also introduced in-service.